

THE IMPACT RESPONSE OF COMPOSITE SANDWICH STRUCTURES

Thesis submitted in accordance with the requirements of
the University of Liverpool for the degree of
Doctor of Philosophy by

Hazizan Md. Akil

February 2002



THE UNIVERSITY
of LIVERPOOL

Department of Engineering

List of publications:

- Md. Akil Hazizan and W.J. Cantwell, “The low velocity impact response of foam-based sandwich structures”, *Composites: Part B*, 33, pp. 193-204, 2002.
- Md. Akil Hazizan and W.J. Cantwell, “The low velocity impact response of aluminium honeycomb sandwich structures”, Submitted to *Composites Part: B (Engineering)*, 2002.

Acknowledgements

I would like to take this opportunity to acknowledge the invaluable assistance of my supervisor Professor W.J. Cantwell. In my opinion he is the best supervisor that you can find in the Department. I would also like to gratefully acknowledge the contribution of the technical staff in Materials Science and Engineering namely, Dave Whitehurst, Monica Hughes, Chris Jackson, Tony and Pete. Thanks also due to the secretarial and clerical staff, in particular Pauline and Pat Owen. The companionship of my colleagues in the Composites Group is also warmly acknowledged, in particular Fernando, Graham, James, Kevin, German, Pak and Pedro. Thanks are also due to Alusuisse Airex AG for supplying the foam-core material, especially to Dr. Lukas Berger. Special thanks to my beloved wife for her patience in waiting until this research was completed and also to my two kids, Hafiz and Husna who witnessed all the struggles and strife during this research work. To my mum and dad, this thesis is truly a present for you both for bringing me up with an appreciation for the importance of a knowledge in life.

Abstract

The aim of this research study is to investigate and model the impact response of a wide range of sandwich structures. In order to achieve this aim, a series of drop-weight impact tests were conducted on a range of structures and geometries. The impact response of these structures was predicted using an energy-balance model which accounts for energy absorption in flexure, shear, membrane and contact effects. The impact energy was varied by varying the drop-height of the impactor in order to investigate the elastic impact response of the target and highlight the failure modes at slightly higher energies. The resulting damage in the sandwich structures was also examined by evaluating cross-sections of damaged specimens. In each case, the maximum impact force was used as an indicator to characterise the impact response of the composites and sandwich structures and the values provided by the model were compared with those obtained from the tests.

The rate sensitivity of key material properties such as the elastic modulus of the skin and the shear modulus of the core were found to be rates-insensitive over the range of crosshead displacement rates considered. The contact stiffness parameters were also evaluated and found to be unaffected by changes in the crosshead displacement rate. Agreement between the predicted values offered by the energy-balance model and the experimental values was found to be good for the range of composite structures considered in this study. However, the accuracy of the model diminished as damage occurs in these systems. Examinations of the cross-sections of the foam-based sandwich structures indicated that the mode of failure is strongly dependent upon the properties of the foam core. The maximum impact force for a given impact energy was found to increase with the stiffness of the core material. Energy absorption in the low modulus core systems is dominated by a shear deformation mechanism. In contrast, in high density core systems, contact effects are the dominant factor in energy absorption mechanism.

TABLE OF CONTENTS

1.0 INTRODUCTION.....	1
1.1 Preface.....	1
1.2 Fibres.....	5
1.2.1 Glass fibres.....	5
1.2.2 Carbon fibres.....	6
1.2.3 Kevlar fibres.....	8
1.3 Matrices.....	9
1.3.1 Thermoset resins.....	9
1.3.2 Thermoplastic resins.....	10
1.4 Interphase region.....	11
1.5 Structural sandwich construction.....	12
1.5.1 Skin materials.....	13
1.5.2 Core materials.....	14
1.5.2.1 Honeycomb cores.....	14
1.5.2.2 Balsa wood.....	16
1.5.2.3 Cellular foams.....	16
1.5.2.3.1 Polyurethane foam (PUR).....	17
1.5.2.3.2 Polyvinyl chloride (PVC).....	17
1.5.2.3.3 Polystyrene foam (PS).....	17
1.5.2.3.4 Polymethacrylimide foam (PMI).....	18
1.5.3 Adhesive systems.....	18
1.6 Application of laminated composites.....	19
1.6.1 Automotive applications.....	19
1.6.2 Marine applications.....	21
1.6.3 Biomedical applications.....	21
1.6.4 Aerospace applications.....	22
1.7 Applications of sandwich structures.....	23
1.8 Reasons for the increasing use of composites.....	24

1.9 Problems associated with composite materials.....	24
1.10 References.....	26
2.0 LITERATURE REVIEW.....	29
2.1 The influence of constituent properties on the impact response of composite materials.....	29
2.1.1 Fibres.....	29
2.1.2 Matrix.....	33
2.1.3 Interphase.....	42
2.2 The effect of specimen geometry on the impact response of composite materials.....	50
2.3 The effect of stacking sequence on the impact response of composite materials.....	54
2.4 The effect of projectile characteristics on the impact response of composite materials.....	58
2.5 The effect of loading rates on the impact response of composite materials.....	62
2.6 Aims and objectives of the research.....	66
2.7 References.....	68
3.0 THEORETICAL APPROACHES AND IMPACT MODEL.....	78
3.1 Introduction.....	78
3.2 Types of impact loading.....	79
3.2.1 Low velocity impact loading.....	80
3.2.2 High velocity (ballistic) impact loading.....	81
3.3 Contact problem in impact.....	82
3.3.1 Indentation of laminates.....	85
3.3.2 Indentation of sandwich structures.....	86
3.4 Mathematical models.....	87
3.4.1 Solution to dynamic equation of motion.....	87
3.4.2 Mass-spring models.....	89

3.4.2.1 Single degree of freedom.....	90
3.4.2.2 Two degree of freedom.....	92
3.4.3 Energy balance models.....	94
3.5 References.....	98
4.0 MATERIAL PROPERTIES AND PREPARATIONS.....	102
4.1 Skin material.....	102
4.2 Core materials.....	103
4.2.1 Foam-core materials.....	103
4.2.1.1 R63 Foams.....	104
4.2.1.2 R82 Foams.....	104
4.2.1.3 C70 Foams.....	105
4.2.2 Aluminium honeycomb core material (Aeroweb 3003).....	106
4.3 Materials preparation.....	108
4.3.1 Preparation of the composite plates and skin materials.....	109
4.3.2 Preparation of the core material.....	109
4.4 The manufacture of the sandwich panels.....	110
4.4.1 The manufacture of the foam-core sandwich panels.....	110
4.5 References.....	113
5.0 EXPERIMENTAL PROCEDURE.....	114
5.1 Impact tests.....	114
5.1.1 Impact tests on the composite and sandwich beams.....	116
5.1.2 Impact tests on circular plates and sandwich panels.....	116
5.2 Three-point bend tests on foam-core materials.....	118
5.3 Determination of bending and shear stiffness of the sandwich structures.....	118
5.3.1 The three-point bend tests for determining the value of D and G for aluminium honeycomb beams.....	119

5.3.2	Determination of D from the properties of the constituents for sandwich foam core beams	121
5.4	Indentation tests on sandwich beams	123
5.5	Single edge notch bend (SENB) tests	125
5.6	Compression tests	127
5.7	Centre notch flexure (CNF) tests	127
5.8	Optical microscopy	128
5.9	References	129
6.0	Energy-balance model	130
6.1	Energy-balance models	130
6.1.1	Energy-balance model for a laminated composite beam	130
6.1.2	Energy-balance model for a circular composite plate	132
6.1.3	Energy-balance model for a composite sandwich beam	136
6.2	References	139
7.0	RESULTS AND DISCUSSION	140
7.1	Characterising the behaviour of the constituent materials	140
7.1.1	The effect of crosshead displacement rate on the flexural modulus of the glass fibre reinforced skin	141
7.1.2	The effect of loading rate on the flexural modulus of the foam core materials	143
7.1.3	The fracture properties of the foams	153
7.1.4	The effect of loading rate on the indentation properties of the sandwich structures	158
7.1.5	The influence of loading rate on the mechanical properties of aluminium-core sandwich materials	171
7.1.6	Characterisation of the skin-core interfacial fracture properties	174
7.1.7	Compression properties of the foam core materials	176

7.1.8 Summary of the rate-dependent properties of the composites and sandwich structures.....	184
7.2 Impact test results on GFR epoxy beams and plates.....	185
7.2.1 Impact tests on the GFR epoxy beams.....	185
7.2.2 Impact test on the GFR epoxy plates.....	192
7.3 Impact test results on foam-based sandwich structures.....	195
7.4 Energy absorption analysis for the foam-core sandwich structures.....	202
7.5 Impact test results on the aluminium honeycomb sandwich structures.....	206
7.5.1 Impact tests on the aluminium honeycomb sandwich beams.....	206
7.5.2 Impact tests on the aluminium honeycomb sandwich panels.....	215
7.6 Energy absorption analysis for the aluminium honeycomb sandwich structures.....	218
7.7 Damage development under low velocity impact loading.....	221
7.7.1 Impact damage in laminated composite beams.....	221
7.7.2 Impact damage in the aluminium honeycomb beams and panels.....	224
7.7.3 Impact damage in the foam core sandwich beams.....	229
7.8 References.....	235
8.0 CONCLUSIONS AND FURTHER WORK.....	237
8.1 Mechanical tests.....	237
8.2 Energy-balance model.....	237
8.3 Impact response and damage.....	238
8.4 Suggestions for further work.....	239

CHAPTER 1: INTRODUCTION

This chapter will give a brief overview of composite materials explaining why they are finding increasing use in a wide range of engineering structures. The chapter also contains brief summaries of the type of fibres and matrix materials used in the manufacture of composite materials as well as an introduction to load-bearing sandwich structures.

1.1 Preface

Composite materials are widely used in a variety of applications, ranging from engineering and aerospace structures to medical and surgery components replacing metallic materials such as aluminium and titanium alloys. Composites, offering light weight coupled with high strength and stiffness properties, are being used in the manufacture of satellites, high performance aircraft, and luxury sailboats as well as submarines. A comparison of some typical values of the properties of common engineering materials at room temperature is given in Table 1.1. On the basis of strength and stiffness alone, composites do not offer clear advantages over conventional materials particularly since their elongation to fracture is often much lower than for example, steel. Clear advantages only appear when the specific modulus and specific strength of these engineering materials are considered as shown in Figure 1.1. In the recent years, there has been a rapid growth in the use of composites and it is likely that this will continue. The main engineering properties of composite materials are derived predominantly from the properties of the fibre reinforcement. The groups of fibre reinforcement include continuous and discontinuous long and short fibres. Various forms of composite materials are based on this fibre reinforcement including woven, non-woven, braided and knitted composites. All of these reinforcement types are possible and each provides a unique set of engineering properties. For example, continuous and long discontinuous fibre-reinforced composites offer high levels of translation of fibre properties into the finished composite. High performance composites offer combinations of engineering properties which cannot be achieved using

homogeneous metallic materials such as steel, titanium and aluminium. More recent developments have led to the commercial availability of a wide range of high strength, high stiffness organic and inorganic fibrous materials for use in high performance engineering applications.

Material	Density (kgm ³) x10 ³	Young's Modulus (GPa)	Tensile Strength (MPa)	Specific Modulus (GPa/Mgm ⁻³)	Specific Strength (MPa/ Mgm ⁻³)	Heat Resistance (°C)
High strength Al-Zn-Mg Alloy	2.8	72	503	25.7	180	350
Quenched and tempered Low alloy steel	7.85	207	2050-600	26.4	261-76	800
Carbon fibre-epoxy Parallel to fibres	1.62	220	1400	135	865	260
Glass fibre-polyester Parallel to fibres	1.93	38	750	19.7	390	250

Table 1.1: A comparison of typical properties of some engineering materials at 20°C [1].

A composite is defined as a material system that consists of a combination of two or more components, typically the fibre and matrix [2]. The fibres are stiff and relatively long and are embedded in a matrix that holds them in place. A low power micrograph of a glass fibre reinforced composite is shown in Figure 1.2. Here, the fibres can be clearly seen. Hull [1] categorised composites as follows:

- 1) The material consists of two or more physically distinct and mechanically separable materials.

- 2) The material can be made by mixing the separate materials in such a way that the dispersion of one material in the other can be done in a controlled way to achieved optimum properties.
- 3) The properties are superior, and possibly unique in some specific respects, to the properties of the individual components.

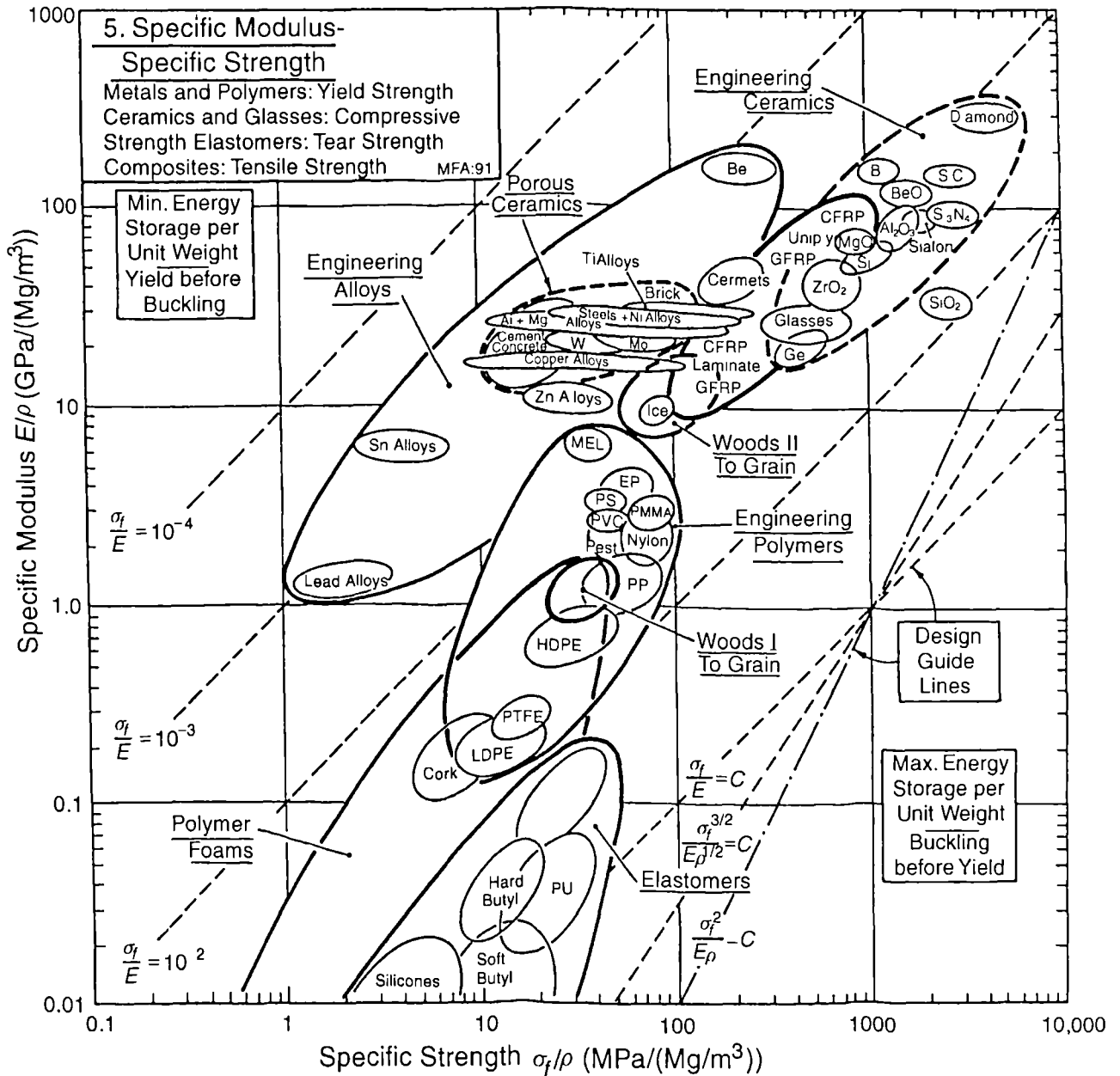


Figure 1.1: A plot of specific modulus (E/ρ) against specific strength (σ_f/ρ) for various types of engineering materials, adapted from [3].

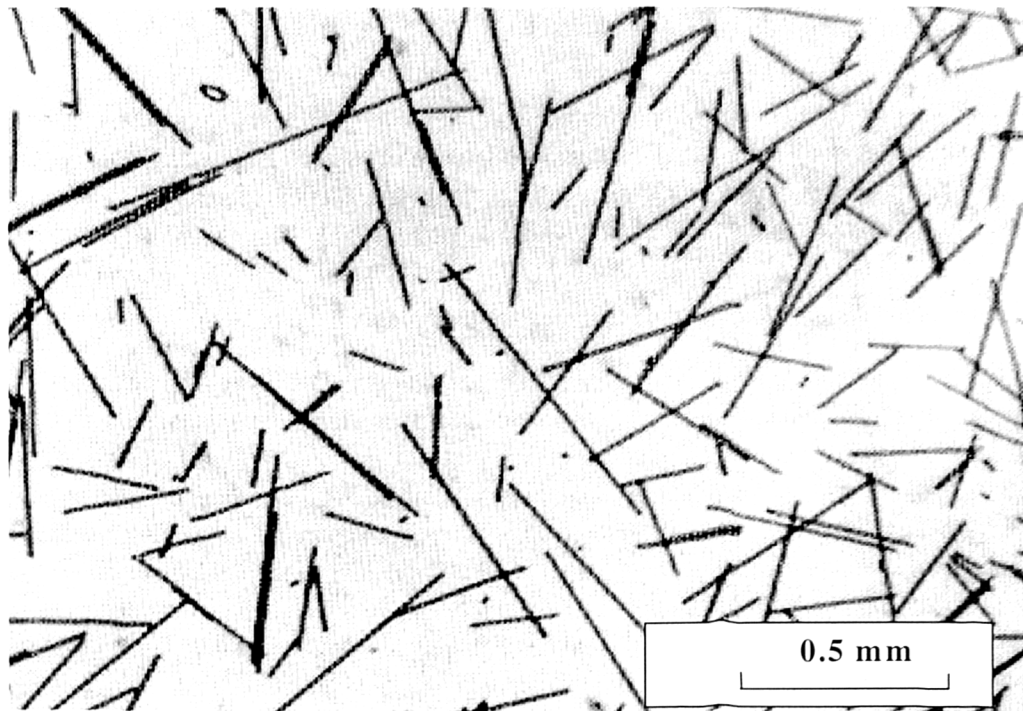


Figure 1.2: Micrograph of a short glass fibre reinforced polypropylene composite after injection moulding [4].

Generally, the fibres are strong and stiff relative to matrix. There are many types of fibre available commercially such as glass, Kevlar, carbon, polyethylene and boron. Each fibre has unique properties and offers distinctive characteristics when used in combination with the matrix. Other types of reinforcement can be in the form of particulates such as spheres, ellipsoids, plates and rods. The matrix phase in a composite material is often based on a polymeric material (e.g. epoxy resins, polyesters, polypropylene etc.), although other matrices such as metallic, ceramic or carbon are finding increasing use. Both the fibre and matrix phase retain their individual characteristics and directly influence the final properties of the particular composite material. The properties of the composite can be controlled by varying the fibre diameter, fibre volume fraction and fibre orientation, although tooling and manufacturing processes can also be manipulated. Another important constituent of a composite material is the interphase region between the fibre and matrix. Clearly, the

characteristics and properties of this region will greatly affect the mechanical properties of the resulting composite. The following section will deal individually with the constituents of composite materials giving a brief outline on their classifications and properties.

1.2 Fibres

Fibres are the main load-bearing constituents of a composite, providing the material with much of its strength and stiffness. There are many fibre types available in the market and the range is still growing rapidly. The aim of this section is to present briefly the fibres that are commonly used in the aerospace, automotive and marine industries. Although the fibres can be classified into two main categories, these being organic and inorganic fibres, the most common fibres used are:

- Glass fibres
- Carbon fibres
- Kevlar

1.2.1 Glass fibres

Glass fibre reinforced composite materials have found extensive use in low performance non-structural applications as well as high performance engineering structures. Glass fibre composites offer acceptable engineering properties however glass fibre surfaces are sensitive to moisture attack under certain conditions of exposure and above a threshold stress level. Many different compositions of mineral glasses have been investigated and are currently used in manufacturing glass fibre reinforcements. The most popular and widely used is a silica-based glass fibre containing additions of oxides such as calcium, boron, sodium, iron and aluminium. Typical examples of commercially-available glass fibres are E-glass, C-glass and S-glass. E-glass is known to offer good electrical properties as well as good stiffness and strength at a low cost. C-glass fibres offer a superior chemical corrosion resistance but this type of fibre is more expensive and weaker than the E-glass fibre. S-glass fibres offer a superior high temperature resistance

and a higher value of Young's modulus compared to E and S glass fibres. S-glass fibres are used in the aircraft industry, where their higher modulus properties justify the extra cost incurred. S-glass fibres contain greater amounts of alumina compared to E-glass fibres. Typical compositions of glass fibres are given in Table 1.2.

Components	Grade of glass			
	A (High alkali)	C (Chemical)	E (Electrical)	S (High strength)
Silicon oxide	72.0	64.6	54.3	64.2
Aluminium oxide	0.6	4.1	15.2	24.8
Ferrous oxide	-	-	-	0.21
Calcium oxide	10.0	13.2	17.2	0.01
Magnesium oxide	2.5	3.3	4.7	10.27
Sodium oxide	14.2	7.7	0.6	0.27
Potassium oxide	-	1.7	-	-
Boron oxide	-	4.7	8.0	0.01
Barium oxide	-	0.9	-	0.2
Miscellaneous	0.7	-	-	-

Table 1.2: Glass fibre compositions (weight %) [5].

1.2.2 Carbon fibres

Carbon fibres offer the highest specific strength and stiffness properties amongst the commonly- used fibres and hence they are extensively used in aerospace applications where minimum weight and high strength and stiffness are fundamental design requirements. Carbon fibres are also used in the manufacture of sports equipment where reduced weight can significantly enhance performance. As a result of recent advances, carbon fibres are now available offering a wide range of mechanical properties at a competitive price. Carbon fibres are manufactured by a thermal decomposition method using an organic precursor such as rayon or polyacrylonitrile (PAN). PAN is a polymer

that has a molecular conformation closely resembling that of polyethylene. During the decomposition process, every alternate hydrogen side group of polyethylene is replaced by nitrile groups. The process involves an accurately-controlled heat treatment process and the application of tension to produce a highly ordered carbon or graphite structure. In carbon fibre composites, the bond strength can be enhanced through an oxidation process of the carbon fibre surface [6]. Dorey [7] showed that the interlaminar shear strength of unidirectional CFRP rapidly increased with the level of surface treatment up to a certain level. In contrast, he also reported that the notched tensile strength of multidirectional CFRP reduced significantly with increasing surface treatment as shown in Figure 1.3. PAN-based carbon fibres that are presently available offering modulus values between 280 and 450 GPa and tensile strengths between 4140 and 5170 MPa.

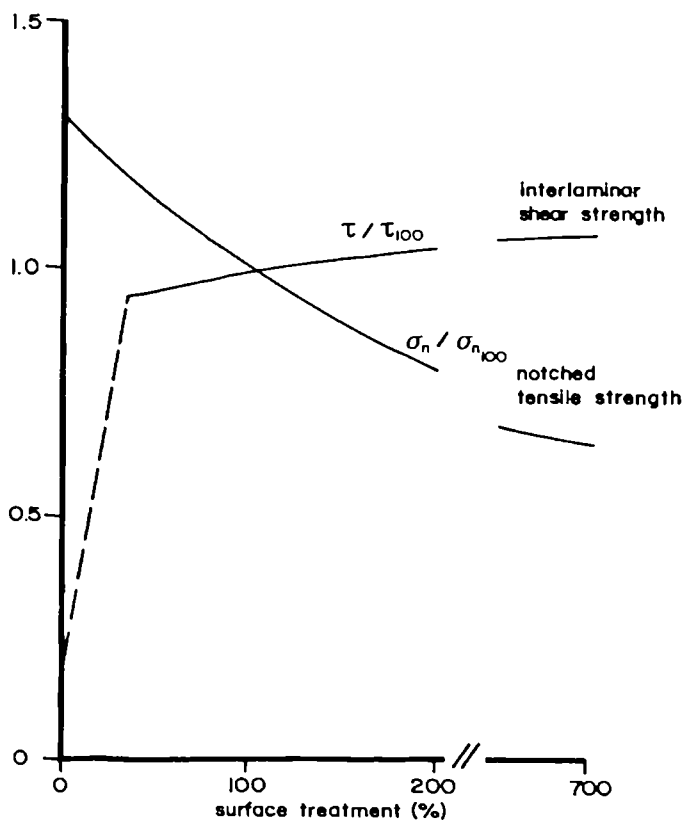


Figure 1.3: The effect of fibre surface treatment on the interlaminar shear strength of a unidirectional carbon fibre epoxy composite and on the notched tensile strength of a multi-directional carbon fibre epoxy composite [7].

1.2.3 Kevlar fibres

Kevlar fibres are amongst the most successful organic fibres available and are manufactured by the Du Pont company. This fibre was introduced in 1972. Initially, Kevlar fibres were developed for cord reinforcement in the tyre-making industries. The actual chemical structure of this material is not fully known but it is believed that it is based on an aromatic polyamide poly (paraphenylene terephthalamide). There are various types of Kevlar fibre available and the two most commonly used are Kevlar 29 and Kevlar 49. Kevlar 29 offers good overall mechanical properties and is used as an all purpose yarn whereas Kevlar 49 offers a much higher modulus. Some typical properties of Kevlar fibres together with other high performance fibres are summarised in Table 1.3. Kevlar is known to offer good heat resistance with melting and glass transition temperatures above 375 °C and 530 °C respectively [8].

Fibre type	Density (kg/m ³)	Tensile strength (MPa)	Tensile modulus (MPa)	Elongation at fracture (%)	Specific modulus (MPa/kgm ⁻³)	Specific strength (MPa/kgm ⁻³)	Max. use temp. (°C)
Kevlar 29	1430	2900	70000	3.6	49.0	2.0	250
Kevlar 49	1450	2900	135000	2.8	93.1	2.0	250
Nomex	1380	600	17000	22	12.3	0.4	250
Technora	1390	3300	70000	4.3	50.4	2.4	250
Boron	2500	2550	400000	1.0	160.0	1.0	2000
PBI	1430	400	5700	30	4.0	0.3	250
Ekonol	1400	3800	136000	2.6	97.1	2.7	150
SiC	2800	4000	420000	0.6	150.0	1.4	1300
E glass	2550	2600	72000	3	28.2	1.0	350
S glass	2480	4800	85000	5.3	34.3	1.9	300

Table 1.3: A comparison of the properties of several high performance fibres [9].

1.3 Matrices

The matrix phase in a composite material serves a number of functions including [10]:

- To hold the fibres
- To transfer and distribute the applied load from one fibre to another
- To carry interlaminar shear

The choice of matrix system is often limited by the end use of the composite. In general, the matrix phase should offer [10]:

- Low moisture absorption characteristics
- Low shrinkage
- Low coefficient of thermal expansion
- Exhibit elastic properties
- Have reasonable strength, modulus and elongation

Polymeric matrices can be broadly classified into thermoset and thermoplastic resins. The most common thermoset matrices are polyesters, epoxies, bismaleimides and polyimides. Thermoplastic-based composites were first introduced in the 1980s as a result of the need to achieve a faster manufacturing time with fewer manufacturing stages, high delamination resistance and superior damage tolerance properties coupled with a low moisture absorption response. These systems also offer a very low level of toxicity compared to thermoset resins. Popular thermoplastic resins include polypropylene, high-density polyethylene, polycarbonate, polyethersulphone, polyphenylene sulphide and polyphenylene oxide.

1.3.1 Thermoset resins

In thermosetting polymers, the liquid resin is converted into a solid through a chemical cross-linking procedure known as a curing process. This process can be done at room temperature but the most common practice is to heat the resin at several temperatures for pre-determined times to achieve an optimum density of cross-linking. This process is then followed by a high temperature post-curing processes in order to minimise any

further curing and subsequent change in properties during the service-life. Thermosets are usually isotropic and their most distinctive behaviour compared to thermoplastic resins is that they do not melt upon heating. Thermosets are generally brittle solids. Polyester matrices have been used for many years in a wide range of structures and applications. The composition of polyester resins consists of up to 50% by weight of unsaturated monomers and solvents such as styrene. Polyesters can be cured using a catalyst such as peroxide resulting in an exothermic reaction that can be initiated at room temperature. Another widely used thermosetting matrix is epoxy resin. Epoxies generally offer advantages such as good interfacial adhesion, low shrinkage, solvent and chemical resistance, resistance to creep and fatigue, a wide range of curing options, strength and flexibility and good electrical properties. However, they do not have the high temperature resistance associated with bismaleimides or polyamides and they cost more than polyesters [11].

1.3.2 Thermoplastic resins

In contrast to thermosets, thermoplastics are not based on a crosslinking network and their strength and stiffness properties are dictated by the inherent properties of the monomer repeat units and its molecular weight [12]. Thermoplastic matrices fall into two categories, namely amorphous and semi-crystalline polymers. Both amorphous and semi-crystalline thermoplastics are said to have a certain degree of anisotropy. The degree of the anisotropy depends on the conditions of the solidification process.

Amorphous thermoplastics contain high concentrations of molecular entanglements that effectively act as crosslinks whereas a high degree of molecular order and alignment can be seen in semi-crystalline polymers. Thermoplastic matrices are often reinforced with short fibres or platelets. Generally, a wide range of properties can be obtained by varying the molecular weight, molecular weight distribution and molecular chemistry. Most thermoplastics undergo large deformations before fracture and their mechanical properties are strongly dependent on the temperature and applied strain rate. A common

and well-known characteristic of many thermoplastic polymers is the creep phenomenon where strain increases under constant applied load.

1.4 Interphase region

As stated earlier in the definition of a composite material, there must be at least two or more components that are separated by an interface or interphase within the composite material. The interphase region between the fibre and matrix is of vital importance since it plays a major role in determining the mechanical and physical properties of the composite. In particular, the stresses acting on the matrix are transmitted to the fibre across the interface. Some appreciation of the physical properties and characteristics of the interface is essential in order to gain an understanding of composite materials. For example, the interface is a dominant factor in determining the fracture toughness properties of composite materials and their response to corrosive and aqueous environments [13-15].

Composite materials with weak interfaces have relatively low strength and stiffness but offer high resistance to fracture whereas materials with strong interfaces generally have high strengths and stiffnesses but are very brittle [1]. Generally, high toughness composites can be achieved by promoting a 'crack blunting' mechanism whereas high mechanical strength can be achieved through a uniform stress transfer between the matrix and the fibre via a strong interface bond [3]. Therefore, it is extremely difficult to simultaneously improve a number of key mechanical properties such as stiffness, strength and fracture toughness. For example, certain types of polyester laminate offer high toughness values but relatively lower strength values.

In order to improve the strength of a bond, the surfaces of carbon fibres are treated via an oxidative process whilst glass fibres are frequently treated with a coupling agent. The interphase region can affect the type of failure mode occurring in the composite. In many cases, the strength of the interface between the fibre and matrix can be

manipulated in order to achieve an optimum level of treatment but this often results in a reduction in the mechanical properties of composite materials.

1.5 Structural sandwich construction

The American Standard for Testing Materials, ASTM, defines a sandwich structure as “a special form of a laminated composite comprising of a combination of different materials that are bonded to each other so as to utilise the properties of each separate component to the structural advantage of the whole assembly”. The faces are usually thin and stiff in order to provide the required bending and shear stiffness and to carry the edgewise and bending loads as well as the in plane shear loading. The properties of the core vary depending on the application. However the main function of core material is to stabilise the facings and carry shear loads through the thickness. It should therefore be rigid and as light possible. Three main elements of sandwich construction are:

- Two thin and strong sheets (skins)
- A thick layer of low density material which may be less stiff and strong than the skins (core)
- An adhesive joint attachment to hold the skins and core in place to form a continuous structure

Today, sandwich structures are widely used in the fabrication of primary and secondary structures of civil and military aerospace components. The design principle behind a sandwich structure is based on an I-beam, which is an efficient structural shape because much of the material is placed in the flanges situated farthest from the neutral axis. Only enough material is left in the connecting web to make the flanges act in concert and to resist shear and buckling loads. In a sandwich structure, the face takes the place of the flanges and the core takes the place of the web. The difference is that the core of a sandwich is of a different material from the faces and is as a continuous support for the faces rather than concentrated in narrow web in I-beam. Since the face and the core are

of the different materials, an adhesive is used to bond these materials. The adhesive that is used to bond the faces to the core are therefore of critical importance.

According to history, a Frenchman called Duleau first discovered the concept of sandwich construction in 1820 as stated in reference [16]. Although the concept was discovered as early as this, it was only applied and made available commercially one hundred years later. One of the earliest sandwich panels produced was an asbestos-faced sandwich panel with a fireboard core prior to World War Two. Another early application of sandwich construction was in the Mosquito aircraft produced in Britain in which part of the aircraft body was made of a balsa core sandwich panel with bonded Veneer faces.

The development of high performance core materials started in the 1940s and efforts still continue in order to reduce the weight of engineering sandwich structures. Balsa was the first core material considered and used in the manufacture of cruising yachts and launches. Honeycomb core materials appeared in the late 1940s and early 1950s and are currently used in many aerospace applications. Polymeric core materials such as polyvinyl chloride (PVC) and polyurethane (PU) appeared in the late 1950s and early 1960s.

1.5.1 Skin materials

Almost any structural material can be used as a skin material in a sandwich panel provided that it is available in the form of thin flat sheet [17]. The main function of the skin in a sandwich structure is to provide bending and shear stiffness and to carry the bending and shear loads. Basically, the skin should offer or exhibit a high stiffness, high strength, good surface finish, high impact and environmental resistance and a good wear resistance. The most commonly used skin materials can generally be divided into two categories, namely metallic and non-metallic.

The metallic group of skin materials contains stainless steel, aluminium and titanium alloys. In contrast, the non-metallic group consists of wood derivative products such as pine and plywood as well as fibre composites including unidirectional, bi-directional and random fibre composites. Fibre composite materials are capable of providing strength properties similar to, or even higher than those of metals. However, the stiffness properties are often slightly lower than metals.

1.5.2 Core materials

In general, core materials can be divided into four different groups, these being corrugated, honeycomb, balsa wood and cellular foams. As indicated above, the core should be as light as possible but it is also expected to offer a reasonable modulus to withstand shear loads in the transverse direction. The following section will discuss briefly the core materials that are commonly used in sandwich construction.

1.5.2.1 Honeycomb cores

Honeycomb-type cores are widely used in a number of aerospace applications. Common types of honeycomb include products made from uncoated and resin-impregnated kraft paper, various aluminium alloys, aramid paper and carbon fibre reinforced plastics. Honeycomb materials can be produced with a variety of cell shapes but the most popular is honeycomb. Other shapes include rectangular, square and over-expanded hexagonal cells. Several types of honeycomb core are presented in Figure 1.4.

Honeycombs based on steels are used in smaller quantities compared to other types of honeycomb materials. Most honeycomb cores are adhesively-bonded to the skin by means of a suitable adhesive system. Aluminium honeycomb core materials have been widely used in aerospace and aircraft applications. These aluminium alloys are general-purpose aluminium alloys with a good high temperature resistance and they are available with a corrosion-resistant surface treatment.

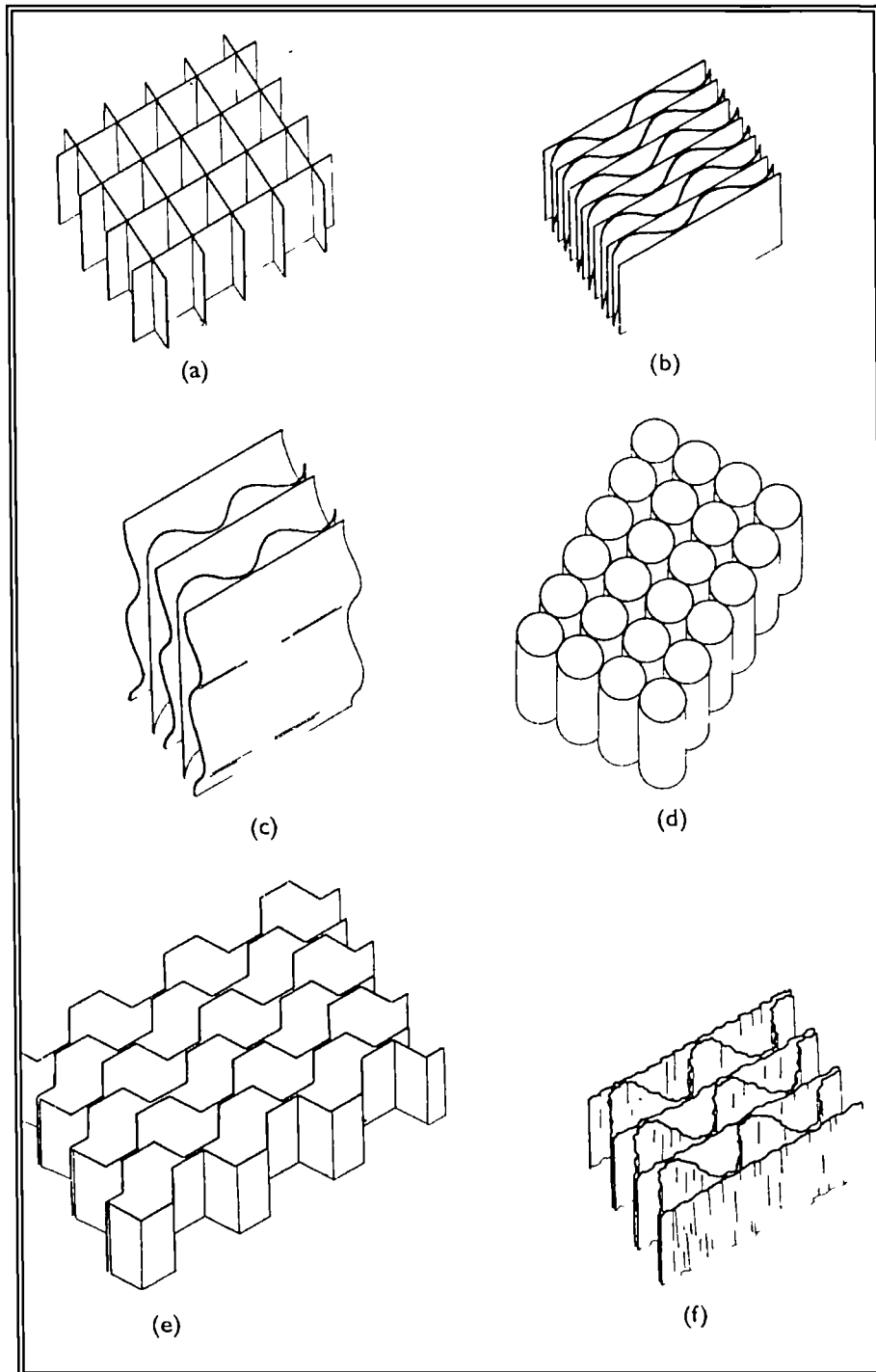


Figure 1.4: Types of honeycomb core. a) Interlocking straight strips, b) and c) a combination of flat and corrugated sheets, d) balsa grain-like honeycomb, e) deformed honeycomb and f) multiwave honeycomb [17].

1.5.2.2 Balsa wood

Balsa was the first core material used in a sandwich structure and it is still in use in the manufacture of launches, and cruising yachts. Balsa is also used in the majority of snow skis, although a few of the higher performance skis employ honeycomb foam or reinforced plastic cores. The traditional advantage of this low cost material coupled with its excellent durability led to significant usage, particularly of selected grades of end-grain balsa. Naturally, balsa contains highly oriented grains parallel to the direction of growth. Therefore, the properties of balsa are superior in the direction of growth but poor in other directions. Balsa is available in a wide range of densities between 100 kgm^{-3} to 300 kgm^{-3} and as a result, it offers a wide a range of mechanical properties. However, balsa is very sensitive to moisture and its mechanical properties deteriorate rapidly with increasing water content. The problem of poor water resistance is usually overcome by employing “end-grain” balsa.

1.5.2.3 Cellular foams

Polymeric foam core materials are widely used in many engineering sectors. Although cellular foams do not offer similar stiffness to weight ratios to honeycomb cores, they offer other advantages such as lower cost and ease of manufacture. In addition, cellular foams offer high thermal insulation properties, acoustical damping and buoyancy on water. In manufacturing polymeric foams, the polymers are foamed by introducing a gas bubble into the liquid monomer or hot polymer, allowing the bubble to form, grow and stabilise followed by a solidification process [18]. The method of introducing the gas into the polymer melts or monomer is done by either using a mechanical stirrer or by mixing it with blowing agents. There are two types of blowing agent available, these being chemical and physical blowing agents. Usually, chemical blowing agents are categorised as additive and normally decompose during heating. Physical blowing agents used are usually an inert gaseous which are passed through the polymer melt at high pressure. Another method of producing polymeric foams is using a low melting point liquid that is mixed with the polymer. The liquid is allowed to evaporate during heating leaving a closed-cell foam structure. The following section will describe briefly

the common cellular foam core materials that are used in sandwich structures and some of their useful properties are given in Table 1.4.

1.5.2.3.1 Polyurethane foam (PUR)

The process of manufacturing PUR foam involves a reaction between isocyanate and polyol with tri-chloro-fluoro-methane or carbon dioxide as a blowing agent vaporised by the heat released during the exothermal reaction [16]. PUR foams are available in various grades from soft to hard textures with a wide range of densities. The properties of these foams can be improved by using additives such as phosphorus to improve flammability resistance etc.

1.5.2.3.2 Polyvinyl chloride (PVC)

PVC foams are available in two different forms, linear PVC and cross-linked PVC (modified PVC). Linear PVC foam is known to have high ductility, good mechanical properties but a poor heat resistance. In contrast, crosslinked PVC foam has greater mechanical properties and a higher heat resistance but the toughness properties are not as good as linear PVC foam. Usually, PVC foams are supplied in finite size blocks with densities between 30 and 400 kgm⁻³. In general, the average mechanical properties of both types of PVC foam are greater than PUR (polyurethane) and PS (polystyrene) foams. However, both are more expensive.

1.5.2.3.3 Polystyrene foam (PS)

Polystyrene foam can be produced in two ways, either by extrusion or by expansion with the help of blowing agents. Usually, the plastic is mixed with the blowing agent and allowed to expand at elevated temperature. The main problem associated with PS foam is that the common blowing agent used is CFC.

1.5.2.3.4 Polymethacrylimide foam (PMI)

Acrylimide cellular plastics are often made from expanded imide modified polycryates. The mechanical properties are very good, perhaps the best of all commercially-available cellular foam. PMI is relatively brittle with an ultimate elongation in tension of approximately 3%. The main advantage is its temperature resistance, making it possible to use PMI foam in conjunction with epoxy prepregs in autoclave manufacturing at temperatures up to 180°C.

Density (kgm ⁻³)	Shear modulus of core material, G _c (MPa)	Thermal conductivity, λ (W/m °C)
<u>Balsa wood</u>		
96	108	0.0509
130	134	0.0588
180	188	0.0710
<u>Polyurethane foam</u>		
30	3	0.025
40	4	0.025
<u>Polystyrene foam</u>		
30	8	0.035
60	20	0.035
<u>PVC foam (linear)</u>		
80	18	0.034
<u>PVC foam (cross-linked)</u>		
45	18	0.024
80	31	0.028
100	40	0.030
130	52	0.034
200	85	0.043

Table 1.4: Typical mechanical and thermal properties of some core materials [19,20]

1.5.3 Adhesive systems

There is a wide range of adhesive systems available for fabricating sandwich structures. These systems are usually developed for specific purposes and each system may only be

good for a limited number of materials. For example, toughened epoxy resins are used to bond composites to aluminium alloys and polyurethane (PUR) is commonly used for bonding to stainless steel. The primary function of the adhesive is to provide satisfactory bonding strength to hold the skin and core materials together. Other concerns about the adhesive system relates to whether the material can withstand the environment that it will be subjected to during its entire service-life. Following concerns over environmental pollution and greenhouse effects, the adhesive system must also comply with environmental guidelines and regulations. In general, the most widely used adhesive systems are those based on epoxy resins. This is due to the stability of the resin at room temperature and also the fact that curing can be done at room temperature.

1.6 Application of laminated composites

Composites are used in a wide range of engineering applications. The marine, aerospace and off-shore industries are among the principal users of these materials. Lightweight, high stiffness to weight ratios, a superior corrosion resistance, high specific modulus and strength and the capability of being tailored to suit a given application explain why they are preferred over more conventional materials such as aluminium and steel. Coupled with these improvements in general overall performance is the fact that the cost of manufacturing components from composite materials is often less than that of more conventional metals.

1.6.1 Automotive applications

Polymer composites started to appear in cars just after the Second World War. Among the first structures made from polymer composites were small components under the hood and inside the passenger compartment. In 1953, a glass fibre reinforced polyester body panel was used on the Corvette, together with other small parts i.e. bumper beams, leaf springs, radiator support, seat backs and the rear floor plan [21]. The body panels were first manufactured using the open mould technique. With increasing usage, demands on composite parts increased rapidly and the existing manufacturing

techniques were no longer capable of coping with the demand. As a result, compression-moulded sheet moulding composites (SMC) emerged. This compression moulding technique offered improved surface finish characteristics and higher production rates. SMC grille opening panels were introduced in the late 1960s and became very popular as a result of the reduced cost through significant part consolidation and weight saving. The use of composites in the automobile industry has grown steadily since and in 1994 the average car produced in the USA contained 50 kg of fibre reinforced composites. Similar trends were also observed in trucks and other vehicles [21]. A summary of composite applications in the automotive sector is given in Table 1.5.

Application	Under trial	Limited production	Well established
Body	Front rails, roof frame	Radiator support, floor pan, cowl panel and EV battery tray	Grille opening panel, rear-end panel. Hood and bumper.
Chassis	Front cross-member and transmission support	Wheels and stabiliser bar links	Leaf spring and disc brake pistons
Interior	Car jack and steering wheel	Knee bolster and window frame/trim	Seat back, seat support, load floor and glove box

Table 1.5: Composite materials in automotive applications [21].

Excellent surface finish, light weight, dent and corrosion resistance are among the advantages of using composites in the design of a car body. One of the most successful automotive structural applications is the composite leaf spring. The composite leaf spring weights 3.6 kg, is made of a filament wound E glass/ epoxy and replaces a ten-leaf steel spring weighing approximately 19 kg [21]. The exceptional weight saving and outstanding durability have been the keystones to the success of the composite spring. Based on fatigue tests and field service [21], composite leaf springs last at least five

times longer than the equivalent steel leaf spring. Durability and light weight also encouraged railroad applications such as in the Secured Modular Automotive Rail Transport (SMART) which serves as a car rack to protect cars from damage and theft during transit. The superior durability of polymer composites has also lead to their extensive use in seats in buses and trains. Composite sandwich panels with glass fibre reinforced phenolic skins bonded to aramid or aluminium honeycomb cells are used in walls, ceilings and floors of many European mass transit cars.

1.6.2 Marine applications

There are two major advantages of using composite materials in marine environments, these being the elimination of galvanic corrosion and ease of tailoring structures for a given application. The use of composite materials in marine applications is widespread and includes mine counter measure vessels, boats, sonar domes, fairings, diving equipment, cables, buoys and floats, propeller shafts and decking [22-24]. Mine counter measure vessels are among the largest GFRP boats ever fabricated. The primary advantage is that the composite is a non-magnetic material therefore reducing the threat from magnetic mines. The use of composite materials in diving applications offers numerous advantages over the standard navy deep-sea diving suit consisting of copper and brass and weighing over 90 kg when out of water [25,26]. The modern dress consists of a fibreglass helmet with a neoprene rubber suit and weighs only 45 kg on land [26]. Surface-supplied gas tubes for oxygen supply to divers made from fibre glass can be charged up to a pressure of 20.6 MPa representing a fifty percent weight saving over traditional steel cylinders.

1.6.3 Biomedical applications

Among the early application of composites in the biomedical field were reinforced acrylics which were used as dental fillings. The resin consists of a polymer matrix and inorganic filler such as barium glass or silica. Another area of interest is in bone replacement. In orthopaedic implants, the potential of using a composite as an implant material was investigated in more specific areas such as femoral components for total

hip replacement, pins, plates, screws for fracture fixations as an alternative material over the metal alloys. In femoral implants, the components are expected to last for entire lifetime of the patient. However, the common problem with components made from existing materials is that it is very stiff and much of the applied joint load is bypassed around the normally highly stressed proximal-medial region of the femur (calcar) [27]. Therefore composites have become an alternative material and two types of fibre reinforced have been extensively investigated, these being carbon fibre reinforced polysulphone (CF/PSu) and carbon fibre reinforced polyether etherketones (CF/PEEK) [27]. There are still many prospects for composites in biomedical applications such as in bone cements, articulation components and soft tissues.

1.6.4 Aerospace applications

The early composite materials used in aerospace applications were based on carbon fibre reinforced plastic. In the aerospace industry where the weight of the component is highly important, engineers and designers have been forced to investigate and consider composite materials for many applications. In the early years, composites were considered too flexible to be used in primary structures in aerospace applications and therefore composites were limited to the secondary structure such as launch vehicles, aircraft frames and wing spars. Even so, the selection of composites was justified by the higher coefficient of thermal expansion of aluminium and superior specific properties compared to steel. As a result, numerous telescopes, optical benches and reflectors were made from carbon fibre reinforced plastics. One of the most recent examples of carbon fibre composites in an aerospace application was in the Eurofighter shown in Figure 1.5. Here, more than seventy percent of its fuselage is made of carbon fibre composite materials. Although carbon fibre reinforced plastics tended to dominate, Kevlar-49 has also been shown to be ideal for manufacturing antenna reflectors [28]. Typical examples of antenna reflectors made from Kevlar-49 include the SatCom-F, Telstar, ANIK-E, SpaceNet and Superbird SCS.

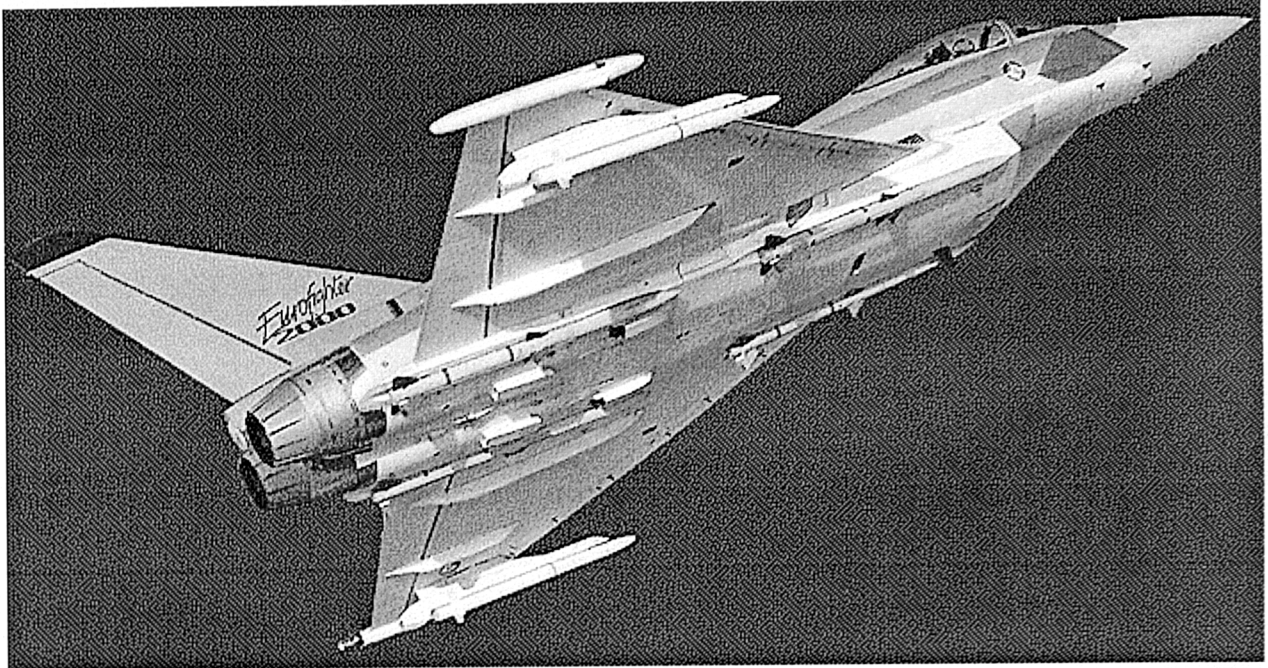


Figure 1.5: The Eurofighter (Typhoon) fuselage is comprised of more than 70% carbon fibre composite and glass fibre reinforced plastics [29].

1.7 Applications of sandwich structures

The primary advantage of sandwich composites is their high stiffness-to-weight-ratios and high bending strength-to-weight ratios. Therefore, they are used in applications where enhanced flexural rigidity is required at a minimum structural weight. For example, GRP terrain vehicles use sandwich design to obtain higher stiffness and strength properties and integrated thermal insulation. Low structural weight is an important feature of the vehicle enabling it to operate in deep snow conditions. A similar application is the manufacturing of sandwich containers, which offer low weight coupled with high thermal insulation for the transportation of cold goods such as fruits, foods etc. Sandwich structures are also used for a range of transportation applications, including cars, subway cars and trains with an aim of reducing weight, emissions and manufacturing costs, acoustical and thermal insulation. Sandwich designs are also used in flooring, interior and exterior panels. In addition, there are a variety of pleasure boats and ships made in sandwich design typically decks and hull structures. In civil

engineering applications, sandwich panels have been used for many years for their low weight and thermal insulation properties. In the aerospace, sandwich constructions have been used for manufacturing components such as wings, doors, control surfaces, radomes, tailplanes, stabilisers, space structures and antennae.

1.8 Reasons for the increasing use of composites

As briefly mentioned in the previous section, composites offer many advantages over conventional materials. A summary of reasons for this increased use and their end application is given in Table 1.6.

Applications	Materials selected	Reason for use
Military and commercial aircraft	Boron and all carbon fibres	Lighter, stiffer and stronger
Spacecraft with high positional accuracy requirements for optical sensors	Very high modulus carbon fibres	Controlled or zero thermal expansion
Tank and piping	Glass fibre, vinyl esters, bisphenol A fumarates and chlorendic resins	Environmental resistance
CNG tanks	High strength carbon fibres, glass fibre, hybrids and epoxy	Lightweight and damage tolerance
High-speed aircraft	High strength and modulus carbon /epoxy	More reproducible complex surfaces
Tennis and squash racquets	Carbon/epoxy	Less pain and fatigue
Commercial boats	Glass fibre	Water resistance
Racing cars	Carbon/epoxy	Crashworthiness

Table 1.6: Typical applications and the reasons for selecting composites [10].

1.9 Problems associated with composite materials

As stated earlier, composites offer many advantages over traditional materials when specific properties are considered. However, composite materials do suffer from a number of limitations. The major limitation associated with composite materials is their

poor impact resistance. Laminated and sandwich composites are more susceptible to impact damage than similar metallic structures. Furthermore, the damage induced by the impact event is often visually undetectable and it may grow under subsequent loading. This damage causes a reduction in strength and reduces the structures integrity. Impacts are simple events with many complicated effects, and what appears as a logical conclusion in one situation seems to be completely reversed in another [30]. The response of composite materials under impact loading is very different to that of metals. For low and intermediate incident energies, metals absorb energy through elastic and plastic deformation [31]. In composites, the ability to undergo plastic deformation is extremely limited with the result that energy is frequently absorbed in creating large areas of fracture with ensuing reductions in both strength and stiffness [32,33]. The problem of poor impact resistance coupled with other problems often prevents composites from being used in aerospace and other applications. In order to maintain the durability and reliability of composites for these applications, the impact problem needs to be studied and investigated so that its effects can be controlled and minimised.

1.10 References

1. D. Hull, "An Introduction to Composite Materials," Cambridge Solid State Series, Cambridge University Press, 1981.
2. T. Whelan, "Dictionary of Polymer Science and Composites", Chapman & Hall, New York, 1994.
3. M.F. Ashby, "Materials Selection in Mechanical Design", Butterworth-Heinemann Publication, London, 2000.
4. D. Pennington, PhD thesis, University of Liverpool, 1979.
5. D.J. Vaughan, "Fibreglass reinforcement", in Handbook of Composites, Edited by S.T. Peters, Chapman and Hall, London, pp 131-153, 1998.
6. D.V. Dunford, J. Harvey, J. Hatching and C.H. Judge, "The effect of surface treatment of two types of carbon fibres on CFRP properties", RAE TR 81096, 1981.
7. G. Dorey, "Impact Crashworthiness of Composite Structures", Edited by G.A.O. Davies, Elsevier Applied Sciences Publishers, London, pp 155-192, 1984.
8. A.M. Hindeleh and S. M. Abdo, "Polymer", 30, pp 218-230, 1989.
9. H.H. Yang, "Kevlar Aramid Fibre", John Wiley and Sons, 1993.
10. S.T. Peters, "Introduction, composite basics and road map", in Handbook of Composites, Edited by S.T. Peters, Chapman and Hall, London, pp 1-47, 1998.
11. H. Lee and K. Neville, "Handbook of Epoxy Resins", McGraw-Hill, New York, 1967.
12. A.F. Johnson, "Engineering Design Properties of GFRP", British Plastics Federation, London, 1988.
13. P. Ehrburger and J.B. Donnet, "Interface in composite materials", Phil. Trans. Royal. Soc. London, A294, pp 495-505, 1980.
14. P.W. Erickson and E.P. Plueddeman, "Historical background of the interface-studies and theories", Composite Materials, 6, Edited by E.P. Plueddeman, Academic Press, New York, pp1-29, 1974.
15. N.L. Hancox and H. Wells, "The effect of fibre surface coating on the mechanical properties of CFRP", Fibre Science Technology, 10, pp 9-22, 1977.

16. D. Zenkert, "An Introduction to Sandwich Construction", Chameleon Press Limited, U.K., 1995.
17. H.G. Allen, "Analysis and Design of Structural Sandwich Panels", Pergamon Press, Oxford, 1969.
18. K.W. Suh and R.E. Skochdopole, "Encyclopaedia of Chemical Technology", Third Edition, Ed. Kirk-Othmer, 2, pp 82-83, 1980.
19. Airex, Technical Airex Ltd, Speciality Foams, CH-5654, Sins, Switzerland.
20. Rohacell and Rohacell WF, Technical Data Sheets, Rohm Ltd., Germany.
21. D.L. Denton, "Load transportation applications", in Handbook of Composites, Edited by S.T. Peters, Chapman and Hall, London, pp 905-915, 1998.
22. E. Greene, "Use of fibreglass reinforced plastic in marine industry", Ship structure Committee Report SSC 360, 1990.
23. C.S. Smith, "Design of Marine Structures in Composite Materials", London and New York, 1990.
24. P. Davies and L. Lemoine, "Nautical construction with composite materials", Proc. Int. Conference on Off-shore Mechanics and Arctic Engineering, Paris, 1992.
25. P. Hoffman and J.J. Kelly, "Manufacture of advanced composite submarine structure (MACSS)", Proc. 37th Int. SAMPE Symposium, 1992.
26. W.C. Tucker and T. Juska, "Marine Applications", in Handbook of Composites, Edited by S.T. Peters, Chapman and Hall, London, pp 916-930, 1998.
27. S.W. Shalaby and R.A. Latour, "Composite biomaterials", in Handbook of Composites, Edited by S.T. Peters, Chapman and Hall, London, pp 957-966, 1998.
28. C.G. Krumweide and E.A. Derby, "Aerospace equipment and instrument structure", in Handbook of Composites, Edited by S.T. Peters, Chapman and Hall, London, pp 1004-1021, 1998.
29. http://www.eurofighter.pso-online.com/Eurofighter/structure_ie.html#top.
30. S. Abrate, "Impact on Composite Structures", Cambridge University Press, 1998.
31. P.J. Shadbolt, R.S.J. Corran and C. Ruiz, "A preliminary investigation of plate perforation by projectiles in the subordnance range", Report No 1372/81 (Univ. of Oxford, UK), 1981.

32. A. Rotem, "Residual flexural strength of FRP composite specimen subjected to transverse impact loading", SAMPE Journal, 24, pp 19-25, 1988.
33. P.W Manders and W.C Harris, "A parametric study of composite performance in compression-after-impact-testing", SAMPE Journal, 22, pp 47-51, 1986.

CHAPTER 2: LITERATURE REVIEW

In this section, the factors affecting the impact response of plain composites and sandwich structures are presented and discussed. The following section will focus on a number of factors that influence the impact performance of composite materials. These include the effect of constituent materials, the projectile characteristics, stacking sequence and stitching, specimen geometry, environmental conditions, pre-load and strain rate effects.

2.1 The influence of constituent properties on the impact response of composite materials

As stated in the previous chapter, fibre reinforced composites consist of three distinctive phases namely the fibre, the matrix and the interphase. These constituents play a major role in determining the impact performance of a composite material. For example, the interphase region between the fibre and the matrix strongly influences the process of damage initiation in composites. The fibres transfer the applied load to the matrix, which acts as a medium to hold the fibres in place. However, it is often difficult to study and understand the effect of varying the mechanical properties of constituents such as strength and stiffness together with other effects such as fibre shape and diameter. The constituents also affect the failure mechanisms in composite materials. A number of detailed studies using optical and scanning electron microscopy techniques have identified failure mechanisms such as delamination, interlaminar matrix cracking, longitudinal matrix splitting, fibre/matrix debonding, fibre pull-out and fibre fracture [1-4]. Again, the relative energy-absorbing capability of these fracture modes is strongly influenced by the properties of the constituent materials. The following chapter will focus on the effect of the constituents including fibre, matrix and interphase on the impact response of composite materials

2.1.1 Fibres

Fibres play an important role in bearing a significant percentage of the applied load as well as determining the overall composite stiffness. Several types of fibre have been

described in the previous section. Within each group of fibres, specific fibres offer a range of physical and mechanical properties, which can be chosen for a particular application. For example, glass fibre composites offer a relatively high impact resistance due to their high strain to failure whereas carbon and boron fibre composites offer higher stiffness and find use in stiffness-sensitive structures [5]. Previous studies [5] have shown that the relative Izod impact resistances of continuous fibre reinforced composites based on S-glass fibre and Kevlar fibres were over five times greater than that of Modmor II carbon fibre reinforced composites. Beaumont *et al.* [6] defined the ductility index (DI), which is the ratio of the energies associated with the crack propagation phase (the area after maximum load) and the initiation phase (the area up to the maximum load) for three different types of composite systems. They reported DI values for Kevlar-49, E-glass and HMS carbon/epoxy of 2.3, 0.4 and 0 respectively. They concluded that Kevlar fibres offer a superior energy absorbing capability compared to the other two fibres [6].

Further investigations have been conducted to study the effect of fibre properties on the impact resistance of composite materials in which type I and II carbon fibres were subjected to low velocity impact loading [7,8]. It was shown that the impact resistance of composites with type II carbon fibres offered a greater impact resistance than type I carbon fibre composites. Dorey *et al.* [9] conducted drop-weight impact tests on carbon/epoxy and Kevlar/epoxy laminates and showed that Kevlar fibre reinforced epoxy laminates offered a significantly higher impact resistance than a carbon fibre reinforced epoxy. The threshold energies for the onset of damage in the Kevlar laminates were up to five times higher and the fracture energies were three times greater than that of the carbon fibre reinforced epoxy. In addition, the post-impact tensile and flexural strengths of the Kevlar fibre reinforced epoxy laminates were consistently higher over the range of incident energies studied [9].

Cantwell *et al.* [10] performed a detailed study in order to investigate the effect of varying fibre properties on the residual compressive strength of impact-damaged composite materials. Two material systems based on an epoxy resin were used. The first

system was reinforced with AS4 carbon fibres with a mean tensile strength of 3.59 GPa, an elastic modulus of 235 GPa and a strain to failure of 1.53%. The second system was reinforced with carbon fibres with a tensile strength, elastic modulus and strain to failure of 2.70 GPa, 235 GPa and 1.14 % respectively. The same elastic modulus (235 GPa) was used in order to minimise the effect of bending rigidities on the impact response. The AS4 carbon fibre composite, with a superior strain energy absorbing capacity to that of the XAS carbon fibre composites offered superior residual properties as shown in Figure 2.1.

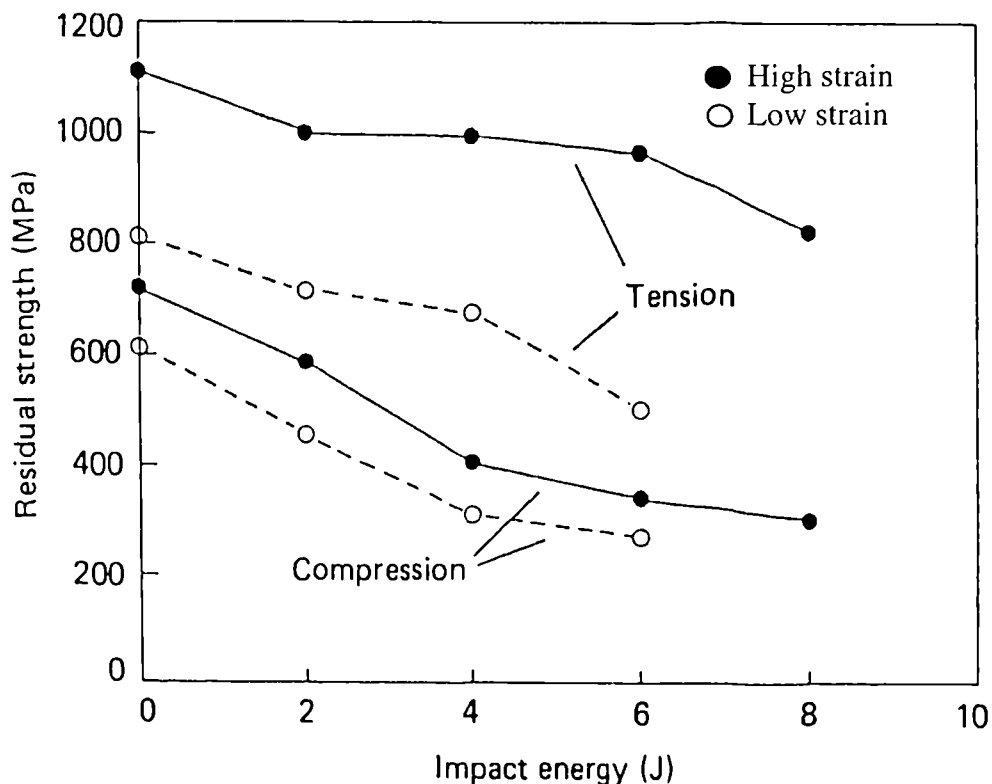


Figure 2.1: Variation of residual tensile and compressive strength with impact energy of low and high strain to failure carbon fibres [10].

Many attempts have been made to gain a greater understanding of the parameters that control the energy absorption process in fibre reinforced composites [11-13]. Chamis *et al.* [12] performed Izod impact tests on a wide range of composite systems. The total impact energy was calculated based on the area under the stress-strain curve. They found

that flexure and interlaminar shear deformations are dominant energy-absorbing mechanisms in composite materials during impact. Composite systems with large areas under the stress-strain curve are likely to absorb more energy during impact. The findings of this study are presented in Figure 2.2. Clearly, fibres with high strain energy absorbing properties offer improved Izod energies and therefore an improved impact resistance.

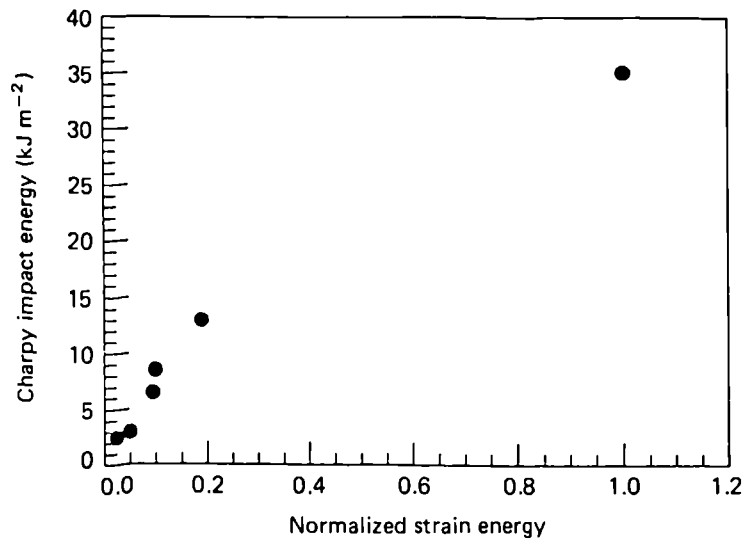


Figure 2.2: Variation of Charpy impact energy with normalised strain energy absorbing capacity of a fibre [12].

Although the elastic energy capacity of the fibres is useful for characterising the impact resistance of a composite, it is necessary to take into account energy dissipation during the failure process such as that associated with the fibre pull-out mechanism [11]. Beaumont [13] developed equations to characterise micro-mechanical failure mechanisms such as debonding and fibre pull-out and suggested that post-debond fibre sliding is the main energy absorbing mechanism in glass fibre composites, whereas, fibre pull-out predominates in carbon fibre composites. Previous work has shown that, an increased pull-out resistance can be achieved by increasing the fibre diameter [3,14].

In contrast, reducing the diameter of carbon fibres can significantly increase their strain to failure and hence improve the fracture toughness [3,14]. Therefore, in recent years,

fibre manufacturers have been improving the strain to failure of the fibre by reducing its diameter [11]. The average diameter of the first generation of carbon fibres was between 7 and 8 μm whereas for more recent carbon fibres, for example IM6 fibres, the diameter is approximately 5 μm . However, a smaller fibre diameter is often associated with the poorer compressive properties due to the fact that the compressive strength depends strongly on the stability of the fibres [11]. Results from Davies *et al.* [15] showed that the interlaminar fracture toughness of IM6/PEEK with a superior strain energy absorbing capability is higher than that of AS4/PEEK. Clearer benefits associated with employing higher energy absorbing fibres can be seen under high velocity impact conditions. Here, increasing the fibre diameter may lead to an increase in energy absorption thereby improving the impact resistance of the composite. Under such loading conditions, the target response is more localised and the impact energy is dissipated over an area close to the point of impact. Consequently, the global energy absorbing mechanisms are less important and local failure mechanisms such as fracture and fibre pull-out become more significant. It appears that for low velocity impact loading, the ability of the fibres to absorb and store the energy elastically is a key parameter in determining the impact response of a composite.

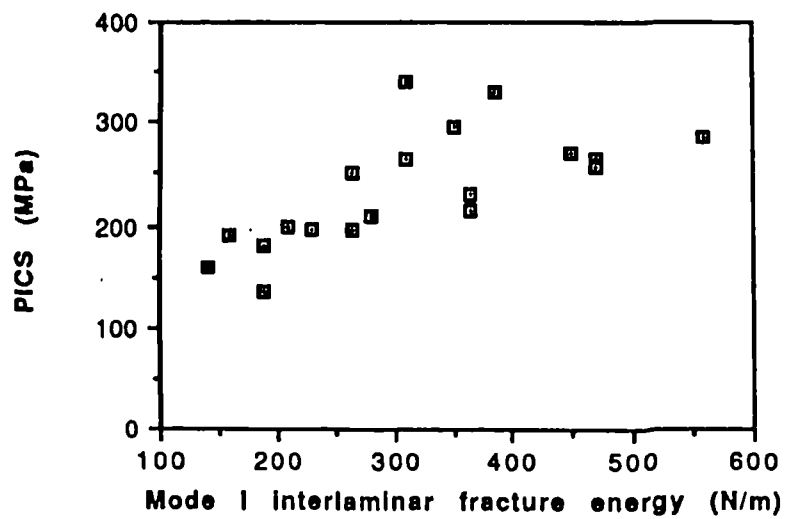
2.1.2 Matrix

The matrix has a significant affect on the impact response of composite materials. Previous studies [16-19] have shown that the impact resistance of many composites is strongly influenced by the properties of the matrix. As outlined earlier, thermoplastics and thermosetting matrices respond differently under localised impact loading. Reduced levels of delamination have been observed in thermoplastic-based composites compared with thermosetting systems, an effect that is attributed to the inherently higher fracture toughness of thermoplastic matrices [20-24]. Interlaminar fracture has been shown to reduce the load-bearing capability of a composite by as much as fifty percent [25]. Therefore, a number of studies have been conducted to understand the effect of varying matrix properties on the impact resistance of composite materials. There are a number of ways in which the matrix can be modified in order to improve the impact resistance of a composite. Examples include the use of plasticiser modifiers [14], the addition of rubber

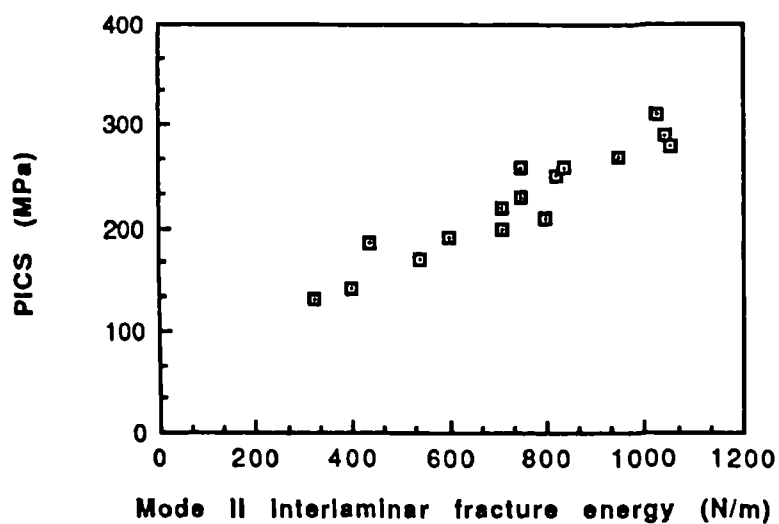
particles (rubber toughening) [26-28], the addition of thermoplastic particles such as polyetherimide (PEI) and polyethersulphone (PES) [19,29,30], a reduction in the cross-linking density (typically for epoxy resins) [31,33], the use of thermoplastic matrices and the introduction of a thermoplastic interleaf at critical ply interfaces [33-36].

An extensive study of the impact resistance of a carbon fibre/epoxy resin has been undertaken by Williams and Rhodes [28]. Their study of twenty-four types of modified and unmodified carbon fibre/epoxy showed that the severity of damage and subsequent load-bearing properties varied greatly from one system to another. They showed that brittle matrix composites fail by extensive delamination whereas the tougher matrices tend to fail as a result of transverse shear cracks. The authors also stated that the tensile properties of the matrix have a direct influence on the impact response of the composite and concluded that in order to provide a significant improvement in impact resistance, the tensile strength of the matrix should be greater than 69 MPa.

Bradshaw *et al.* [14] reported a significant increase in the Mode I fracture toughness of Epikote 828 epoxy resin when a plasticiser was used. Morton and Godwin [37] conducted impact tests on carbon fibre PEEK and carbon fibre/epoxy laminates. The carbon fibre PEEK specimen exhibited permanent indentation on the impacted surface. Fibre breakage with a small amount of delamination was also evident through the cross-section of the specimen. They showed that the damage in the carbon fibre/PEEK sample was localised to the point of impact and concluded that the damage was of a similar type to that described by Dorey [38] who referred to it as “compression shear band” failure. The impact damage tolerance of a composite is directly linked to the toughness characteristics of the matrix. It has been shown that the compression after impact (CAI) strength is related to the maximum strain to failure of the resin and the mode II interlaminar delamination energy [34-36]. Figure 2.3 shows the correlation between CAI and modes I and II interlaminar fracture energies [36].



a)



b)

Figure 2.3: a) Relationship between post impact compression strength (PICS) properties and Mode I interlaminar fracture energy, G_{Ic} , of CFRP laminates [39] and b) Relationship between PICS properties and Mode II interlaminar fracture energy, G_{IIc} , of CFRP laminates [36].

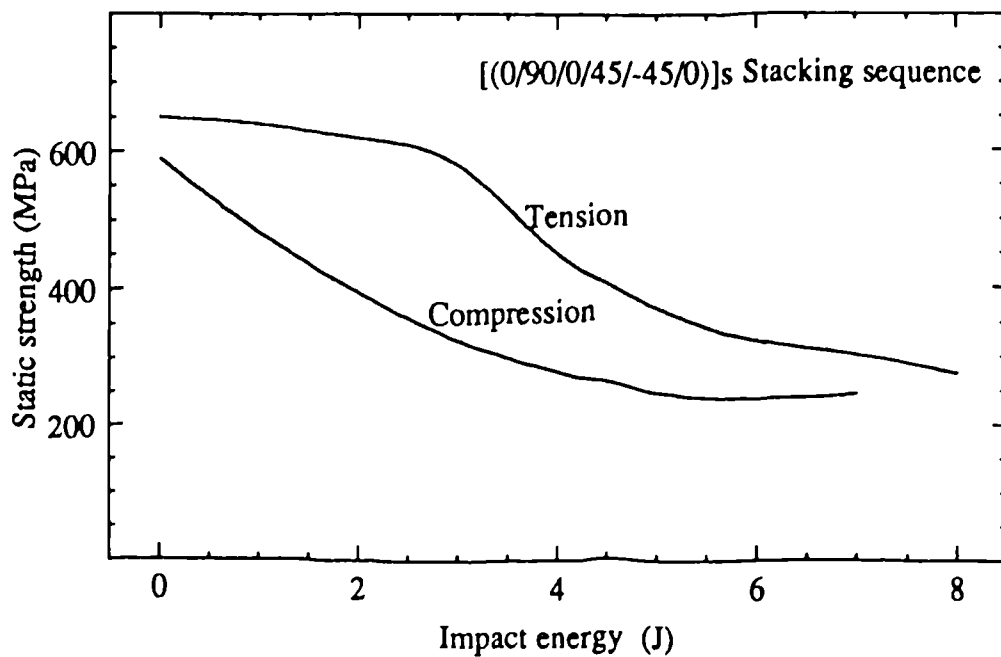


Figure 2.4: Reduction of tensile and compression strength after impact of a (0, 90, ± 45) carbon fibre composite material [40].

It has been shown that for low energy impact loading, composite materials suffer a much greater strength reduction in compression than in tension [24,38]. Dorey [40] conducted post-impact tensile and compression tests on a carbon/epoxy laminate as shown in Figure 2.4. Clearly, the reduction in compression strength is much greater than in tension. Dorey showed that the residual property i.e. tensile and compressive strengths, were not greatly improved by replacing the standard epoxy matrix by a tough epoxy matrix as shown in Figure 2.5. He also demonstrated that the use of a modified epoxy matrix containing elastomeric particles reduced the level of delamination after impact leading to enhance residual compressive properties as shown in Figure 2.6. It has been suggested that impact-damaged composites are most sensitive to compressive loading since impact-generated delaminations tend to reduce stability of the load-bearing plies resulting in premature failure through buckling [11].

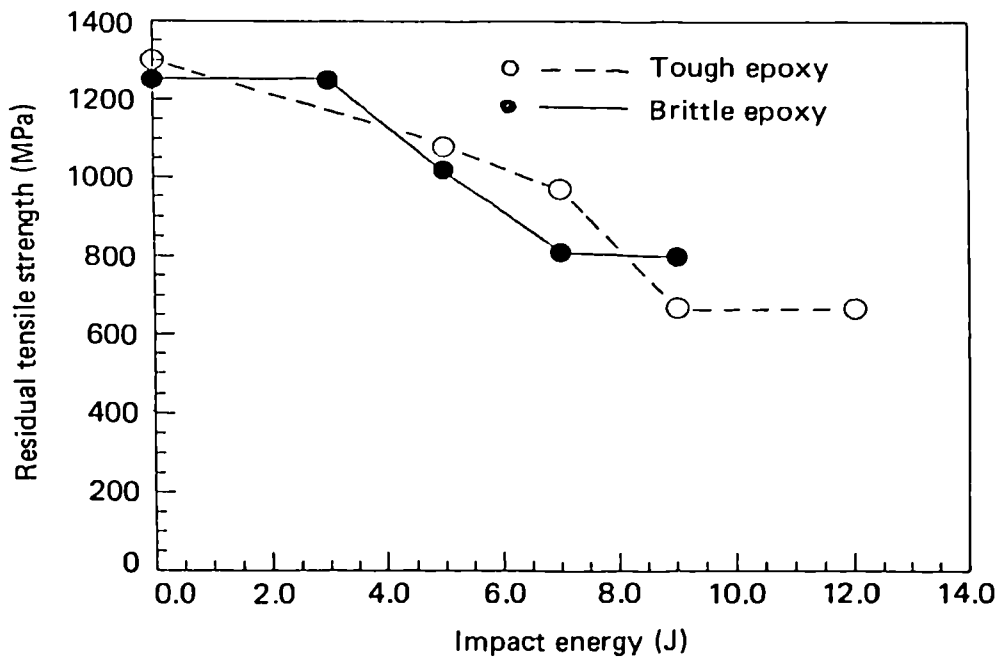


Figure 2.5: The variation of residual tensile strength with impact energy for a tough and a brittle epoxy- based carbon fibre composite [40].

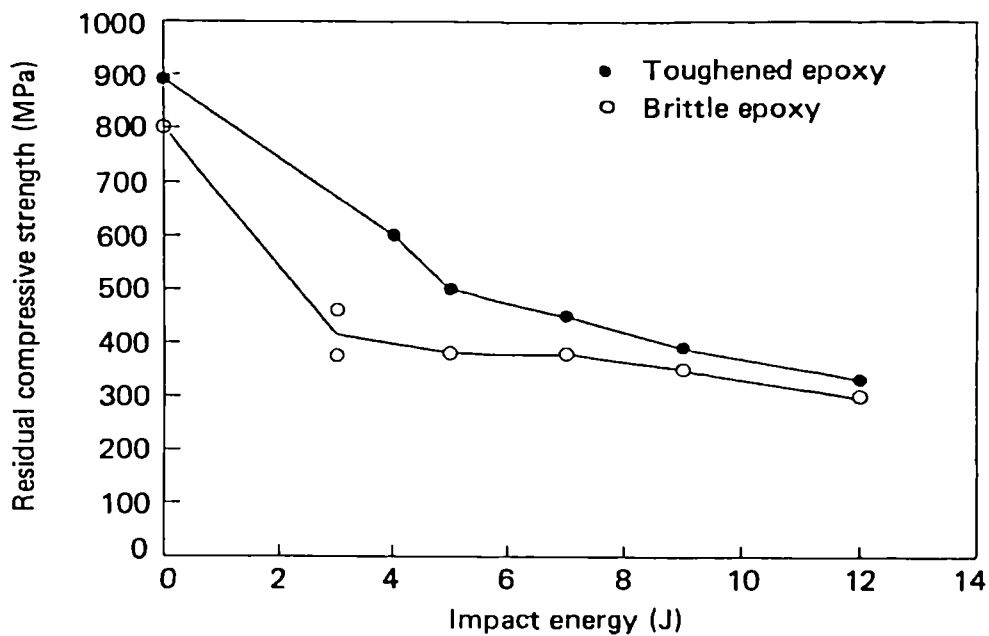


Figure 2.6: Residual compressive strength of a toughened and a brittle epoxy-based carbon fibre composite as a function of impact energy [40].

The compression after impact (CAI) properties of a composite have been found to be strongly influenced by the properties of the resin [35-36, 39]. Hull and Shi [41] stated that improvements in the damage tolerance of a composite depends on the properties of the resin and the fibre-resin interface. They stated that, in order to develop a damage-tolerant composite system, an understanding of the relationship between strength and toughness of the constituents is important and should be established.

The effect of varying resin properties on the delamination resistance of composite materials has been studied by Hunston *et al.* [42]. They investigated the properties of a variety of thermoset, toughened-thermoset and thermoplastic based composites by determining the Mode I critical strain energy release rate using the double cantilever beam specimen. Following fracture tests on neat resins and their corresponding composite specimens, they identified a strong correlation between the Mode I critical strain energy release rate of the neat resin and the interlaminar fracture toughness, G_{Ic} of the associated composite. A clear link between the properties of the matrix and those of the composite materials was observed for brittle polymers, here the value of G_{Ic} was slightly greater than the resin values as shown in Figure 2.7. For tough matrix resins, an increase of 3 J/m^2 in the resin G_{Ic} resulted in a 1 J/m^2 increase in the interlaminar fracture energy of the composite. For brittle resins, the Mode I interlaminar fracture toughness G_{Ic} is generally greater than the G_{Ic} of the neat resin values due to the fact that a full transfer of the neat resin toughness to the composite occurs. In addition, crack growth promotes other toughening mechanisms such as fibre pull-out and breakage which are not present in the bulk resin systems [42]. The transition between the tough and brittle resins occurs when the size of the crack tip deformation zone is similar to that of the interfibre distance. Hunston [26] also conducted similar tests as reported in reference [42] in order to establish the correlation between the matrix properties and composite fracture toughness. From three sources of data, he drawn a definite correlation between the resin fracture energy and composite interlaminar fracture energy as shown in Figure 2.8.

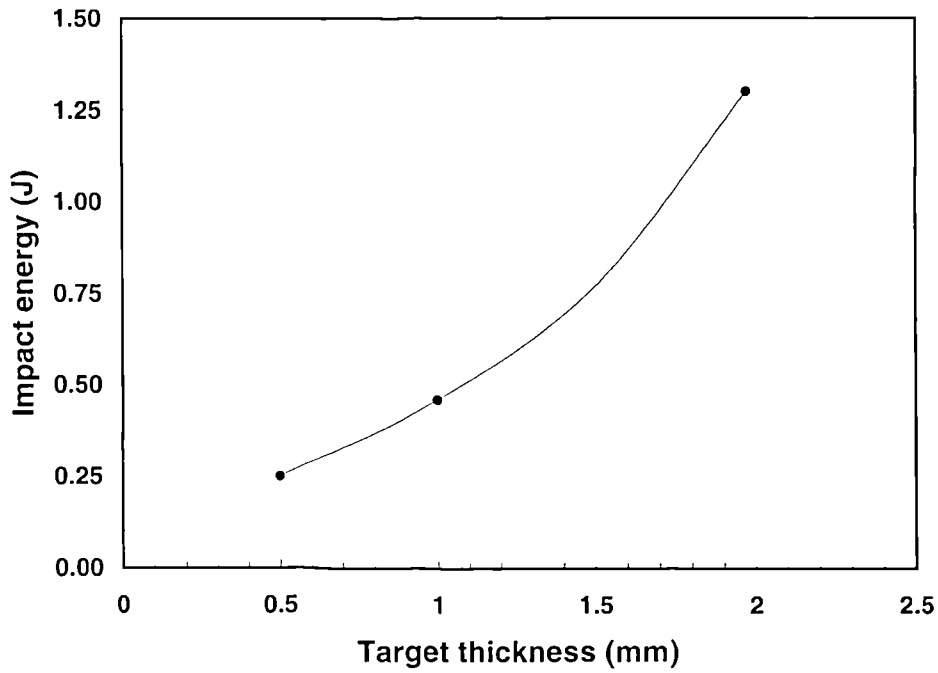


Figure 2.7: The effect of resin properties on the Mode I interlaminar fracture toughness of a range of composite materials [42].

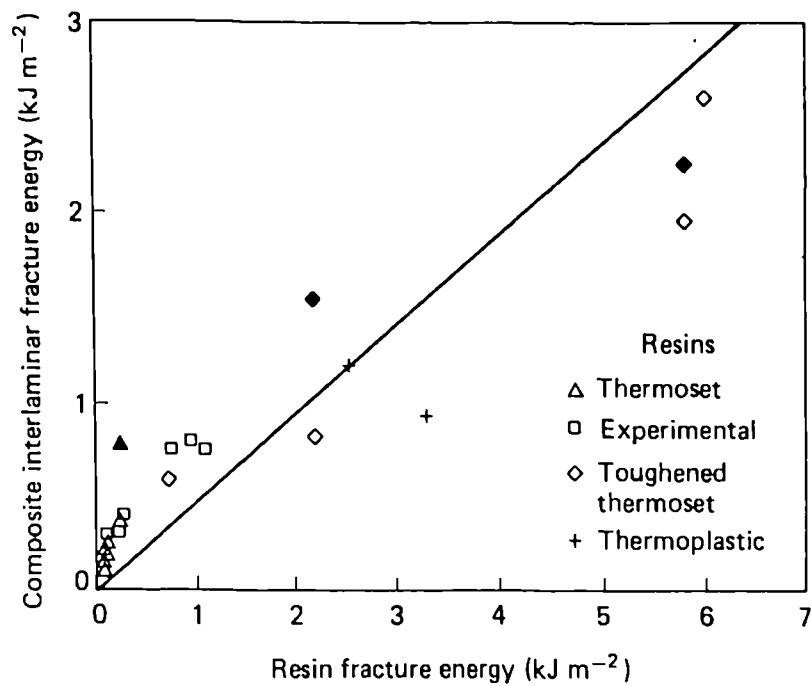


Figure 2.8: Variation of composite Mode I interlaminar fracture energy with resin fracture energy [26].

Another method that has been shown to improve the impact resistance of a composite material is the insertion of thermoplastic interleaves [43-45]. This method involves introducing a discrete layer of ductile polymer at critical interfaces within the composite structure. Experimental evidence has shown that the impact resistance of a number of carbon composites can be greatly improved using this technique [33-36]. Rechak and Sun [33] conducted a stress analysis on a composite system with adhesive layers placed at certain interfaces of the laminate. They demonstrated that the interlayer can significantly reduce the interlaminar shear stresses generated during impact, which in turn results in reduced levels of delamination. Hirschbuehler [36] conducted an investigation on a large number of plain and interleaved laminates and established a correlation between matrix properties and the compression after impact strength. He found that the residual compressive properties of a number of plain and interleaved composite systems increased with the flexural strain to failure of the pure resin as shown in Figure 2.9.

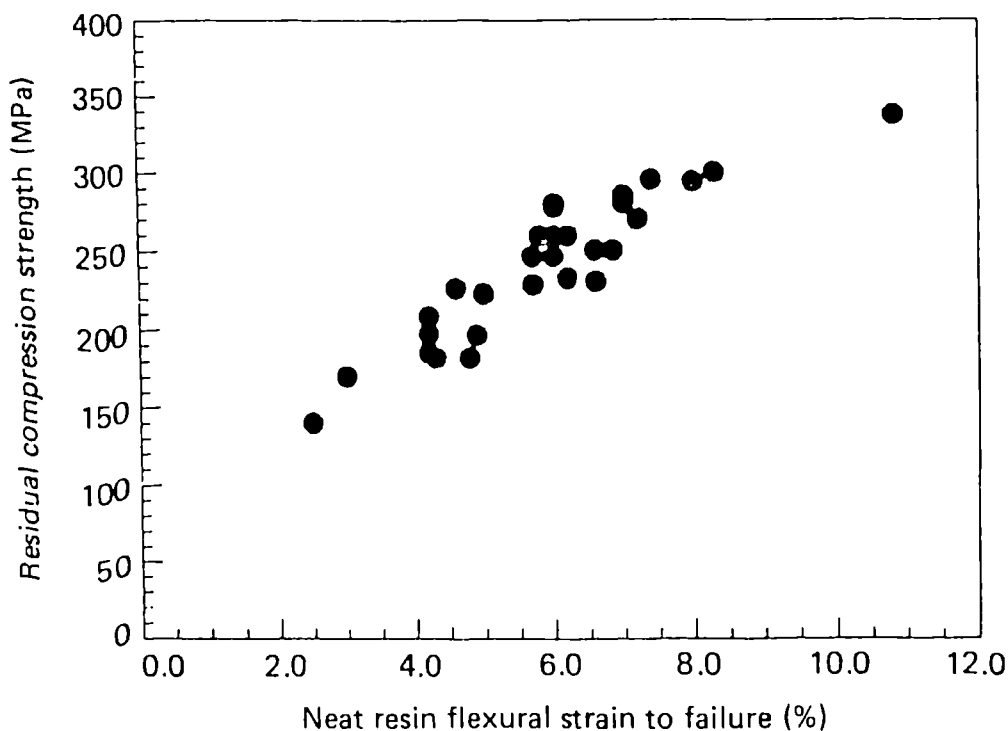
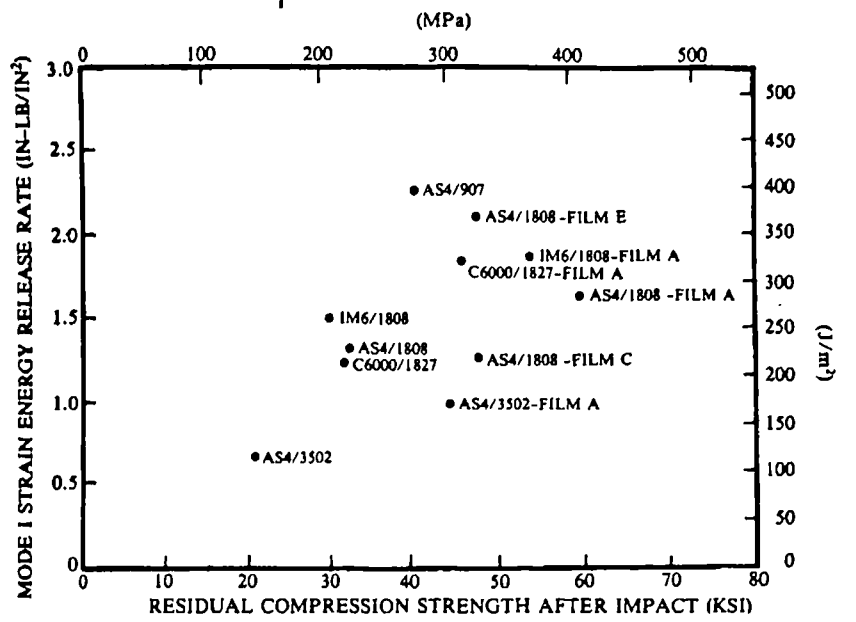


Figure 2.9: Variation of residual compressive strength of a range of impact-damaged composites with neat resin flexural failure strain [36].

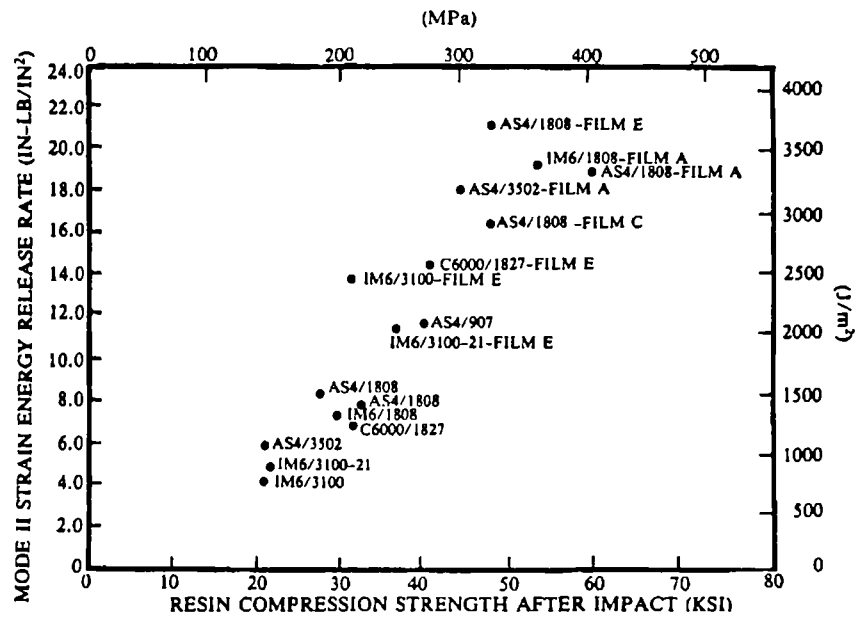
Masters [35] studied the effect of interleaving on the impact and delamination resistance of several carbon/epoxy and carbon fibre/bismaleimide systems. He concluded that interleaving using a thermoplastic ply significantly improved the impact damage tolerance of both types of system. An increase in residual compression strength was reported for both systems and the increase was as much as eighty percent in some cases. From this work, Masters also confirmed that there is a correlation between impact delamination resistance and the interlaminar fracture toughness of the interleaved laminate. A good correlation between interlaminar toughness and impact resistance was evident when the value of G_{IIc} was plotted against residual compression strength as shown in Figure 2.10. Masters [35] stated that although the use of thermoplastic interleaves is claimed to promote ductile behaviour, the test results demonstrated only nominal increases in the Mode I strain energy release rate of the interleaved laminate.

Masters [35] also reported that the general trend of increased damage tolerance with increasing G_{IIc} does not hold and concluded that G_{IIc} is a much more accurate indicator in determining the impact resistance of laminated materials. Similar observations were reported by Tobukuro *et al.* [46].

Pintado *et al.* [47,48] showed that interleaving improves the impact resistance of a composite and that the energy absorbing capacity of a laminate under quasi-static three point bending tests can be used to predict the impact strength of composite structures. Ishai and Shargai [49] discussed the toughening and crack arresting contribution of interleaved layers introduced between the 0° and 90° layers of a laminate. Peiffer [50] showed that the impact resistance of glass-epoxy composites can be significantly improved by introducing a rubbery interface between the glass fibres and the rigid epoxy matrix.



a)



b)

Figure 2.10: a) The influence of interlaminar fracture toughness on the CAI properties of a range of composites, a) Mode I and b) Mode II [35]

2.1.3 Interphase

The mechanical performance of a polymer composite is highly influenced by the strength of the bond between the fibre and matrix. A number of studies have been

undertaken in order to understand the effect of interfacial adhesion on the impact performance of composite materials [14, 51-56].

The interface region is strongly dependent on the degree of adhesion between the fibre and the matrix. Therefore, a number of studies have been undertaken in order to increase the level of adhesion between the fibre and matrix through the application of a fibre surface treatment [52,55]. Many studies have concentrated on determining the optimum level of the surface treatment as well as the effect of the surface treatment on the mechanical properties of the composite [14, 52-54].

Previous studies [14, 52-54] have shown that fibre surface treatments can significantly enhance the mechanical properties of a composite and alter the failure modes during fracture. Rogers *et al.* [54] investigated the effect of improving fibre/matrix adhesion on the impact response of a carbon fibre epoxy system. They reported that by improving the interfacial bond strength, a fourfold increase in incident impact energy required to initiate damage of the same size.

Dorey [55] reported that at higher incident energies, the load-bearing capability of systems based on treated fibres drops dramatically until the perforation threshold is reached. Bless and Hartman [56] conducted experiments to establish the perforation threshold of treated and untreated fibre laminates. They showed that the threshold energy of a treated fibre laminate is much lower than that of an untreated laminate. This effect was explained by Dorey [55] who showed that the transverse fracture energy, which is the key parameter for determining a composites resistance to penetration and perforation, is strongly dependent upon the interfacial bond between the fibre and the matrix. Untreated carbon fibre reinforced epoxy composites offer fracture energies up to 60 kJm^{-2} whereas transverse failure in composites with high levels of surface treatment absorb less energy [55]. At energies above that required to induce perforation, damage in a surface-treated composite tends to be localised and often takes the form of a clean hole [54]. The post-impact properties of composites with treated and untreated fibres were studied by Dorey [55] and these results are shown in Figure 2.11. Clearly, the post-

perforation residual properties of the treated composites are generally superior to those of the untreated composites.

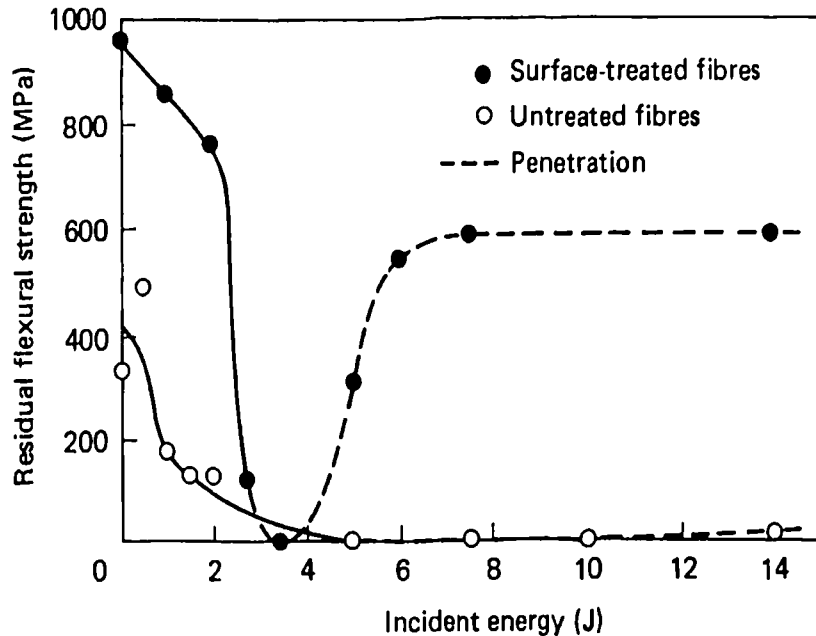


Figure 2.11: The variation of the residual flexural strength of treated and untreated carbon fibre composites subjected to ballistic impact loading [55].

The level of surface treatment applied to the fibres in a composite has a significant effect on both its impact resistance and post-impact performance. Dorey [55] showed that treating the fibres improves the post-impact compressive properties as shown in Figure 2.12. Localised impact loading on treated fibre composites results in a smaller, more localised damage zone, a lower perforation threshold and improved compressive properties. However, the post-impact tensile strength is significantly reduced. The explanation offered was that fibre surface treatment has the adverse effect of increasing the notch sensitivity of the composite, resulting in reductions in tensile strength after impact as shown in Figure 2.12. In contrast, impact loading on composites with low levels of surface treatment generates large areas of delamination and splitting with severe effects on the compressive properties of the materials. Therefore, the level of

surface treatment applied to the fibre in a multidirectional composite will depend on the application and its operational environment which the component will encounter. In general, a compromise is sought in terms of the level of surface treatment applied to a composite.

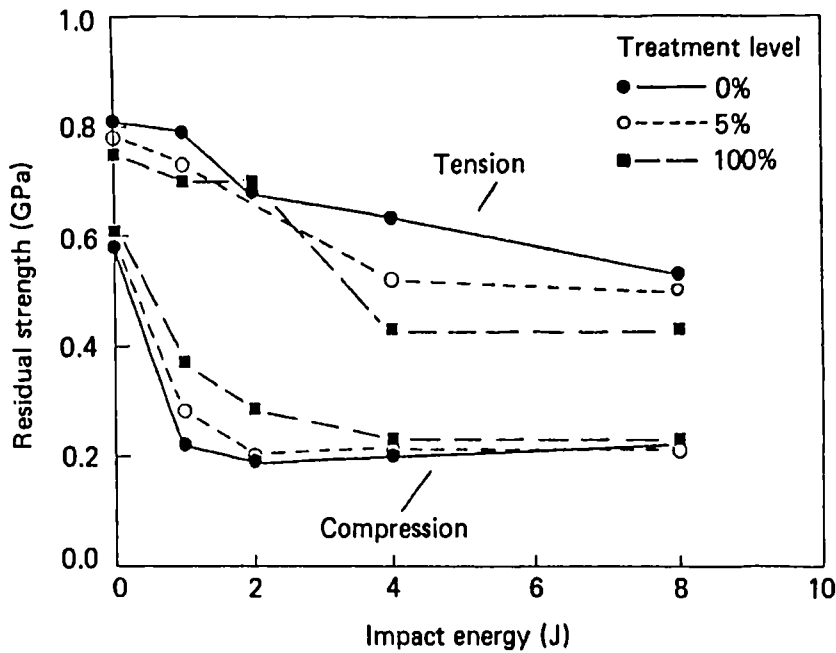


Figure 2.12: Variation of residual tensile and compressive strength of treated and untreated carbon fibre reinforced composite as a function of impact energy [55].

In carbon-fibre/PEEK thermoplastic fibre composites, several authors [57,58] have suggested that the outstanding fibre/matrix strength in this composite system results from the ability of the PEEK matrix to form trans-crystalline zones around the carbon fibre.

The impact resistance of a polymer composite can be significantly improved by promoting greater interfacial adhesion between the fibre and matrix. Studies carried out

by Tissington *et al.* [59] showed that a significant increase in fibre/matrix adhesion can be achieved by applying an oxygen plasma treatment to the reinforcement fibre in the composite. A similar surface treatment was employed by Montes-Moran *et al.* [60] in order to investigate the effect of surface treatment on the interfacial properties of ultra-high modulus carbon fibres in an epoxy resin matrix. The effects of the oxidation plasma treatment on the surface morphology and surface chemistry of the interface were studied using SEM/STM and XPS analysis. Further theoretical investigations by Ying [61] showed the importance of the fibre/matrix interface on the impact performance of a composite. He demonstrated that for a single fibre embedded in a matrix, loads are transferred at the fibre end from the matrix to the fibre through shear stresses. He stated that the relationship between the critical transfer length, l_c , for load transfer and the shear strength of the interface, τ_y , can be expressed as,

$$l_c = \frac{\sigma_f d_f}{2\tau_y} \quad (2.1)$$

where σ_f is the tensile strength of the fibre and d_f is the fibre diameter. A strong link was reported between the critical transfer length determined from single filament tests and the fracture toughness of the composite as characterised by the energy required for fracture initiation. Similar work was conducted by Greszczuk [62] to establish a relationship between fibre strength and interfacial strength. A simple relationship between these two parameters was obtained which could be used to establish the optimum interface strength in order to promote overall composite failure instead of localised fibre-matrix interface failure.

Deng and Ye [63] investigated the influence of fibre-matrix adhesion on the interlaminar and in-plane shear properties of a carbon/epoxy composite. They showed that increasing the level of adhesion between the fibre and matrix increases the Mode I and Mode II interlaminar fracture toughness as well as the in-plane shear strength by between 15 and 30 percent. Typical results from Mode I interlaminar tests are shown in Figure 2.13.

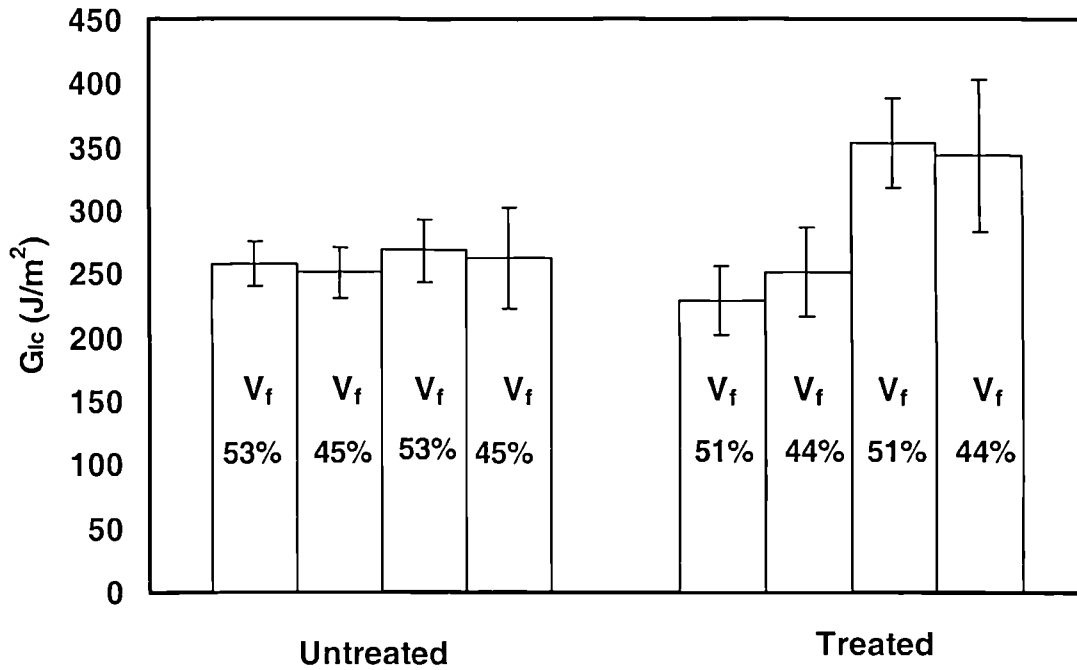


Figure 2.13: Mode I interlaminar fracture toughness of two composite systems with different fibre volume fractions with shaded and unshaded columns represents visual and propagation [63].

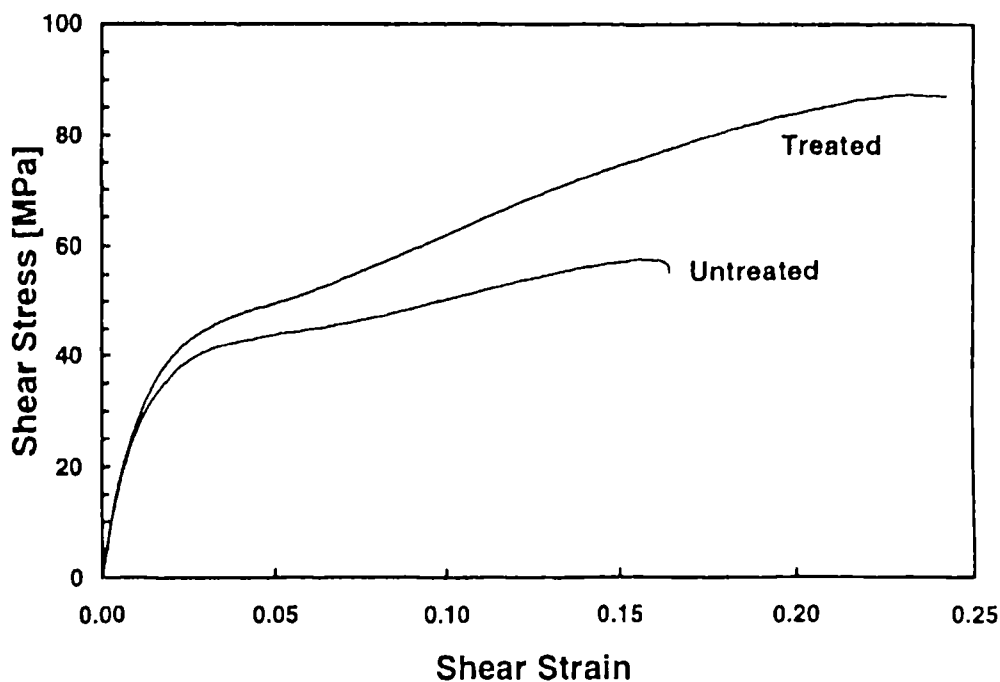


Figure 2.14: Typical in-plane shear stress versus shear response of a treated and untreated $[\pm 45]_{3S}$ carbon fibre reinforced composite [63].

Deng and Ye [64] extended their investigation by conducting an experimental study on the same composite using two different surface treatments in order to identify the effect of fibre-matrix adhesion on the impact and dynamic mechanical properties of a composite. The specimens were subjected to both Charpy and falling-weight impact tests. They failed to observe any clear influence of fibre-matrix adhesion on the impact properties of their composite laminates, as shown by the impact load-displacement plot in Figure 2.15. The authors suggested that this was due to the highly localised damage process under impact loading, in which damage is dominated by fibre breakage with little delamination and fibre pull-out.

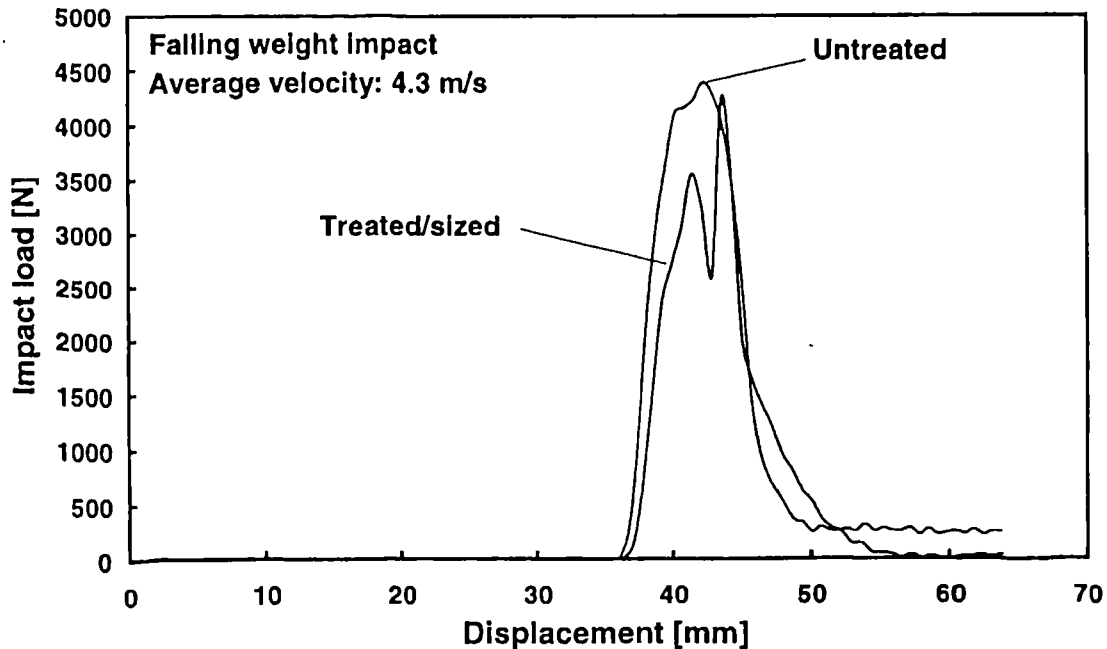


Figure 2.15: Typical impact load versus displacement curves for composite with treated and untreated fibre systems subjected to falling-weight impact tests [64].

Madhukar and Drzal [65, 66] conducted tests to establish the relationship between fibre-matrix adhesion measured by single fibre interfacial shear tests and in-plane and interlaminar shear properties of carbon/epoxy composites. They stated that surface modification doubled the interlaminar shear stress while fibre dominated properties remain unchanged. They also demonstrated that by increasing the level of adhesion between the carbon fibres and epoxy matrix, an increase in both inplane and interlaminar shear stress could be achieved.

2.2 The effect of specimen geometry on the impact response of composite materials

The geometry of the test specimen is an important parameter that influences the impact response of a composite material [14,37,40,67,68]. Parameters such as the span-to-depth ratio, specimen size, length of the beam, radius (of a circular plate) and curvature are some of the parameters that have been shown to have a significant effect on the impact response of a composite structure [11,14,67]. Low velocity impact tests on CFRP have shown that the failure modes in a simple beam specimen vary depending on the span-to-depth ratio [14]. Long and thin beams were observed to fail in flexural modes whereas short and thick beam specimen failed in interlaminar shear [11].

Broutman and Rotem [67] conducted low velocity impact tests on CFRP composites and found that an increase in energy-absorbing capability could be achieved by increasing the size of the specimen but the increase was not linear i.e. doubling of the specimen size does not necessarily result in a two fold increase in the energy absorbing capability.

Cantwell and Morton [68] studied the influence of specimen geometry on the low velocity impact response of a carbon fibre reinforced laminate. A series of eight CFRP laminates with different stacking sequences and thicknesses were subjected to drop-weight impact loading. The variation of energy to initiate first damage in the specimen was determined as a function of beam length as shown in Figure 2.16. Clearly, there are two distinctive regions in the plot, corresponding to the two different failure modes during impact. They stated that in the first region of the curve, damage initiates at the lower surface of the target due to the flexural stress field within the beam. At this point, increasing the target thickness will result in an increase in the damage threshold. They also concluded that the failure processes in small and simple specimens differ significantly from those observed in large and more representative structures. They suggested that care should be taken when using data obtained from tests on laboratory specimens.

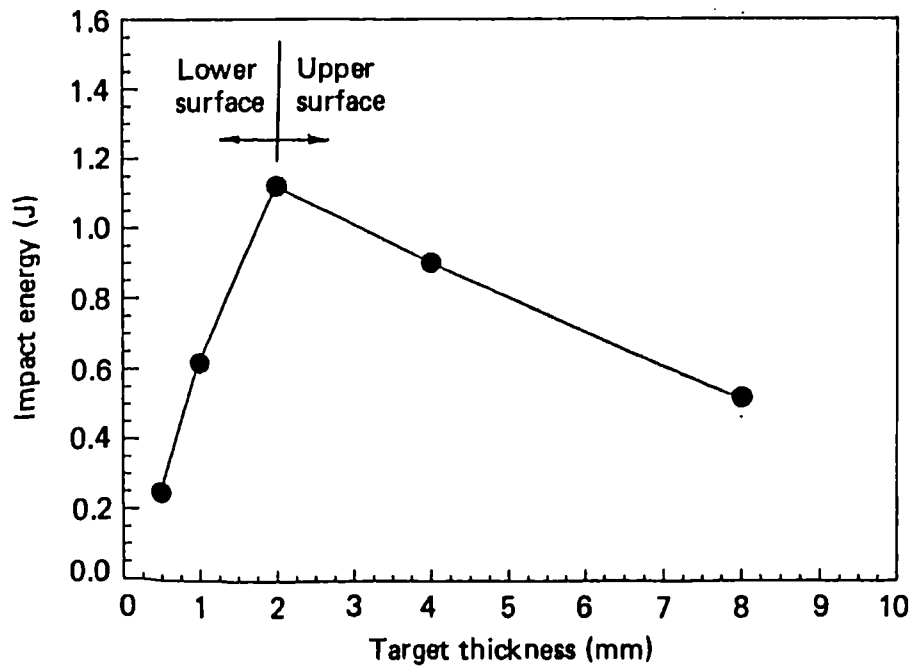


Figure 2.16: variation of the incident energy to initiate first damage with target thickness in $[\pm 45^\circ]$ CFRP laminates [68].

Cantwell and Morton [68] also investigated the effect of varying beam length on the low velocity impact response of CFRP laminates. They showed that increasing the size of the specimen resulted in an increase in the energy-absorbing capability of the target as shown in Figure 2.17. They also showed that varying the specimen geometry in this way leads to a change in the initial mode of failure. The shorter and stiffer beams initially failed due to the contact stress field whereas the longer, flexible targets failed in a splitting mode between the lower surface 0° fibres. Investigations concerning the effect of bending stiffness on impact response showed that for flexible targets with a low flexural stiffness, impact damage initiated in the lowest ply due to the flexural response of the beam. As a result, the matrix cracks initiated in the top layer laminate and deflected to the lower faces to form delaminations. In contrast, for stiffer targets,

interlaminar fracture was a dominant mode of failure. They also conducted similar tests on circular laminated plates and these results are shown in Figure 2.18. Cantwell and Morton [68] showed that for high velocity impact loading, varying the length of a beam specimen or the diameter of circular plate had no influence on the damage initiation threshold energy due to the localised deformation near the impact region. They suggested that high velocity impact loading by a light projectile induced a localised form of target response in which much of the incident energy of the projectile is dissipated over a small area immediate to the point of impact [69].

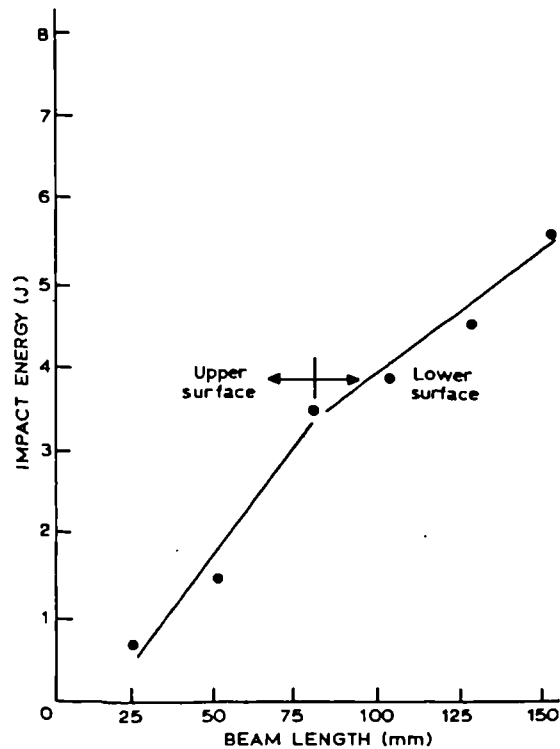


Figure 2.17: Variation of the incident energy to initiate first damage with beam length in $[\pm 45^\circ]$ CFRP laminates [68].

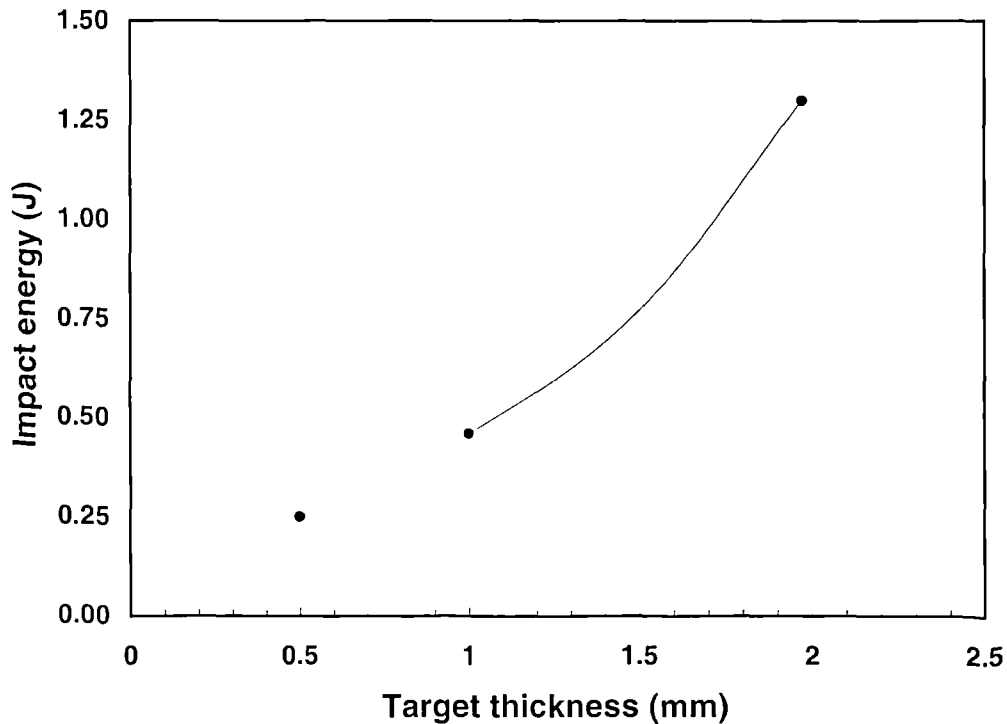


Figure 2.18: Variation of perforation energy with target thickness for the $[\pm 45^\circ]$ laminates [68].

Dorey [70] presented force-time curves from impact tests on simply-supported beams and circular composite plates. He showed that the damage threshold energy for a circular CRFP specimen was less than that of flexible beam. Robinson and Davies [71] studied the influence of specimen diameter on damage initiation in GFRP laminates. They stated that GFRP specimens with larger diameters required higher impact energies to induce damage of the same size. This was attributed to the greater strain energy absorbing capacity of the larger plates.

2.3 The effect of stacking sequence on the impact response of composite materials

It has been shown that the arrangement of the plies in composite materials strongly influences the mechanical properties of the resulting composites [37, 72-74]. In general, unidirectional composites in which all of the fibres are aligned in one direction, fail by splitting at very low energies and such composites are therefore unsuitable for use in impact-loaded structures [14]. Dorey [72] and Morton and Godwin [37] showed that composite laminates with a stacking sequence of $(0^\circ, \pm 45^\circ)$ offer a greater impact resistance and improved residual strengths than that of a $(\pm 45^\circ, 0^\circ)$ laminate. They suggested that a $(0^\circ, \pm 45^\circ)$ fibre arrangement results in an increased target flexibility leading to an enhanced elastic energy-absorbing capacity. It is also been suggested that the presence of $(\pm 45^\circ)$ plies on the surface of a $(0^\circ, \pm 45^\circ)$ laminate composite serve to protect the load-bearing of 0° plies against damage induced by projectiles [75]. This view was further supported by Stevanovic *et al.* [76], who conducted instrumented Charpy impact tests on multi-directional T300 carbon fibre composites. They showed that the energy-absorbing capability of $(\pm 45^\circ)$ laminates is much greater than $(0^\circ, 90^\circ)$, $(0^\circ, \pm 45^\circ)$ and $(0^\circ, 90^\circ, \pm 45^\circ)$ laminates.

Dorey [75] suggested that increasing the flexural stiffness of the target can significantly enhance its impact resistance. This is true for laminates in which initial failure occurs at the top surface of the specimen. However, in more flexible targets where failure is unlikely to occur on the top surface, reducing the flexural stiffness of the target may precipitate failure at a lower incident energy [11].

Hong and Liu [77] conducted a comprehensive study to investigate the development of impact damage in a range of composites. The aim of this work was to identify the fundamental parameters responsible for damage in glass fibre reinforced plastic (GFRP) under high impact loading conditions. They showed that increasing the angle θ in a $(0_s^\circ, \theta, 0_s^\circ)$ laminate increased the damage area for a given incident energy as shown in Figure 2.19. They found that an increase in θ also reduced the damage threshold energy.

Liu [77] extended this work by developing a simple theoretical model for predicting the delamination site in a number of composites. He suggested that delamination in multi-angle composite is more likely to occur at an interface where the mismatch in bending stiffness is greatest, for example, between $\pm 45^\circ$ plies. Their experimental results showed that the level of damage increased by increasing the angle θ in a $(0, \theta)$ laminate.

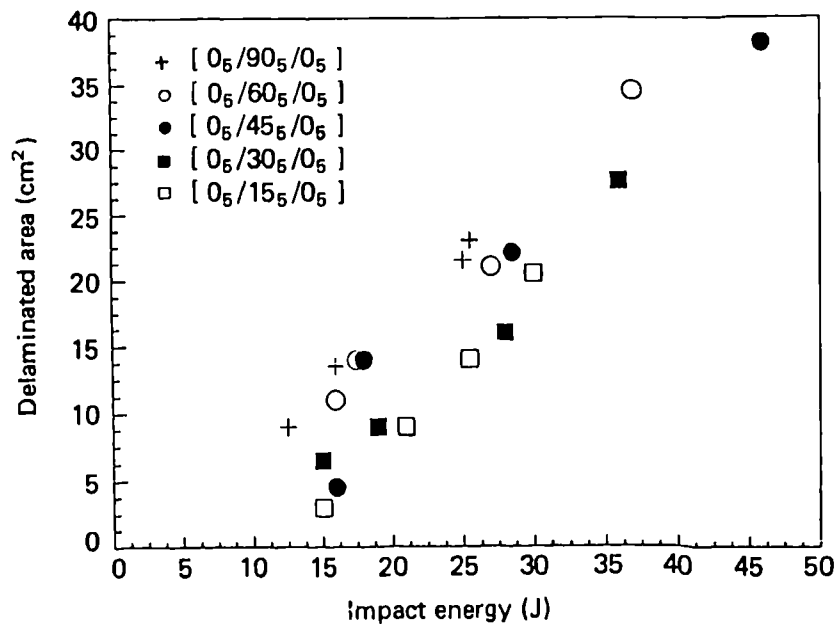


Figure 2.19: Delaminated area versus impact energy for a range of $(0^\circ, \theta^\circ, 0^\circ)$ GFRP laminates [77].

Other methods for reducing delamination include the use of woven fabrics [25,78], hybridization [79, 80-82] and three-dimensional stitching [83,84]. The use of woven fabric involves replacing the unidirectional $\pm 45^\circ$ plies in a multidirectional composite by a $\pm 45^\circ$ woven fabric. The nature of the fabric helps suppress the formation of delamination at critical interfaces [25]. Hybridization is the process where the impact resistance of composite material is enhanced by incorporating plies of lower modulus

fibres [79, 80-82]. The matrix is normally the same in both materials in order to ensure that they are fully compatible. Hancox and Wells [81] conducted Izod impact tests on a HT-S carbon fibre composite hybridised with E-glass fibre. They showed that the Izod impact energy could be increased by 500% through a hybridization process. The authors also claimed to have reduced the price of the composite and alter the mode of fracture in these materials. Helfinstine [79] also studied the effect of hybridization by performing Charpy impact test on a range of Kevlar T300 carbon fibre hybrids and drew similar conclusions to Hancox and Wells [81]. Dorey *et al.* [9] conducted high velocity impact tests on carbon-Kevlar hybrid laminates and found that the addition of the lower modulus Kevlar fibres increased the threshold energy for the onset of the damage by up to four times its original value. Three-dimensional stitching of composite materials involves processes such as weaving and braiding and can lead to improvements in the damage tolerance of composites [83-86].

Su [85] performed a series of Mode I delamination tests on both stitched and non-stitched AS4 carbon fibre/J1 composites. He showed that stitching with a Kevlar fibre increased its Mode I interlaminar fracture toughness by 100%. Instrumented drop-weight impact tests on a series of 2-D and 3-D composites indicated that the 3-D composite offered a superior impact and delamination resistance. However, the 3-D composite was not considered to be cost effective as a longer production time is required resulting in additional material costs.

The effect of the fibre stacking sequence on post-impact residual strength has also received considerable attention [25,37,75,86]. As mentioned in the previous section, much of the available literature focuses on the compression after impact strength since the reduction in residual strength is greater in compression than in tension. The potential conflict between the need to optimise the post-impact residual strength and improved impact resistance by manipulating its stacking sequence may well exist. For example, Dorey [75] suggested that in order to improve the impact resistance of a laminate, the $\pm 45^\circ$ fibres should be placed on its outermost surface. This stacking sequence may not be ideal where the stability of the laminate in compression is concerned. Here, stiffer

laminates with large amounts of 0° fibres are better suited to resisting compressive loads than 45° laminates [11]. Morton and Godwin [37] showed that a $(0_2^\circ, \pm 45^\circ)_2$ carbon fibre/PEEK laminate exhibits inferior properties to those offered by a $(\pm 45^\circ, 0_3^\circ, \pm 45^\circ, 0^\circ)_5$ laminate, Figure 2.20. Cantwell *et al.* [25] showed that the use of woven $\pm 45^\circ$ fabrics in $(0^\circ, \pm 45^\circ)$ laminates resulted in a reduction in the overall level of delamination under impact loading. Therefore, the residual strength of the mixed-woven composites was greater than those of standard composite materials as shown in Figure 2.21.

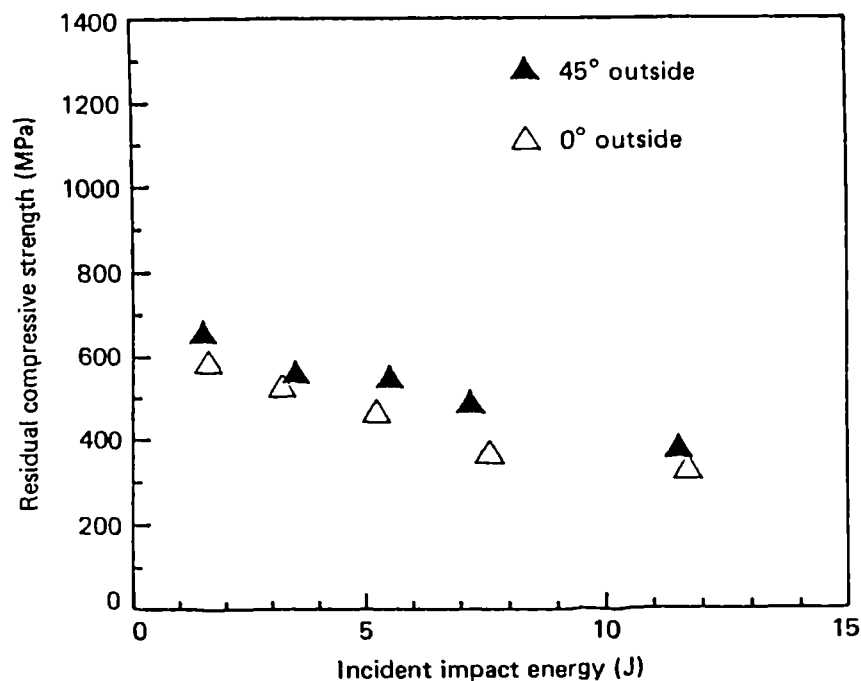


Figure 2.20: The effect of placing 45° plies on the outer surface of a 16-ply carbon fibre/PEEK laminate [37].

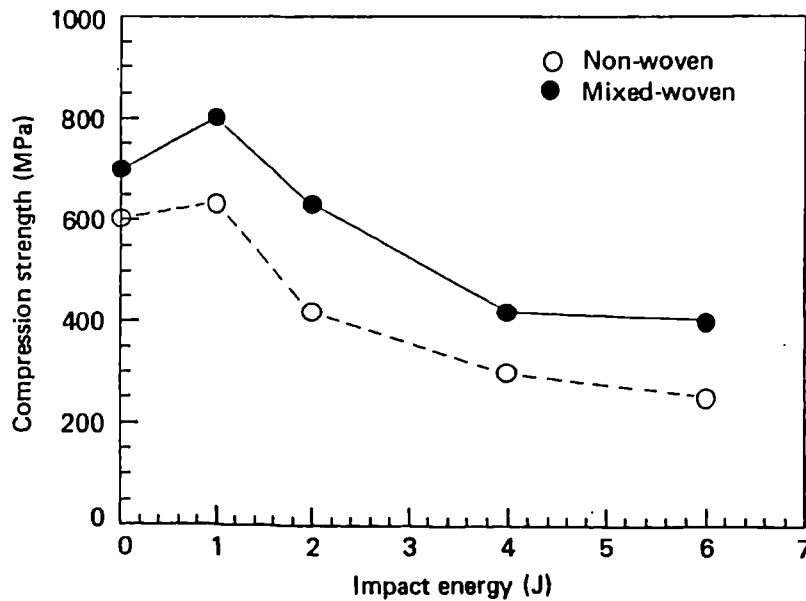


Figure 2.21: The effect of replacing the ($\pm 45^\circ$) plies in a 16-ply ($0^\circ, \pm 45^\circ$) CFRP composite with a woven fabric [25].

Similar results have been reported following impact tests on stitched carbon fibre composites [86]. The compressive strength after impact of stitched AS4/3501-6 laminates was up to 100 percent greater than similar non-stitched laminates based on the same fibres and stacking sequence.

2.4 The effect of projectile characteristics on the impact response of composite materials

The impactor or projectile plays an important part in dictating the impact response of composite materials. For example, the impactor material, size, shape and the angle of incidence relative to the surface of the specimen are all aspects of the projectile that have a significant affect on the impact response of the composite. The effect of the impactor

material on the impact response of a composite material was studied by Kumar and Rai [87]. Steel and aluminium cylindrical impactors were chosen in order to study the influence of material properties on the impact response and damage development in composite materials. Tests were undertaken on 32-ply carbon/epoxy plates with lay-ups of $[0^\circ, \pm 45^\circ, 90^\circ]_{4S}$ and $[0_2^\circ, \pm 45^\circ, 0^\circ, 90^\circ, 0_2^\circ, \pm 45^\circ, 0^\circ, 90^\circ, 0_2^\circ, \pm 45^\circ]_S$ respectively. Damage was characterised by measuring the delamination area as shown in Figure 2.22. A significant difference in the size of the delamination area developed by the steel and aluminium impactors was observed for a given impact velocity. They suggested that the difference is due to the fact that the mass of the steel impactor was about three times greater than that of the aluminium projectile.

Consequently, the contact stresses between the impacting steel projectile and the CFRP laminate were higher than the contact stresses developed by the aluminium projectile. They further evaluated the variation of delamination damage with projectile velocity for both projectiles. They showed that at a given impact velocity, the delamination damage generated by the steel projectile was several times greater than that due to the aluminium projectile as shown in Figure 2.23. From Figure 2.23, it is clear that for the same impactor, the total delamination area seems to be independent of the lay-up of the composites.

Finally, the large difference between the impact damage generated by the two different projectiles was attributed to factors such as the mass of the projectile and the acoustic impedance of the projectile.

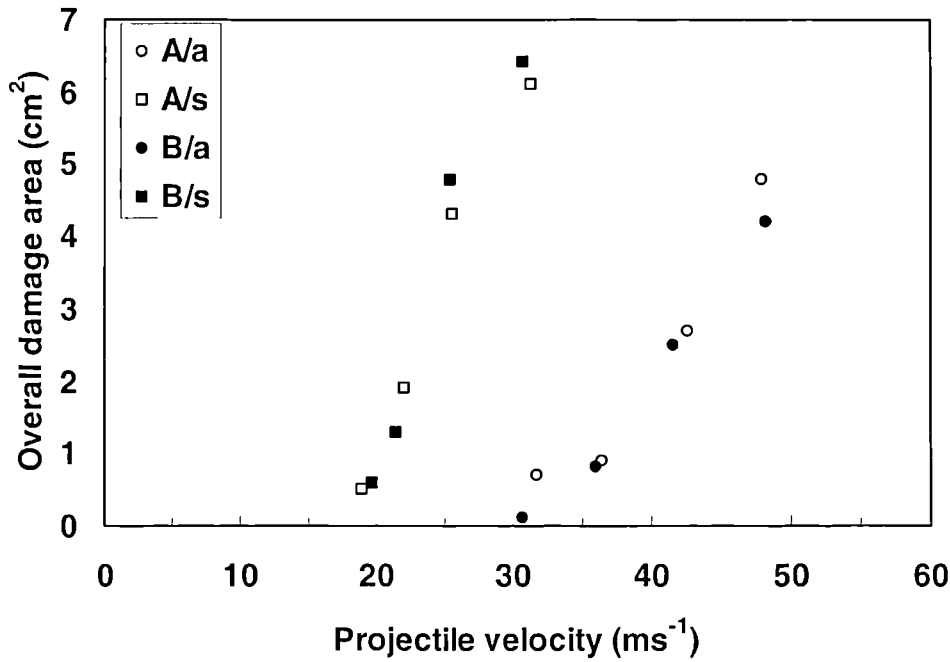


Figure 2.22: Damage area versus impact velocity for impact with steel and aluminium impactors [87]. ‘a’ and ‘s’ representing aluminium and steel impactors respectively, whereas ‘A’ and ‘B’ subscripts are for $[0^\circ, \pm 45^\circ, 90^\circ]_{4S}$ and $[0_2^\circ, \pm 45^\circ, 0^\circ, 90^\circ, 0_2^\circ, \pm 45^\circ, 0^\circ, 90^\circ, 0_2^\circ, \pm 45^\circ]_S$ composites respectively.

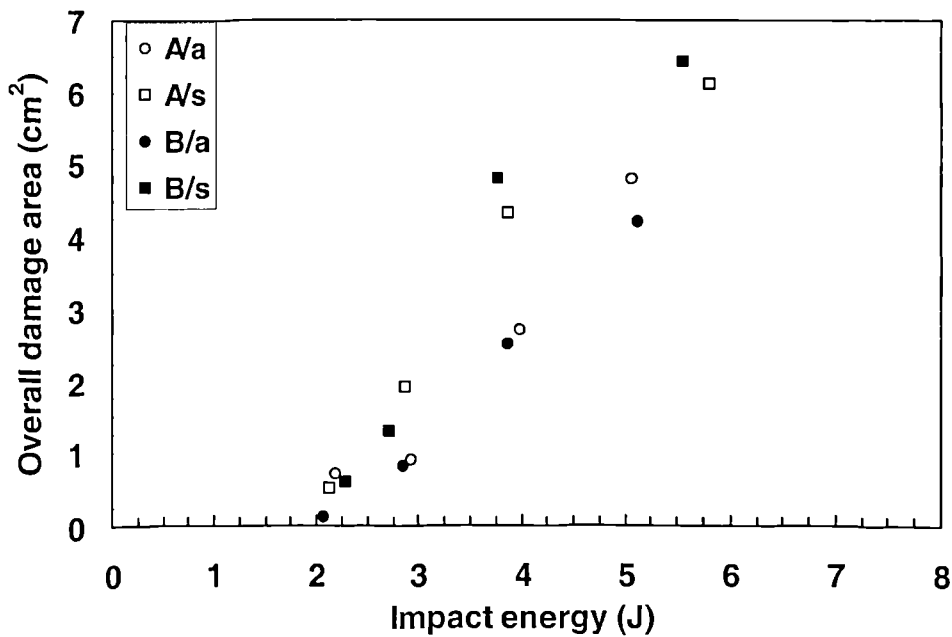


Figure 2.23: Damage area versus kinetic energy for impact with steel and aluminium impactors [87]. The subscripts have the same meaning as those in Figure 2.23.

Most of the published literature involves testing under normal impact conditions where the incident angle is 90° to the surface of the target. However, under general operating conditions, oblique impacts do occur where the incident angle is not 90° to the surface of the target. Several studies have been undertaken to investigate oblique impact [88,89]. Ghaffari *et al.* [88] showed that the damage area under oblique impact loading conditions was dependent on the angle of incidence. Further investigation [89] showed that when the damage area is plotted versus the normal component of initial velocity, the data collapse into a single curve as shown in Figure 2.24.

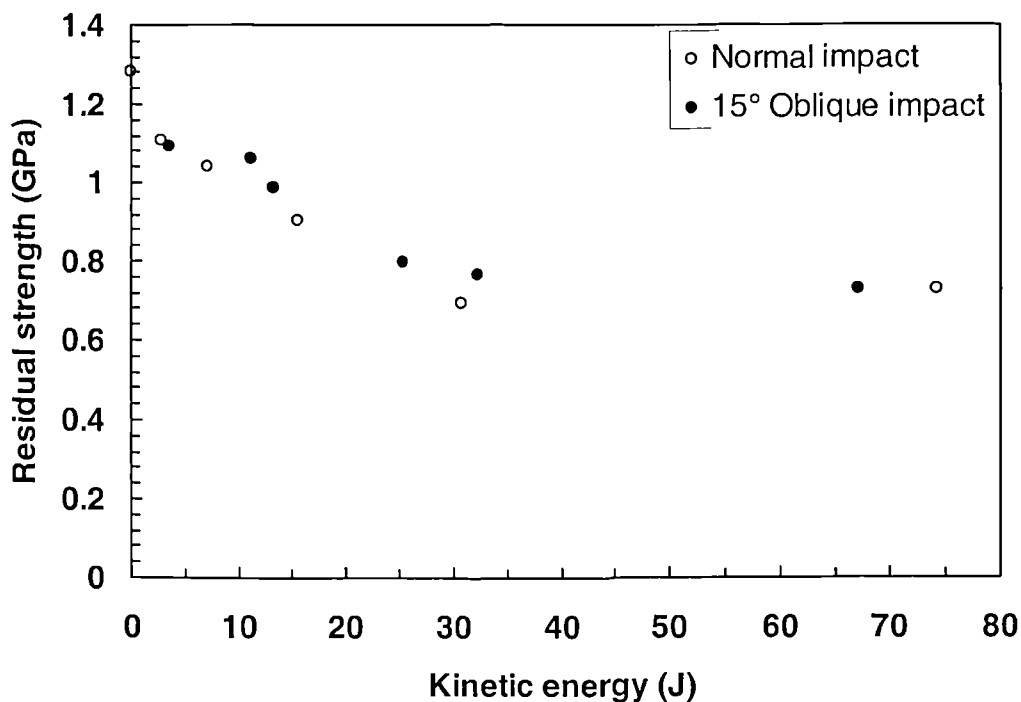


Figure 2.24: The effect of impact angle on the residual tensile strength of a $[0^\circ/90^\circ/0^\circ]$ glass/epoxy laminate impacted by a tip-ended projectile [89].

As mentioned earlier, the impactor mass has a significant influence on the amount of damage generated under impact loading. Jackson and Poe [90] performed an extensive experimental study to investigate the effect of impactor mass on the maximum impact force for a given kinetic energy of the impactor. The maximum impact force was

calculated based on the simple energy balance model. Their study was undertaken on 48-layer quasi-static carbon/epoxy square laminated plates. The specimens were either simply-supported or clamped on all sides. They found that for a very large impactor mass, i.e. larger than 10 kg, an energy balance model was still capable of computing the maximum impact force accurately. They also showed that, the impactor to target mass ratio needs to be large to ensure that a quasi-static solution can be used. In contrast, they found that for a small impactor mass at a given impact energy, the maximum impact force was almost the same and independent of the plate size and boundary conditions. They also showed that clamped plates with a higher stiffness exhibit a response that is much closer to static equivalent one.

2.5 The effect of loading rates on the impact response of composite materials

In recent years, attention has been concentrated in studying the effect of loading rate on the fundamental properties of the constituent materials [91-96]. Harding and co-workers [93-94,97,99] examined the strain-rate sensitivity of a number of fibres and composites including Kevlar, glass and carbon fibre reinforced composites. From their results, they found that carbon fibres are not sensitive to loading rate when tested in fibre-dominated modes (interlaminar fracture), whereas Kevlar and glass fibre reinforced plastics composite (GFRP) exhibit a pronounced dependence on strain rate. The interlaminar fracture toughness has been widely used as a parameter to study the sensitivity of the matrix-dominated modes to loading rate [99,100]. Such tests are particularly important since the compressive strength of composites is sensitive to the matrix-dominated modes of failure such as delamination [101,102]. Double cantilever beam (DCB) tests on carbon fibre/epoxy composites have shown that the Mode I interlaminar fracture toughness, G_{Ic} , does not vary with strain rate [103], as shown in Figure 2.25. However, when similar tests are performed on carbon fibre/PEEK (APC2) composite, a distinctive rate dependent threshold has been shown and the toughness value drops significantly with increasing strain rate as shown in Figure 2.25. It is clear that over a wide range of strain rates, the Mode I fracture toughness (G_{Ic}) remains unaffected until a critical

threshold is reached where the toughness drops by about 20 percent of its original value. Impact tests on carbon fibre/PEEK showed that beyond a certain threshold of impact velocity, a change in failure mode can occur [37] with the material undergoing a sudden drop in mechanical performance [104].

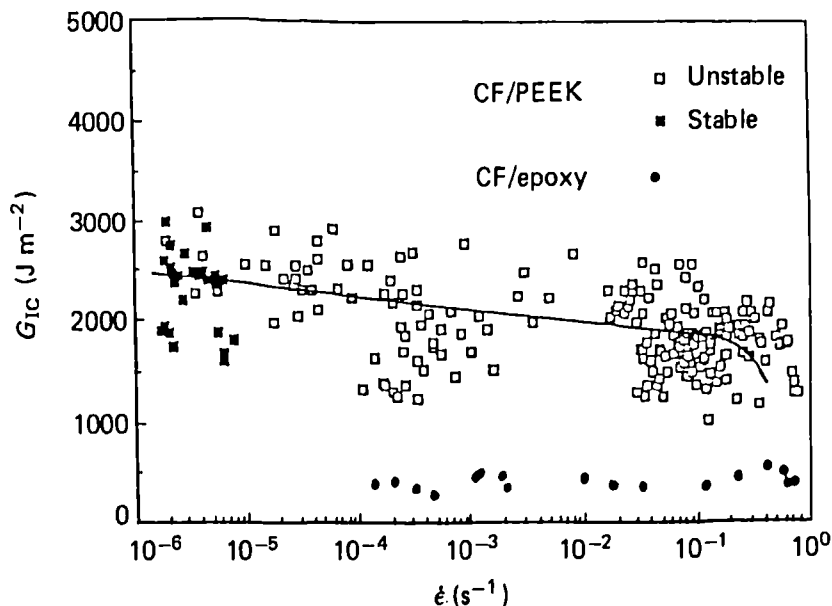


Figure 2.25: Variation of G_{Ic} with strain rate for carbon fibre/PEEK composite [103].

A number of other studies [105-107] have reported on the effect of loading rate on the interlaminar crack resistance of composite materials. Miller *et al.* [105] studied the effect of loading rate on the Mode I interlaminar fracture toughness (G_{Ic}) of a carbon/epoxy laminate using the width-tapered DCB specimen. From their study, they showed that G_{Ic} does not exhibit any rate sensitivity when tested at crosshead displacement rates between 0.025 and 50 mm/minute. Hunston and Bascom [106] observed a pronounced rate-dependent in an elastomer-modified epoxy, with the fracture energy decreasing with the increase of loading rate. Aliyu and Daniel [107] in their study, found that the Mode I strain-energy release rate of a unidirectional carbon/epoxy increases slightly with strain rate. Aliyu and Daniel [107] also investigated a carbon fibre/epoxy based composite having an elastomer modified epoxy resin matrix and revealed that there is an increase in G_{Ic} with increasing rate. A more recent study [108]

on loading rate effects in the interlaminar fracture toughness of a carbon fibre/epoxy under Mode I and Mode II found that both fracture toughnesses decreased with increasing loading rate. Mall *et al.* [100] studied the effect of loading rate on the Mode I fracture toughness of a carbon fibre/PEEK composite. DCB specimens were used and tested under displacement control mode using an Instron testing machine. The results are shown in Figures 2.26. Clearly, the critical strain-energy release rate of carbon/epoxy composite decreases with increasing loading rate. Mall *et al.* [100] also presented a comparative study of the effect of loading rate on the delamination initiation toughness of four different composite systems, these being AS4/3501-6 [107,108], a toughened epoxy system (T300/F185) [109] and two thermoplastic systems, APC-2 [108] and a woven carbon/PEEK. The findings are shown in Figure 2.27. Clearly, the interlaminar fracture toughness of the tough composites, T300/F185, APC2 and the woven carbon/PEEK decreases with increasing loading rate. The results of the unidirectional carbon fibre/PEEK (APC2) showed that G_{Ic} remains fairly constant around 1700 J/m² to 1500 J/m² over four decades of loading rate and decreases by up to 75 percent over the next decade in strain rate.

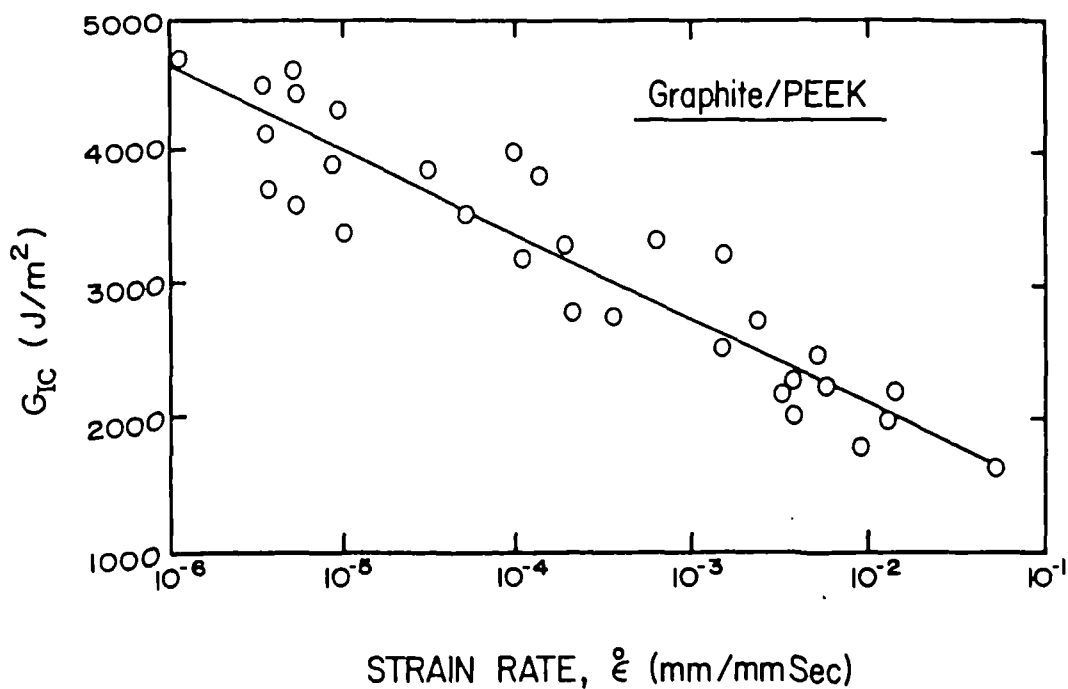


Figure 2.26: Interlaminar-fracture energy of a woven carbon/PEEK composite as a function of strain rate [100]

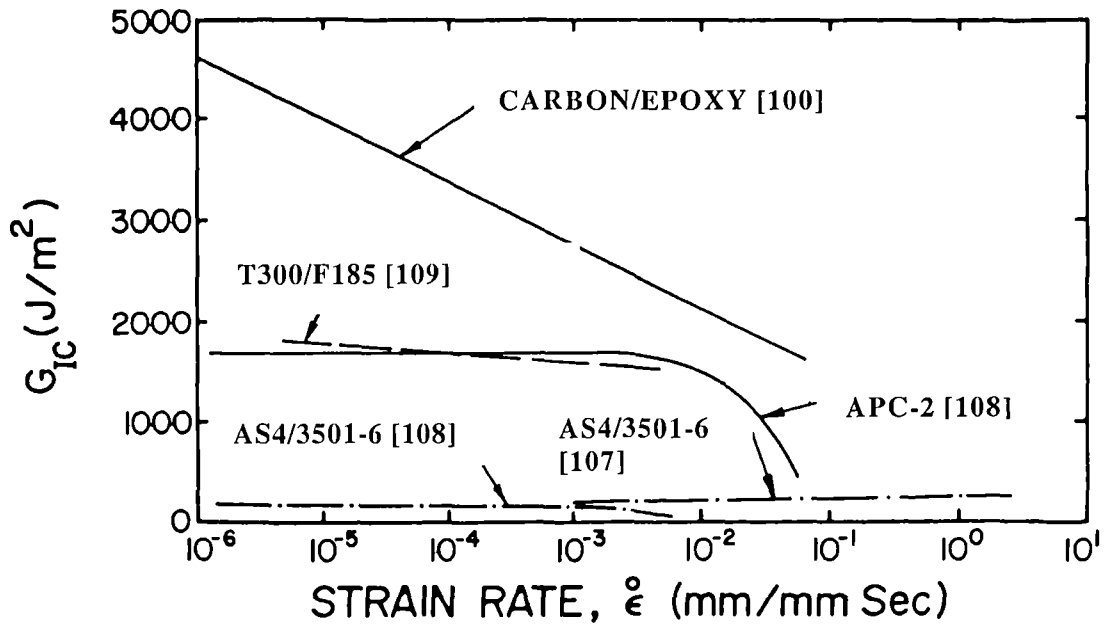


Figure 2.27: Relationship between mode I interlaminar fracture energy and strain rate of four composites [100]

Smiley and Pipes [102,110] conducted a series of studies to establish the effect of loading rate on the Mode I and Mode II interlaminar fracture toughness of composites using the DCB specimen. AS4/3501-6 and APC-2 carbon fibre reinforced PEEK composites were used in their study. The fracture toughness values were determined at the onset of crack growth and the Mode I interlaminar fracture toughness was determined as a function of crack tip opening as shown in Figure 2.28. The results illustrate that APC-2 is considerably tougher than AS4-3501-6.

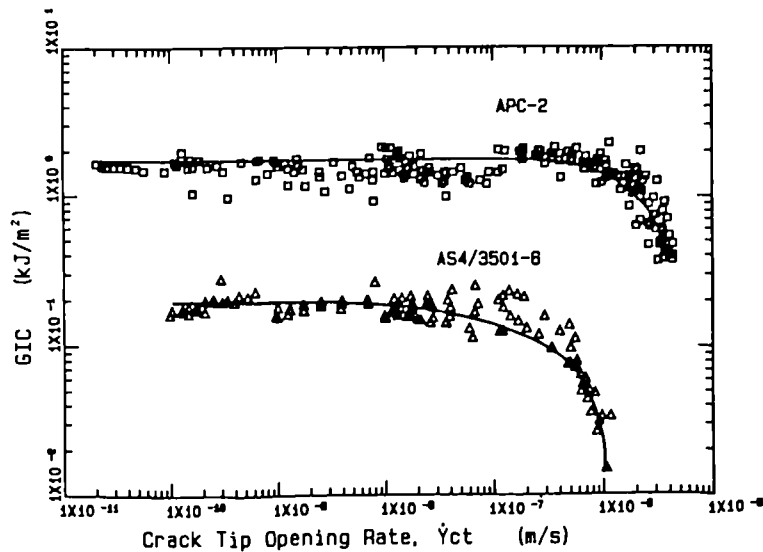


Figure 2.28: Rate sensitivity of Mode I interlaminar fracture toughness [102].

2.6 Aims and objectives of the research

The objectives of this research study are to investigate and understand the impact response of sandwich composite materials under low velocity impact loading. Part of this research work involves modelling and predicting the impact response of a number of laminates and sandwich structures under low velocity impact loading conditions. The first step to gain an understanding to the impact problem is to develop a simple energy balance model. This model will then used to predict the impact response of simple structures such as a simply-supported beam. The effect of varying the skin and core properties of a range of sandwich structures will also be investigated during the research. The next step will be to evaluate the model using more representative structures such as circular plates. The test regime is summarised in Figure 2.29. The study will also investigate the failure modes in sandwich structures subjected to impact loading and identify the role of core properties in determining the failure mechanisms in sandwich structures. It is hoped that this approach will lead to a greater understanding of the impact response of sandwich structures.

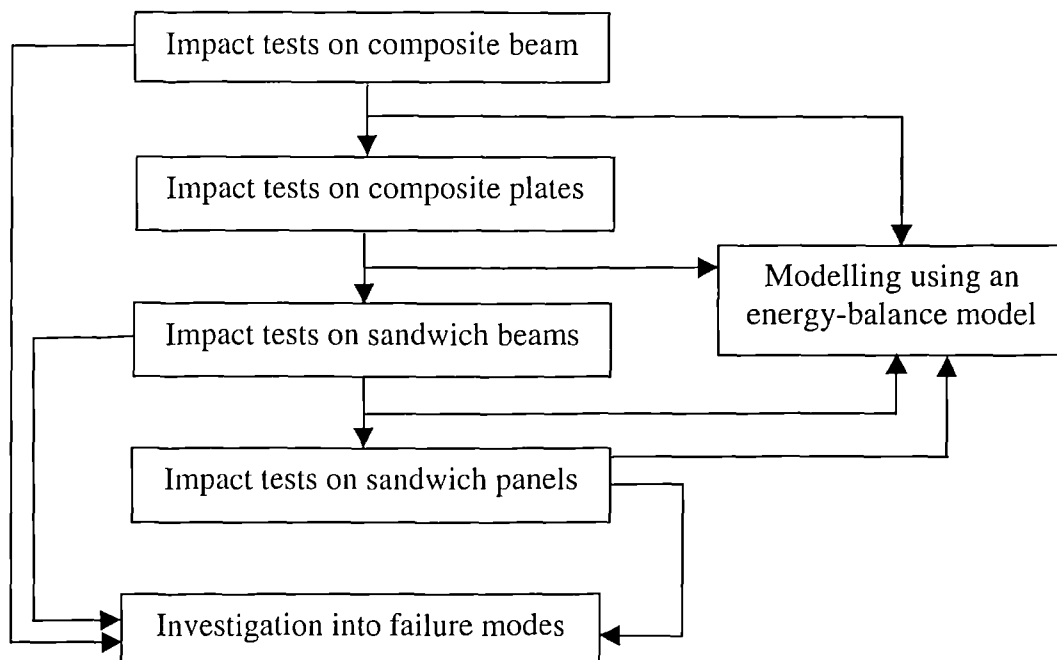


Figure 2.29: A summary of the test regime used to gain an understanding of the impact response of the composite materials and sandwich structures.

2.7 References

1. W.J. Cantwell, "Impact damage in carbon fibre composites", PhD thesis, University of London, U.K., 1985.
2. W. Elber, "Failure mechanics in low velocity impact on thin composite plates", NASA Technical Paper 2152, 1988.
3. M. Vedula and M.J. Koczak, "Impact resistance of cross-plyed polyphenylene sulfide composites", Proc. Fourth Japan-U.S. Conference on Composite Materials, Technomic Publication Co. Inc, pp 72-81, 1988.
4. G. Clark, "Modelling of impact damage in composite laminates", *Composites*, 20, pp 209-214, 1989.
5. D.F. Adams and A.K. Miller, "An analysis of the impact behaviour of hybrid composite materials", *Material Science and Engineering*, 19, pp 245-260, 1975.
6. P.W.R. Beaumont, P.G. Riewald and C. Zweben, "Methods for improving the impact resistance of composite materials", ASTM STP 568, pp 134-158, 1974.
7. N.L. Hancox, "Izod impact testing of carbon fibre reinforced plastics", *Composites*, 2, pp 41-45, 1971.
8. M.G. Bader and R.M. Ellis, "The effect of notches and specimen geometry on the pendulum impact strength of uniaxial CFRP", *Composites*, 5, pp 253-258, 1974.
9. G. Dorey, G.R. Sidey and J. Hutchings, "Impact properties of carbon fibre/Kevlar 49 fibre hybrid composites", *Composites*, 9, pp 25-32, 1978.
10. W.J. Cantwell, P.T. Curtis and J. Morton, "An assessment of the impact performance of CFRP with high strain carbon fibres", *Composites Science and Technology*, 25, pp 133-148, 1986.
11. W.J. Cantwell and J. Morton, "Impact resistance of composite materials - a review", *Composites*, 22, pp 347-362, 1991.
12. C.C. Chamis, M.P. Hanson and T.T. Serafini, "Impact resistance of unidirectional fibre composites" in *Composite Materials: Testing and Design (Second Conference)*, pp 324-349, 1985.
13. P.W.R. Beaumont, "Fracture mechanisms in fibrous composites", in *Fracture Mechanics*, Edited by R.A. Smith, Pergamon Press, pp 211-233, 1979.

14. F.J. Bradshaw, G. Dorey and G.R. Sidey, "Impact resistance of carbon reinforced plastics" RAE TR 72240, MOD, 1972.
15. P. Davies, W.J. Cantwell, H. Richard, C. Moulin and H.H. Kausch, "Interlaminar fracture testing of carbon fibre/PEEK composites validity and applications", in *Developments in the Science and Technology of Composite Materials*, Proc. ECCM3, Edited by A.R. Bunsell, P. Lamicq and A. Massiah, Elsevier Applied Science Publication, pp 747-755, 1989.
16. K.T. Teh and J. Morton, "Impact damage development and residual compression performance of advance composite systems", 34th AIAA Structure, Structural Dynamics and Materials Conference, pp 877-886, 1993.
17. J.K. Kim, D.B. Mackay and Y.W. Mai, "Drop-weight impact damage tolerance of CFRP with rubber-modified epoxy matrix", *Composites*, 24, pp 485-494, 1993.
18. G.S. Chen, G.M. Bidinger and M.C. Lou, "Impact damage tolerance of thin wall composite structures", 34th AIAA Structure, Structural Dynamics and Materials Conference, 2, pp 847-858, 1993.
19. H.G. Recker, T. Allspach, V. Alstadt, T. Folda, W. Heckman, P. Itteman, H. Tesch and T. Weber, "Highly damage-tolerance carbon fibre epoxy for primary aircraft applications", *SAMPE Quarterly*, 21, pp 46-51, 1989.
20. K.B. Su, "Mechanisms of interlaminar fracture in a thermoplastic matrix composite laminate", 5th International Conference on Composite material (ICCM V), 3, pp 995-1006, 1985.
21. P. Davies and F.X. de Charentenay, "The effect of temperature on the interlaminar fracture of tough composites", 6th International Conference on Composite material (ICCM VI) and ECCM II, 3, Elsevier Publication, pp 284-294, 1987.
22. T.J. Chapman, A.J. Smiley and R.B. Pipes, "Rate and temperature effects on mode II interlaminar fracture toughness in composite materials", 6th International Conference on Composite material (ICCM VI) and ECCM II, 3, Elsevier Applied Science Publishers, pp 295-304, 1987.
23. I. Verpoest, L. Li and L. Doxsee, "A combined micro and macro mechanical study of impact behaviour of carbon and glass fibre epoxy composites", 7th International Conference on Composite Materials (ICCM VII), pp 316-321, 1989.

24. S. Abrate, "Impact on laminated composites: Recent advances", *Applied Mechanics Review*, 11, pp 517-544, 1994.
25. W.J. Cantwell, P.T. Curtis and J. Morton, "Low velocity impact damage tolerance CFRP laminates containing woven and non-woven layers", *Composites*, 14, pp 301-305, 1983.
26. D.L. Hunston, "Composite interlaminar fracture: effect of matrix fracture energy", *Composites Tech. Review*, 6, pp 176-180, 1984.
27. W.D. Bascom, R.L. Cottingham, R.L. Jones and P. Pesyer, "The fracture of epoxy and elastomer modified epoxy polymers in bulk and as adhesives", *J. Applied Polymer Science*, 19, pp 2545-2562, 1975.
28. J.G. Williams and M.D. Rhodes, "Effect of resin on impact damage tolerance of graphite/epoxy laminates" in *Composite Materials: Testing and Design (Sixth conference)*, ASTM STP 787, Ed. I. Daniel, pp 450-480, 1982.
29. C.B. Bucknall and I.K. Partridge, "Phase separation in epoxy resins containing polyethersulphone", *Polymer*, 24, pp 639-644, 1983.
30. J. Diamant and R.J. Moulton, "Development of resins for damage tolerant composites- a systematic approach", *SAMPE Quarterly*, 16, pp 13-21, 1984.
31. L.D. Bravenec, A.G. Phillipov and K.C. Dewhirst, "New concept in damage to tolerant composites-lightly cross-linked thermosets", 34th Int. SAMPE Symposium, pp 714-725, 1989.
32. G.F. Sykes and D.M. Stoakley, "Impact penetration studies of graphite/epoxy laminates", 12th Nat. SAMPE Tech. Conference, pp 482-493, 1980
33. S. Rechak and C.T. Sun, "Optimal use of adhesive layers in reducing impact damage in composite laminates", in *Composite Structures*, 2, pp 218-231, 1987.
34. R.E. Evans and J.E. Masters, "A new generation of epoxy composites for primary structural applications: materials and mechanics", ASTM STP 937, pp 413-436, 1987.
35. J.E. Masters, "Correlation of impact and interleaved laminates", 6th International Conference on Composite material (ICCM VI), Edited by F.L Matthew, N.C.R. Buskell, J.M. Hodgkinson and J. Morton (Elsevier Applied Science Publications, pp 3.69-3.107, 1987.

36. K.R. Hirschbuehler, "A comparison of several mechanical tests used to evaluate the toughness of composites", ASTM STP 937, pp 61-73, 1987.
37. J. Morton and E.W. Godwin, "Impact response of tough carbon fibre composites", Composite Structures, 13, pp 1-19, 1989.
38. G. Dorey, "Impact crashworthiness of composite structures", In Structural Impact and Crashworthiness, Elsevier Applied Science, London, pp 155-192, 1984.
39. H.G. Recker, T. Allspach, V. Alstadt, T. Folda, W. Heckman, P. Itteman, H. Tesch and T. Weber, "Toughened thermosets for damage tolerance carbon fibre reinforced composites", SAMPE Journal, 26, pp 73-78, 1990.
40. G. Dorey, "Damage tolerance and damage assessment in advanced composites", In Advanced Composites, ed. I.K. Partridge, Elsevier Applied Science, pp 369-398, 1989.
41. D. Hull and Y.B. Shi, "Damage mechanism characterisation in composite damage tolerance investigation", Composite Structures, 23, pp 99-120, 1993.
42. D.L. Hunston, R.J. Moulton, N.J. Johnston and W.D. Bascom, "Matrix resin effects in composite delamination: Mode I fracture aspects", Toughened Composites, ASTM STP 937, Ed. N.J. Johnston, pp 923-943, 1989.
43. W. Zhong and B.Z. Jang, "Material design approaches for improving impact resistance of composites", Key Engineering Materials, Vols. 141-143, Trans Tech Publications, pp 169-186, 1998.
44. K.R. Hirschbuehler, "An improved 270°F performance interleaf system having extremely high impact resistance", SAMPE Quarterly, 17, pp 46-49, 1985.
45. G.V. Gandhe and O.H. Jr. Griffin, "Post-impact characterisation of interleaved composite materials", SAMPE Quarterly, 20, pp 55-58, 1989.
46. K. Tobukuro, N. Odagiri, Y. Ito and T. Nishimura, "High impact resistance CFRP from thermosetting system of Torayca T800/3900 prepreg", in New Generation Materials and Processes, Ed. By F. Saporiti, W. Merati and L. Peroni, SAMPE, pp 293-306, 1988.
47. P. Pintado, T.J. Vogler and J. Morton, "Impact damage development in thick composite laminates" Composites Engineering, 1, pp 195-210, 1991.

48. P. Pintado, T.J. Vogler and J. Morton, "Impact damage tolerance of thick graphite-epoxy composite material systems", 8th International Conference on Composite material (ICCM VIII), pp 1-12, 1991.
49. O. Ishai and A. Shargai, "Effect of impact loading on damage and residual compressive strength of CFRP laminated beams", *Composites Structures*, 14, pp 319-337, 1990.
50. D.G. Peiffer, "Impact strength of thick interlayer composites", *Journal of Applied Polymer Science*, 24, pp 1451-1455, 1979.
51. J.C. Goan and S.P. Prosen, "Interfaces in composites", ASTM STP 452, pp 3-26, 1969.
52. S. Lehman, C. Megerdigian and R. Papalia, "Carbon fibre/resin matrix interphase: effect of carbon fibre surface treatment on composite performance", *SAMPE Quarterly*, 16, pp 7-13, 1985.
53. L.T. Drzal and M.J. Rich, "Effect of carbon fibre/epoxy matrix adhesion on composite fracture behaviour", in *Recent Advances in Composites in United States and Japan*, pp 16-26, 1991.
54. K.F. Rogers, G.R. Sidey and D.M. Kingston-Lee, "Ballistic impact resistance of carbon fibre laminates", *Composites*, 2, pp 237-241, 1971.
55. G. Dorey, "Relationship between impact resistance and fracture toughness in advanced composite materials", in *Effect of Service Environment on Composite Materials*, AGARD CP 288, 1980.
56. S.J. Bless and D.R. Hartman, "Ballistic penetration of S-2 glass laminates", 21st Int. SAMPE Conference, pp 852-866, 1989.
57. F.N. Cogswell, "Microstructure and structure of thermoplastic aromatic polymer composites", Int. SAMPE Symposium Exhibition, 28, pp 528-534, 1983
58. Y. Lee and R.S. Porter, "Crystallisation of PEEK in carbon fibre composites", *Polymer Science and Engineering*, 26, pp 633-639, 1986.
59. B. Tissington, G. Pollard and I.M. Ward, "Study of the impact behaviour of ultra-high-modulus polyethylene fibre composites", *Composites Science and Technology*, 44, pp 197-208, 1992.

60. M.A. Montes-Moran, A. Martinez-Alonso, J.M.D. Tascon and R.J. Young, "Effects of plasma oxidation on the surface and interfacial properties of ultra-high modulus carbon fibres", *Composites: Part A*, 32, pp 361-371, 2001.
61. L. Ying, "Role of fibre/matrix interphase in carbon fibre/epoxy composite impact toughness", 38th Annual Conference Preprint - Reinforced Plastics/Composites Institute, Society of the Plastics Industry, RP/C '83: Composite Solutions to Material Challenges, 1983.
62. L.B. Greszczuk, "Theoretical studies of the mechanics of the fibre-matrix interface in composites", *ASTM STP 452*, pp 42-58, 1969.
63. S. Deng and L. Ye, "Influence of fibre-matrix adhesion on mechanical properties of graphite/epoxy composites: II. Interlaminar Fracture and Inplane Shear Behaviour", *J. Reinforced Plastics and Composites*, 18, pp 1041-1057, 1999.
64. S. Deng and L. Ye, "Influence of fibre-matrix adhesion on mechanical properties of graphite/epoxy composites: III. Impact and dynamic mechanical properties", *J. Reinforced Plastics and Composites*, 19, pp 689-703, 2000.
65. M.S. Madhukar and L.T. Drzal, "Fibre-matrix adhesion and its effect on composite mechanical properties: I. Inplane and interlaminar shear behaviour of graphite/epoxy composites", *J. Composite Materials*, 25, pp 933-957, 1991.
66. M.S. Madhukar and L.T. Drzal, "Fibre-matrix adhesion and its effect on composite mechanical properties: II. Longitudinal (0) and transverse (90) tensile and flexure behaviour of graphite/epoxy composites", *J. Composite Materials*, 25, pp 958-991, 1991.
67. L.J. Broutman and A. Rotem, "Impact strength and toughness of fibre composite materials", *ASTM STP 568*, pp 114-133, 1975.
68. W.J. Cantwell and J. Morton, "Geometrical effects in the low velocity impact response of CFRP", *Composite Structures*, 12, pp 35-59, 1986.
69. W.J. Cantwell, "The influence of target geometry on the high velocity impact response of CFRP" *Composite Structures*, 10, pp 247-265, 1988.
70. G. Dorey, "Impact damage in composites-development, consequences and prevention", 6th International Conference on Composite Materials (ICCM VI) & ECCM 2, 3, pp 1-26, 1987.

71. P. Robinson and G.A.O. Davies, "Impactor mass and specimen geometry effects in low velocity impact of laminated composites", *Int. J. Impact Engng*, 2, pp 189-207, 1992.
72. G. Dorey, "Fracture behaviour and residual strength of carbon fibre composites subjected to impact loads", in *Failure Modes of Composite Materials with Organic Matrices and Their Consequences in Design*, AGARD CP 163, paper no. 8, 1975.
73. L.B. Ilcewicz, E.F. Dost and R.L. Coggeshall, "A model for compression after impact strength evaluation", 21st Int. SAMPE Technical Conference, pp 130-140, 1989.
74. E. Demuts and P. Sharpe, "Tougher advanced composite structures", 28th Structures, Structural Dynamics and Materials Conference, pp 385-393, 1987.
75. G. Dorey, "Fracture of composites and damage tolerance", in *Practical Consideration of Design, Fabrication and Tests for Composite Materials*, AGARD Lecture series 124, 1982.
76. M. Stevanovic, M. Kostic, T. Stecenko and D. Briski, "Impact behaviour of CFRP composites of different stacking geometry", in *Composites Evaluation*, Proc. TEQC 87, pp 78-83.
77. S. Hong and D. Liu, "On the relationship between impact energy and delamination area", *Exptl Mech*, 13, pp 115-120, 1989.
78. M. Vedula and M.J. Koczak, "Impact resistance of cross-plyed polyphenylene sulphide composites", *J. of Thermoplastic Composite Materials*, 2, pp 154-163, 1989.
79. J.D. Helfinstine, "Charpy impact of unidirectional carbon/Aramid/epoxy hybrid composites", in *Composite Materials: Testing and Design*, ASTM STP 617, pp 375-388, 1977.
80. P.K. Mallick and L.J. Broutman, "Static and impact properties of laminated hybrid composites", *J. of Testing and Evaluation*, 5, pp 190-200, 1977.
81. N.L. Hancox and H. Wells, "Izod impact properties of carbon fibre/glass fibre sandwich structures", *Composites*, 4, pp 26-29, 1973.

82. D.F. Adams and J.L. Perry, "Static and impact behaviour of carbon/epoxy composite laminate containing third-phase reinforcement materials", *J. Testing and Evaluation*, 5, pp 114-123, 1977.
83. F.K. Ko and D. Hartman, "Impact behaviour of 2D and 3D glass/epoxy composites", *SAMPE Journal*, 22(4), pp 26-30, 1986.
84. J.W. Herrick, "Impact resistant multi-directional composites", 12th Nat SAMPE Conference, pp 845-856, 1986.
85. K.B. Su, "Delamination resistance of stitched thermoplastic matrix composite laminates", *ASTM STP 1044* edited by G.M. Newaz, pp 279-300, 1989.
86. M.B. Dow and D.L. Smith, "Damage tolerant composite materials produced by stitching carbon fabrics", 21st Int. SAMPE Technical Conference, 1989.
87. P. Kumar and B. Rai, "Delamination of barely visible impact damage in CFRP laminates", *Composite Structures*, 23, pp 313-318, 1993.
88. S. Ghaffari, T.M. Tan and J. Awerbuch, "An experimental and analytical investigation on the oblique impact of carbon/epoxy laminates", 22nd Int. SAMPE Technical Conference, pp 494-508, 1990.
89. S.T. Jenq, S.B. Wang and J.D. Wu, "Effect of normal and oblique impact damages on the strength degradation of composite laminates", 8th Int. Conference on Composite Materials (ICCM/8), pp 1-9, 1991.
90. W.C. Jackson and C.C. Poe, *J. Composites Technology and Research*, 15, p.282, 1993.
91. J.W. Gillespie Jr, L.A. Carlsson and A.J. Smiley, "Rate dependent Mode I interlaminar crack growth mechanisms in carbon/epoxy and carbon/PEEK", *Composites Science and Technology*, 28, pp 1-15, 1987.
92. S. Amijima and T. Fuji, "Compressive strength and fracture characteristics of fibre composites under impact loading", in *Progress in Science and Engineering of Composites*, 4th Int. Conference on Composite Materials, pp 399-413, 1982.
93. J. Harding and L. Welsh, "A tensile testing technique for fibre-reinforced composites at impact rates of strain", *J. Materials Science*, pp 1810-1826, 1983.

94. L.M. Welsh and J. Harding, "Effect of strain-rate on the tensile failure of woven-reinforced polyester resin composites", Report OUEL 1578/85, University of Oxford, UK, 1985.
95. I.M Daniel, G. Yaniv and J.W. Auser, "Rate effect on delamination fracture toughness of carbon/epoxy composites" in *Composite Structures*, 2, pp 258-272, 1984.
96. J. Karger-Kocsis and K. Friedrich, "Temperature and strain-rate effects on the fracture toughness of PEEK and its short glass-fibre reinforced composite", *Polymer*, 27, pp 1753-1760, 1986.
97. Y. Bai and J. Harding, "Fracture initiation in glass-reinforced plastics under impact compression", in *Structural Impact and Crashworthiness* edited by J. Morton, 2, pp 482-493, 1984.
98. L.M. Welsh and J. Harding, "Effect of strain-rate on the tensile failure of woven-reinforced polyester resin composites", Report OUEL 1578/85, University of Oxford, UK, 1985.
99. J. Harding, "Impact damage in composite materials", *Science and Engineering of Composite Materials*, 1, pp 41-68, 1989.
100. S. Mall, G.E. Law and M. Katouzian, "Loading rate effect on interlaminar fracture toughness of a thermoplastic composite", *J. Composite Materials*, 21, pp 569-579, 1987.
101. J.H. Starnes, M.D. Rhodes and J.G. Williams, "Effect of impact and holes on compressive strength of a carbon/epoxy laminate", in *Non-destructive Evaluation and Flaw Critically for Composite Materials*", ASTM STP 696, edited by R.B. Pipes, pp 145-171, 1979.
102. A.J. Smiley and R.B. Pipes, "Rate effects on Mode I interlaminar fracture toughness in composite materials", *J. Composite Materials*, 21, pp 670-687, 1987.
103. M. Barbezat, "The influence of loading rate on the behaviour of epoxy composites", Ph.D. Thesis, Ecole Polytechnique Federale de Lausanne, Switzerland, 1990.

104. E. Dan-Jumbo, A.R. Leewood and C.T. Sun, "Impact damage characteristics of bismaleimides and thermoplastic composite laminates", ASTM STP 1012 edited by P.A. Lagace, pp 356-372, 1989.
105. A.G. Miller, P.E. Hertzberg and V.W. Rantala, "Toughness testing of composite materials", SAMPE Quarterly, pp 36-42, 1981.
106. D.L. Hunston and W.D. Bascom, "Effects of layup, temperature and loading rate in double cantilever beam (DCB) tests on interlaminar crack growth", Composites Technology Review, 5, pp 118-119, 1983.
107. A.A. Aliyu and I.M. Daniel, "Effects of strain rate on delamination fracture toughness of carbon/epoxy", ASTM STP 876, pp 336-348, 1985.
108. A.J. Smiley, "Rate sensitivity of interlaminar fracture toughness in composite materials", M.S. Thesis, University of Delaware, 1985.
109. I.M. Daniel, I. Shareef and A.A. Aliyu, "Rate effects of delamination fracture toughness of carbon/epoxy", ASTM STP 876, 1985.
110. A.J. Smiley and R.B. Pipes, "Rate sensitivity of Mode II interlaminar fracture toughness in carbon/epoxy and carbon/PEEK composite materials", Composites Science and Technology, 29, pp 1-15, 1987.

CHAPTER 3: THEORETICAL APPROACHES AND IMPACT MODELS

The first step in gaining a complete understanding of the impact problem is to develop a suitable mathematical analysis to model the dynamic event. In this chapter, a number of theoretical models that have been used to model the impact response of composite laminates and sandwich structures are presented. Although a wide range of detailed and complex models exists in the literature, particular attention will focus on relatively simple models that can be readily applied by industry and other end-users.

3.1 Introduction

Laminated composite materials and sandwich structures are used extensively in aerospace, marine and off-shore applications. These materials are renowned for their high specific strengths and high specific moduli and their capability to be tailored for a given load-bearing application. However, their behaviour under impact loading conditions is a cause for concern since impact loading can occur during manufacture, normal operation or routine maintenance operations. The situation is frequently critical because even though the damage that has been introduced is often undetectable during visual inspection, it can provoke a significant reduction in the strength and stiffness of the structure. In order to understand and minimise this problem, the response of composites and sandwich structures under impact loading needs to be studied and understood. Clearly, one can undertake impact tests on a particular material system and structure and obtain useful information regarding its impact response. However, it is not necessarily the case that these results can be directly related to other structures or systems. One way to overcome this problem is to develop a simple model that can be used under a wide range of test conditions on an equally wide range of laminates.

Impact of two colliding bodies is strictly a three-dimensional dynamic problem. During the impact event, the shape and size of the contact zone and the state of the stresses in the two bodies are changing continuously with respect to time. Three-dimensional solutions to impact problems are quite formidable, even with the assistance of numerical method such as three-dimensional finite element analysis (3D-FEA). In order to simplify the problem, assumptions are often made so that an analytical solution can be determined. The first assumption is that the projectile is assumed to be rigid and inextensible in the transverse direction as compared to the target. Following the first assumption, the impactor can be treated as a rigid body and hence the equation of motion of the system is greatly simplified. The second assumption is that the global deformations of the target are assumed to be adequately modelled using applicable structural theories e.g. beam/ plate/ shell theories. This will be applicable in most thin-walled structures. In the case of thick structures, simplifications can be obtained by treating the structure as a half-space with appropriate structural theories. The local interaction between the impactor and the target is approximated by a corresponding static contact model within the same magnitude of contact force. In the case of plates, the response of the target can be separated into contact, local deformation and plate bending effects. By neglecting inertia effects in the plate and by assuming that the impactor mass is large compared to the target, one can reduce the complexity of the impact problem to static equivalent case. Such simplifications, as discussed before, are clearly not applicable to structures or systems subjected to localised high velocity impact loading.

3.2 Types of impact loading

The types of impact loading can be characterised in number of ways. Zukas *et al.* [1] classified the impact response of materials as a function of the striking velocity and strain rate and identified six types of impact response. These are summarised in Table 3.1. Zukas *et al.* [1] suggested that these impact groupings should only be treated as a reference since these transitions are very flexible because the deformation process under impact loading is influenced by a number of parameters other than just the impact

velocity. For example, the impact angle, the geometry of the structure and the characteristics of target and the projectile may also influence the impact response of the structure. Olsson [2] classified the impact process in terms of wave-controlled impact and boundary-controlled impact. He stated that the impact response of a composite plate is controlled by the boundary conditions of the structure if the duration of the impact event is greater than the time for transient flexural waves to reach the target boundary [2]. He also stated that the impact event can be modelled using a quasi-static model if the duration of the impact event is significantly longer than the largest vibration period of the structure. Olsson also stated that if no major flexural waves reach the boundary of the plate during the impact event, the response of the target will be determined by wave propagation effects [2].

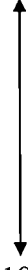
Strain rate (mm/mm)s ⁻¹	Impact velocity	Effect of impact loading	Method of loading
10^8  10^4	$>12 \text{ kms}^{-1}$	Explosive impact-colliding solids vaporised	-
	$3-12 \text{ kms}^{-1}$	Hydrodynamic-material compressibility not ignorable	Powder gun Gas gun
	$1-3 \text{ kms}^{-1}$	Fluid behaviour in material, pressures approach or exceed material strength, density is dominant parameter	Powder gun
	$500-1000 \text{ ms}^{-1}$	Viscous-material, strength still significant	Powder gun
10^2	$50-500 \text{ ms}^{-1}$	Primarily plastic	Mechanical devices Gas gun
10^0	$<50 \text{ ms}^{-1}$	Primarily elastic with some local plasticity	Mechanical devices Gas gun

Table 3.1: Impact response of materials [1].

3.2.1 Low velocity impact loading

Cantwell and Morton [3] classified low velocity impact as up to 10 ms^{-1} whereas Abrate [4] in his review stated that low velocity impact loading occurs when the impact velocity

is less than 100 ms^{-1} . Most workers [5,6] define low velocity impact as events, which can be treated as a quasi-static problem. During low velocity impact loading, the contact duration should be sufficiently long for the entire structure to respond to the impact event. Davies and Robinson [7,8] defined low velocity impact loading as being one in which through-thickness stress waves make no significant contribution to the distribution of the stress within the structure. Several authors [9,10] have suggested that low velocity impacts generate delamination-type damage whereas high velocity impact loading results in perforation-type damage.

3.2.2 High velocity (ballistic) impact loading

High velocity or ballistic impact can be classified as a highly energetic process in which some of the incident energy may be converted into light [1]. This type of impact is of interest for a wide range of engineering applications, e.g. hail and debris impact on aircraft structures, secondary blast effects on offshore and industrial installations and armour for military vehicles. The main features of damage associated with high velocity impact are penetration and perforation of the target and severe losses of structural integrity of the target. Penetration may be defined as the entrance of a missile or projectile into a target without fully completing its passage through the structure [11]. This generally results in the embedding of the missile or projectile in the target and the formation of a crater [1]. In contrast, perforation can be defined as the complete piercing of a target by a projectile or missile. There have been a number of experimental studies conducted to investigate the perforation behaviour of a variety of composite laminate structures, e.g. a thermoset resin reinforced with glass fibres [12-14], aramid fibres [15], carbon fibres [16], polyethylene fibres [17] as well as fibre reinforced thermoplastic composites [18]. As a result of these detailed studies, several models have been developed in order to determine the perforation performance of composite materials and structures. Zhu *et al.* [15] calculated the force acting on the conical projectile during perforation whereas Vinson and Walker [19] developed a conical shell model and solve the perforation problem by employing the finite-difference technique. Sun and Potti [20] developed a simple ring model to model a cylindrical impactor striking a thick

composite which was then solved numerically in order to predict residual velocities. Abrate [21] reviewed a large number of papers on the ballistic impact response of composites and concentrated on predictive models for the ballistic limit and residual velocities. He stated that for a given target-projectile combination, the ballistic limit could be defined as the minimum initial velocity of the projectile that will result in complete penetration of the target. At this critical condition, the residual velocity is considered to be zero. It was also shown that the residual kinetic energy of the projectiles increases linearly with the initial kinetic energy of the projectile [21]. Abrate [21] then related the initial kinetic energy, perforation energy and residual kinetic energy of the projectile by:

$$\frac{1}{2}mv_i^2 = U_p + \frac{1}{2}mv_r^2 \quad (3.1)$$

Where U_p is the perforation energy and v_i and v_r are the incident and residual velocities respectively. Clearly, this equation indicates that the energy required to perforate the laminates is independent of the projectile velocity and also the penetration process is rate independent.

3.3 Contact problem in impact

Localised impact loading on composite structures will generate a localised deformation at the point of contact as a result of the contact between the impactor and the target. In many cases, the local indentation has a significant effect on the contact force history and must be taken into account during the analysis. In early studies, local deformations were neglected as a result of assumption that the structures were inextensible in the transverse direction. Therefore, local deformations in the contact zone were not modelled with beam, plate or shell theories. The indentation depth is defined as the difference between the displacement of the projectile and that of the back face of the structure. The indentation problem can be treated dynamically if the two components involved during the impact i.e. the target and the projectile are considered as two solids. However, this

approach does not offer an explanation concerning differences between loading and unloading during the indentation process. The problem can be greatly simplified if the contact force is expressed as a function of the indentation, the resulting equation is known as a contact law. For most laminated composite materials, the contact response is recognised as being rate-independent and statically-determined contact laws are used by many investigators. Typically, the Hertzian force-indentation law is expressed as:

$$P = k\alpha^3 \quad (3.2)$$

Where P is the contact force, α the indentation and the contact stiffness, k , is given by:

$$k = \frac{4}{3}ER^{\frac{1}{2}} \quad (3.3)$$

Where E is the Young's modulus and R is the radius of the impactor. Equation 3.2 has been shown to apply for a wide variety of materials even for anisotropic laminated composites. This equation has been verified for both static [22,23] and dynamic [24] loading on laminates. A general form of Equation 3.2 was proposed by Meyer:

$$P = C\alpha^n \quad (3.4)$$

Here C and n are empirical constants, which must be determined experimentally from a quasi-static indentation test. Meyer's Law has proven very useful for studying isotropic materials [25] as well as composites [23,24]. A theoretical verification of Meyer's Law was undertaken by Hill *et al.* [26] whose results showed that the exponent ' n ' is constrained to be in the region of $1 < n < 1.5$ with $n = 1$ for an ideally plastic material and $n = 1.5$ for a linearly elastic material. The contact law for composites during the loading and unloading phases has been found to differ considerably even when the loading curve follows a linear Hertzian contact law. An investigation was carried out to explain these

phenomena and the following contact law was proposed by Crook [27] following a study of the indentation of a steel plate by spherical indenter:

$$P = P_m \left[\frac{\alpha - \alpha_0}{\alpha_m - \alpha_0} \right]^n \quad (3.5)$$

Where P_m is the maximum force during loading phase, α_m is the maximum indentation, α_0 is the permanent indentation after the unloading phase and n is the contact stiffness parameter in the contact law. The value of α_0 is considered to be zero when the maximum indentation, α_m , remains below a critical level. The permanent indentation was found to follow the relationship:

$$\alpha_0 = \alpha_m \left[1 - \left(\frac{\alpha_{cr}}{\alpha_m} \right)^n \right] \quad (3.6)$$

Where α_{cr} is the critical indentation that is required to produce permanent indentation. These expressions have been adopted by several researchers and the exponent n has been shown to be 2.5. Tan and Sun [23] also used a similar relationship when investigating the indentation response of a carbon fibre reinforced plastic. Test results showed that the loading curve followed a 1.5 power law whilst the indices for the unloading curve varied between 1.5 and 2.5.

Indentation curves for sandwich structures are known to differ significantly from those of monolithic laminates. Here, the indentation response is dominated by the properties of the core materials. Lee *et al.* [28,29] studied the indentation behaviour of a polyurethane foam core sandwich plate with carbon/epoxy facings. They concluded that for a given force level, the indentation force of the sandwich structure is much higher than that for monolithic laminate. One reason for this was that the foam undergoes crushing and

densification during the indentation test which gives a stiffening effect under the point of the contact. The contact law used took the form of:

$$P = k\alpha^n \quad (3.7)$$

The parameters k and n in Equation 3.7 were determined experimentally by conducting indentation tests on sandwich plates. They showed that the value of n was 0.8 for their sandwich system [28,29].

3.3.1 Indentation of laminates

As a result of the difficulties observed in modelling the contact behaviour of laminated composites using a three-dimensional finite element analysis, most effort has been concentrated on static indentation tests to establish a suitable contact law. There are only a few analytical and numerical studies on the contact problem in laminated composites. Sun and co-workers [30,31] and Timoshenko [32] used a static indentation test to study the contact behaviour of laminated composites. During a static indentation test, there are a number of quantities that are usually measured, these being the contact force, the displacement of the indenter, also known as the displacement at the contact point, and the magnitude of the indentation.

Tan and Sun [23] used a static indentation law to study the impact response of carbon/epoxy laminated plates. Their results highlighted a linear relationship between the maximum force and permanent indentation following the unloading curve. This linear relation was then used to determine the coefficient of the unloading curve as stated in Equation 3.6.

Tan and Sun [23] further evaluated their contact law using a nine-node isoparametric plate finite element analysis and showed that the predicted results correlated very well with the experimental data. Wu and Yen [33] studied the effects of parameters such as the indenter size, varying material properties, stacking sequence, span and thickness of the

carbon/epoxy laminates on the indentation law. They concluded that the contact force is proportional to the Young's modulus, E_3 in the thickness direction for the same amount of indentation by an identical indenter characteristic. However, other elastic constants such as the shear modulus did not have significant effect on the contact behaviour. Wu and Shyu [34] studied the response of carbon/epoxy under low velocity impact conditions. They stated that the modified Hertz law was inappropriate in the case of a thin plate impacted by a large indenter. Above the damage threshold, they showed that the delamination area was proportional to the applied contact load. They also showed that the indentation relationship between force and indenter remains independent of the indenter size and stacking sequence as long as the contact force is relatively small.

3.3.2 Indentation of sandwich structures

The indentation response of a sandwich structure differs in several respects from the indentation behaviour of a flat laminated structure since contact effects in these materials are based on thin skins bonded to a soft-core material [2]. Therefore, indentation tests on sandwich structures may involve large displacements relative to the thickness of the loaded skin. Another important difference is the low shear stiffness of sandwich structure compared to plain a laminate. The low shear stiffness of the structure is due to the low elastic modulus of the core material. Observations of the load-indentation curves following tests on a honeycomb sandwich and various foam core sandwich structures showed that a change in the contact stiffness occurs as a result of cell buckling at low applied loads [35].

In the intermediate loading stage (post-buckled regime), the curves showed an almost linear relationship between load and indentation confirming a typical plastic contact. Following unloading, there was evidence of permanent deformation in the load-indentation curve. Further observations on the effect of core thickness [36] reported that the contact stiffness is independent of the core thickness provided that the width of the core cell is substantially smaller than the core thickness. Feri and Sankar [37] conducted extensive indentation/flexure tests on simply-supported foam-core carbon/epoxy

sandwich plates. According to their results, compression of the core is much more significant than the magnitude of the indentation on the top face sheet. They also stated that the indentation response of the face sheet could be ignored in the analysis of such a system. Ericsson and Sankar [38] developed a quasi three-dimensional theory for sandwich plates. The theory enabled them to compute the core compression of sandwich plates associated with an applied force over a small area on the face sheet. In the analysis, the core was assumed to respond in a linear elastic manner and the results showed that core compression was proportional to the applied load. They also found that core compression was independent of plate size but strongly dependent on the Young's modulus of the core material.

3.4 Mathematical models

The following sections will review some of the impact models that are widely used. These include the solution to the dynamic equation of motion for an isotropic beam, mass-spring models and energy balance models.

3.4.1 Solution to the dynamic equation of motion

Rotem [39] used the solution to dynamic equation of motion of an isotropic beam to model the impact response of a carbon fibre and a glass fibre reinforced resin. He showed that the maximum deflection of the beam can be obtained by solving the dynamic equation of motion. The dynamic equation of motion of an isotropic beam is given as:

$$-k\delta + m_0g = m_0 \left(\frac{d^2\delta}{dt^2} \right) \quad (3.8)$$

where k is the spring constant of the beam, g is the acceleration due to gravity, m_0 is the mass of the impactor, δ is the displacement of the beam and t is the time. By solving Equation 3.8, he showed that the maximum deflection at the midspan is:

$$\delta_{\max} = \frac{m_0 g}{k} \left[1 + \left(1 + \frac{kv^2}{m_0 g^2} \right)^{1/2} \right] \quad (3.9)$$

Where v is the impact velocity. From beam theory, the spring constant k , is given by [40]:

$$k = \frac{48EI}{L^3} \quad (3.10)$$

With E is the apparent flexural modulus of the laminate in the beam, I is the moment of inertia and L is the span. Substituting k into Equation 3.9 gives:

$$\delta_{\max} = \frac{m_0 g L^3}{48EI} \left[1 + \sqrt{1 + \frac{48EI}{m_0 g^2 L^3} v^2} \right] \quad (3.11)$$

The maximum contact force between the impactor and the beam, at maximum deflection, is given as [41]:

$$P_{\max} = \frac{48EI\delta_{\max}}{L^3} \quad (3.12)$$

Using Equation 3.12, the maximum impact force can be predicted for any drop height and impact velocity. Recently, Cantwell *et al.* [42], used this model to study the impact response of a range of carbon, glass and Kevlar fibre reinforced composites and showed that the impact force can be accurately predicted over a wide range of impact conditions. Figure 3.1 shows the variation of impact force with drop-height for a glass fibre reinforced epoxy beam. From the figure, it is clear that the model accurately predicts the impact force over the range of energies considered.

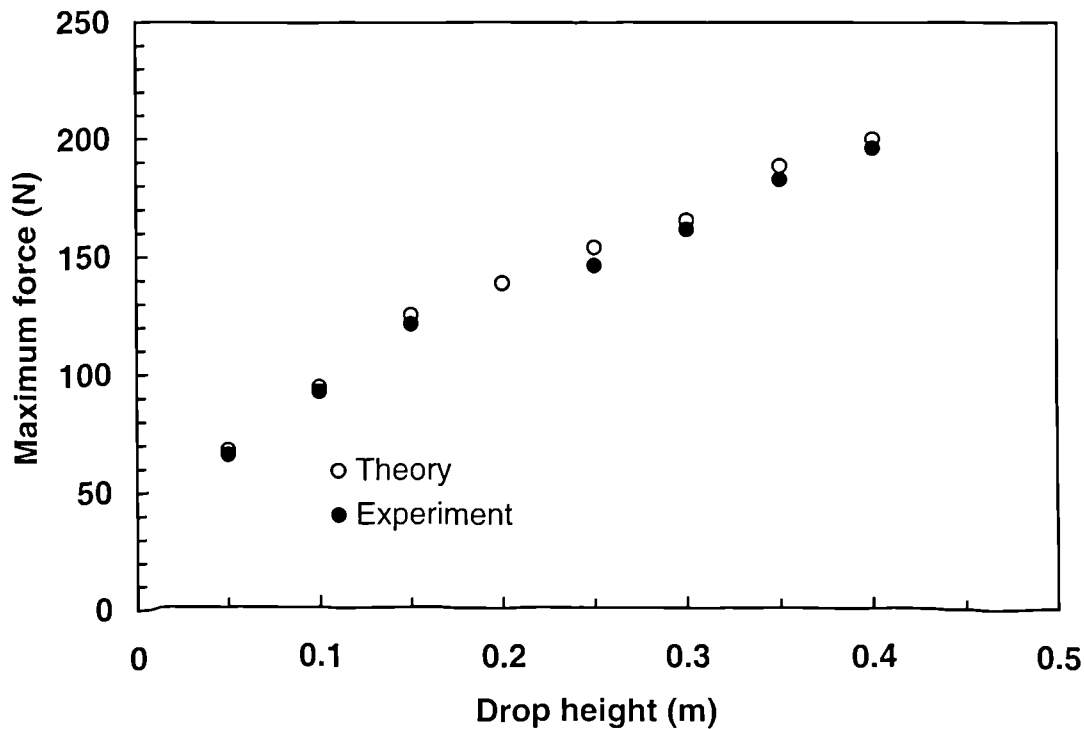


Figure 3.1: The variation of the maximum force with drop-height for a $((0^\circ, 90^\circ, +/- 45^\circ)_4)_s$ GFRP laminate. The span was 200 mm and the impactor mass was 472 g [42].

3.4.2 Mass-spring Models

Mass-spring models provide a simple and accurate solution for predicting the quasi-static impact response of composites. Shivakumar *et al.* [43], successfully predicted the maximum impact force and the force history during the impact event using this type of model. Generally, this model can be divided into two categories namely two-degree of freedom and single degree of freedom mass-spring models. The two degree of freedom (TDOF) mass-spring model is a more complete model since it considers bending and shear as well as membrane stiffening effects. The single degree of freedom (SDOF) mass-spring model is less complete since it neglects membrane stiffening effect.

3.4.2.1 Single degree of freedom

During low velocity impact loading, one of two situations may occur depending upon the ratio, M , of the target mass to the mass of the impactor. For high values of M , a significant percentage of the total energy in the system is converted into vibrations and therefore vibrational effects must be considered in the analysis [10]. In contrast when the value of M is very small (i.e. impact of a heavy impactor on a light structure), vibrational effects can be neglected. In such cases, the plate mass can be neglected in the system and the two degree of freedom mass-spring model can be reduced to a single degree of freedom model. Caprino *et al.* [44] used a single degree of freedom model as shown in Figure 3.2 to study the elastic behaviour of a glass cloth/polyester composite under low velocity impact.

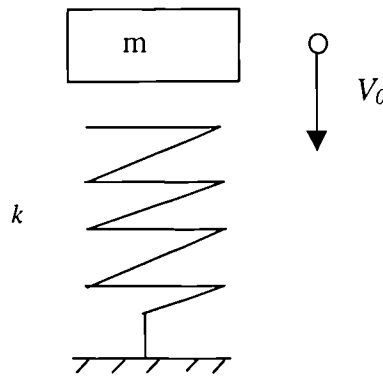


Figure 3.2: Linear spring with a spring constant k impacted by striker of mass m with an initial velocity V_0 [44].

By assuming that the energy losses are negligible, the energy balance at an instant t is given as [44]:

$$U_0 = U_i + U_p \quad (3.13)$$

Where U_0 is the energy of the impactor before impact, U_i is the impactor energy at time t and U_p is the strain energy stored by the plate at time t . The contact force, F , at a given time can be written as [45]:

$$F = F_{\max} \sin \pi \frac{t}{t_c} \quad (3.14)$$

Where

$$F_{\max} = \sqrt{2U_0k} = V_0\sqrt{mk} \quad (3.15)$$

where V_0 is the impact velocity and t_c is the contact duration. Both parameters can be defined as follows:

$$t_c = \pi \sqrt{\frac{m}{k}} \quad \text{and} \quad V_0 = \sqrt{2gh} \quad (3.16)$$

Where h is a drop-height. Caprino *et al.* [44] applied this model to study the impact response of a glass cloth/polyester composite and their results are presented in Figure 3.3. Clearly, the experimental data agree well with the theoretical prediction at low and intermediate velocities. They also stated that impact energy of the projectile is the governing parameter in the elastic region and concluded that this simple analysis could be used to study the impact response of the composites within their elastic limit.

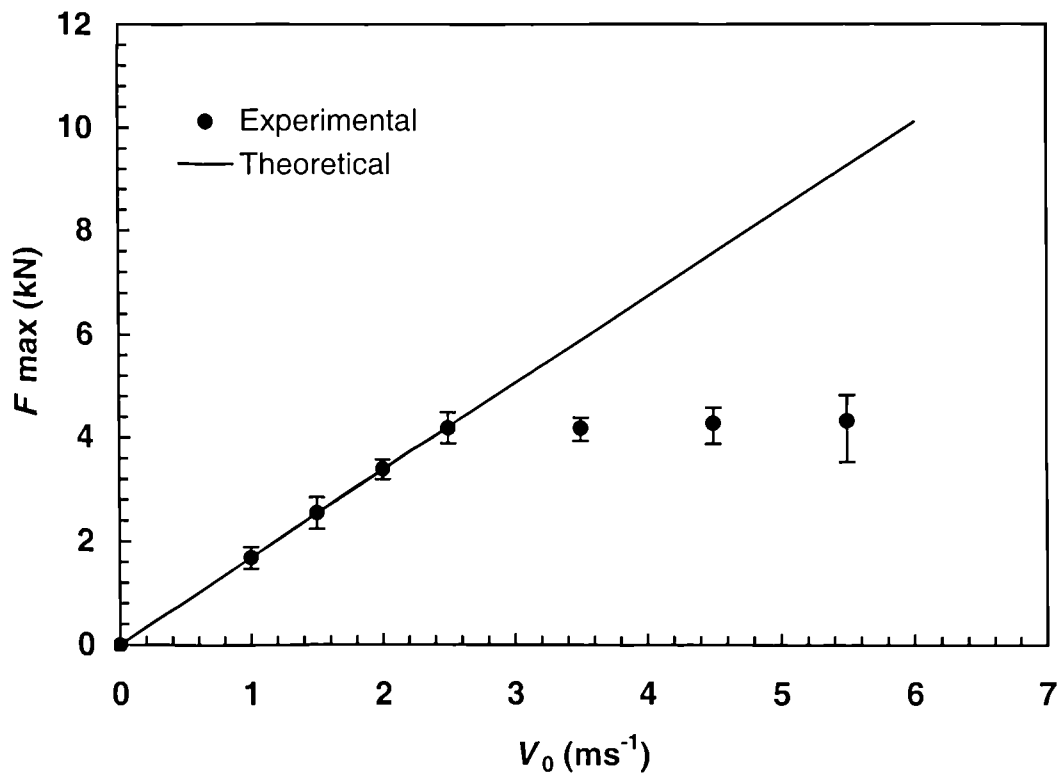


Figure 3.3: Variation of maximum contact load, F_{\max} , with impact velocity, V_0 for a glass cloth/polyester composite [44].

3.4.2.2 Two degree of freedom

A two degree of freedom (TDOF) mass-spring impact model is shown in Figure 3.4. The model consists of two rigid masses, M_1 and M_2 , representing the mass of projectile and the effective mass of the plate respectively, and two springs, representing the linear stiffness of the plate (K_{bs}) and the non-linear membrane stiffness (K_m) respectively. The terms δ_1 and δ_2 represent the deflections due to M_1 and M_2 respectively. Studies on the free vibrations of a plate with an attached central concentrated mass have indicated that

the effective plate mass (M_2) contributing to the inertial effect is one fourth of the total plate mass [45,46]. Hence the ratio of M_1 to its total plate mass is taken as 1:4. Simplifications can be made in the case when shear deformations are negligible by replacing the constant K_{bs} by K_s . From the free body diagrams of two masses M_1 and M_2 , the equation of motion for the systems can be written as:

$$M_1 \ddot{\delta}_1 + P = 0 \quad (3.17a)$$

$$M_2 \ddot{\delta}_2 + K_{bs} \delta_2 + K_m \delta_2^3 - P = 0 \quad (3.17b)$$

Where P is the contact force which is a highly non-linear function of $(\delta_1 - \delta_2)$. When $\delta_1 > \delta_2$, the expression for P is defined as:

$$P = P(\delta_1 - \delta_2) \quad (3.18)$$

Where Equation 3.18 could be any contact law describing a particular indentation between the target and impactor. In the case of $\delta_1 < \delta_2$, contact ceases and $P = 0$. Therefore, Equation 3.18 governs the free vibration of the model. The appropriate initial conditions for the system described by Equations 3.17a and 3.17b are as follows:

$$\delta_1(0) = 0, \quad \dot{\delta}_1(0) = v_0 \quad (3.19)$$

Equation 3.19 can also be studied numerically. The expressions for stiffness used in the mass-spring model can be found in many textbooks or they can be determined numerically using the finite element method (FEM).

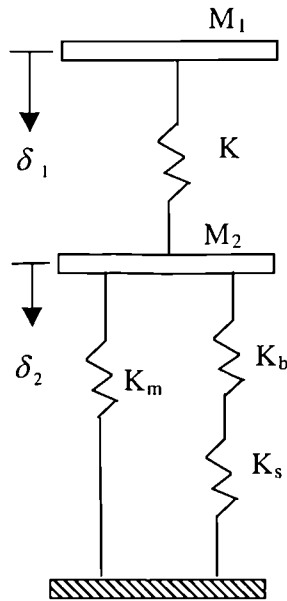


Figure 3.4: Two degree of freedom mass-spring model.

3.4.3 Energy balance models

The energy balance model has been used successfully to predict the force during a low velocity impact event. Shivakumar *et al.* [43] used the energy balance model to predict the impact force during low velocity impact tests on carbon/epoxy circular plates. In the analysis, they assumed that the kinetic energy of the projectile was transformed into strain energy as a result of contact, bending, shear and membrane deformations. Using the principal of conservation of total energy, they stated that:

$$\frac{1}{2}mv^2 = E_c + E_{bs} + E_m \quad (3.20)$$

Where E_c , E_{bs} and E_m are the corresponding strain energies due to contact, bending and shear, and membrane deformations respectively. The contact energy, E_c , was obtained by integrating Hertz's load-indentation relation given as:

$$E_c = \int_0^{\alpha} P d\alpha \quad (3.21)$$

Following integration and simplification, E_c can be re-written as follows:

$$E_c = \frac{2}{5} \frac{P^{5/3}}{C^{2/3}} \quad (3.22)$$

Shivakumar *et al.* [43] then resolved the reactive force, P from the plate into two components as;

$$P = P_{bs} + P_m \quad (3.23)$$

where P_{bs} is the force associated with bending and shear deformations and P_m is the force associated with membrane deformation. Equation 3.23 can also be written in terms of the target deflection as [48]:

$$P = K_{bs} w + K_m w^3 \quad (3.24)$$

Where K_{bs} is the effective stiffness due to bending and shear which can be expressed in a more general form as:

$$K_{bs} = \frac{K_b K_s}{K_b + K_s} \quad (3.25)$$

Where the constants K_b , K_s and K_m are the bending, shear and membrane stiffnesses respectively. Several expressions for K_b and K_m resulting from different boundary conditions are presented in [43]. The expression for K_s is given as [49]:

$$K_s = \frac{4\pi G_{zr} h}{3} \left(\frac{E_r}{E_r - 4\nu_{zr} G_{zr}} \right) \left(\frac{1}{\frac{4}{3} \log \frac{a}{a_c}} \right) \quad (3.26)$$

Where a is the radius of the target and a_c is the radius of the contact area which strongly depends on the applied force P . The value for a_c is given as [50]:

$$a_c = \left[\frac{3\pi}{4} P(K_1 + K_2)R_1 \right]^{\frac{1}{3}} \quad (3.27)$$

The impact force, P in Equation 3.27 is not known at the beginning of the impact event and therefore the value of a_c cannot be directly determined. Shivakumar *et al.* [43], used a value of a_c equal to $h/2$ for determining P in Equation 3.27. The energy due to bending and shear E_{bs} and the energy due to membrane effects, E_m was calculated by integrating the forces in Equation 3.23 and 3.24 with respect to the deflection, w . Therefore, the energies associated with bending and shear can be written as:

$$E_{bs} + E_m = \frac{1}{2} K_{bs} w^2 + \frac{1}{4} K_m w^4 \quad (3.28)$$

Using Equation 3.20, the energy balance of the system can therefore be re-written as:

$$mv^2 = K_{bs} w^2 + \frac{K_m w^4}{2} + \frac{4}{5} \left[\frac{(K_{bs} w + K_m w^3)^5}{C^2} \right]^{\frac{1}{3}} \quad (3.29)$$



Equation 3.29 was solved to yield the deflection, w , using the Newton-Raphson numerical technique. Knowing the deflection, the impact force P can be obtained by substituting its value into Equation 3.24. Shivakumar *et al.* [43], used the energy balance model to predict the impact response of a circular carbon fibre reinforced epoxy plate. Their results suggest that the simple energy balance model can accurately predict the impact force for a wide range of loading conditions. Figure 3.5 shows the variation of impact force with impact velocity for plates subjected to low velocity impact conditions. Clearly, agreement between the predicted data and the experimental results is very good.

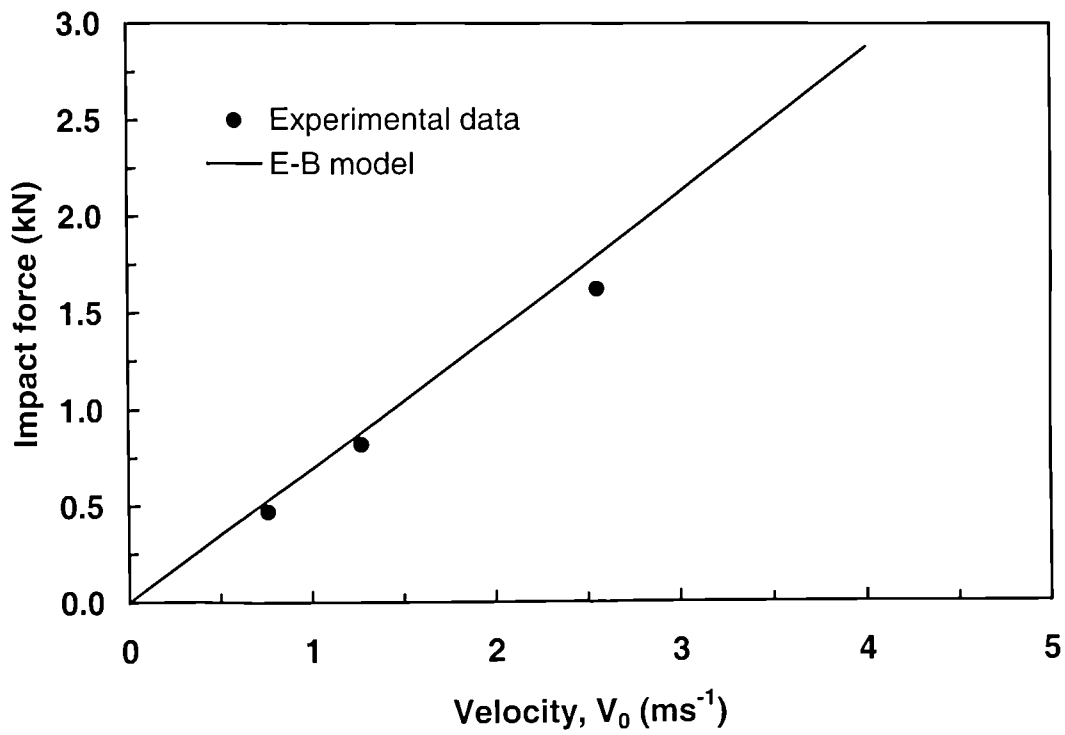


Figure 3.5: The variation of impact force with impact velocity for a carbon fibre reinforced epoxy resin [43].

3.5 References

1. J.A. Zukas, T. Nicholas, H.F. Swift, L.B. Greszczuk and D.R. Curran, "Impact Dynamics", John Wiley & Sons Publication, 1982.
2. R. Olsson, "Impact response of composite plates-a guide to closed form solutions", FFA TN 1992-33, The Aeronautical Research Institute of Sweden, 1992.
3. W.J. Cantwell and J. Morton, "The impact resistance of composite materials- a review", *Composites*, 22, pp 347-362, 1991.
4. S. Abrate, "Impact on laminated composite materials", *Appl. Mechanics Review*, 44, pp 155-190, 1991.
5. P.O. Sjoblom, J.T. Hartness and T.M. Cordell, "On low velocity impact testing of composite materials", *J. Composite Materials*, 22, pp 30-52, 1988.
6. K.N. Shivakumar, W. Elber and Illg, "Prediction of low velocity impact damage in thin circular plate", *AIAA Journal*, 23, pp 442-449, 1985.
7. P. Robinson and G.A.O. Davies, "Impactor mass and specimen geometry effects in low velocity impact of laminated composites", *Int. J. Impact Engineering*, 12, pp 189-207, 1992.
8. G.A.O. Davies and P. Robinson, "Predicting failure by debonding/delamination", *AGARD: 7th Structures and Materials Meeting*, 1992.
9. D. Liu and L.E. Malvern, "Matrix cracking in impacted glass/epoxy plates", *J. Composite Materials*, 21, pp 594-609, 1987.
10. S.P. Sun and C.T. Sun, "Impact-induced fracture initiation and detailed dynamic stress field in the vicinity of impact", In *Proceedings of the American Society of Composites, 2nd Technical Conference*, pp 177-185, 1987.
11. M.E. Backman and W. Goldsmith, *Int. J. Eng. Sci.*, 16, pp 102-115, 1978.
12. R.A.W. Mines, A.M. Roach and N. Jones, "High velocity perforation behaviour of polymer composites", *Int. J. Impact Engineering*, 22, pp 561-588, 1999.
13. H.M. Wen, T.Y. Reddy, S.R. Reid and P. Soden, "Indentation, penetration and perforation of composite laminates and sandwich panels under quasi-static and projectile loading", *Key Eng. Materials*, 144-143, pp 501-552, 1998.

14. E. Wu, C.Z. Tsai and Y.C. Chen, "Penetration into glass/epoxy composite laminates", *J. Composite Materials*, 28, pp 1783-1802, 1994.
15. G. Zhu, W. Goldsmith and C.K.H. Dharan, "Penetration of laminated Kevlar by projectiles-II: Analytic model", *Int. J. Solids Structures*, 29, pp 421-436, 1992.
16. S.W.R. Lee and C.T. Sun, "Dynamic penetration of graphite/epoxy laminates by a blunt ended projectile", *Composites Science and Technology*, 49, pp 369-380, 1993.
17. B.L. Lee, J.W. Song and J.E. Ward, "Failure of Spectra polyethylene fibre reinforced composites under ballistic impact loading", *J. Composite Materials*, 28, pp 1202-1226, 1994.
18. H. Morita, T. Adachi, Y. Tateishi and H. Matsumoto, "Characterisation of impact damage resistance of CF/PEEK and CF/Toughened epoxy laminates under low and high velocity impact tests", *J. Reinforced Plastics Composites*, 16, pp 131-143, 1997.
19. J.R. Vinson and J.M. Walker, "Ballistic impact into composite material and structures", *American Society of Aerospace and Astrophysics*, Paper no. AIAA-95-1338-CP, 1995.
20. C.T. Sun and S.V. Potti, "A simple model to predict residual velocities of thick composite laminates subjected to high velocity impact", *Int. J. Impact Engineering*, 16, pp 1-15, 1995.
21. S. Abrate, "Impact on Composite Structures", Cambridge University Press, 1998.
22. A. Henriksson, "Transverse compressive behaviour of carbon-epoxy laminates and its influence on contact laws", FFA TN 1990-26, The Aeronautical Research Institute of Sweden, 1990.
23. T.M. Tan and C.T. Sun., "Use of statical indentation laws in the impact analysis of laminated composite plates", *J. Appl. Mechanics*, 52, pp 6-12, 1985.
24. R. Olsson, "Theory and experimental verification of the impact response of composite plates", *Eng. Science Preprint* 28, 91002, 28th Annual Technical Meeting of Society of Eng. Science, 1991.
25. W. Goldsmith, "Impact", Edward Arnold, London, 1960.
26. R. Hill, B. Storakers and A. Zdunek, "A theoretical study of the Brinell hardness test", *Proc. of Royal Soc. of London*, 423, pp 301-330, 1989.

27. A.W. Crook, "A study of some impacts between metal bodies by a piezoelectric method", Proc. Royal Soc., London, 212, pp 377-390, 1952.
28. L.J. Lee, K.Y. Huang and Y.J. Fann, "Dynamic responses of composite sandwich plates subjected to low velocity impact", 8th Int. Conference on Composite Materials (ICCM/8), 32.D.1-10, 1991.
29. L.J. Lee, K.Y. Huang and Y.J. Fann, "Dynamic response of composite sandwich plate impacted by a rigid ball", J. Composite materials, 27, pp 1238-1256, 1993.
30. C.T. Sun, ASTM STP 617, 1977.
31. C.T. Sun, B.V. Sankar and T.M. Tan, "Advances in Aerospace Structures and Materials", American Society for Mechanical Engineers, New York, pp 99-100, 1981
32. S.P. Timoshenko, Zeits. Math. Phys., 62, pp 98-99, 1913.
33. E. Wu and C.S. Yen, "The contact behaviour between laminated composite plates and rigid spheres", J. Applied Mechanics, 61, pp 60-66, 1994.
34. E. Wu and K. Shyu, "Response of composite laminates to contact loads and relationship to low velocity impact", J. Composite Materials, 27, pp 1443-1464, 1993.
35. C.T. Sun and C.L. Wu, "Low velocity impact of composite sandwich panels", AIAA/ASME/ASCE/AHS 32nd Structures, Structural Dynamics and Materials Conference, pp 1123-1129, 1991.
36. P.H.W. Tsang and J. Dugundji, "Damage resistance of graphite/epoxy sandwich panels under low speed impacts", J. American Helicopter Society, 37, pp 75-80, 1992.
37. R. Ferri and B.V. Sankar, Proceedings of the American Society for Composites – Ninth Technical Conference, Technomic Publications, Lancaster, Pennsylvania, U.S.A., 1994.
38. A. Ericsson and B.V. Sankar, "Sandwich Constructions 2", 1, Eng. Materials Advisory Services Ltd., U.K., 139, 1992.
39. A. Rotem, "Residual flexural strength of FRP composite specimens subjected to transverse impact loading", SAMPE Journal, pp 19-25, 1988.

40. Z. Hashin, "Plane anisotropic beams", J. Applied Mechanics, pp 267-272, 1967.
41. C.T. Sun and S. Chattopadhyay, "Dynamic response of anisotropic laminate plates under initial stress to impact of a mass", J. Applied Mechanics, Transactions of the ASME, pp 257-273, 1975.
42. W.J. Cantwell, M. Busser and H.H. Kausch, "An analysis of the impact response of a composite beam", Composites Engineering, 1, pp 293-307, 1991.
43. K.N. Shivakumar, W. Elber and W. Illg, "Prediction of impact force and duration due to low velocity impact on circular plate", J. Appl. Mechanics, 52, pp 674-680, 1985.
44. G. Caprino, I.C. Visconti and A.D. Ilio, "Elastic behaviour of composite structures under low velocity impact", Composites, 15, pp 231-234, 1984.
45. J.P. Den Hartog, "Mechanical Vibrations", McGraw-Hill, New York, 1947.
46. A.W. Leissa, "Vibrations of plates", NASA SP-160, 1969.
47. W. Goldsmith, "Impact", Edward Arnold Ltd., London, 1960.
48. A.S. Volmir, "A translation of flexible plates and shells", AFFDLTR-66-216, 1967.
49. S.A. Lukasicwicz, "Introduction of concentrated loads in plates and shells", Progress in Aerospace Science, 17, pp 109-146, 1976.
50. L.B. Greszczuk, "Damage in composite materials due to low velocity impact", in J.A. Zukas *et al.* Eds, Impact Dynamics, John Wiley & Sons, New York, 1982.

CHAPTER 4: MATERIAL PROPERTIES

In this section, the materials used in the skin and core are described. Here, the mechanical properties of these systems are presented and discussed. Many of the properties that are quoted are based on data furnished by the appropriate materials supplier.

4.1 Skin material

The prepreg material used here was PN900-44-43 from Stesalit Ltd, Switzerland. The system is based on an E-glass fibre fabric, US-Style 120, impregnated with a polymerised aromatic cyanate ester compound. The prepreg was supplied in the form of a roll with width, thickness and length dimensions of 1 metre x 0.1 mm x 50 metres. This resin system is known to have high thermal and chemical stability after curing at elevated temperatures (i.e. at temperatures in excess of 125°C) [1]. In the prepreg state, the material has excellent properties such as easy processability and handling, low volatile content and a very low emission rate of volatiles during the curing process.

In addition, the material contains no toxic additives. In the cured state, this glass fibre reinforced composite is known to offer high mechanical properties with a relatively low sensitivity to moisture and a low smoke density in fire conditions. In addition, the thermal stability of this system can be enhanced through a post-curing process (for example post-curing at 180°C for 120 minutes yields a glass transition temperature, T_g , of 195°C and curing at 220°C for 120 minutes yields a glass transition temperature, T_g , of 245°C). The main applications of this material are in the aviation and marine industries.

Property	Temperature (°C)	Units	Value
Flexural Strength (Warp)*	Room temperature	MPa	650
	95	MPa	600
	110	MPa	560
Flexural Modulus (Warp)*	Room temperature	GPa	25
	95	GPa	23
	110	GPa	22
Interlaminar shear strength (ILS) short beam (Warp)	-55	MPa	47
	Room temperature	MPa	45
	95	MPa	37

Table 4.1: Summary of the key mechanical properties of the cured PN900-44-43 laminate. The data is taken from the manufacturer's data sheets [1]. (*Values normalised at 50% fibre volume fraction).

4.2 Core materials

Two types of core material were investigated in this research, namely foam and aluminium honeycomb core materials. Details of each material are given in the following sections.

4.2.1 Foam-core materials

The polymeric foam core materials investigated in this research programme were supplied in the form of 10 mm thick sheets with dimensions of 1500 mm x 1000 mm by Alusuisse Airex AG, Switzerland. The foams were supplied in three main grades these being R63, R82 and C70. Each grade has unique properties. Within the same grade, a number of different densities were supplied and clearly the material properties are strongly dependent on the density of the material. Details of the properties of the R63, R82 and C70 foams are given in the Tables 4.2, 4.3 and 4.4 respectively.

4.2.1.1 R63 Foams

AIREX-R63 is a resilient, closed cell, linear PVC foam with an extremely high damage tolerance. It is cold-formable to simple three-dimensional contours. It can also be thermo-formed to more complex three-dimensional shapes. It is a suitable core material for dynamically-loaded, shock-absorbing sandwich structures. The main applications of this material are in the manufacture of hulls of ships and ferries, racing boats, yachts, surfboards and dynamically-loaded structures. Some useful characteristics include its extremely high impact resistance, non-brittle failure modes and excellent fatigue resistance.

Properties	Test method	unit	R63.50	R63.80	R63.140
Nominal density	ISO 845	kg/m ³	60	90	140
Compressive strength	ISO 844	N/mm ²	0.4	0.9	1.6
Compressive modulus	DIN 53457	N/mm ²	30	56	135
Tensile strength	DIN 53455	N/mm ²	1.1	1.8	2.4
Tensile modulus	DIN 53457	N/mm ²	37	56	90
Shear strength	ISO 1922	N/mm ²	0.5	1.2	1.85
Shear modulus	ASTM C393	N/mm ²	12	21	37

Table 4.2: Summary of the key material properties for the R63 family of foams.

4.2.1.2 R82 Foams

AIREX-R82 is thermoplastic linear PEI (Polyether imide) foam, combining outstanding fire performance with a high service temperature. The foam absorbs a negligible amount of water and offers excellent dielectric properties. It is a closed cell, resilient foam for use in fire and structural applications within an operating temperature range of -194°C to 180°C. These materials are widely used in the manufacture of aircraft interiors, structures for road and rail transportation, marine industries and cryogenic tanks and covers. The key assets of this material are that it has high impact resistance and that it exhibits non-brittle failure under impact loading.

Properties	Test method	unit	R82.60	R82.80
Nominal density	ISO 845	kg/m ³	60	80
Compressive strength	ISO 844	N/mm ²	0.6	0.95
Compressive modulus	DIN 53457	N/mm ²	33	54
Tensile strength	DIN 53455	N/mm ²	1.2	1.8
Tensile modulus	DIN 53457	N/mm ²	37	52
Shear strength	ISO 1922	N/mm ²	0.7	1.1
Shear modulus	ASTM C393	N/mm ²	14	22

Table 4.3: Summary of the key material properties for the R82 family of foams.

4.2.1.3 C70 Foams

HEREX-C70 is rigid, closed cell PVC/PUR foam with a high stiffness and strength to weight ratio. As with the R82 foams, these materials absorb negligible water and have an excellent resistance to various media as well as a low thermal conductivity. The foams are ideally suited as a core material for lightweight sandwich structures. This foam system is commonly used in the manufacture of deck, interior panels and superstructures of boats, wind turbine blades and catering service trolleys. High strength and stiffness to weight ratios, good compression strength, good thermal insulation and self-extinguishing are among the valuable characteristic of these foams [2].

Properties	Test Method	C70.40	C70.55	C70.75	C70.90	C70.130	C70.200
Nominal Density kg/m ³	ISO 845	40	60	80	100	130	200
Compressive strength N/mm ²	ISO 844	0.45	0.85	1.30	1.80	2.60	4.80
Compressive modulus N/mm ²	DIN 53457	34	58	83	110	155	255
Tensile strength N/mm ²	DIN 53455	0.70	1.30	1.95	2.60	3.70	6.60
Tensile modulus N/mm ²	DIN 53457	28	45	63	81	109	178
Shear strength N/mm ²	ISO 1922	0.5	0.8	1.2	1.6	2.2	3.5
Shear modulus N/mm ²	ASTM C393	14	22	30	38	50	81

Table 4.4: Summary of the key material properties for the C70 family of foams.

4.2.2 Aluminium honeycomb core material (Aeroweb 3003)

The aluminium honeycomb sandwich material used in this study was supplied by Hexcel Ltd. Aeroweb 3003 panels were supplied in the form of pre-fabricated panels which can be readily cut into the desired shape. The Aeroweb 3003 panels are a lightweight, high performance structural sandwich panel consisting of woven glass fibre epoxy resin skins bonded to a lightweight aluminium honeycomb core. The panel exhibits superior mechanical and physical properties, it is easy to install and can be readily cut and machined in the laboratory or workshop. A summary of the key mechanical and physical properties of these panels is given in Table 4.5. The panels were cut using a diamond circular saw to minimise the amount of damage incurred

during the preparation process. Details of the aluminium honeycomb structure within the panel are given in Figure 4.1.

Property	Specification
Density (kg/m^3)	84
Cell size (mm)	6.4
Foil thickness (mm)	0.64
E_{11} (Pa)	0.947×10^6
ν_{12}	0.3

Table 4.5: Mechanical properties of Aeroweb 3003 aluminium honeycomb core [3].

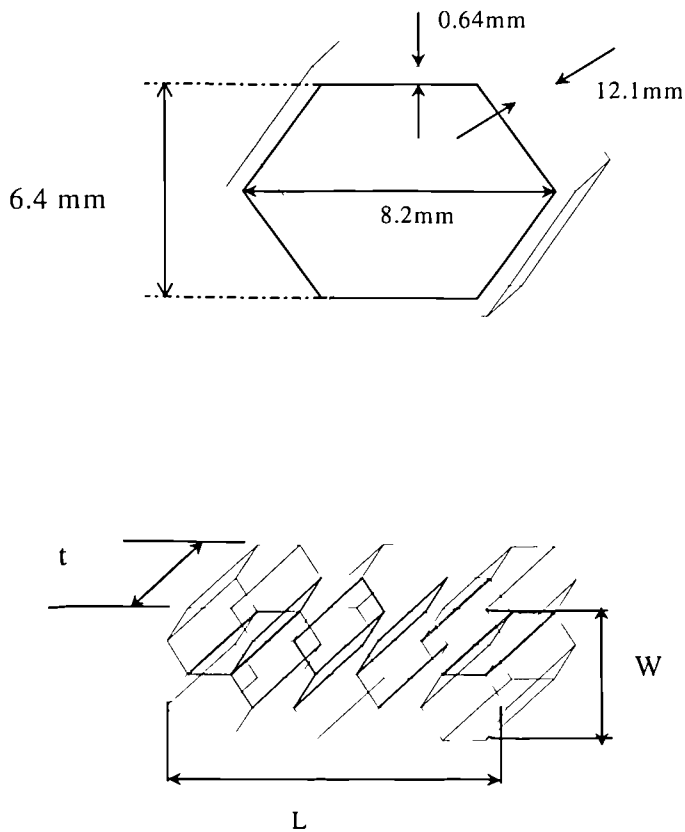


Figure 4.1: Honeycomb cell dimensions and configuration

4.3 Materials preparation

In this section, details of the preparation procedures used to manufacture the sandwich structures are described. The first section will deal with the manufacture of the skin materials and the subsequent section will address the procedures used to manufacture the sandwich panels.

4.3.1 Preparation of the composite plates and skin materials

Table 4.6 gives details of the number of woven 0°, 90° plies used to manufacture the composite structures considered in this research programme. Individual plies of the glass fibre/cynate ester resin prepreg with dimensions of 200 mm x 190 mm were cut into the shape of the mould plate using a sharp razor blade. The plies were then wrapped in polyethylene film and placed in the picture frame mould. The composite was cured in a hot press at 125°C for 120 minutes employing an initial heating rate of 3°C/minute. A pressure of 0.7 bar was maintained in order to minimise the void content in the laminate. After the curing process was completed, the laminate was held under pressure until it had cooled to room temperature.

Following manufacture, one side of the laminate was roughened using gritted paper in order to improve adhesion to the foam core materials. The skin was then cleaned and washed using ethanol to eliminate any dust generated during sanding process.

Composite structure	No of plies	Cured thickness (mm)
Skin for sandwich beams and panels	2	0.6
Composite beams	8	2.1
Circular plate (Thick)	16	4.9
Circular plate (Thin)	8	2.1

Table 4.6: Description of the number of plies used to manufacture the glass fibre reinforced epoxy beams and plates investigated in this programme.

4.3.2 Preparation of the core material

The majority of the foams were cut using a circular saw which resulted in negligible damage being incurred at the edges of the panel. The foam panels were cut to the same dimensions as the facing skins. Care was taken when cutting the brittle core materials, especially the C70.40 and C70.55 foams in order to avoid introducing damage to the

edge of the panels. The panels were then sprayed using a compressed air gun to remove any dust generated during the cutting procedure.

4.4 The manufacture of sandwich panel

Two types of sandwich construction were considered in this study namely aluminium honeycomb and foam-core sandwich composite materials. The aluminium honeycomb was selected since it represents a high performance sandwich structure used in the marine and aerospace industries and it provides a useful comparison with the foam-based sandwich structures.

4.4.1 The manufacture of the foam-core sandwich panels

In order to successfully manufacture the foam-core sandwich systems, a suitable adhesive is required to achieve a good bond strength between the core and skin materials. In this study, Araldite LY5082 epoxy resin combined with an Araldite AY103 hardener were used. This system was chosen as a result of its low temperature curing, typically between 20°C and 90°C, and its low shrinkage characteristics during curing. The principal disadvantage of this system is the long curing time required for the epoxy to harden. However the quality provided by this system was exceptional.

Details of the bonding procedure are as follows:

The epoxy resin (LY5082) was mixed in a container with the hardener (AY103) in the ratio of 2:1. The solution was then mixed uniformly and applied to both the skin and foam core materials. After the resin was applied, the skin and core materials were left for two hours at room temperature to allow the resin to pre-cure. The laminated sandwich plate was then placed in a cold press under a light pressure and left overnight to ensure complete curing.

The cured sandwich panel was then cut into coupons with dimensions 190 mm x 20 mm in preparation for testing. Schematic diagrams of the manufacturing processes are

given in Figure 4.2 and 4.3. Since the foam-core sandwich panels were produced using hot-compression technique, the variation of the applied pressure may occur which may effect resin distribution over the surface of the skin and hence, thickness variation may occur. A summary of the beam dimension is given in Table 4.7.

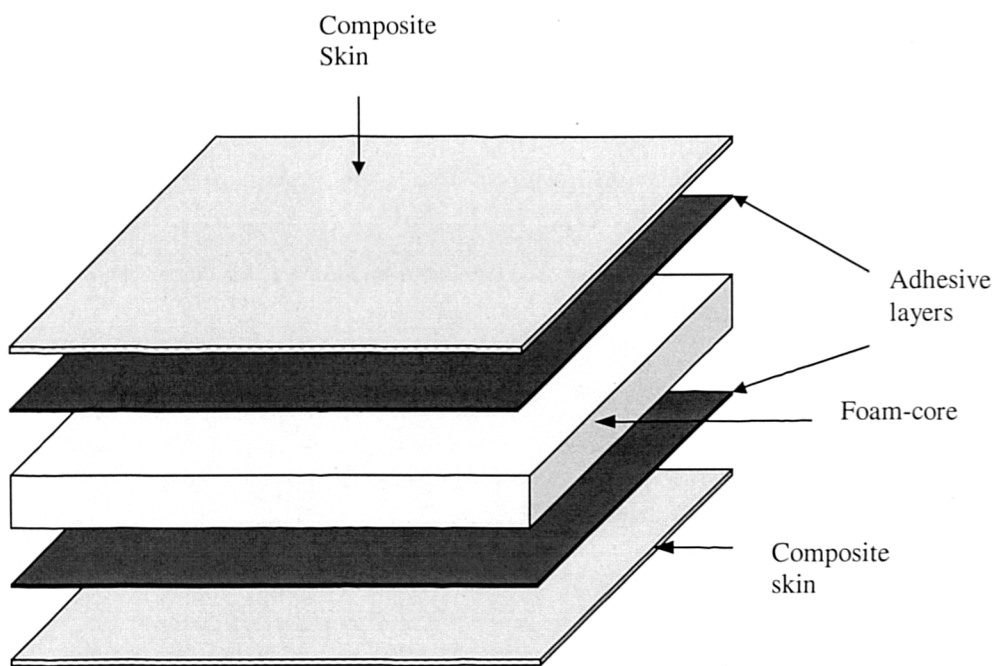


Figure 4.2: Schematic of the structure of the foam sandwich panels.

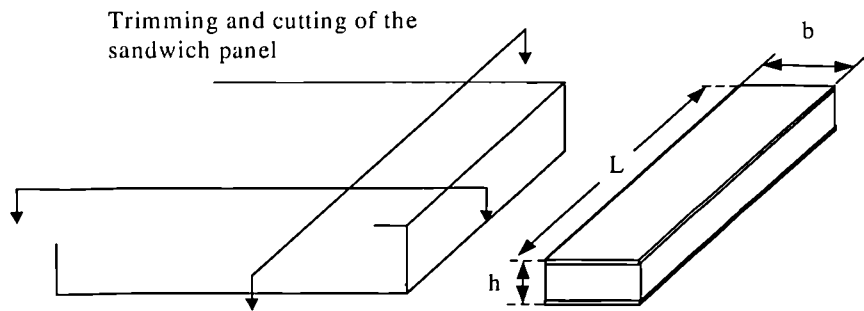


Figure 4.3: Production of the foam-based sandwich beams showing the characteristic dimensions of the specimen.

Foam	h (mm)	L (mm)	b (mm)
C70.40	9.88 – 10.10	175	20.60 – 21.18
C70.55	9.92 – 10.2	175	20.86 – 21.48
C70.75	9.92 – 10.18	175	20.76 – 21.48
C70.90	9.74 – 10.18	175	20.78 – 21.46
C70.130	10.04 – 10.20	175	20.48 – 21.00
C70.200	9.92 – 10.10	175	21.00 – 21.90
R63.50	10.08 – 10.32	175	20.60 – 21.34
R63.80	10.04 – 10.20	175	20.58 – 21.50
R63.140	10.02 – 10.22	175	20.92 – 21.48
R82.60	9.96 – 10.10	175	21.14 – 21.40
R82.80	10.16 – 10.44	175	20.88 – 21.36

Table 4.7: Summary of the dimensions of the foam-core sandwich beams.

4.5 References

1. Product data sheet, “Stesapreg PN900”, Stesalit Ltd, Advanced Composite Systems, CH-4234 Zullwil.
2. Manufacturer’s data sheet, Alusuisse Airex AG, Speciality Foams, CH-5643 Sins, Switzerland.
3. R.A.W. Mines, C.M. Worrall and A.G. Gibson, “ Low velocity perforation behaviour of polymer composite sandwich panels”, Int. J. Impact Engineering, 21, pp 855-879, 1998.

CHAPTER 5: EXPERIMENTAL PROCEDURE

The following sections detail the experimental procedure that was adopted to characterise the impact response of the sandwich structures and to determine the material properties required for modelling the dynamic response of these systems.

5.1 Impact tests

Drop-weight impact tests have been widely used in previous studies in order to evaluate the low velocity impact response of composite materials and sandwich structures [1-3]. One of the advantages of this type of test with respect to Charpy and Izod tests is that a wider range of test geometries can be considered, thereby enabling more complex components to be investigated. In general, the impact event does not cause complete destruction of the specimen but rebounds, enabling the residual energy to be calculated. In this research programme, impact testing was undertaken using the instrumented drop-weight impact rig shown in Figure 5.1.

Here, a 1.976 kg carriage with a 10 mm diameter hemispherical indenter was released from heights of up to 1.0 metre. Incident impact energies in the range of 0.1 to 1.94 Joules were achieved by changing the drop-height whilst keeping the carrier mass constant. In order to ensure that the impact occurred at the desired location, two vertical steel columns were fixed to the base of the impact tower to guide the falling carriage. The specimens were supported on two 10 mm diameter steel cylinders located on moveable right angle supports. The guides were lubricated to minimise any friction generated during the descent of the carriage. After impact, the carriage was caught manually in order to avoid secondary impacts. The impact force history during the test was measured using a Kistler 5011 piezo-electric load cell located just above the impactor tip. The signals from the load cell were then amplified by a strain gauge amplifier and recorded by a dedicated personal computer.

Following each test, the maximum signal was noted and used as the parameter for characterising the impact response of each specimen. The signal recorded in millivolts was converted to a force by calibrating the load cell. Here, the load cell was loaded with a series of 5 kilogram weights and the signal generated was recorded as a function of the static load. A plot of the applied force against resulting signal was drawn and a linear relationship between the two was established. As a result, the maximum force during the impact event was noted during each test.

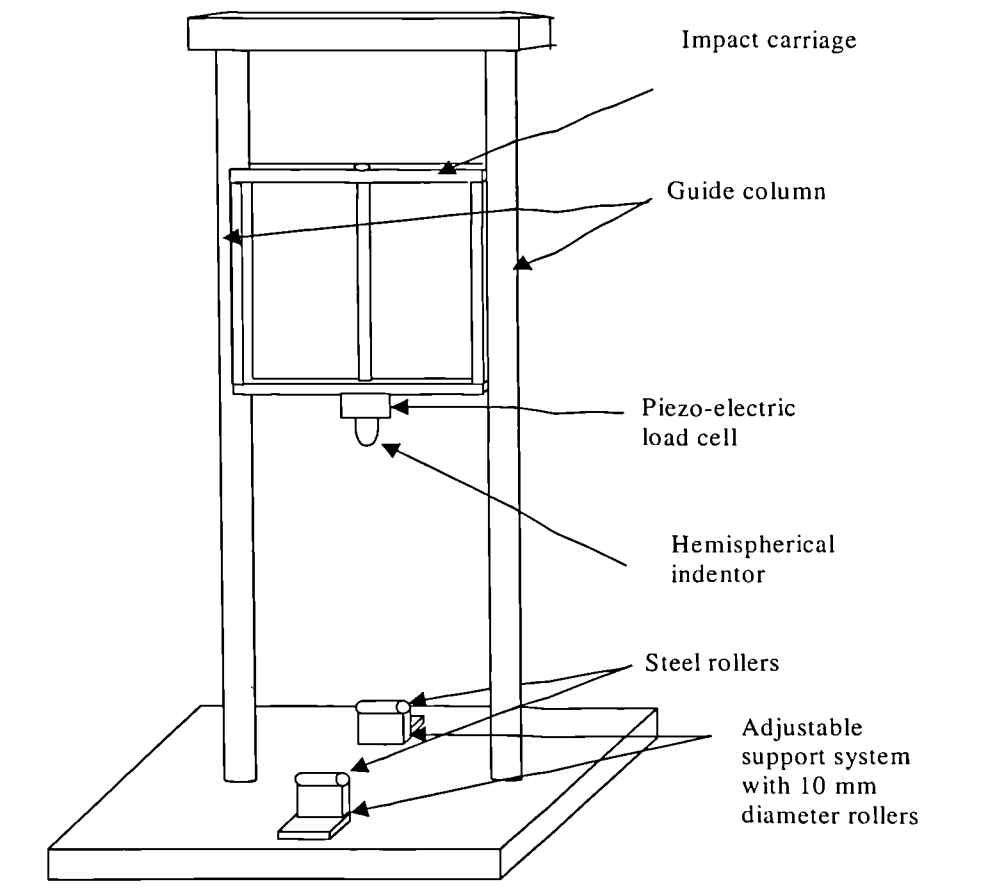


Figure 5.1: Schematic diagram of drop-weight impact tower (DWIT)

5.1.1 Impact tests on the composite and sandwich beams

Impact tests on the composite and sandwich beams were conducted using the drop weight impact tower presented in Figure 5.1. The specimens were simply supported on two 10 mm steel cylinders in a three-point bend test configuration. The carriage was dropped vertically onto the centres of specimen supported over spans ranging between 120 mm and 500 mm. Details of the spans used for each of the materials are given in Table 5.1.

Material/structure	Span (mm)	Drop height (mm)
GFR Epoxy beams (Thin)	160,170,180,190 and 200	10 to 100
GFR Epoxy beams (Thick)	120, 130, 140, 150 and 160	10 to 100
GFR Epoxy plates (Thin)	-	10 to 100
Aluminium-honeycomb beams (12 mm core)	170, 180, 190 and 200	5 to 40
Aluminium-honeycomb beams (24 mm core)	200, 300, 400 and 500	10 to 100
Aluminium-honeycomb plates (12 mm core)	-	10 to 100
Foam-core sandwich	175	10 to 100

Table 5.1: Summary of the beam geometries used for the laminated and sandwich composite beams

5.1.2 Impact tests on the circular plates and sandwich panels

Impact tests on the circular composite plates and sandwich panels were conducted using the instrumented drop weight impact tower presented in Figure 5.1. The support system used in this part of the study is illustrated in Figure 5.2. Here, three steel rings with diameters between 43.8 mm and 82.3 mm were used during the impact tests on the plain composite plates whilst a larger ring structure with an internal diameter of 203 mm was employed during tests on the sandwich panels. Details of the ring supports are summarised in Table 5.2.

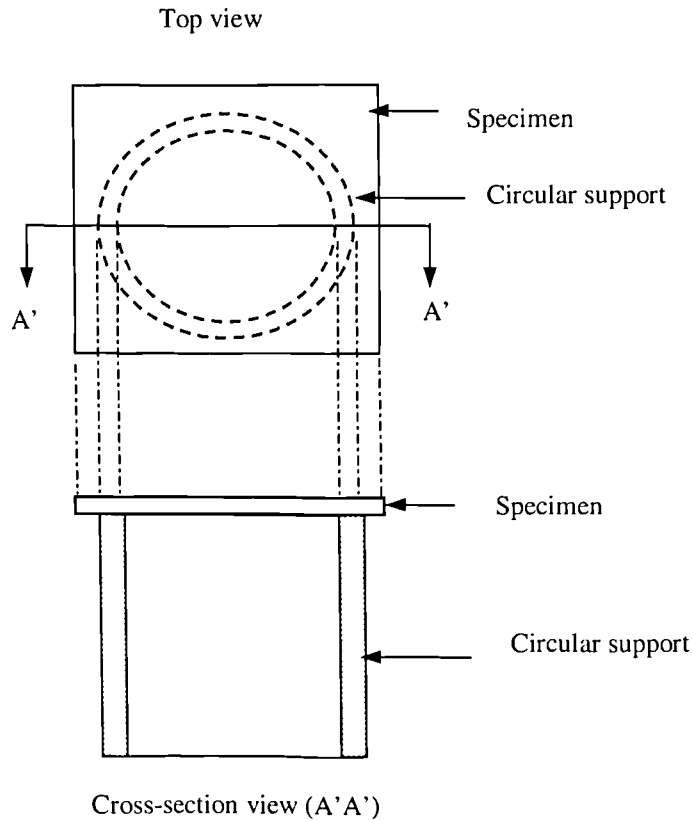


Figure 5.2: Schematic of the support system used during impact tests on the circular plates and circular sandwich panels.

Specimen configuration	Support number	Internal diameter (mm)	External diameter (mm)
Circular plate	1	43.8	50.8
	2	63.4	69.9
	3	82.3	89.0
Circular sandwich panel	4	203.0	260.0

Table 5.2: Summary of the diameters of the circular support systems.

5.2 Three-point bend tests on foam core materials

A series of three point bend tests were conducted on an Instron 4505 universal test machine in order to characterise the rate sensitivity of the foam materials. Crosshead displacement rates of 1, 10, 100 and 1000 mm/minutes were employed during this part of study. The specimens were simply-supported on two 10 mm diameter cylinders over a span of 175 mm. Care was taken to accurately determine the beam dimensions since small errors in these measurements can lead to a significant discrepancies in the properties measured. A 10 mm diameter steel indenter was used to load the samples. During each test, the load versus displacement trace was recorded and the flexural modulus of the core material was determined using:

$$E_f = \frac{PL^3}{48\delta I} \quad (5.1)$$

$$I = \frac{bt^3}{12} \quad (5.2)$$

Where

P = Applied load (N)

δ = Displacement of load point (m)

I = Second moment of area (m⁴)

b = Width of the composite beam (m)

t = Thickness of the composite beam (m)

L = Support span (m)

5.3 Determination of bending and shear stiffness of sandwich structures

The bending stiffness, D and shear modulus, G , is required in order to model the impact response of sandwich materials. For the aluminium honeycomb sandwich beam, D was determined using the approach outlined by Allen [4] which also yield the value of shear modulus, G . Details of this approach are presented in Section 5.3.1. For the foam-core sandwich beam, D was determined using beam theory and G is obtained from the manufacturer's data sheet. A detail of the later approach is described in Section 5.3.2.

5.3.1 The three-point bend test for determining the value of D and G for aluminium honeycomb beam

Sandwich beams are commonly used to determine a range of sandwich properties including the shear modulus, G and bending stiffness, D . These properties can be obtained by conducting a series of three-point bend tests at different spans. The shear stiffness of the sandwich structure is required in order to model the impact response of the sandwich structures. In this work, a simple three-point bend test was used to determine the shear modulus. Here, series of three-point bend tests were carried out on sandwich beams supported over the spans of 150, 200, 250 and 300 mm. These specimens were loaded at a crosshead displacement rates of 1 mm/minute. Details of the specimen dimensions are given in Table 5.3.

Span, L (mm)	Dimensions (mm)	Length of overhang (mm)
150	20 x 13.2 x 160	10
200	20 x 13.2 x 210	10
250	20 x 13.2 x 260	10
300	20 x 13.2 x 310	10

Table 5.3: Summary of the specimen geometries used to determine the shear modulus of the sandwich beams.

During each test, the load-displacement curve was recorded. Based on sandwich beam theory [4], the deflection under the central point load is:

$$\delta = \delta_b + \delta_s = \frac{PL^3}{48D} + \frac{PL}{4AG} \quad (5.3)$$

Where

δ_b = Deflection due to bending (m)

δ_s = Deflection due to shear (m)

P = Applied load (N)

D = Flexural stiffness of the sandwich beam (Nm^2)

AG = Shear stiffness of the sandwich beam (N)

$$A = \frac{bd^2}{c} \text{ (m}^2\text{)}$$

b = Width of the specimen (m)

$$d = \frac{h+c}{2} \text{ (m)}$$

c = Thickness of the core (m)

L = Support span (m)

Clearly, if the deflection is measured on two beams supported over different spans, Equation 5.3 can be solved for D and AG . This can only be true if one span is large enough to ensure that the deflection is predominantly due to bending and the other is small enough to ensure that the deflection is due mainly to shear [4]. Therefore the most reliable method is to recast Equation 5.3 as follows:

$$\frac{\delta}{PL} = \frac{L^2}{48D} + \frac{1}{4AG} \tag{5.4}$$

$$\frac{\delta}{PL^3} = \frac{1}{48D} + \left(\frac{1}{4AG} \cdot \frac{1}{L^2} \right) \tag{5.5}$$

Equation 5.4 can be represented as a straight line in a plot of δ/PL against L^2 . Similarly Equation 5.5 can be represented as a straight line in a plot of δ/PL^3 against $1/L^2$.

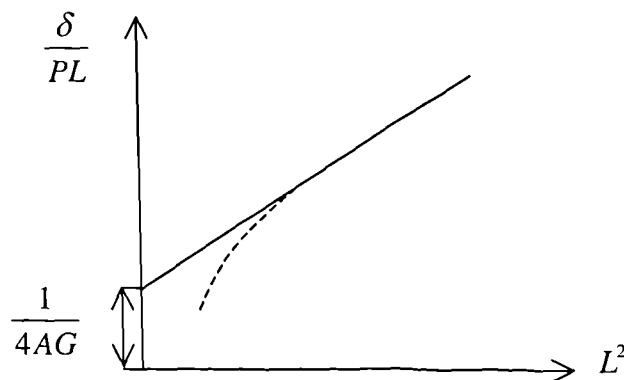


Figure 5.3a: Schematic plot of δ/PL against L^2

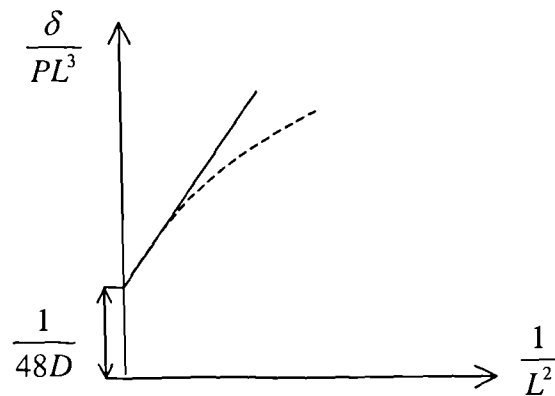


Figure 5.3b: Schematic plot of δ/PL^3 versus $1/L^2$ following a three-point bend test on a simply supported sandwich beam.

The values of G and D were then determined from the intercept values on the y-axes in Figures 5.3a and 5.3b.

5.3.2 Determination of the D from the properties of the constituents for sandwich foam core beams

Another way of determining D is by measuring the specimen geometry with a given value of the flexural modulus of the skin E_f . Details of the sandwich beam configuration used in this research programme are given in Figures 5.4a and 5.4b.

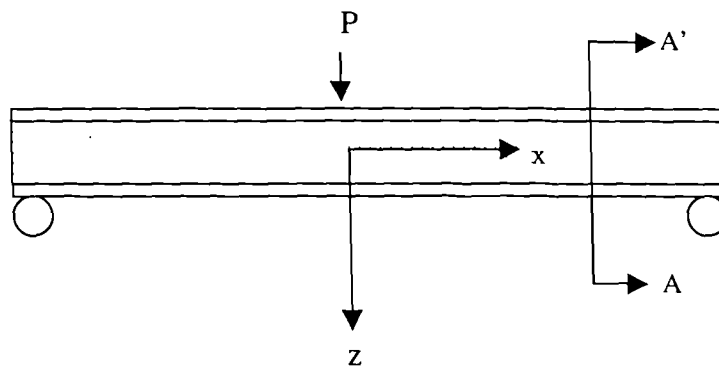


Figure 5.4a: Schematic diagram of the sandwich beam

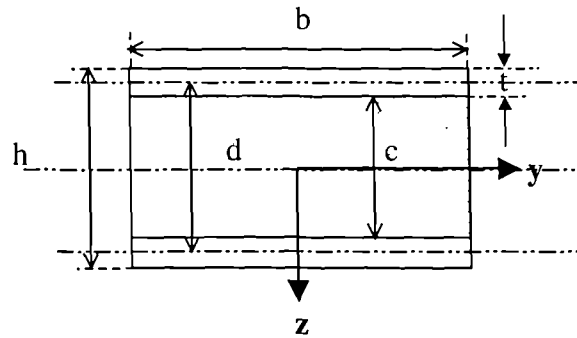


Figure 5.4b: Cross section AA' of the sandwich beam

Using beam theory, the bending stiffness, D , for a sandwich material is given as [6]:

$$D = \frac{E_f b t^3}{6} + \frac{E_f b t d^2}{2} + \frac{E_c b c^3}{12} \tag{5.6}$$

Where E_f and E_c are the modulus of elasticity of the faces and core respectively and d is the distance between the centre lines of the upper and lower faces. Therefore;

$$d = \frac{h + c}{2} \tag{5.7}$$

The faces of a sandwich structure are usually thin compared with the core and therefore the first term of Equation 5.6 can be ignored if:

$$3 \left(\frac{d}{t} \right)^2 > 100 \text{ or } \frac{d}{t} > 5.77 \tag{5.8}$$

Since the core is usually made from a low-density material, it has a much lower modulus than the face and therefore the third term in Equation 5.6 can be ignored if:

$$\frac{6 E_f}{E_c} \frac{t}{c} \left(\frac{d}{c} \right)^2 > 100 \quad (5.9)$$

Thus, for sandwich structures with thin faces and a weak core, the flexural rigidity D can be written approximately as

$$D = \frac{E_f b t d^2}{2} \quad (5.10)$$

Equation 5.10 was used to determine D for the foam-core sandwich beams. The values of shear modulus G were taken from manufacturer's data sheet.

5.4 Indentation tests on the sandwich beams

In order to correctly model the impact response of sandwich structures, account must be made for the energy dissipated in top surface contact effects. In this research programme, a series of indentation tests were carried out at crosshead displacement rates of 0.1, 1, 10 and 100 mm/minutes using the Instron 4505 mechanical test machine. Specimens with dimension of 200 mm x 20 mm x 13 mm were loaded up to a force of similar magnitude to that recorded during the impact test. The indentation tests were conducted by placing sandwich beams on a solid steel support system as presented in Figure 5.5. By placing the samples on a steel support, flexural and shear effects were suppressed. Therefore, the specimens were assumed to undergo only contact effects during indentation tests. In order to determine the contact parameters accurately, the indentation depth was measured using the displacement gauge attached to both the specimen and the indenter. The indenter was the same as that used for the drop-weight impact tests.

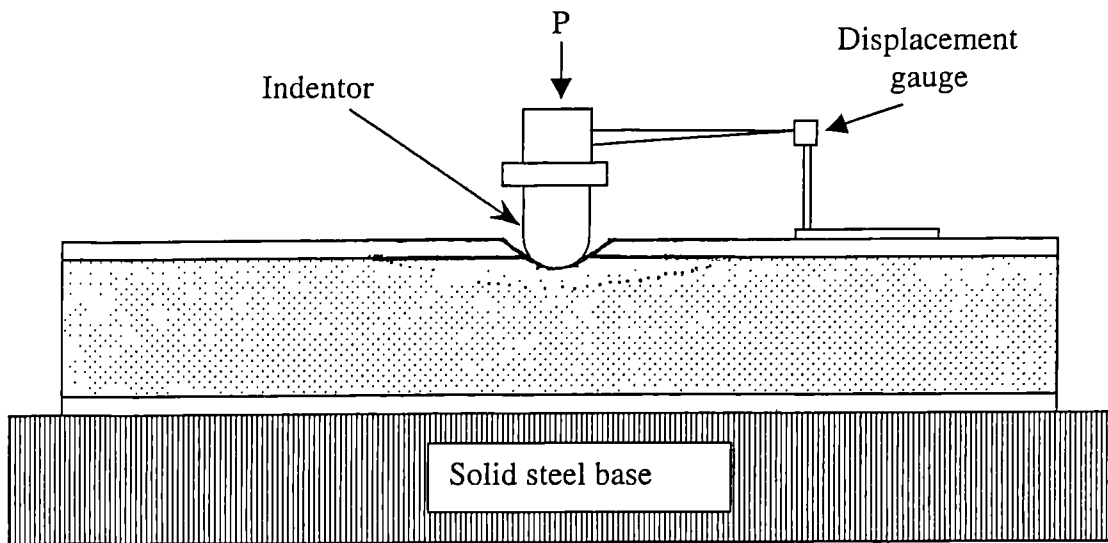


Figure 5.5: Schematic of an indentation test on a sandwich structure.

The relationship between the load P and indentation α during an indentation test can be written in the form of:

$$P = C\alpha^n \quad (5.11)$$

Where n and C are the contact stiffness parameters which can be determined experimentally. Equation 5.11 can be resolved for the value of n and C as follows:

$$\text{Log } P = \text{Log } C + n \text{Log } \alpha \quad (5.12)$$

Following the Equation 5.12, the plot of $\log P$ and $\log \alpha$ was obtained and using the curve-fitting method, the value of n and C were calculated as shown schematically in Figure 5.6.

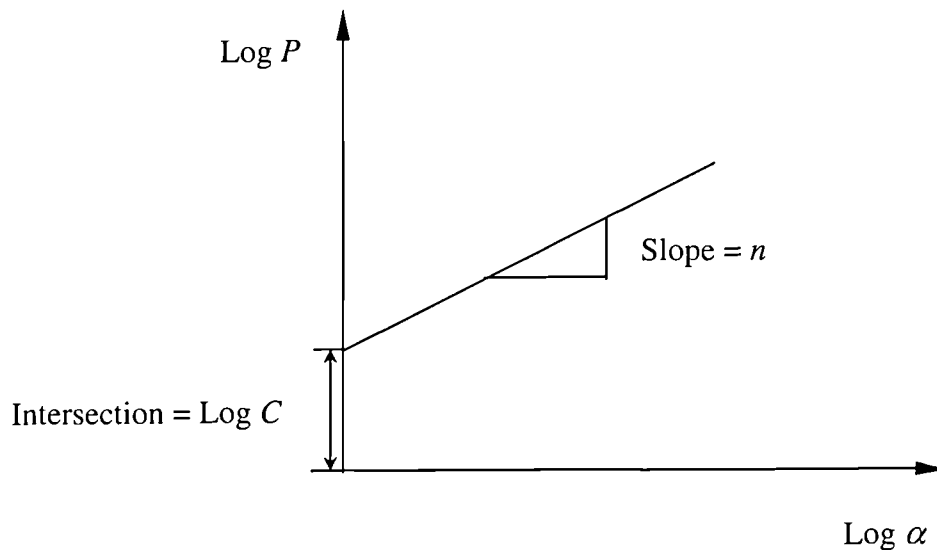


Figure 5.6: Schematic outlining how the contact parameters were determined following the indentation tests.

5.5 Single end notch bend (SENB) tests

The failure modes observed in the impact-loaded foam-core sandwich structures are known to depend on the properties of the foam, for example, on its fracture toughness. In an attempt to correlate the various failure mechanisms observed in the sandwich structures to the properties of the foam-core materials, a series of fracture toughness test were conducted. Here, the foam-core sandwich panels were cut into beams with dimensions of 150 mm x 20 mm x 10 mm using a high speed circular saw. Details of the specimen geometry are presented in Figure 5.7a. A pre-crack of length 'a' was introduced into each specimen using a band saw and the tip of the crack was sharpened using a fresh razor blade. The specimen was loaded at a crosshead displacement rate of 10 mm/minute until it had completely fractured. Following each test, the load-displacement data were recorded. The energy absorbed in crack growth was determined from the area under the load-displacement curve. Each of the curves was weighed and

then converted into an energy from a knowledge of the total area of the graph and its weight. The fracture energy was calculated using:

$$\text{Work of Fracture} = \frac{\text{Energy}}{(W - a)b} \quad (5.13)$$

Where W , b and a are the depth, thickness and crack length. The test configuration is presented in Figure 5.7b.

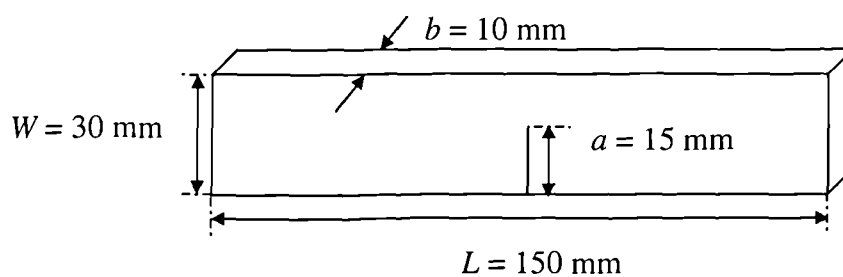


Figure 5.7a: Schematic of the SENB test specimen

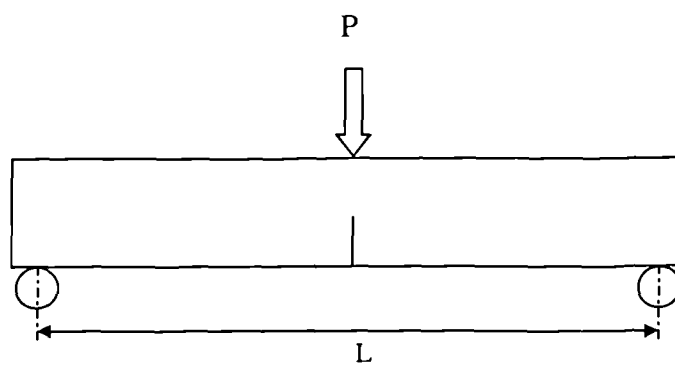


Figure 5.7b: Schematic of the support conditions for the SENB specimen

5.6 Compression tests

The mechanical properties of core materials were also investigated in order to elucidate the fracture behaviour of the sandwich foam core materials as well as their failure modes. The compressive stress-strain curves can provide vital information relating to the point at which the foam undergoes progressive shear crushing, densification as well as the load at failure. In this research programme, a series of compression tests were carried on each of the foams used according to the ASTM D-3574-91. The specimens were cut into squares with dimensions of 25.6 mm x 25 mm x 10.2 mm using a high speed cutter. The specimens were then loaded at crosshead displacement rates of 0.2, 1 and 10 mm/minute up to a similar load as that experienced in the appropriate impact test. Following each test, the stress-strain curve was recorded. The compressive strength of the foams were calculated as follows:

$$\text{Compressive Strength} = \frac{\text{Maximum Force}}{\text{Planar area of the sample}} \quad (5.14)$$

5.7 Centre notch flexure (CNF) tests

Centre notch flexure tests were conducted in order to assess the level of adhesion between the skin and materials in the sandwich structures. The specimens were cut to dimensions of 13 mm x 20 mm x 200 mm by using high speed cutter. Before testing, a 5 mm diameter hole was introduced midway along the sample just above the lowermost skin-core interface. A pre-crack was then introduced by opening the crack manually. Details of specimens are shown in Figure 5.8. A 5 mm steel bar was inserted into the hole and loaded at 10 mm/minutes. The application of the central force caused the crack to extend along the skin-core interface. Upon completion of each test, the delaminated area was calculated using transparent graph paper. The areas method was used to determine the work of fracture for each test specimen. Here, each of the curves was

weighed and then converted into the energy using the total weight of the graph and its total area. The work of fracture was then defined as:

$$\text{Work of fracture} = \frac{\text{Energy under the load - displacement curve}}{\text{Fracture area created during the test}} \quad (5.15)$$

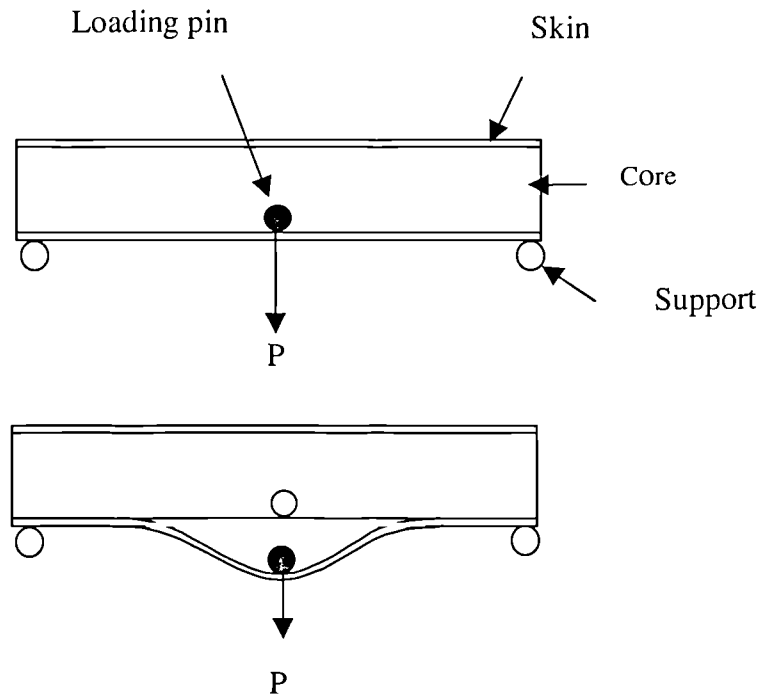


Figure 5.8: Schematic diagram of the centre notch flexure test

5.8 Optical microscopy

The failure modes in the impact-loaded beams and plates were investigated using a Wild-Heerbrug low power microscope. The size of the damage zone was also measured using this microscope and these values were correlated with the incident impact energy.

5.9 References

1. W.J. Cantwell, M. Busser and H.H. Kausch, "An analysis of the impact response of a composite beam", *Composites Engineering*, 1, pp 293-307, 1991.
2. K.N. Shivakumar, W. Elber and W. Illg, "Prediction of impact force and duration due to low velocity impact on circular composites laminates", *J. Appl. Mechanics*, 52, pp 674-680, 1985.
3. P. Davies, D. Choqueuse, L. Riou and A. Wahab, "Response of composite sandwich panels to impact loading", *Revue de l'Institute Francais du Petrole*, 50, Janvier-Fervier, pp 75-82, 1995.
4. H.G. Allen, "Analysis and Design of Structural Sandwich Panels", Pergamon Press, Oxford, 1963.
5. F.J. Plantema, "Sandwich Construction", John Wiley and Sons, Chichester, 1966.
6. S.P. Timonshenko, "Theory of Elasticity", McGraw-Hill, New York, 1934.

CHAPTER 6: ENERGY BALANCE MODELS

In this chapter, attention will focus on the energy-balance models that have been used in this study. Initially, the simple energy-balance model for a laminated composite beam will be considered. Following this, more complicated energy-balance models, such as those used to model the structural sandwich beams and plates will be discussed.

6.1 Energy-balance models

A useful approach for analysing the impact event is to consider the dissipation of energy in the system during the impact event. During drop-weight impact testing, the kinetic energy of the projectile is used to deform the target and, if the incident energy is sufficiently high, to damage the material. According to Rayleigh [1], if the contact duration between the impactor and the target is very long with respect to the natural period of the target, vibrations of the system can be neglected and the impact problem can be treated as a quasi-static analysis. Let us assume that this is indeed the case and that the structure responds in a quasi-static mode. When the structure reaches its maximum deflection, the velocity of the projectile is zero and all of the initial kinetic energy of the projectile has been used to deform the structure. The total energy used can be divided into two categories, these being the energy used to deform the structure in bending/shear and the energy dissipated in contact effects. When the structure behaves quasi-statically, the maximum impact force can be determined using an energy balance approach without having to compute the entire force-time history. The energy-balance model is clearly very simple and it can, in principle, be applied to a wide range of structures.

6.1.1 Energy-balance model for a laminated composite beam

The simplest structure available for studying the impact problem is a beam. Here, contact, shear and membrane effects are ignored. Using the conservation of energy principle, the energy-balance of the projectile-target system can be determined by equating the kinetic energy of the projectile to the energy absorbed in bending, i.e.

$$\frac{1}{2}mv^2 = \int_0^{\delta_{\max}} P d\delta \quad (6.1)$$

Where m is the mass of the impactor, v is the impact velocity, P is the impact force and δ is the displacement of the beam (target). The displacement of an isotropic beam under flexural loading is given as:

$$\delta = \frac{P L^3}{48EI} \quad (6.2)$$

Combining Equation 6.2 with Equation 6.1 gives:

$$\frac{1}{2}mv^2 = \int_0^{\delta_{\max}} \frac{48EI\delta}{L^3} d\delta \quad (6.3)$$

Integrating Equation 6.3 gives:

$$\frac{1}{2}mv^2 = \frac{24EI\delta_{\max}^2}{L^3} \quad (6.4)$$

Replacing δ_{\max} by P_{\max} from Equation 6.2 gives:

$$\frac{1}{2}mv^2 = \frac{P_{\max}^2 L^3}{96EI} \quad (6.5)$$

Solving Equation 6.5 gives the maximum force as:

$$P_{\max} = \sqrt{\frac{48mv^2 EI}{L^3}} \quad (6.6)$$

From Equation 6.6, the maximum impact force can be determined for any given impact energy as long as the dimensions of the test geometry and material properties are known. Here, E was taken as the longitudinal modulus of the composite.

6.1.2 Energy-balance model for a circular composite plate

As previously stated, the energy-balance model is based on the principle of conservation of the total energy of the plate-impactor system. For a laminated circular plate, membrane stiffening and contact effects can be significant since the impact force can be high. Therefore, these effects must be taken into account along with bending and shear deformations. Therefore, the kinetic energy of the impactor is equated to the energy absorbed in bending, shear and membrane deformations (E_{bsm}) and contact effects (E_c). The energy losses due to material damping, surface friction and higher modes of vibration are neglected [1]. The energy-balance for the system can be written as:

$$\frac{1}{2}mv^2 = E_c + E_{bsm} \quad (6.7)$$

Here it is assumed that contact effects can be modelled using a Hertzian [2] approach:

$$P = C\alpha^3 \quad (6.8)$$

where P is the applied force and α is the indentation. The contact energy, E_c , can be calculated using:

$$E_c = \int_0^{\alpha_{\max}} P d\alpha \quad (6.9)$$

Solving the integral and re-arranging in terms of the maximum force gives:

$$E_c = \frac{2}{5} \frac{P_{\max}^5}{C^2} \quad (6.10)$$

The contact stiffness parameter, C , in Equation 6.10 can be calculated from one of two ways:

a) Using the Hertzian contact analysis:

For a spherical, isotropic impactor, the contact parameter, C is given as [3]:

$$C = \frac{4\sqrt{R_1}}{3\pi(K_1 + K_2)} \quad (6.11)$$

where the subscripts 1 and 2 refer to the impactor and target respectively. R_1 is the radius of the impactor and the constants K_1 and K_2 in the case of impact between two isotropic solids are given as [3]:

$$K_1 = \frac{1 - \nu_1^2}{\pi E_1} \quad (6.12)$$

$$K_2 = \frac{1 - \nu_2^2}{\pi E_2} \quad (6.13)$$

Where ν_1 and ν_2 are the Poisson's ratio of the impactor and target respectively and E_1 and E_2 are Young's modulus of the impactor and target respectively.

b) The value of C can also be determined experimentally using a static indentation test.

The resulting load-displacement curve is then used to solve Equation 6.8 as follows:

$$\log P = \log C + \frac{3}{2} \log \alpha \quad (6.14)$$

Plotting $\log P$ against $\log \alpha$ will yield the value of $\log C$ from the intersection of the line with the y-axis as shown in Figure 6.1.

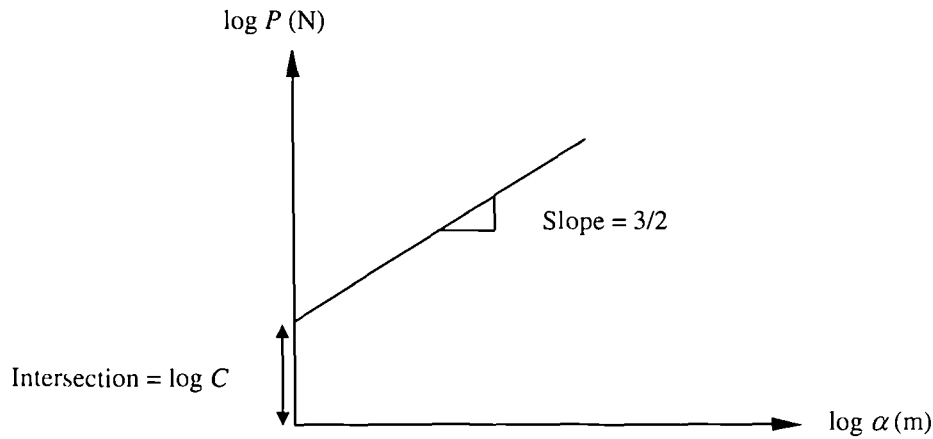


Figure 6.1: Graph showing how the contact parameter ‘C’ was determined using Equation 6.14.

This experimental approach was used to determine the value of the parameter C in this study. The energy associated with bending, shear and membrane deformations can be calculated by integrating the force-displacement relationship as:

$$E_{b,m} = \int_0^{\delta_{max}} P d\delta \quad (6.15)$$

For a circular plate, the relationship between the applied force, P , and the resulting displacement, δ , can be written as [4]:

$$P = K_{bs}\delta + K_m\delta^3 \quad (6.16)$$

Where K_{bs} is the effective bending/shear stiffness of the plate and K_m is the membrane stiffness which accounts for membrane stretching in the plate. The effective bending/shear stiffness can be determined from the individual stiffnesses using [4]:

$$K_{b_s} = \frac{K_b K_s}{K_b + K_s} \quad (6.17)$$

Where K_b and K_s for a simply-supported circular plate are given as [4, 5]:

$$K_b = \frac{4\pi E_r h^3}{3(3 + \nu_r)(1 - \nu_r)a^2} \quad (6.18)$$

$$K_s = \frac{4\pi G_{zr} h}{3} \left(\frac{E_r}{E_r - 4\nu_{zr} G_{zr}} \right) \left(\frac{1}{\frac{4}{3} \log \frac{a}{a_c}} \right) \quad (6.19)$$

Where E_r , ν_r and G_{zr} are the Young's modulus, Poisson's ratio and shear modulus of the plate respectively and a and h denote the plate radius and thickness, respectively. The subscripts z and r denote the thickness and the radial directions of the plate, respectively, with z being the direction of impact. The membrane stiffness K_m for a simply-supported system with moveable edges can be written as [4]:

$$K_m = \frac{\pi E_r h}{a^2(3 + \nu_r)} \left[\frac{191}{648}(1 + \nu_r)^4 + \frac{41}{27}(1 + \nu_r)^3 + \frac{32}{9}(1 + \nu_r)^2 + \frac{40}{9}(1 + \nu_r) + \frac{8}{3} \right] \quad (6.20)$$

The contact radius, a_c , in Equation 6.19 is a function of the applied force P and can be written as [6]:

$$a_c = \left[\frac{3\pi}{4} P (K_1 + K_2) R_1 \right]^{1/4} \quad (6.21)$$

In this study, the value of impact force P is initially unknown and therefore it is not possible to determine a_c . Instead, a value of $a_c = 1$ mm was used in Equation 6.19. The energy due to shear/bending deformation and membrane effects ($E_{b_{sm}}$), was determined

by substituting Equation 6.16 into Equation 6.15 and integrating with respect to δ giving [7]:

$$E_{b,m} = \frac{1}{2} K_{b,} \delta_{\max}^2 + \frac{1}{4} K_m \delta_{\max}^4 \quad (6.22)$$

Applying an energy-balance according to Equation 6.7 yields:

$$\frac{1}{2} mv^2 = \frac{2}{5} \frac{(P_{\max})^5}{C^3} + \frac{1}{2} K_{b,} \delta_{\max}^2 + \frac{1}{4} K_m \delta_{\max}^4 \quad (6.23)$$

Substituting for P_{\max} in the first term of Equation 6.23 with Equation 6.16 and simplify gives:

$$mv^2 = \frac{4}{5} \frac{(K_{b,} \delta_{\max} + K_m \delta_{\max}^3)^5}{C^3} + K_{b,} \delta_{\max}^2 + \frac{1}{2} K_m \delta_{\max}^4 \quad (6.24)$$

The maximum deflection δ_{\max} can be obtained for any impact energy by varying δ_{\max} until the right-hand side of Equation 6.24 is equal to the left-hand side. Upon obtaining the maximum deflection δ_{\max} from Equation 6.24, the maximum impact force P_{\max} can be calculated using Equation 6.16.

6.1.3 Energy-balance model for a composite sandwich beam

In this energy-balance model, the initial kinetic energy is absorbed in bending, shear and contact effects. Membrane effects are neglected since the out-of-plane deflections are likely to be small. Based on the conservation of energy principle, the energy-balance of the system in the elastic regime is given as:

$$\frac{1}{2}mv^2 = E_{bs} + E_c \quad (6.25)$$

Where E_{bs} is the energy absorbed in bending and shear deformations and E_c is the energy absorbed in contact effects. The force-displacement relationship for a simply-supported sandwich beam is given by [8]:

$$\delta = \frac{PL^3}{48D} + \frac{PL}{4AG} \quad (6.26)$$

Where

δ = Displacement (m)

P = Applied load (N)

L = Span (m)

D = Flexural stiffness of sandwich structure (Nm^2)

G = Shear modulus of sandwich core (N/m^2)

$A = bd^2/c$ (m^2)

The energy absorbed due to bending and shear deformations was calculated as follows:

$$E_{bs} = \int_0^{\delta_{\max}} P d\delta \quad (6.27)$$

After integration, E_{bs} becomes:

$$E_{bs} = \frac{P_{\max}^2}{2} \left(\frac{L^3}{48D} + \frac{L}{4AG} \right) \quad (6.28)$$

With reference to contact effects, the impact force, P , and indentation depth, α , are assumed to follow Meyer's law:

$$P = C\alpha^n \quad (6.29)$$

where C and n are constants that can be determined experimentally by conducting an indentation test. The contact energy is then given as:

$$E_c = \int_0^{\alpha_{\max}} P d\alpha \quad (6.30)$$

Solving Equation 6.30 gives:

$$E_c = \frac{C \left(\frac{P_{\max}}{C} \right)^{\frac{n+1}{n}}}{n+1} \quad (6.31)$$

Substituting Equations 6.28 and 6.31 into Equation 6.25, the energy-balance equation for the system becomes:

$$\frac{1}{2}mv^2 = \frac{P_{\max}^2}{2} \left(\frac{L^3}{48D} + \frac{L}{4AG} \right) + \frac{C \left(\frac{P_{\max}}{C} \right)^{\frac{n+1}{n}}}{n+1} \quad (6.32)$$

Using Equation 6.32, the maximum impact force can be calculated by solving for the value of P_{\max} at any given impact energy.

6.2 References

1. L. Rayleigh, "On the production of vibrations by forces of relatively long duration, with application to the theory of collisions", *Philosophical Magazine*, 11, pp 283-285, 1906.
2. H. Hertz, *Journal of Mathematics (Crelle)*, 92, pp 156-157, 1881.
3. H.D. Conway and Z. Angew, "The pressure distribution between two elastic bodies in contact", *J. Mathematics and Physics*, 7, pp 460-465, 1956.
4. A.S. Volmir, "A translation of flexible plates and shells", AFFDL-TR-66-216, 1967.
5. S.A. Lukasicwicz, "Introduction of concentrated loads in plates and shells", *Progress in Aerospace Science*, 17, pp 109-146, 1976.
6. L.B. Greszczuk, "Damage in composite materials due to low velocity impact," in Zukas *et al.* eds., *Impact Dynamics*, John Wiley & Sons, New York, 1982.
7. K.N. Shivakumar, W. Elber and W. Illg, "Prediction of impact force and duration due to low velocity impact on circular plate", *J. Appl. Mechanics*, 52, pp 674-680, 1985.
8. H.G. Allen, "Analysis and Design of Structural Sandwich Panel," Pergamon Press, Oxford, 1969.

CHAPTER 7: RESULTS AND DISCUSSION

This chapter summarises the findings of a programme of research work investigating the impact response of composite materials. The chapter includes a study of the behaviour of the constituent materials i.e. the skin and core systems. This work includes an investigation of the influence of loading rate on the mechanical properties of the skin and core materials and also tests to characterise the degree of adhesion between the skin and core materials in the sandwich structures. The results of drop-weight impact tests on a series of composite structures including a laminated beam, a laminated plate as well as sandwich beams and panels are also presented and discussed. Finally, the failure mechanisms and fracture processes in the sandwich structures are presented and discussed.

7.1 Characterising the behaviour of the constituent materials

The initial part of the research project focused on characterising the mechanical properties of the constituent materials over a range of loading rates. The flexural modulus of the skin and core materials was measured on an Instron 4505 test machine using a three-point bend test configuration. The aim of this part of study was to investigate how key mechanical properties such as the flexural modulus of the skin and core materials were affected by loading rate. Clearly, any effect of loading rate on the mechanical properties of these materials will have a significant influence on the ability of any impact model to predict the impact response of these sandwich structures. This chapter will also investigate the effect of core toughness on determining the failure modes in the sandwich structures.

7.1.1 The effect of crosshead displacement rate on the flexural modulus of the glass fibre reinforced skin

Three-point bend tests were undertaken to evaluate the rate sensitivity of the flexural modulus of the composite skins. The prepreg material used was PN900-44-43 from Stesalit Ltd, Switzerland. The system is based on an E-glass fibre fabric, US-Style 120, impregnated with a polymerised aromatic cyanate ester compound. The three point bend test was selected since the support configuration and the test conditions resemble those employed during the impact test. As mentioned above, the tests were undertaken on an Instron 4505 universal test machine at crosshead displacement rates of 1, 10, 100 and 1000 mm/minute. The specimens were supported over a span of 200 mm and loaded at their mid-points. Typical examples of load versus displacement curves for the glass fibre reinforced epoxy skin at crosshead displacement rates between 1 and 1000 mm/minute are given in Figure 7.1.

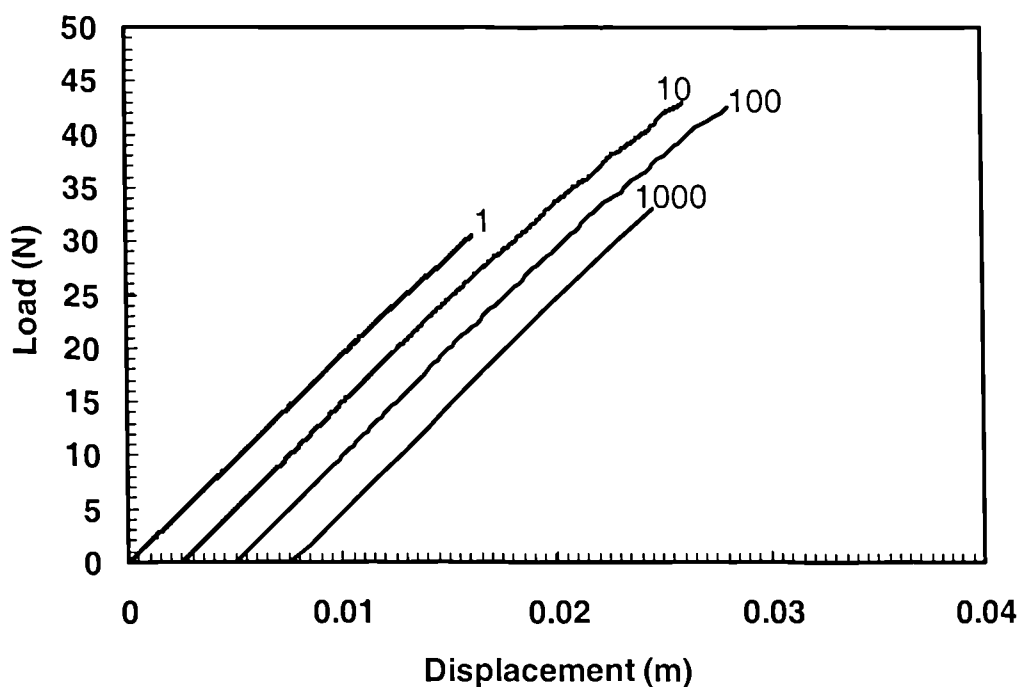


Figure 7.1: Typical load-displacement curves of glass fibre reinforced epoxy skin at various crosshead displacement rates. The numbers indicate the crosshead displacement rate in mm/minute.

From the load-displacement curves taken at the four different rates, it is clear that the data is highly reproducible and that the slopes of the curves, which reflect the Young's modulus of the material, are similar at each rate. As expected, there is some slight non-linearity at higher loads, an effect that is due to both edges of the specimen slipping between the supports. The Young's modulus of the glass fibre reinforced epoxy skin was calculated at each loading rate and the results of these tests are presented in Figure 7.2.

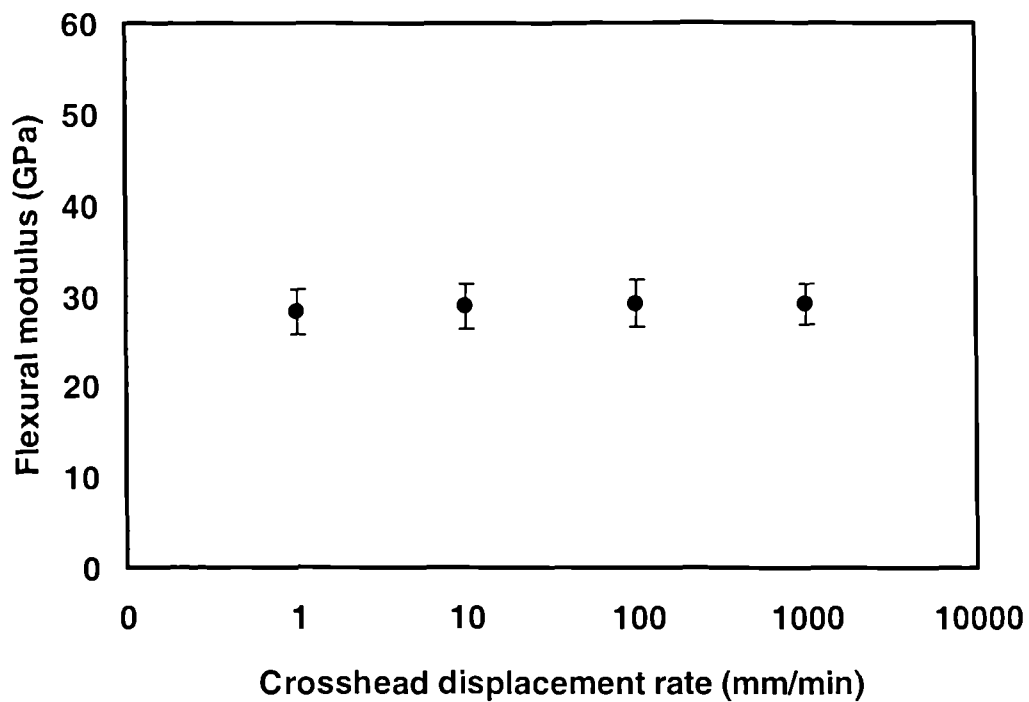


Figure 7.2: The effect of crosshead displacement rate on the flexural modulus of the GFR epoxy skin materials

The error bars shown in the figure indicate the standard deviation for the three tests undertaken at each loading rate. The values obtained from the tests are very similar to the values quoted by the manufacturers, Stesalit, suggesting that the laminates have been correctly processed and tested. From the results, it is clear that the flexural modulus of

the GFR epoxy skin does not display any dependence on loading rate over the range of conditions considered. Therefore, this evidence suggests that the elastic modulus determined at quasi-static rates can be used to model the impact response of this material. This conclusion agrees with the work reported by Cantwell *et al.* [1] following three-point bend tests on a 0° glass fibre reinforced epoxy laminate. These findings are further supported by the work of Rotem [2] who observed that the flexural stiffness of a glass/epoxy laminate remained unchanged over a wide range of loading rates. However, these results contradict the work by Harding and Welsh [3] who showed that GFRP specimens exhibit an increase in modulus with increasing strain rate. Harding and Welsh's tests were conducted on woven roving glass/epoxy laminates using the tensile-Hopkinson bar technique where the specimen is loaded longitudinally rather than in flexure as was the case in this research programme. In conclusion, the results reported here indicate that the flexural modulus of the glass fibre reinforced epoxy skin does not exhibit any rate dependency over the range of loading rates considered here.

7.1.2 The effect of loading rate on the flexural modulus of the foam core materials

In order to model the impact response of the sandwich structures accurately, the rate sensitivity of the foam-core materials needs to be investigated in detail. As outlined in Chapter 4, this research project will consider eleven different types of foam core material in order to study the influence of core properties on the impact response of composite sandwich structures. Here, mechanical tests were carried out to characterise the properties of the foam under flexural loading conditions. Crosshead displacement rates between 1 and 1000 mm/min were used during the course of these tests. Typical load versus displacement plots for the C70.90 foam are presented in Figure 7.3.

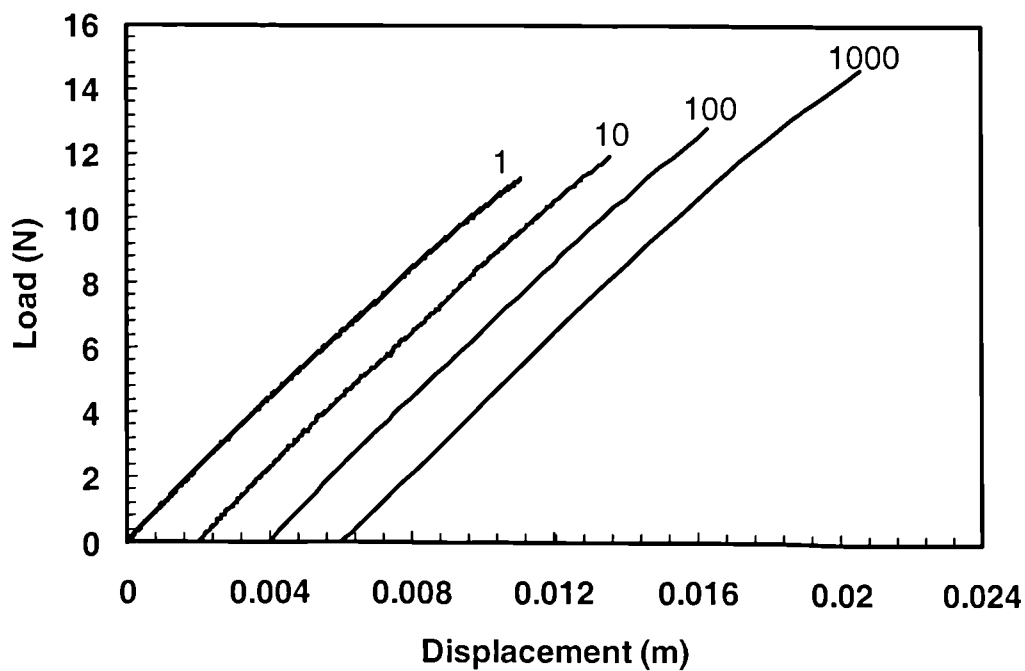


Figure 7.3: Typical examples of load-displacement curves for the C70.90 (PVC/PUR) foam at various crosshead displacement rates. The numbers refer to the crosshead displacement rate in mm/minute.

From the figure, the slopes at the four different rates are similar suggesting no strain rate sensitivity over the range of loading rates considered. As expected, slight non-linearity was observed at higher loads due to indentation effects around the loading pin. The results of these tests are presented in family groupings in Figures 7.4 to 7.6. It should be noted that the scatter in the experimental data was low and hence the standard deviations are not included. As far as the three groups of foam are concerned, there is no significant rate-sensitivity over the range of loading rates considered here. Even though the loading rates considered in this part of the study are somewhat lower than those encountered during the impact event, the trends clearly show that the variation of the modulus is not significant and the results suggest that the impact modulus of each foam is likely to be equal to its quasi-static value. The data indicate therefore, that the statically-determined value of modulus can be used to predict the impact response of the material. Similar findings were reported by Li *et al.* [4] following tests on a wide range of Rohacell-51WF foam materials.

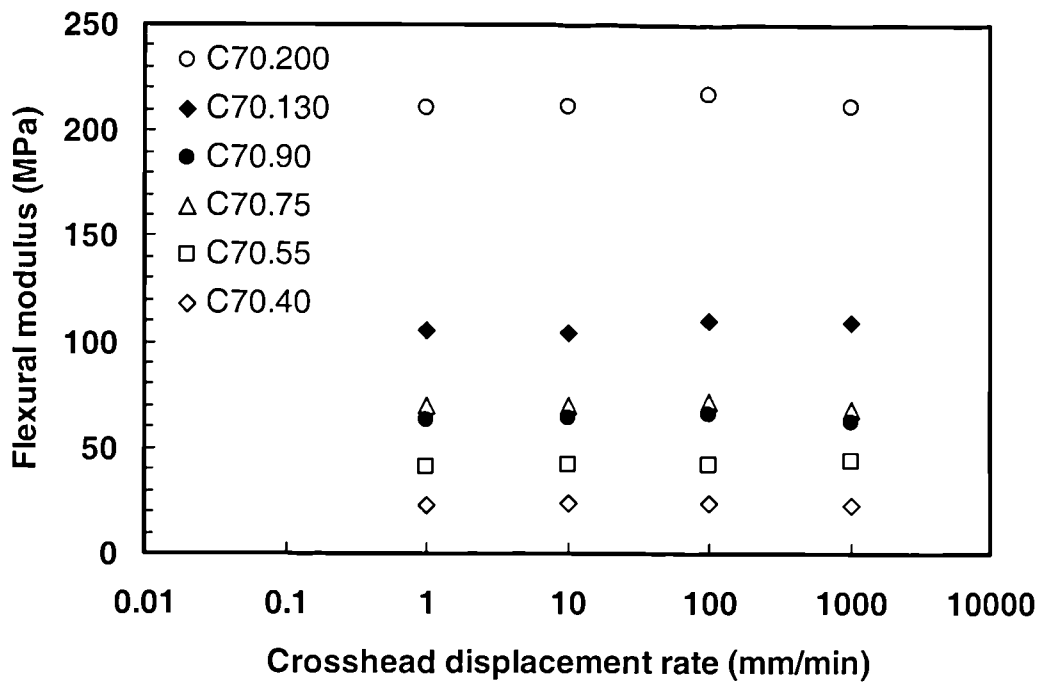


Figure 7.4: The effect of crosshead displacement rate on the flexural modulus of the C70 foams.

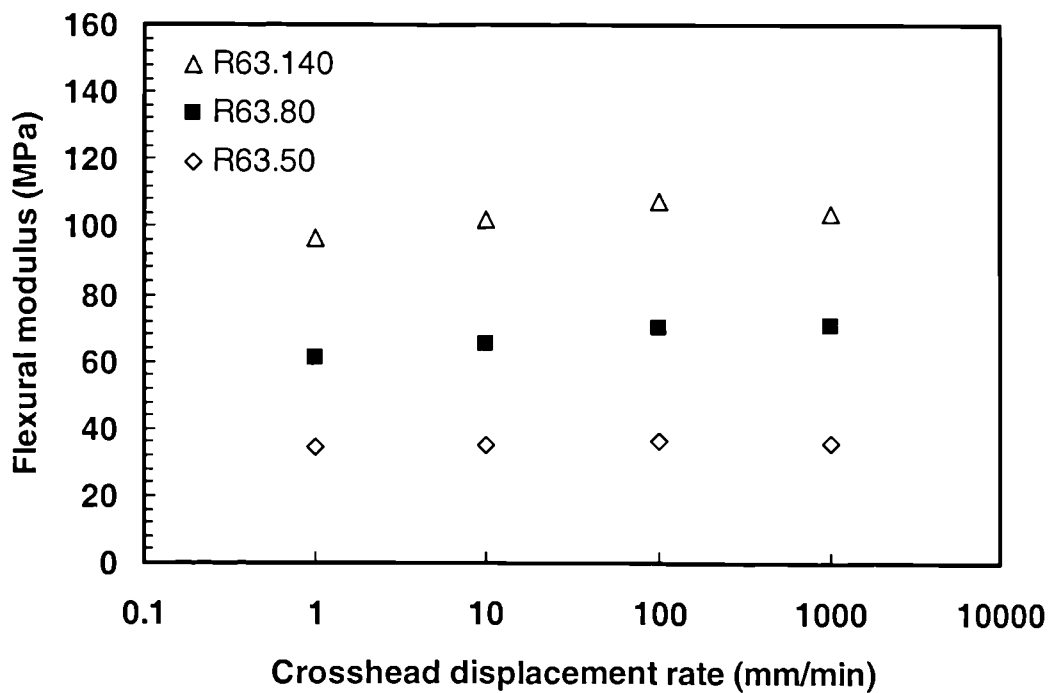


Figure 7.5: The effect of crosshead displacement rate on the flexural modulus of the R63 foams.

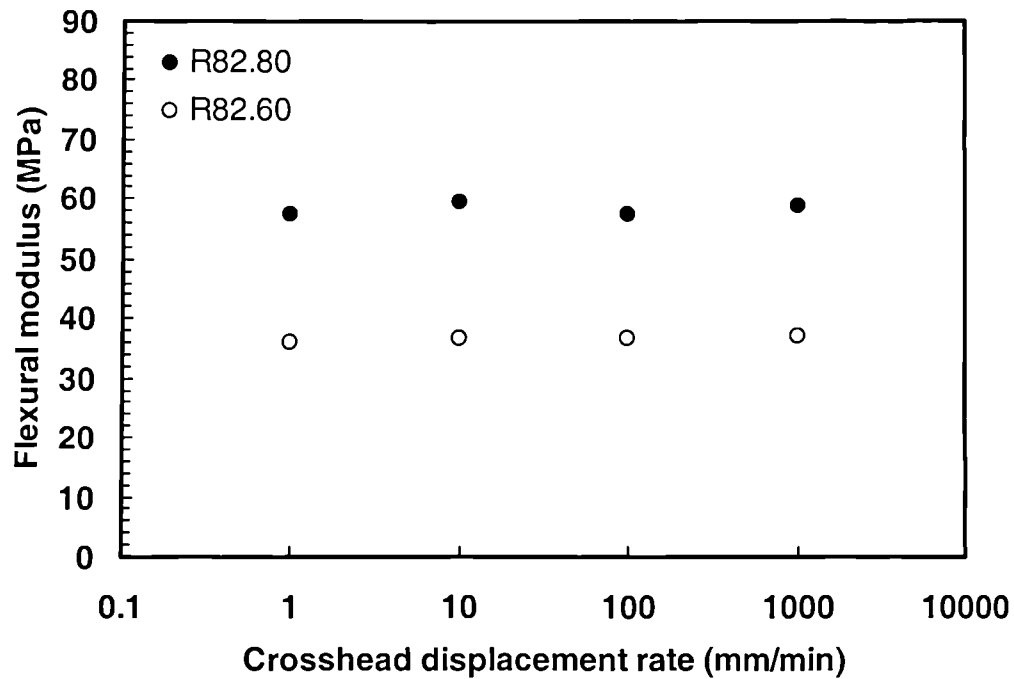


Figure 7.6: The effect of crosshead displacement rate on the flexural modulus of the R82 foams.

The modulus of the foams was also found to increase with increasing density as shown in Figure 7.7 where data obtained at a loading rate of 1 mm/min are shown. It is apparent that the flexural modulus does not depend on the material type with all three families of foams offering a similar value of flexural modulus for a given density. Instead, the experimental data suggest that the flexural modulus of a foam material is principally a function of its density.

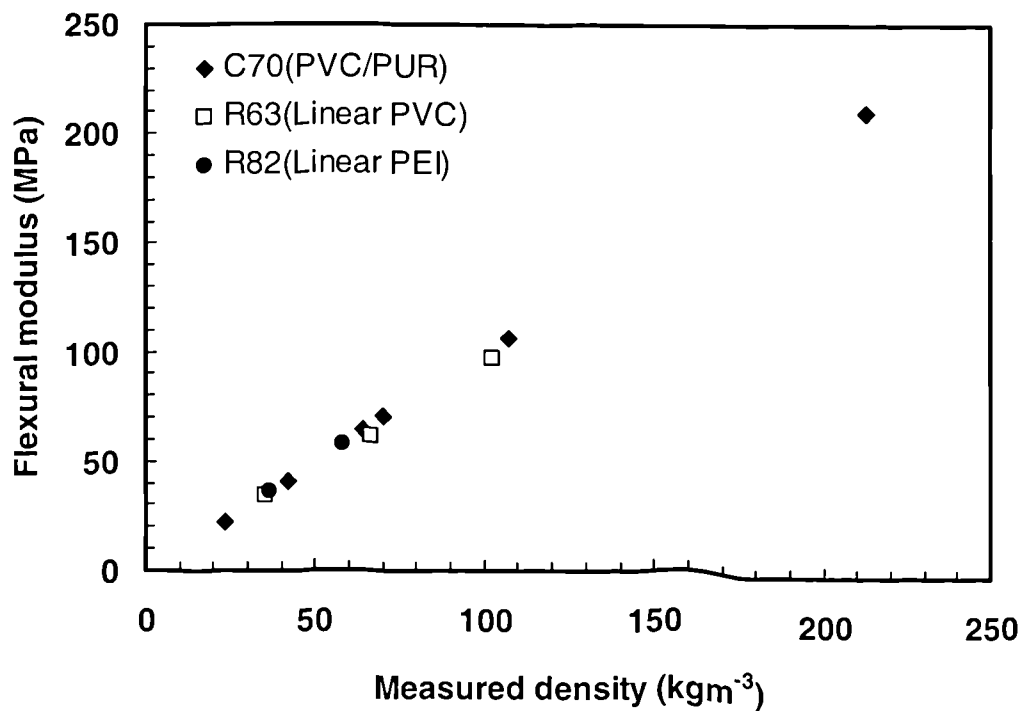


Figure 7.7: The influence of the measured foam density on the flexural modulus of the foam materials at a crosshead displacement rate of 1 mm/min.

A comparison of the experimental and manufacturer's flexural modulus and shear modulus data values is given in Table 7.1. The corrected values of the shear modulus of the foams were determined by measuring the actual density of each of the foams. Using the measured foam density, a linear relationship between the shear modulus quoted by the manufacturer and the nominal density was plotted as shown in Figure 7.8 for the C70 family of foams. The corrected shear modulus was then determined by introducing the experimental density into the relationship between the shear modulus and density. Included in Figure 7.8 is the procedure used to determine the corrected shear modulus for the C70.75 foam. Here, the measured density of this foam was 90.4 kg/m^3 , somewhat higher than its nominal value of 75 kg/m^3 . The vertical at a density of 90.4 kg/m^3 is then extended up until it intersects the curve fit yielding a corrected value of 36 MPa for the

shear modulus of this system. Clearly, this value is higher than the manufacturer's quoted value of 30 MPa.

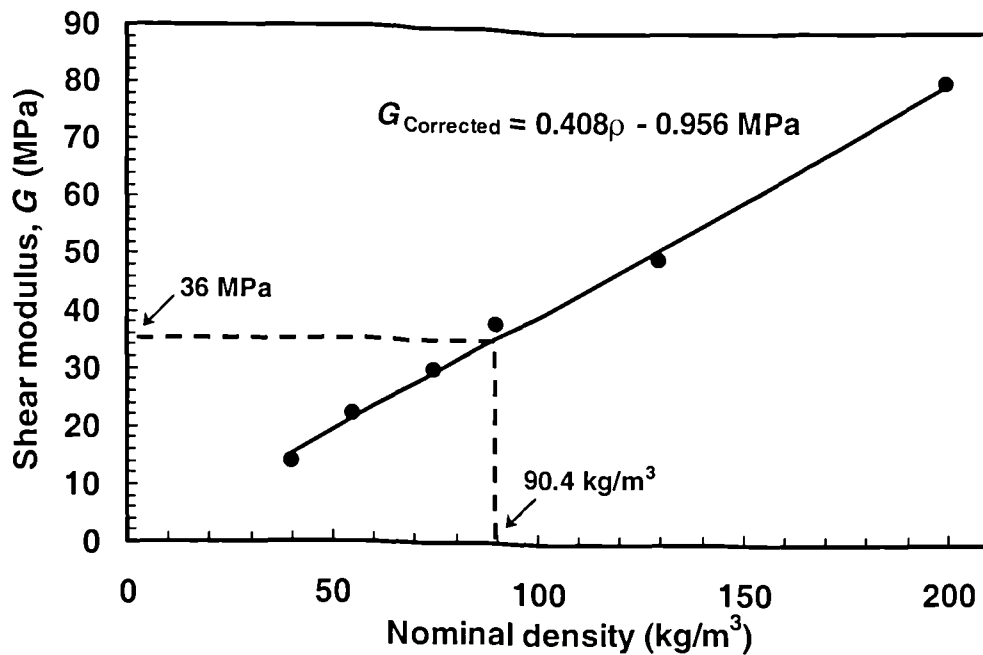


Figure 7.8: Plot of shear modulus versus nominal density for the C70 family of foams. The figure includes a curve-fit used to correct the shear modulus values using the experimentally-determined density. Included in the figure is an example for the C70.75 foam.

Foam	Density kgm ⁻³	Measured density kgm ⁻³	Shear modulus (MPa)		Flexural modulus (MPa)	
			Manufacturer's data sheets	Corrected	Manufacturer's data sheets	Experiment
C70.40	40	41.9	14	17	28	23
C70.55	55	64.7	22	26	45	42
C70.75	75	90.4	30	36	63	70
C70.90	90	89.9	38	36	81	64
C70.130	130	136.8	50	55	115	107
C70.200	200	233.1	81	94	180	213
R63.50	50	61.1	12	15	30	35
R63.80	80	106.5	21	28	50	67
R63.140	140	150.2	37	40	90	102
R82.60	60	62.5	14	15	34	37
R82.80	80	91.0	22	26	52	58

Table 7.1: Comparison of the flexural modulus and shear modulus values of the foam materials.

Clearly, in many cases the measured density values are higher than those quoted by the manufacturer. The reason for this is not known, however, it is possible that these differences may be due to manufacturing variations in the factory in which the foams were produced. It should be noted that only the corrected values of shear modulus were used in modelling the impact response of composite and sandwich materials in this research study. From the table, the measured flexural modulus of the C70.40, C70.55, C70.90 and C70.130 foams were lower than the manufacturer's values. In contrast, the C70.75 and C70.200 systems as well as the R63 and R82 samples offered higher experimental values of modulus than the manufacture's values. Clearly, the test technique adopted by the manufacturer may be different to that employed here. In addition, it has already been shown that the densities of the foams tested here were frequently very different to those quoted by the manufacturer. Further investigations were carried out to study the relationship between the Young's modulus and shear

modulus of a closed cell foam and its density. As expected, this process is always complicated especially when dealing with closed cell structures. This is partly due to the fact that the foams are cellular solids which cannot be treated as a continuous solid. Unlike other solids, the stiffness of the foam structure relies mainly on the properties of the thin cell edges. Many factors affect the modulus of a closed-foam cell structure such as the fraction of solid polymer, the cell geometry and the modulus of the bulk polymer. In order to establish the relationship between the foam properties and its structure, Gibson and Ashby developed a model on this subject [5]. The model was used to characterise a wide range of polymeric foam materials. Gibson and Ashby [5] showed that the relative Young's modulus (modulus of the foam / modulus of the solid polymer) can be written in terms of its relative density (density of the foam / density of the solid polymer) as:

$$\frac{E^*}{E_s} \approx \phi^2 \left(\frac{\rho^*}{\rho_s} \right)^2 + (1-\phi) \frac{\rho^*}{\rho_s} + \frac{P_0(1-2\nu^*)}{E_s \left(1 - \frac{\rho^*}{\rho_s} \right)} \quad (7.1)$$

and the relative shear modulus as:

$$\frac{G^*}{E_s} \approx \frac{3}{8} \left[\phi^2 \left(\frac{\rho^*}{\rho_s} \right)^2 + (1-\phi) \frac{\rho^*}{\rho_s} \right] \quad (7.2)$$

Where:

E^* = Young's modulus of the foam

E_s = Young's modulus of the solid polymer

ϕ = Fraction of the solid polymer in the rib of the closed-cell foam structure

ρ^* = Density of the foam

ρ_s = Density of the solid polymer

P_0 = Atmospheric pressure, 0.101 MPa

ν^* = Poisson's ratio of the foam material, taken as 0.3 in this study.

The last term in Equation 7.1 reflects the contribution of the gas to the compressive stiffness of the closed-foam cell structure. This can be significant under compression loading but can be ignored in the shear mode of loading as shown in Equation 7.2. Any form of trapped air inside the closed-cell can act as a medium that promotes a resistance to the applied force and this effect therefore needs to be incorporated into the calculation. When loaded in shear, the volume of the cell remains unchanged and therefore its effect on the shear stiffness can be ignored. The ratio of $3/8$ is simply the relationship between the Young's modulus, shear modulus and the Poisson's ratio for an elastic material. Previous work by Reitz *et al.* [6] on polyurethane foams has yielded a value of 0.8 for ϕ , this being close to the value of ϕ of 0.76 calculated here. The values of the relative Young's modulus and shear modulus obtained using Equation 7.1 and 7.2 are presented in Figures 7.9 and 7.10 respectively.

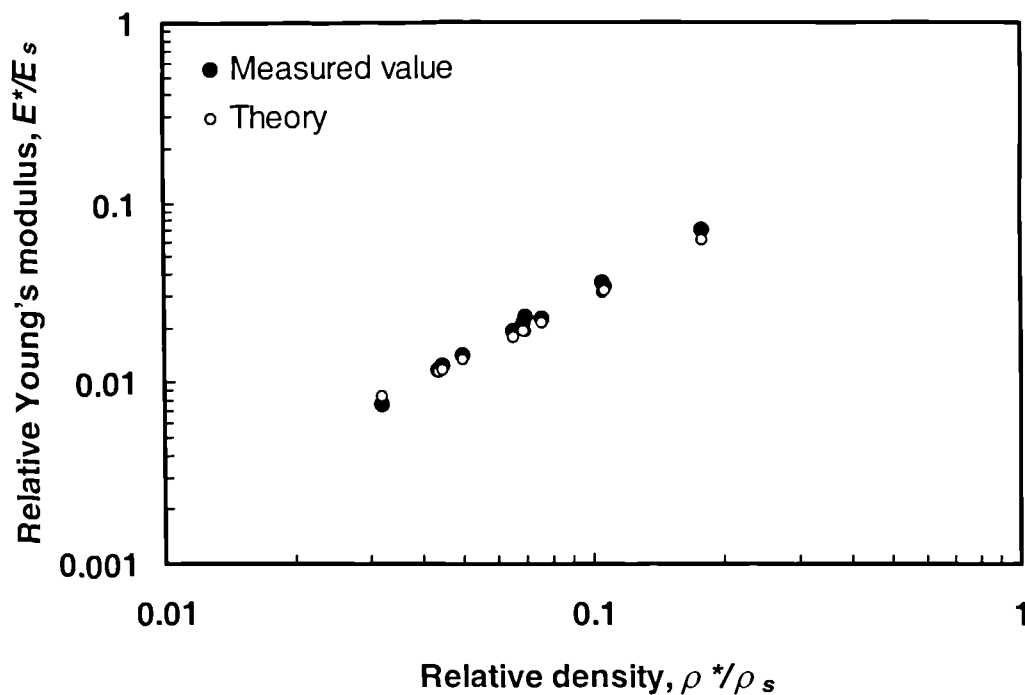


Figure 7.9: Plot of relative Young's modulus versus relative density with $\phi = 0.76$

From Figure 7.9, it is clear that Equation 7.1 has successfully modelled the variation of the relative Young's modulus of the closed-cell over a range of densities considered. The trends observed here agree with results reported elsewhere [5]. The predictions of the relative shear modulus data in Figure 7.10 are not as good as the data in Figure 7.9. Clearly, another value of ϕ would need to be selected to ensure a more accurate fit. However, it is appropriate to choose another value of ϕ since this parameter should be the same for both the Young's modulus and shear modulus data.

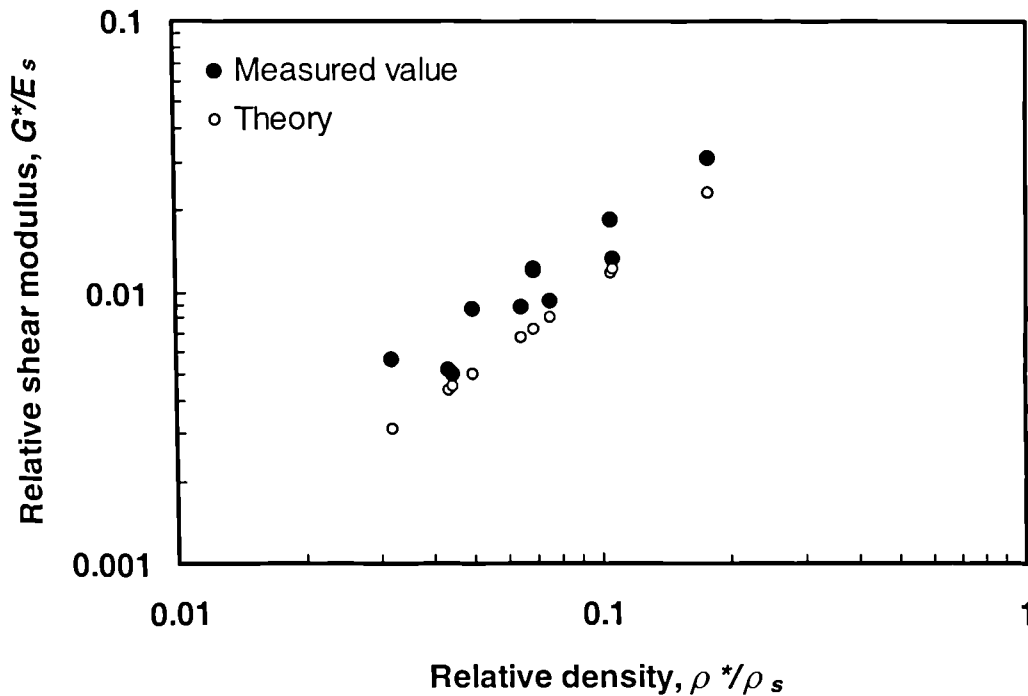


Figure 7.10: Plot of relative shear modulus versus relative density with $\phi = 0.76$

7.1.3 The fracture properties of the foams

Three different families of foam were considered in this research, namely the C70 foams (PVC/PUR), the R63 foams (Linear PVC) and the R82 foams (PEI). Within each group, a range of densities was investigated. For example, the C70 foams offered densities between 40 kgm^{-3} and 200 kgm^{-3} whereas the densities of the R63 foams varied between 50 kgm^{-3} and 140 kgm^{-3} . In the case of R82 foam, two densities were considered, these being 60 kgm^{-3} and 80 kgm^{-3} . Clearly, it is important to establish the effect of varying foam density on the fracture properties of the sandwich core materials. In order to investigate this, the foams were cut into single edge notch bend (SENB) samples with dimensions of $150 \times 30 \times 10 \text{ mm}$ (length, width and thickness) and a 15 mm of pre-crack was introduced as outlined in Chapter 5. The fracture properties of the foams were calculated by determining the work of fracture using Equation 5.13 in Chapter 5.

The application of fracture mechanics principles to foam materials is somewhat different from solid polymers, metals or ceramics, since the foam is discontinuous between the polymer material and the cell gas. The work of fracture was chosen to characterise the properties of the foams rather than G_{Ic} since few foams satisfy the conditions for the successful application of linear elastic fracture mechanics (LEFM) [7-8]. Previous work has shown that the work of fracture can be used to distinguish the fracture properties of a wide range of foam materials [7].

Typical load-displacement curves following tests on the C70, R82 and R63 foams are presented in Figure 7.11. From the figure, it is clear that the C70 foams are the most brittle of the three types of foam and the R63 linear PVC foam is the toughest. The linear PEI R82 foam can be considered as moderate toughness system sitting between the C70 (PVC/PUR) and the R63 (linear PVC) foams. The R63 foams exhibited stable crack propagation with the specimens failing in a ductile manner. In contrast, unstable crack propagation was observed in the C70 foams as revealed by the zig-zag load-displacement curve in Figure 7.11.

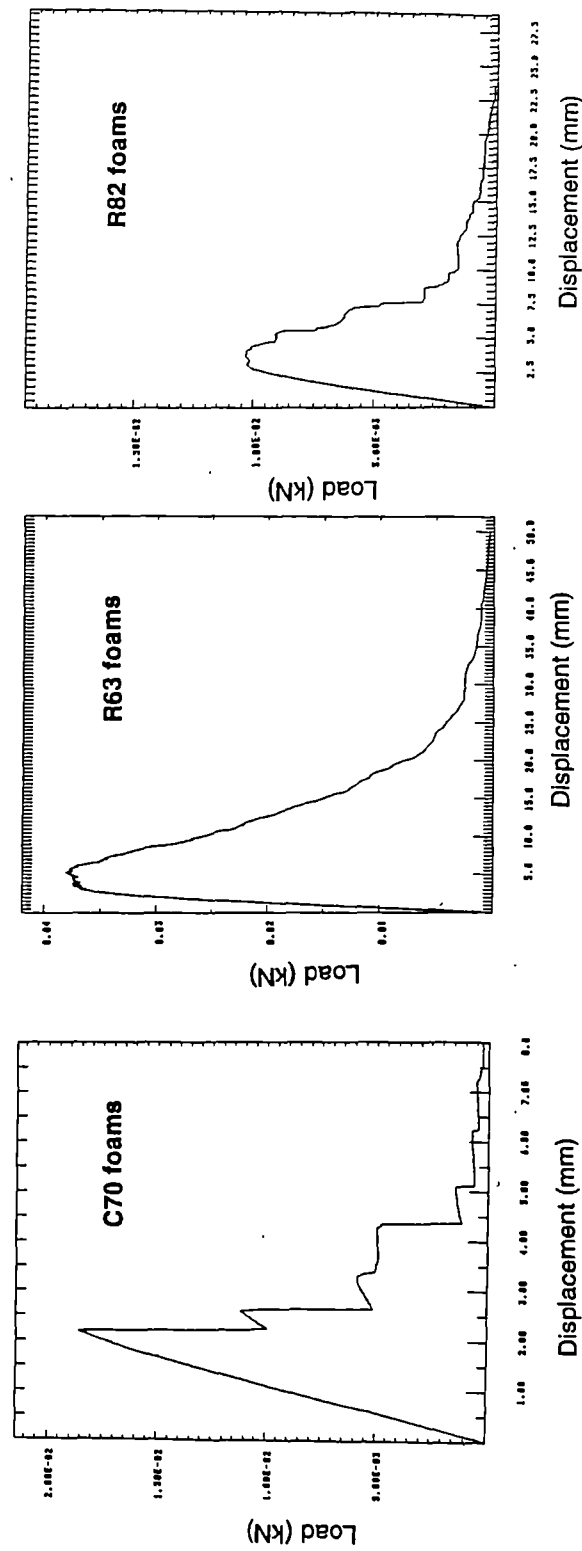


Figure 7.11: Typical load vs displacement plots following SENB tests on the C70, R63 and R82 foams showing the nature of crack propagation behaviour in each of the foams.

These results agree with the work of Cantwell [7] who observed similar types of load-displacement curves following tests on this particular foam. The R63 foams failed in a ductile manner with the crack advancing in a stable mode at a velocity controlled by the crosshead displacement rate of the test machine. This can be seen clearly in Figure 7.11. The R82 exhibits a brittle-ductile failure mode with a smaller zig-zag pattern. Similar forms of load-displacement curves have been reported previously for R82 foams suggesting that the crack had propagated in a series of small steps or jumps [7]. The reason for this mode of failure is not clear, however, it is possible that it is associated with the crack jumping from cell to cell within the ductile PEI foam. For brittle foams such as the C70.75 system, the crack propagates in an unstable manner with several sharp drops in applied load before finally fracturing.

The results of these tests are presented in Figure 7.12 where the work of fracture is plotted against density. The work of fracture of the C70 foams shows a linear dependence on density tending to increase with increasing density. The scatter in the test results was relatively small highlighting the consistency of these foam materials. From these load-displacement curves, the C70 foams, which are based on a PVC/PUR blend, are relatively brittle at all densities suggesting that care should be taken when selecting them for energy-absorbing applications. The data indicate that of the three foams tested, the C70 foams exhibits the lowest values of work of fracture for a given density.

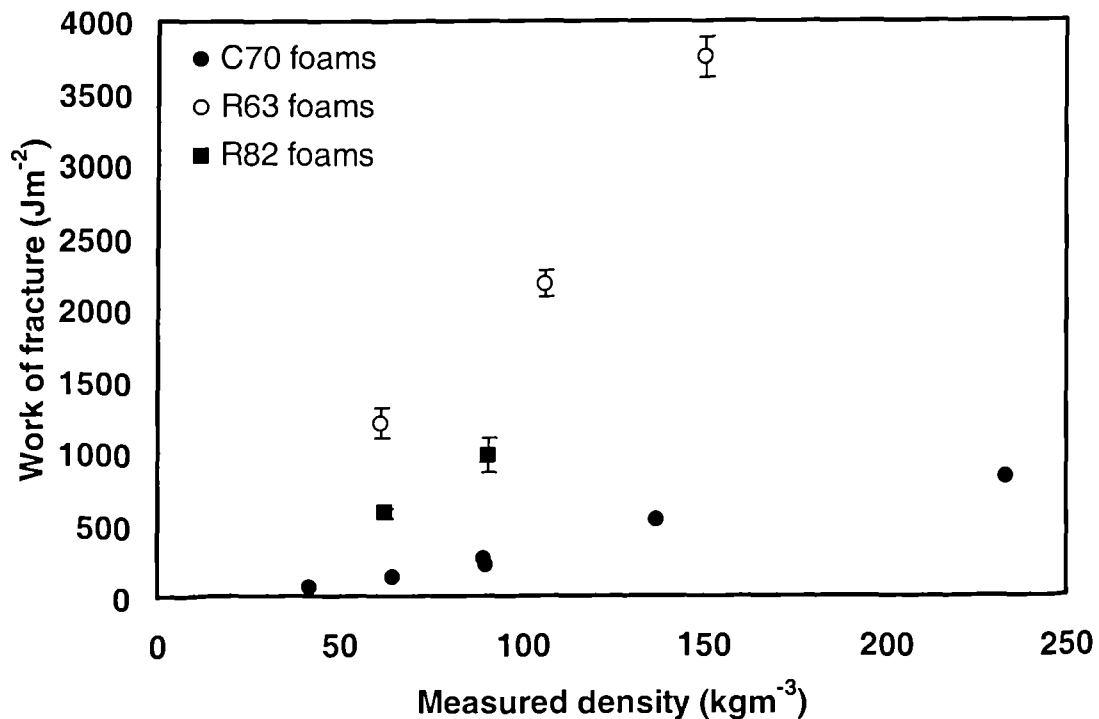


Figure 7.12: The influence of foam density on the work of fracture of the C70, R63 and R82 foams.

As far as the fracture energy is concerned, the R63 foams appear to be the toughest system offering values of work of fracture well above those exhibited by the other two foams. For example, the R63 foam, with a density of 140 kgm^{-3} , exhibited a value of fracture energy of 3744 Jm^{-2} , compared to the C70 foam with a density of 200 kgm^{-3} which offered a value of only 816 Jm^{-2} . These results show that the density of the foam has a significant influence on the fracture properties of the core material. The figure also suggests that the fracture behaviour of the foams is strongly dependent on the type used in its manufacture. The values of the work of fracture obtained here are in line with those reported by Cantwell [7] following single edge notch bend (SENB) tests on various types of foam materials as quoted in Table 7.2.

Foams	Work of fracture (Jm^{-2})	
	Current study	Cantwell [7]
R63.80 (Linear PVC)	2170	2528
R82.80 (PEI)	972	1050
C70.75 (PVC/PUR)	210	185

Table 7.2: Comparison of the measured work of fracture of various foams with published data.

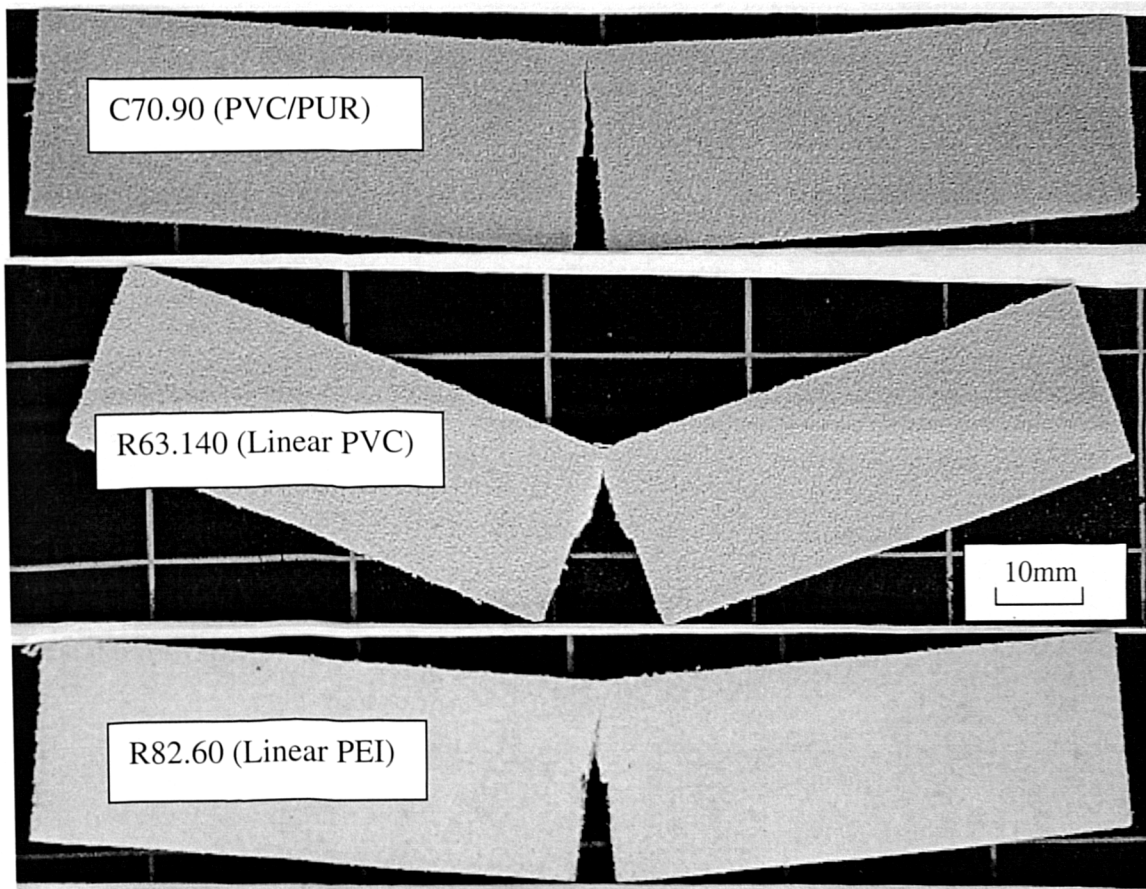


Figure 7.13: Typical failed SENB samples following tests at a crosshead displacement rate of 10 mm/minute.

Figure 7.13 shows typical failed SENB samples from the three families of foam. An examination of the micrographs indicates that the opening of the pre-crack is very small in the C70.90 foam which offered a work of fracture of approximately 250 J/m^2 . The crack opening in the R82.60 which offered a work of fracture of approximately 600 J/m^2 is also quite small. In contrast, the R63.140 which offers an impressive work of fracture of 3700 J/m^2 exhibits significant deformation after fracture.

7.1.4. The effect of loading rate on the indentation properties of the sandwich structures

During impact on a laminated composite beam, indentation effects are frequently small and can often be ignored when predicting the dynamic response of the material. However, in the case of sandwich composite beams, a considerable amount of permanent indentation can occur during the impact event which may absorb an appreciable amount of energy. Therefore, the behaviour of the contact parameters, 'n' and 'C' in the Meyer indentation law ($P = C\alpha^n$) need to be characterised over a range of loading conditions.

During the indentation test, the beams were supported on a solid steel block to eliminate bending in the sandwich beam. The specimens were loaded at crosshead displacement rates of 0.2, 1, 10 and 100 mm/minute. Typical curves of load versus indentation for various foams are presented in Figure 7.14.

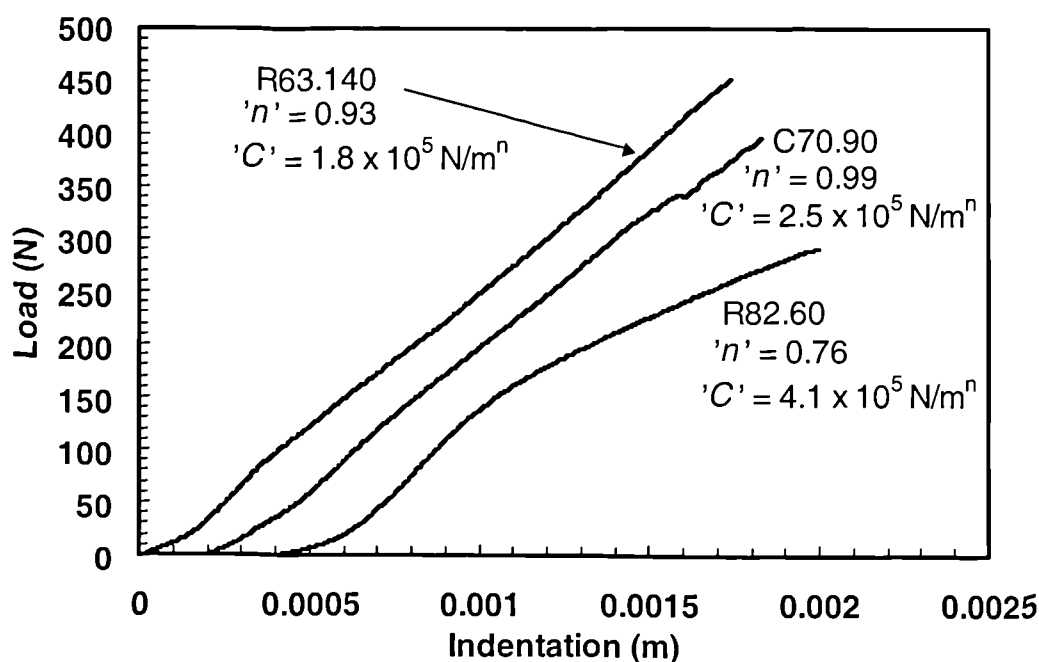


Figure 7.14: Typical load-indentation curves for the R63.140, C70.90 and R82.60 foams at a crosshead displacement rate of 0.1 mm/minute.

As can be seen, the initial parts of the curves in Figure 7.14 are slightly non-linear which may be due to the compliance of the Instron machine. It is also possible that these effects are due to variations in the manufacturing processes which may affect the properties of the materials. From the figure, it is clear that the load-indentation response of the R63.140 and C70.90 foams is quite linear over much of the trace. In contrast, the R82.60 foam exhibits an initial steep rise followed by a lower rate of increase of load with indentation. Here, it proved more difficult to determine values of 'C' and 'n' and the value quoted in the figure corresponds to average values of these parameters over the duration of the test. The change in slope of this foam may be explained by the initiation of local damage such as core crushing under the point of indentation. The same phenomenon was also observed by the Davies *et al.* [9] following static indentation tests on a series of composites and sandwich structures. The values of the parameters 'n' and

'C' were determined by plotting the load-indentation data on a double log plot as shown in Figure 7.15. A curve fit was then applied to the data to yield the constants.

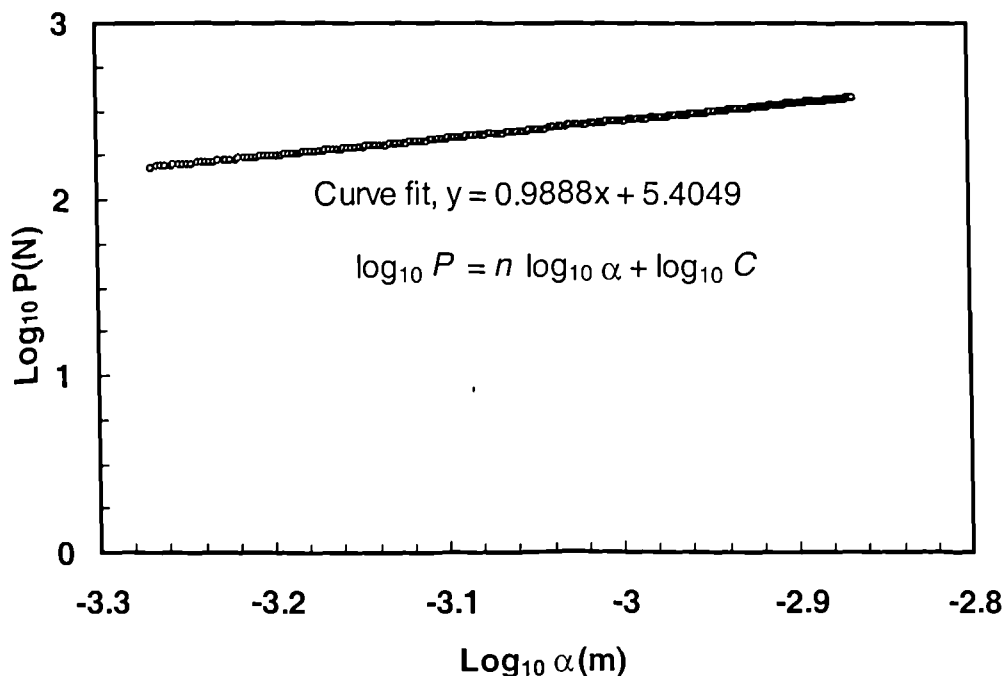


Figure 7.15: A logarithmic plot of force against indentation for the C70.90 foam at 0.2 mm/minute showing the curve fitting method for determining the indentation parameters 'n' and 'C' used in Meyer's law.

The value of the contact parameters 'n' and 'C' in the Meyer Law dictate the shape and slope of the load versus indentation curve [10]. The schematic diagram presented in Figure 7.16 shows how these parameters affect the shape and gradient of the curves. Clearly, the load-indentation curve will be a straight line when the value of the parameter 'n' is equal to one. For values of 'n' which are greater than one, the curve will tend to move upwards as shown in Figure 7.16a. In the case where the parameter 'n' is less than one, the slope of the curve tends to decrease with increasing indentation. Similarly, the value of the parameter 'C' influences the effective slope of the indentation plot as shown for the case where 'n' is equal to unity in Figure 7.16b. Typical load-indentation curves for the C70.90 foam recorded at four different loading rates are presented in Figure 7.17.

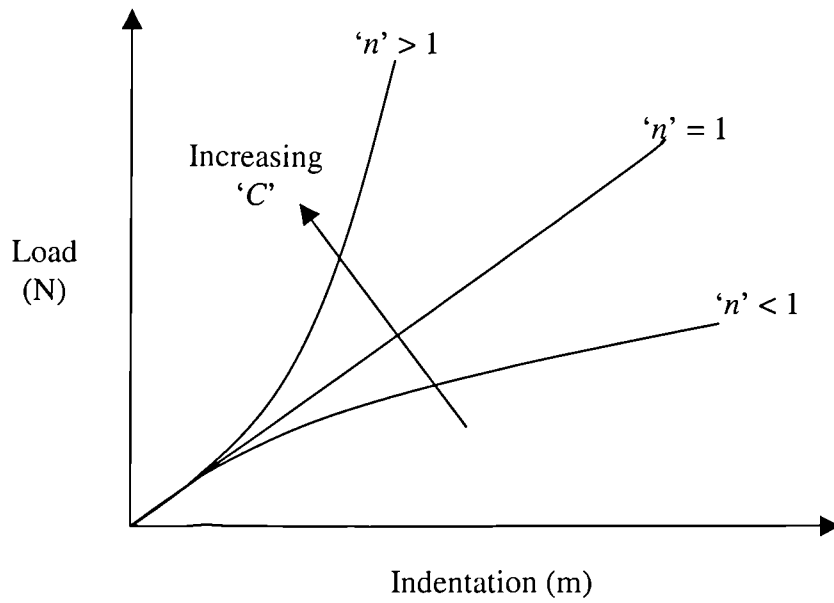


Figure 7.16a: Schematic diagram showing the effect of varying the parameter ' n ' and ' C ' on the load-indentation curve of sandwich structure.

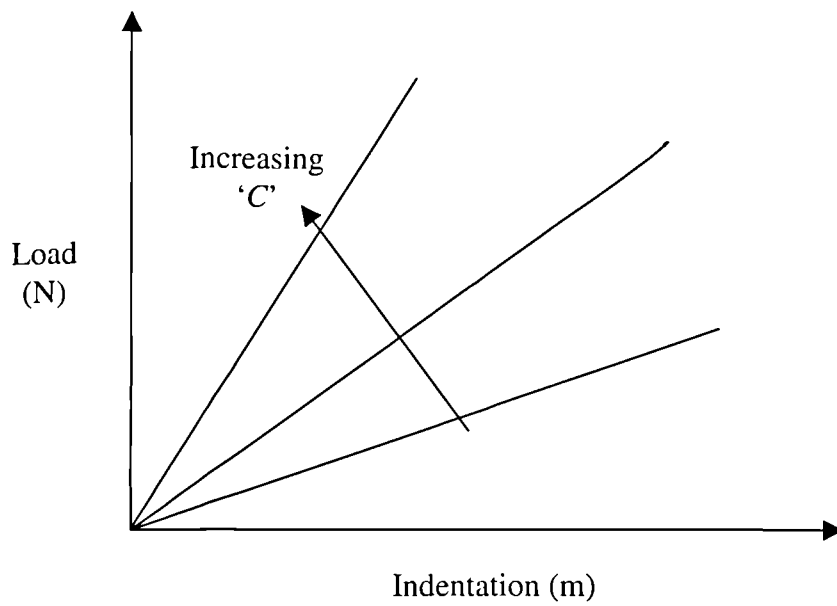


Figure 7.16b: Schematic diagram showing the effect of varying the parameters ' C ' on the load-indentation curve of sandwich structure. For simplicity, ' n ' is assumed to be equal to unity.

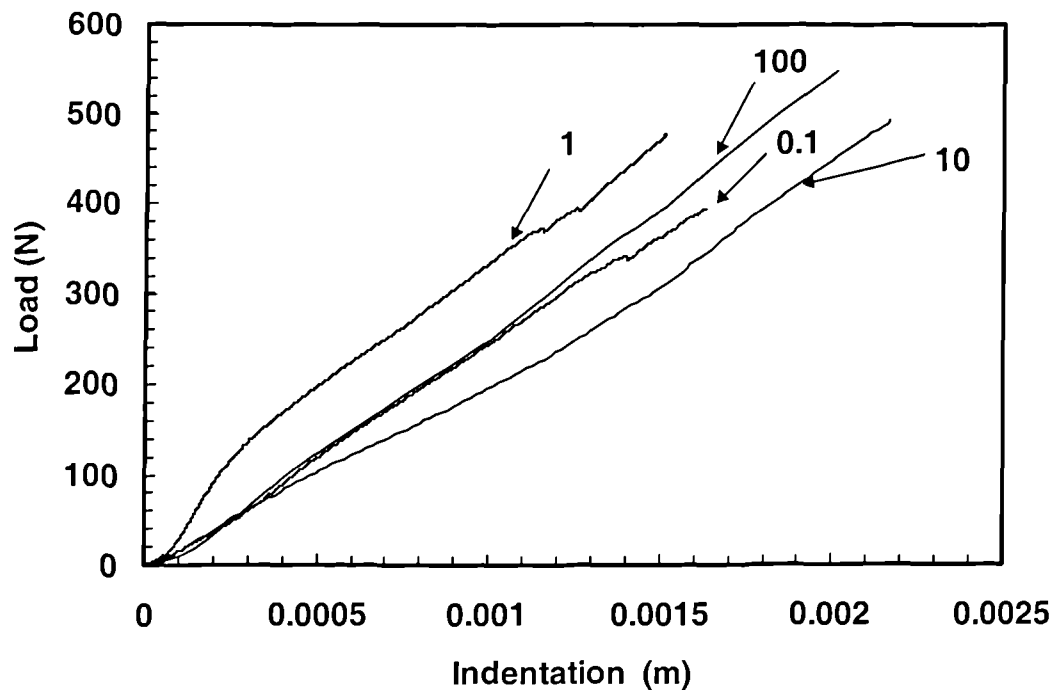


Figure 7.17: Load-indentation curves for the C70.90 foam measured at crosshead displacement rates between 0.1 and 100 mm/minute.

Generally, the initial part of the load-indentation curve shows some non-linearity as a result of the aforementioned machine compliance during the initial phase of the test even though attempts had been made to minimise this. The curve then exhibited a linear region with a constant slope. The change in slope observed at forces between 300 and 400 Newtons was a result of crushing within the core under the point of impact. From the figure, there is no clear rate effect over the range of crosshead displacement rates considered here even though some degree of scatter in the results can be seen. The variation of the parameter ' n ' with loading rate is presented in Figures 7.18 to 7.21. From the C70 foam data in Figures 7.18 and 7.19, it is clear that the average value of ' n ' varies between approximately 0.74 and 1.21 over the range of densities considered. However, the influence of density on the value of ' n ' is not clear. For example, in the case of C70.200 and C70.55 foams, with densities of 200 kgm^{-3} and 55 kgm^{-3} respectively, the average value of parameter ' n ' measured over four different loading

rates appears to be the same, approximately 1.09. In the case of the R63 foams, Figure 7.20, the results are similar to the C70 foams with the average values of ' n ' varying between 0.80 and 1.03 over the range of densities considered. Similarly, the results for the R82 foams, Figure 7.21, indicate that the values of ' n ' are lie between 0.71 and 0.95 for the two systems. The values of ' n ' in Figures 7.18 and 7.19 agree with values quoted in the published literature [10-11]. However, since little work has been published on the systems considered here, direct comparisons are impossible. It is also clear that the values of ' n ' measured here fall well below the value of 1.5 predicted by a Hertzian contact law. This difference is likely to be due to the fact that these sandwich structures are based on cellular materials which fail due to cell buckling and offer a lower resistance to indentation loading than an isotropic solid.

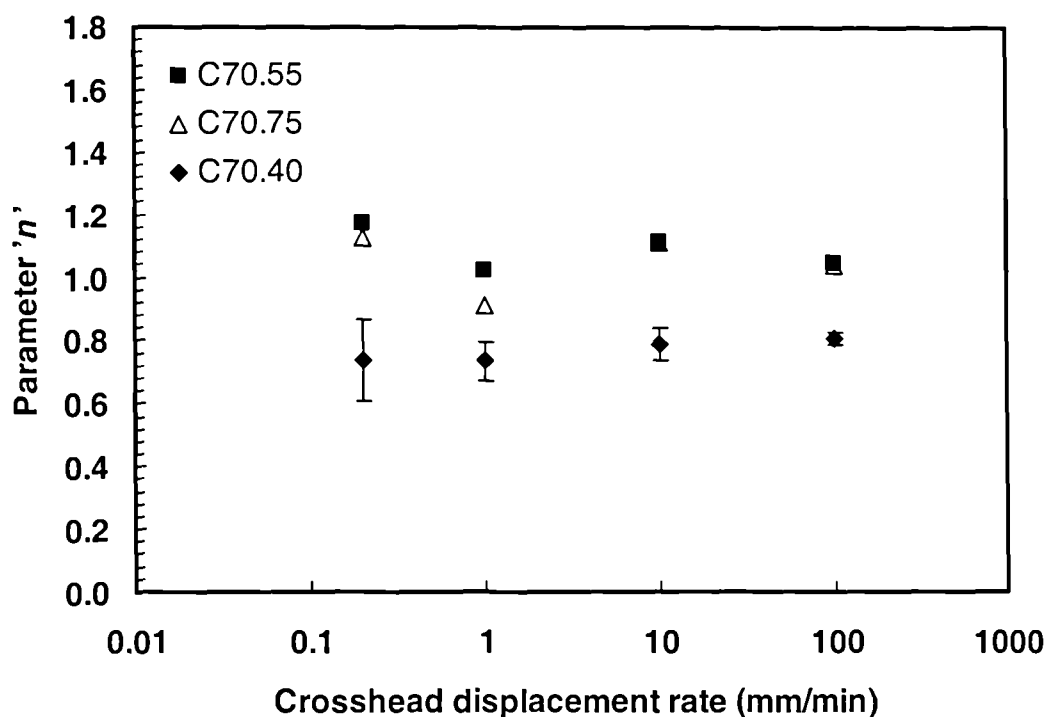


Figure 7.18: The variation of the contact parameter ' n ' with crosshead displacement rate for the C70 foams.

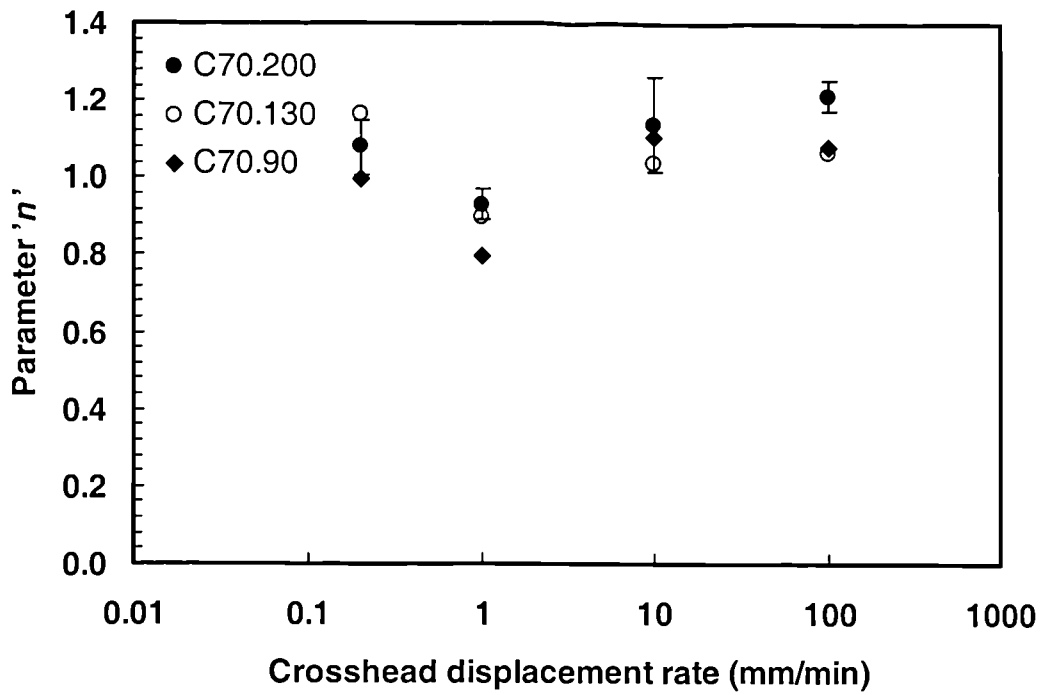


Figure 7.19: The variation of the contact parameter 'n' with crosshead displacement rate for the C70 foams.

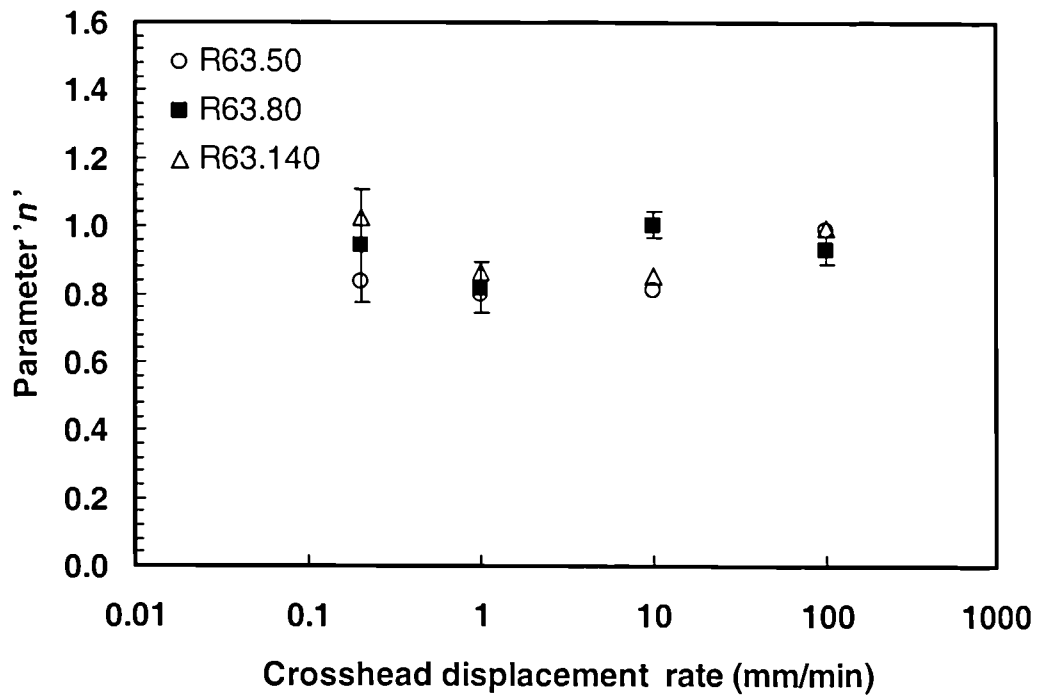


Figure 7.20: The variation of the contact parameter 'n' with crosshead displacement rate for the R63 foams.

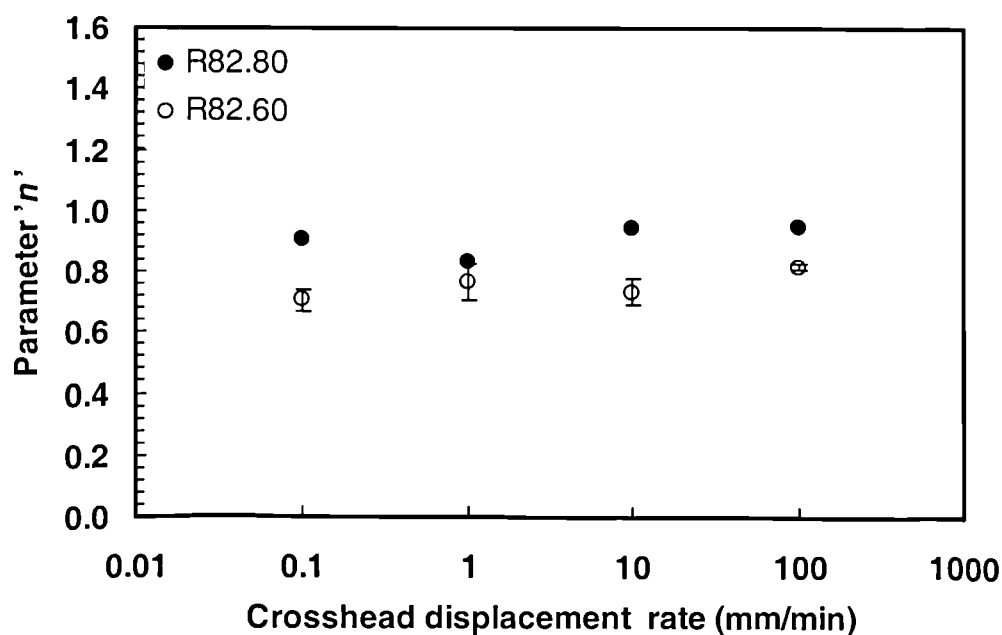


Figure 7.21: The variation of the contact parameter 'n' with crosshead displacement rate for the R82 foams.

Similar results are observed when the parameter 'C' is plotted against the crosshead displacement rate for the three groups of foam as presented in Figures 7.22 to 7.24. As far as the C70 (PVC/PUR) foams are concerned, Figure 7.22, the average value of 'C' determined over four different loading rates varies between $0.25 \times 10^6 \text{ N/m}^{0.99}$ and $0.94 \times 10^6 \text{ N/m}^{1.09}$ with the C70.200 and C70.90 foams offering the highest and the lowest values within the group. Small variations can be seen in the value of parameter 'C' which is slightly higher at a crosshead displacement rate of 1 mm/minute in all foams. The reasons for this are not clear, but it is believed to be a consequence of differences in the test regime (i.e. specimen alignment etc) at 1 mm/minute rather than real effects in the indentation response. Some of the error bars in Figure 7.22 have been removed for reasons of clarity. For the R63 (linear PVC) foams, Figure 7.23, the average value of the parameter 'C' determined over the four loading rates vary between $0.05 \times 10^6 \text{ N/m}^{0.86}$ and $0.18 \times 10^6 \text{ N/m}^{0.93}$. These values are slightly lower than the values obtained in the C70 foams. On the other hand, for the R82 (linear PEI) foams, Figure 7.24, the value of

the parameter 'C' lies in a range between $0.14 \times 10^6 \text{ N/m}^{0.91}$ and $0.41 \times 10^5 \text{ N/m}^{0.76}$. It is also apparent that the value of 'C' for the R82.80 foam increases slightly with increasing crosshead displacement rate. This suggests a slightly rate-dependent response. The data in these figures show that the value of 'C' tends to increase with density. This is perhaps to be expected since increasing the density increases the stiffness of the polymer and therefore the effective slope of load vs. indentation curve.

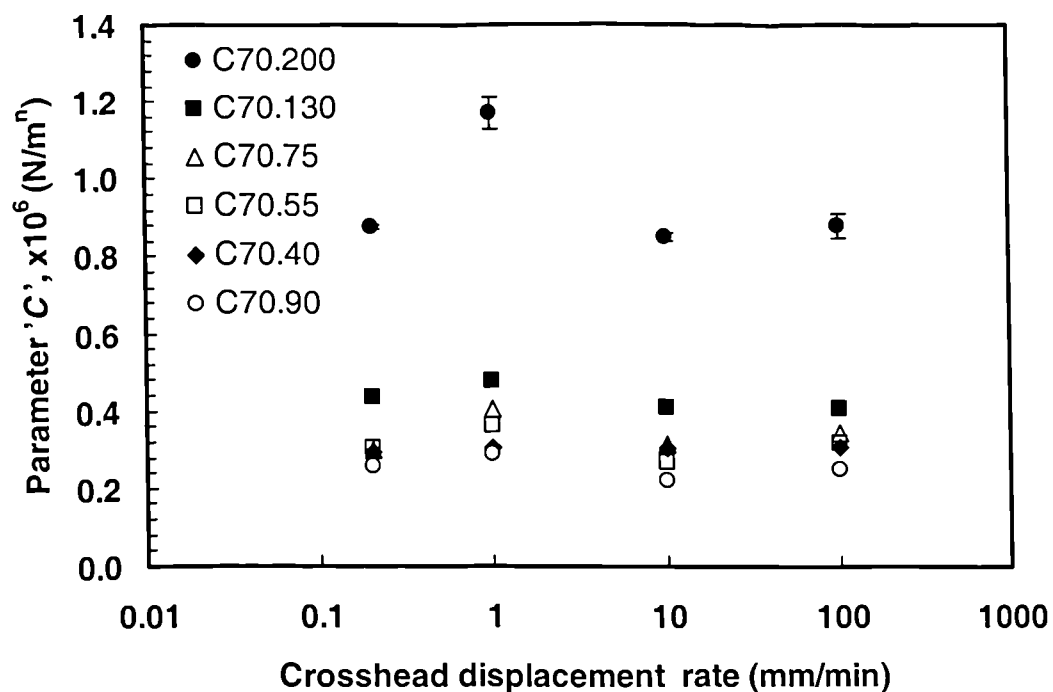


Figure 7.22: The variation of the contact parameter 'C' with crosshead displacement rate for the C70 foams.

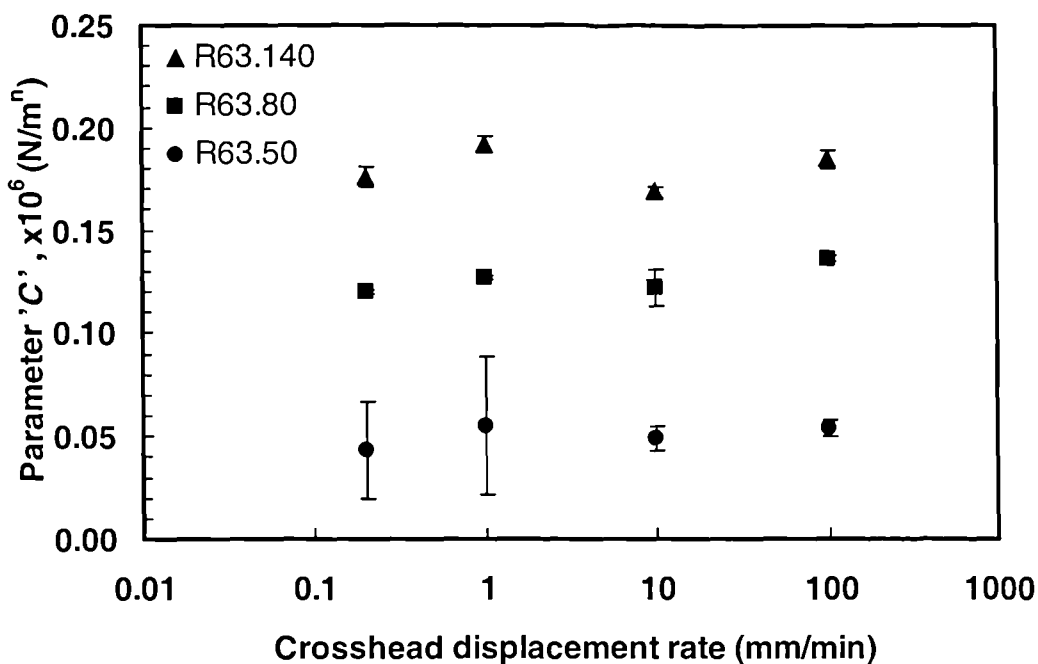


Figure 7.23: The variation of the contact parameter 'C' with crosshead displacement rate for the R63 foams.

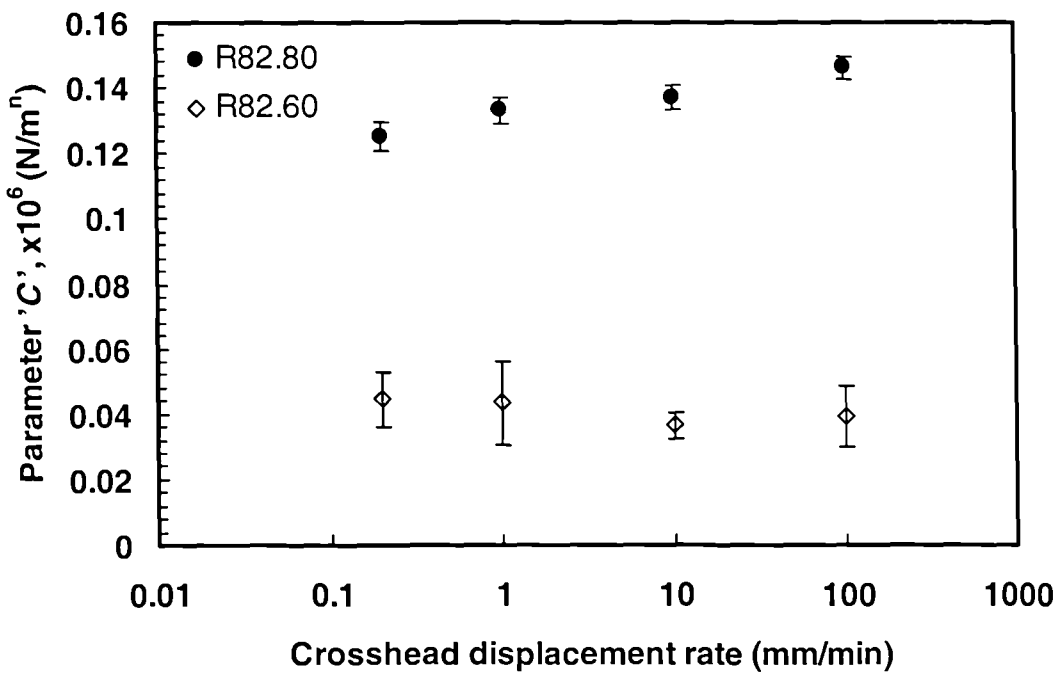


Figure 7.24: The variation of the contact parameter 'C' with crosshead displacement rate for the R82 foams.

All of the foams, with the exception of the R82.80 system, show a rate-independent response over the range of crosshead displacement rates considered. This evidence suggests that in most cases the crosshead displacement rate does not influence the values of the contact parameters, ' n ' and ' C ', in the foam systems examined in this study. The reason for rate-sensitivity of the PEI-based system is not clear.

The indentation tests were repeated on the aluminium honeycomb sandwich structures. In this case, the value of ' n ' also remains constant over the range of loading rates considered and the scatter is relatively small as shown in Figure 7.25. It is interesting to note that the value of ' n ' is significantly greater than the value determined on the polymeric foams and is closer to the ideal value of 1.5. This reflects the elastic response of the aluminium foil used in the manufacture of the honeycomb core.

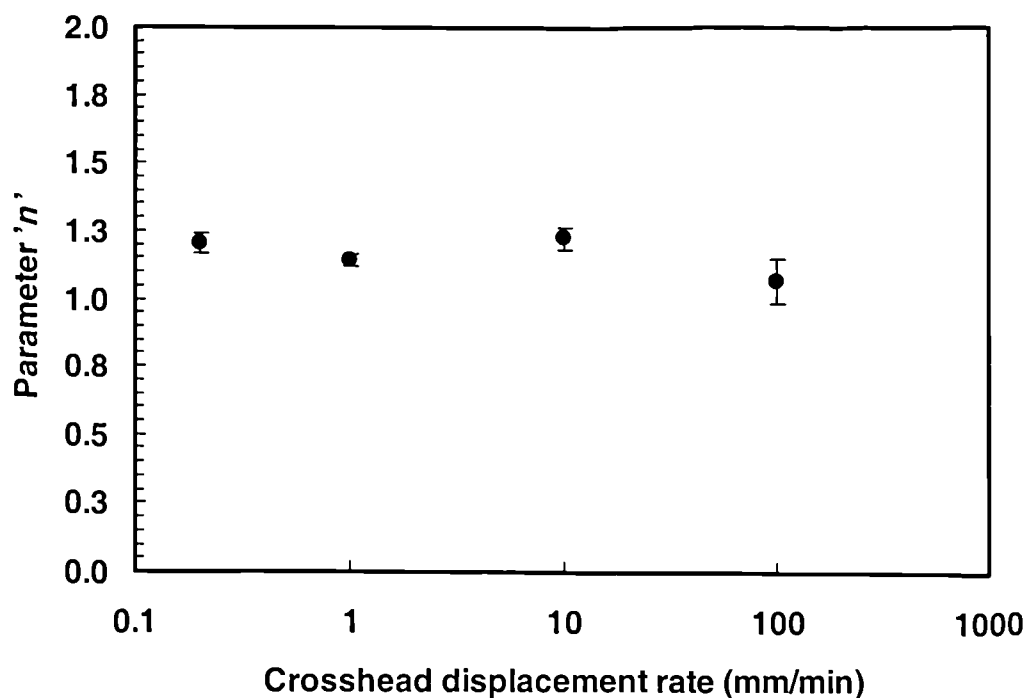


Figure 7.25: The effect of crosshead displacement rate on the contact parameter ' n ' for the aluminium honeycomb core sandwich beam

When the value of ' C ' is considered, the aluminium honeycomb exhibits a relatively large amount of scatter as shown in Figure 7.26. This may be due to the fact that the cell

structure is large with respect to the size of the indenter. Here, indentation at the centre of the cell may yield a different response to that at the edge of the cell directly over a cell wall. It is also interesting to note that the value of 'C' is also much greater than those values measured on the foams. The higher value reflects the stiffer nature of the honeycomb structure.

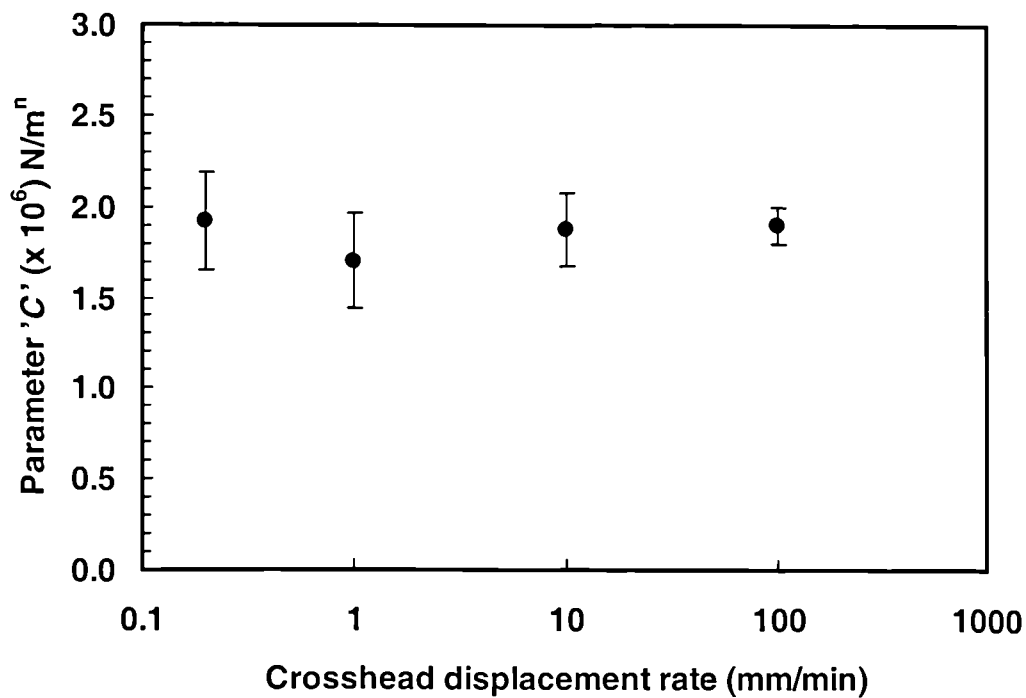


Figure 7.26: The effect of crosshead displacement rate on the contact parameter 'C' for the aluminium honeycomb core sandwich beam

The investigation of the contact behaviour of the foam-core sandwich structures was extended by studying the effect of foam density on the values of 'n' and 'C' at a crosshead displacement rate of 1mm/minute. These results are shown in Figures 7.27 and 7.28. From Figure 7.27, it is clear that the value of the parameter 'n' in Meyer contact law does not depend on the density of the foam material. The average value determined over four different loading rates remains in the range of 0.72 to 1.08 over the range of densities considered. On the other hand, the values of the parameter 'C' in the Meyer contact law, Figure 7.28, shows a slight dependency on foam density.

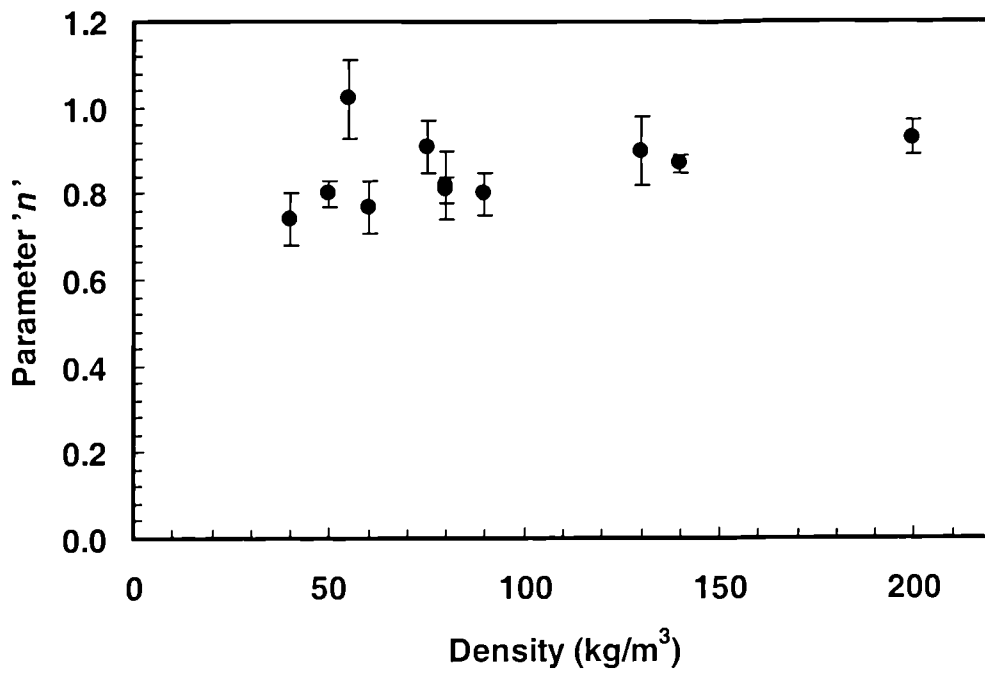


Figure 7.27: The variation of the contact parameter, 'n' with foam density.

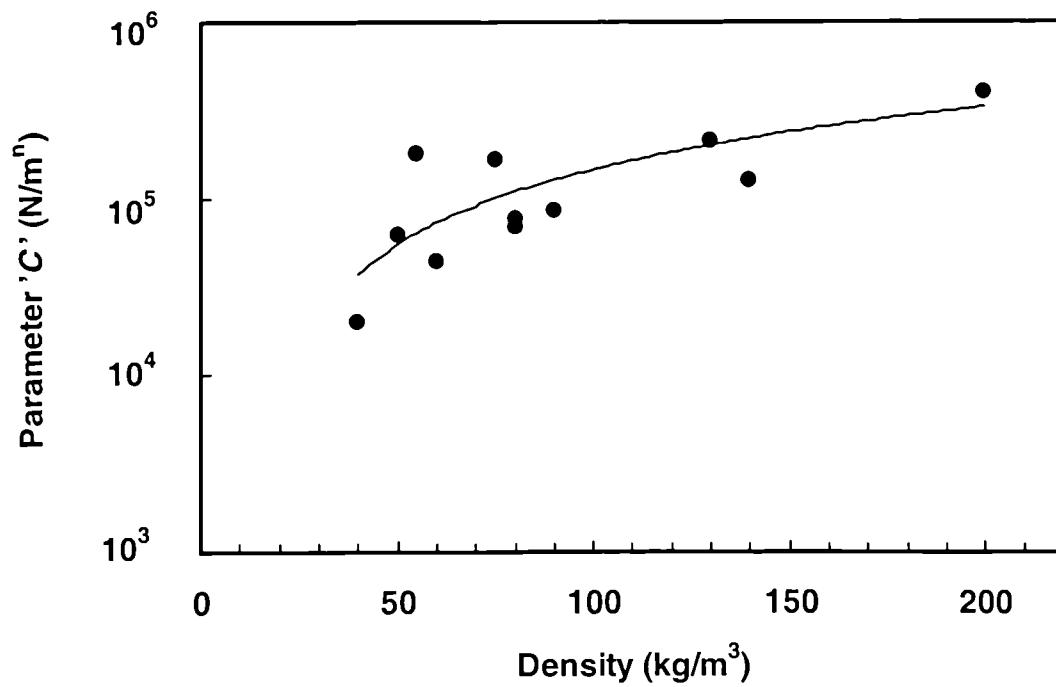


Figure 7.28: The variation of the contact parameter, 'C' with foam density.

Finally, the contact parameters obtained from this study are compared with data from the literature in Table 7.3. From the data, it is clear that the values of the contact parameters determined here are in line with the limited amount of previously determined data.

	Present study	Present study	Present study	Reference [10]
Foam core material	C70.90 (PVC/PUR) foam	R82.60 (Linear PEI) foam	R63.140 (Linear PVC) foam	Polyurethane foam
Skin material	GFR/epoxy	GFR/epoxy	GFR/epoxy	Carbon/epoxy
Core density (kg/m ³)	89.9	62.5	150.2	170.6
Shear modulus of core (MPa)	36.2	15.0	39.9	32
Indenter shape and size	Hemispherical 10mm diameter	Hemispherical 10mm diameter	Hemispherical 10mm diameter	n/a
Parameter 'C' (N/m ⁿ)	2.5 x 10 ⁵	4.1 x 10 ⁵	1.8 x 10 ⁵	1.385 x 10 ⁵
Parameter 'n'	0.99	0.76	0.93	0.8
Crosshead displacement rate (mm/minute)	0.1	0.1	0.1	n/a
Core thickness (mm)	10	10	10	12.7
Skin thickness (mm)	0.5	0.5	0.5	n/a

Table 7.3 Comparison of contact stiffness parameters measured in this study with data reported in the literature.

7.1.5 The influence of loading rate on the mechanical properties of aluminium-core sandwich materials

A series of tests were conducted to determine the shear modulus of the aluminium honeycomb core sandwich structure as outlined in Section 5.3.1. These tests were conducted in order to determine the value of the shear modulus of the core material for

use in the energy-balance impact model. These properties can be obtained by conducting a series of three-point bend tests at different spans. Here, three-point bend tests were carried out on sandwich beams supported over spans of 150, 200, 250 and 300 mm. These specimens were loaded at crosshead displacement rates of 1, 10 and 100 mm/minute. A typical example of a curve of δ/PL vs. L^2 is presented in Figure 7.29.

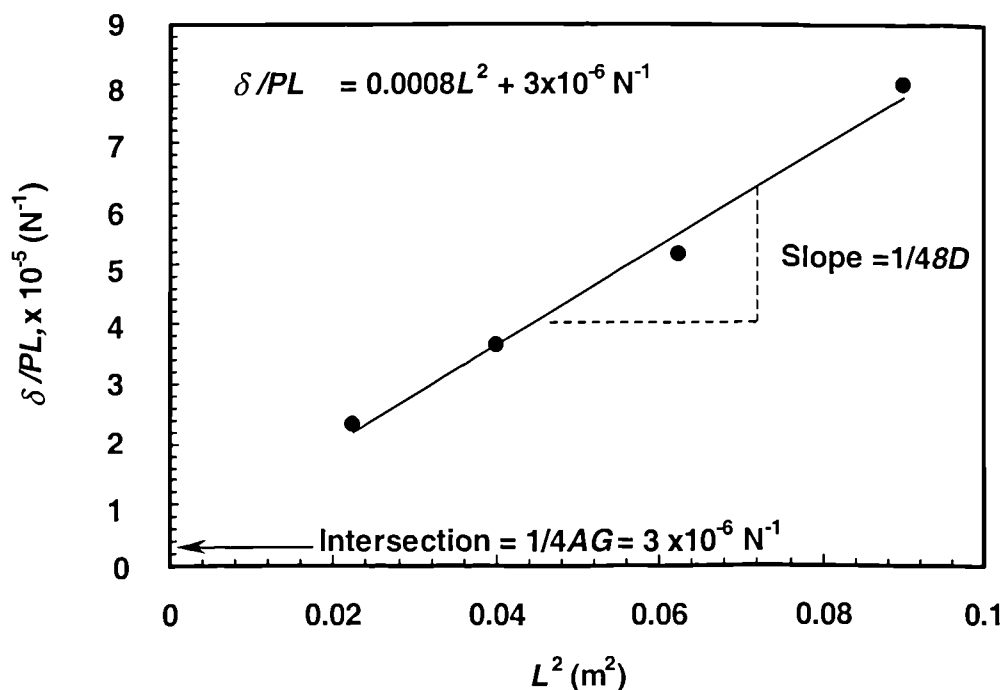


Figure 7.29: Determination of the shear modulus, G and bending stiffness, D for the aluminium honeycomb beams using the method described in Section 5.3.1.

The slope and intersection of the curve was determined by putting a least squares fit through the data. The intersection of this curve with the y-axis ($1/4AG$) was then used to determine the shear modulus. The variation of the shear modulus with crosshead displacement rate is presented in Figure 7.30. From the figure, it is clear that the value of shear modulus remains the same over all loading rates. The shear modulus of this aluminium honeycomb is clearly higher than all of the foam core materials in Table 7.1

reflecting the superior properties of this metallic system. The elastic modulus of the skin material, E_f , remains constant over the range of loading rates considered as shown in Figure 7.31. These observations agree with the earlier findings in Figure 7.2 where the glass fibre/epoxy skin materials were found to be rate insensitive. In conclusion, the results of the tests to characterise the shear and flexural modulus suggest that the statically-determined value can be used in modelling the impact response of these materials. Similar results were also reported by Mines *et al.* [12,13] following tests on panels based on Aeroweb 3003 panel.

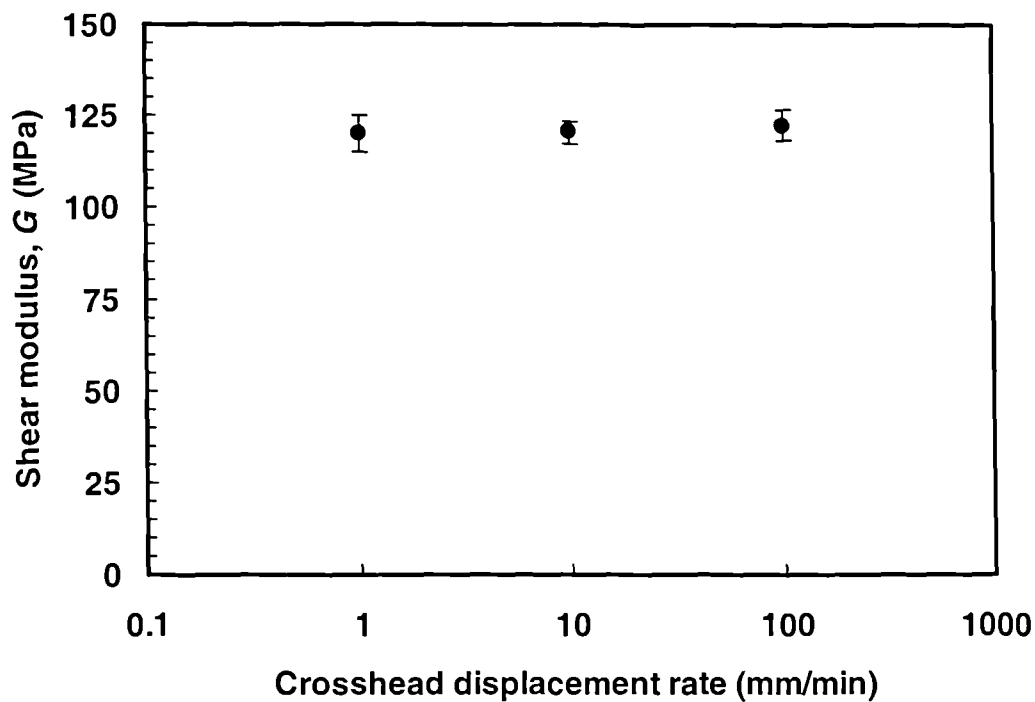


Figure 7.30: The variation of shear modulus of the aluminium honeycomb core with crosshead displacement rate.

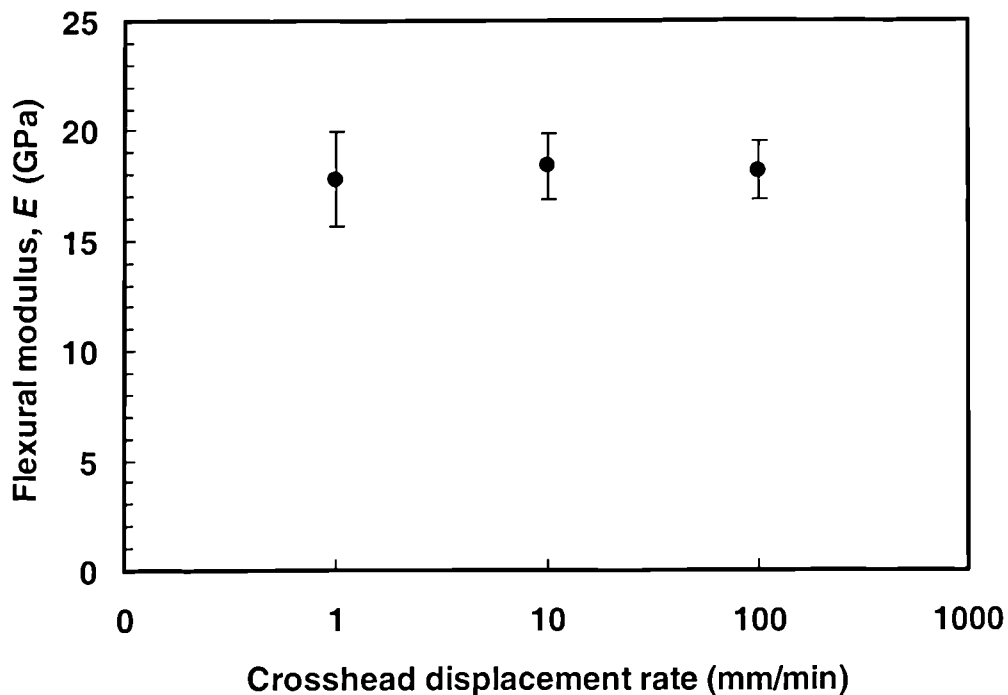


Figure 7.31: The variation of flexural modulus of the skin of the aluminium honeycomb sandwich structure with crosshead displacement rate.

7.1.6 Characterisation of the skin-core interfacial fracture properties

Centre notch flexure tests were conducted on the foam-core sandwich beams in order to evaluate the level of adhesion between the epoxy skins and the foam cores. The work of fracture was determined by dividing the energy dissipated during the test by the resulting fracture surface area. Details of the calculation procedure are given in Section 5.7. The results of these tests are presented in Figure 7.32. As before, the error bars indicate the standard deviation in the experimental data. From the figure, it is clear that C70.200 foam offers the highest work of fracture, highlighting the high level of adhesion between the skin and core materials. The lowest level of adhesion was recorded in the C70.40 foam.

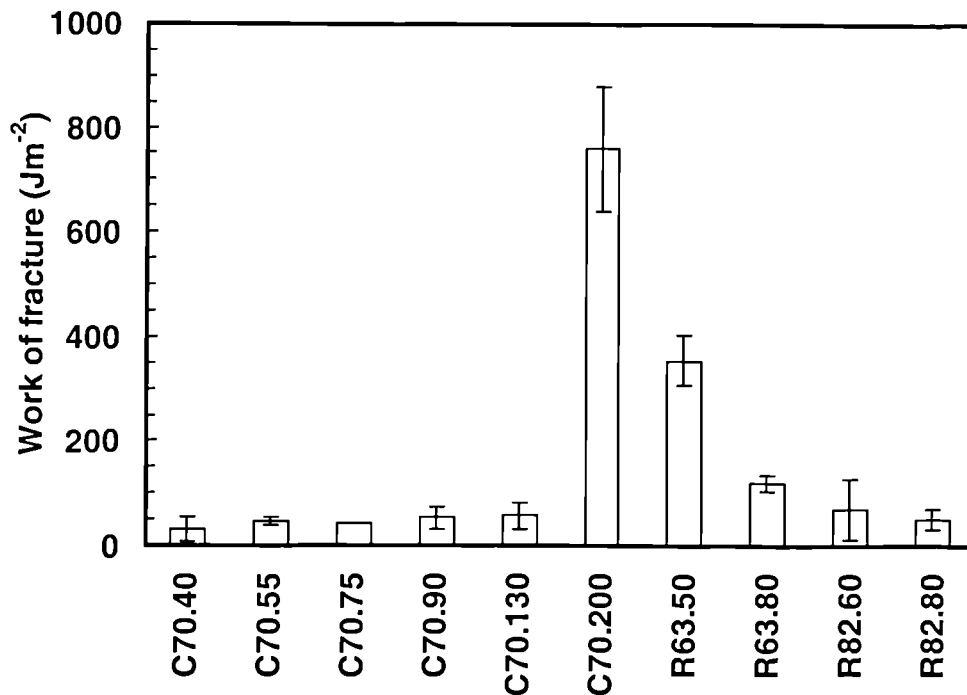
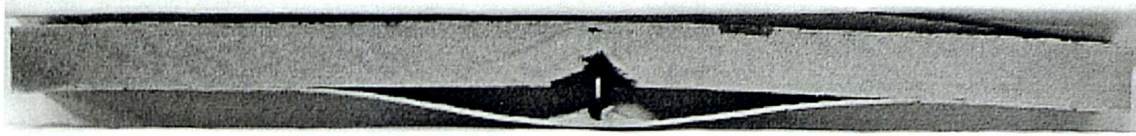


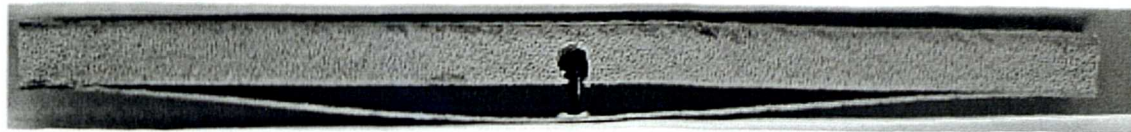
Figure 7.32: The work of fracture of the skin-core interface in the foam-core materials.

Such differences in the level of adhesion observed between the foams may be due to the fact that low density systems tend to absorb the adhesive when it is applied prior to bonding the skins. As a result, the adhesive tends to flow into the porous structure of the foam leaving little resin for bonding the skins. In contrast, in the higher density foams such as the C70.200 system, the adhesive remains close to the interfacial region yielding a high level of adhesion between the skin and core materials. The crack propagated in a stable manner in the R62 and R82 systems whereas crack propagation tended to be unstable in the low density C70 foams. In the case of stable crack propagation systems, the crack advanced along the interface at a velocity determined by the crosshead displacement rate. From visual observations, failure in the C70.40 and the C70.55 foam sandwich structures was due to adhesive failure between the skin and core materials, as shown by the photographs in Figure 7.33. The level of adhesion between the skin and core materials in the sandwich structure serves a vital function, that is to resist shear forces during impact loading and maintain the structural integrity of sandwich during a

variety of loading conditions. It is anticipated that the high levels of adhesion in the C70.200 foam will help the sandwich absorb a significant amount of energy during impact loading.



C70.90 (PVC/PUR)



R63.140 (Linear PVC)



R82.60 (Linear PEI)

Figure 7.33: Typical examples of failed centre notch flexure test (CNF) specimens showing skin-core debonding. The test was used to evaluate the degree of interfacial adhesion between the skin-and core materials.

7.1.7 Compression properties of the foam core materials

The compressive collapse stress of a crushable foam is an important parameter for design purposes in energy-absorbing and structural impact on sandwich constructions. This is due to the fact that the core materials absorb a significant amount of energy under impact loading and tend to fail in compression and shear. Therefore, a series of compression tests were conducted on the eleven types of foams considered in this research study. Initially, the rate sensitivity of the foams under compression was

assessed. Typical stress-strain curves of three different types of foams investigated are presented in Figure 7.34.

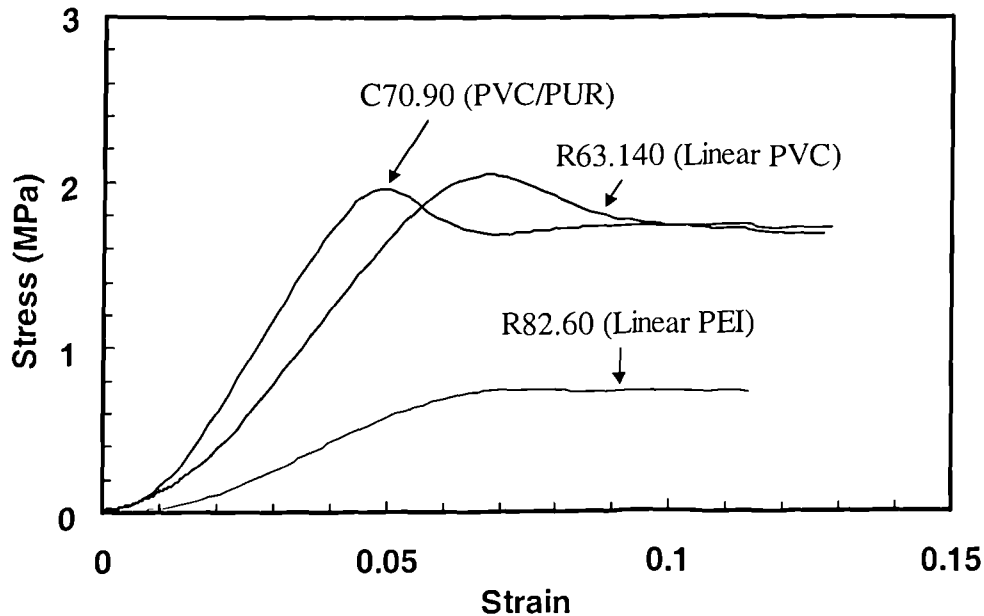


Figure 7.34: Typical examples of stress versus strain curves following compression tests on three different types of foam at a crosshead displacement rate of 1 mm/minute.

As far as the three groups of foam are concerned, the shapes of the compression stress-strain curves were reasonably similar except that the slope of the curves which reflects the compression modulus of the foams, varies from one system to another. From Figure 7.34, it is clear that the stress in the C70.90 and the R63.140 dropped shortly after peak load suggesting some form of instability. In contrast, the stress in the R82.60 plateaued once the maximum value was reached. In order to investigate the strain rate sensitivity of the foam material under compressive loading, a series of compression tests were carried out at crosshead displacement rates up to 10 mm/minute. Typical examples of compression stress-strain curves for the C70.90 foams determined at three different loading rates are presented in Figure 7.35. It should be noted that the tests at 0.2 and 10

mm/minute were stopped immediately after the drop in load whereas the 1 mm/minute test was continued to higher strains.

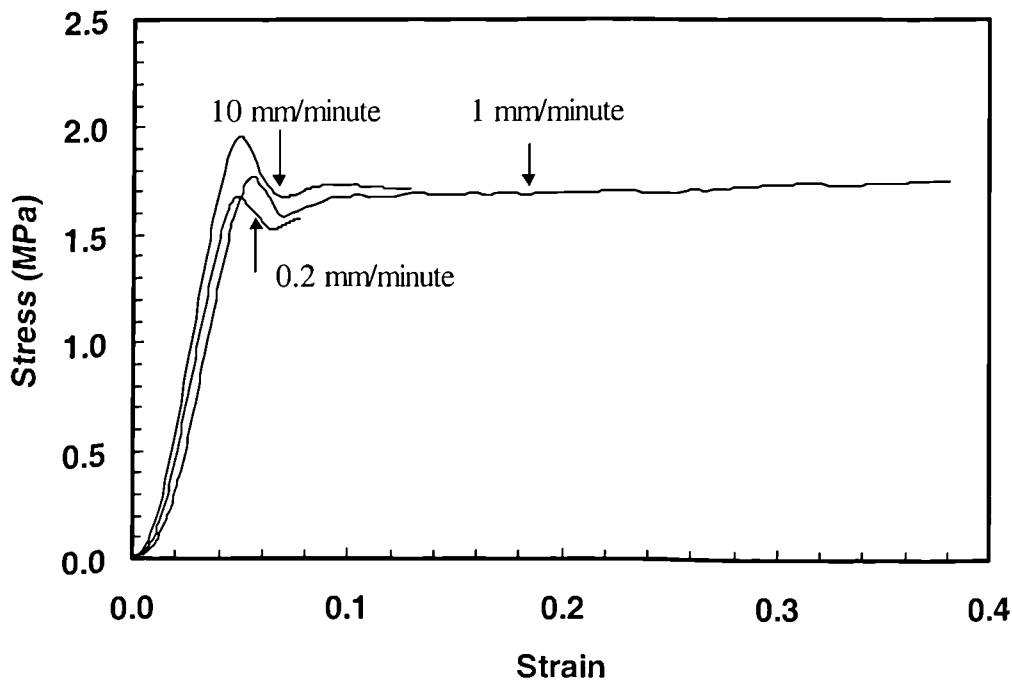


Figure 7.35: Typical compression stress-strain curve for the C70.90 (PVC/PUR) foam showing the effect of crosshead displacement rate.

Generally, the initial part of the stress-strain curve shows some non-linearity as a result of the machine compliance at the start of the test. All of the curves then exhibit a linear region offering a constant slope before reaching the yield point. It is clear that the crosshead displacement rate influences the yield stress of this foam with higher crosshead displacement rates yielding the higher values of yield stress. Beyond the yield point, a sharp drop in stress is apparent suggesting that the foam has undergone plastic deformation and possibly crushing. Indeed, severe crushing in the foams can be seen in Figure 7.36.

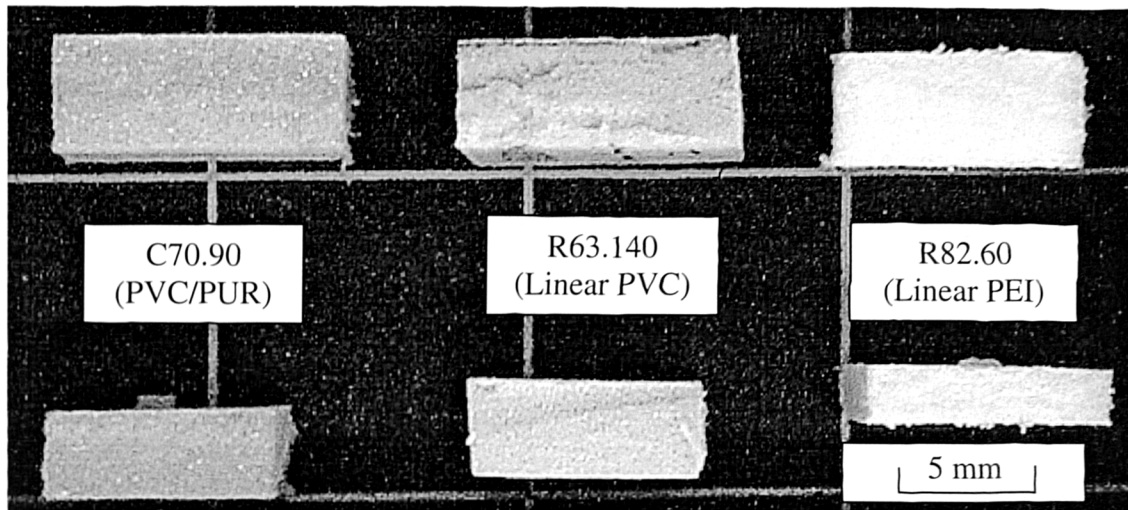


Figure 7.36: Typical examples of specimens before (top micrographs) and after compression testing (lower micrographs).

Similar non-linearity in the compression curves of foam core materials has also been reported by Gilchrist and Mills [14]. In order to illustrate the effect of loading rate, the compression strength of all eleven foams were plotted over three different loading rates. The results obtained for all eleven foams are summarised in Figures 7.37 to 7.39.

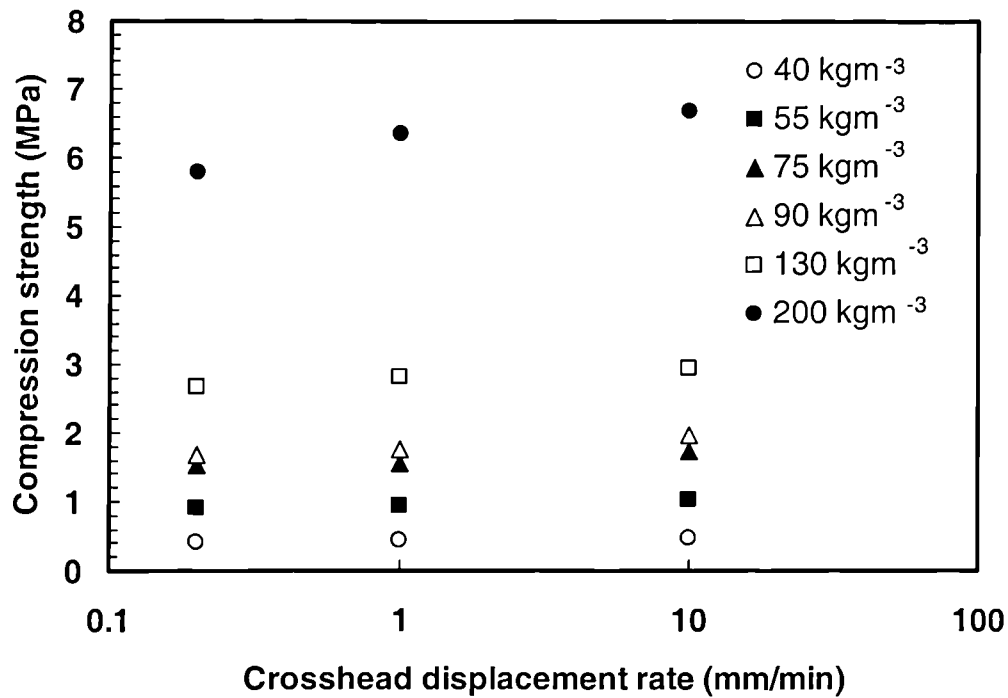


Figure 7.37: The variation of compression strength with crosshead displacement rate of the C70 (PVC/PUR) foams.

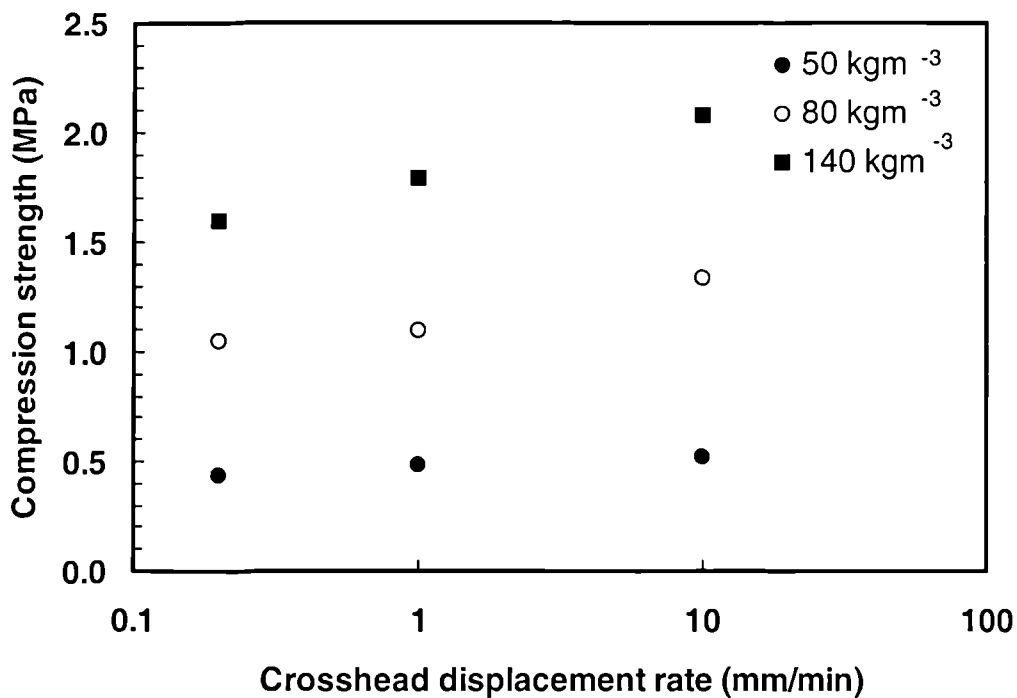


Figure 7.38: The variation of compression strength with crosshead displacement rate of the R63 (Linear PVC) foams.

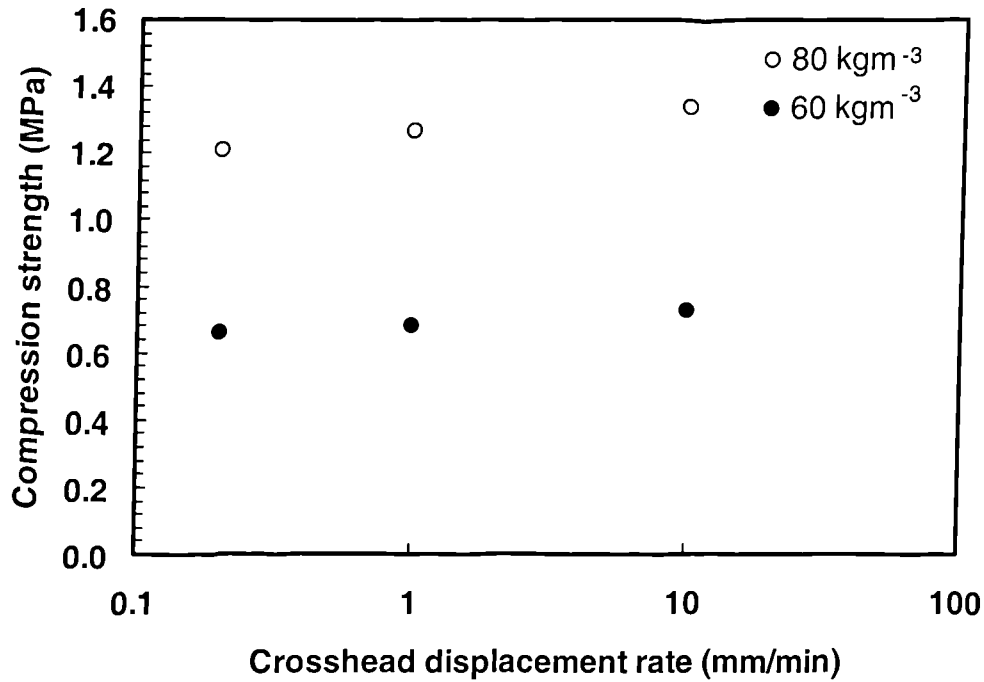


Figure 7.39: The variation of compression strength with crosshead displacement rates of the R82 (Linear PEI) foams

In general, all of the foams tested in this study exhibited a similar compression stress-strain curve. From these figures, it is quite clear that the compressive strength depends on the crosshead displacement rate. This phenomenon is slightly more pronounced in foams with a higher density. For example, rate effects are clear in C70.200 foam whereas such effects are much less obvious in the low density C70.40 foam. A similar pronounced rate-dependent behaviour is observed in the R63 foam with a density of 140 kgm^{-3} in Figure 7.38. These results agree with those reported by Li *et al.* [4] who concluded that rate sensitive effects may be due to a strain-hardening behaviour when the foam is crushed. Miltz and Ramon [15] also found that the compression properties of polymeric foam materials are affected by loading rate. The compression strength of all eleven polymers was plotted as a function of density and the strength was found to increase with increasing foam density as shown in Figure 7.40. Here, the data appear to fall on three unique curves. This evidence suggests that the compressive strength of a polymeric foam depends largely upon its density. Clearly, the density influences the size

of the cells in the polymeric foam. Increasing the density will result in a decrease in the cell size and increase in the cell resistance to buckling.

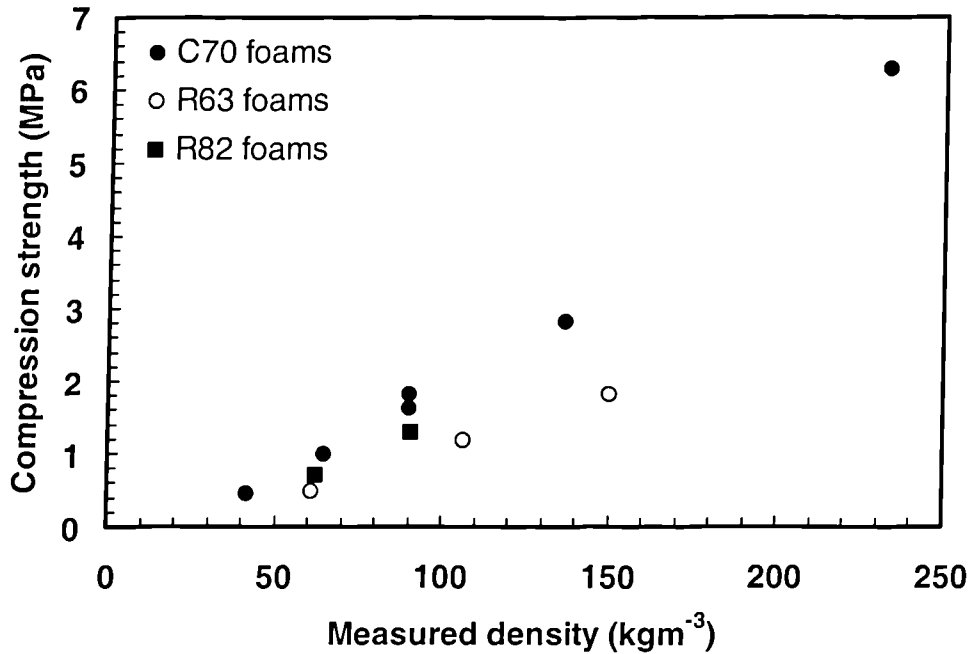


Figure 7.40: The variation of the compression strength of the foams with density of the eleven foam materials.

Further investigations were carried out to evaluate the strain-rate dependence of the compressive collapse stress. The strain-rate dependent of the compressive yield stress can be expressed as [4]:

$$\sigma_c = \sigma_{rc} + A \log \left(\frac{\dot{\delta}}{\dot{\delta}_r} \right) \quad (7.3)$$

Where:

σ_c = Yield stress (MPa)

σ_{rc} = Reference yield stress (MPa)

$\dot{\delta}$ = Crosshead displacement rate (mm/min)

$\dot{\delta}_r$ = Reference crosshead displacement rate (mm/min)

A = Material characteristic (MPa/decade of crosshead displacement rate)

The parameter A in Equation 7.3 characterises the rate-sensitivity of the foams under compression. Higher values of 'A' indicate a higher rate-sensitivity and vice versa. The reference yield stress was taken at a crosshead displacement rate of 0.2 mm/minute and this was also taken as the reference crosshead displacement rate. Details of the values of the parameters in Equation 7.3 are given in Table 7.4.

Foam	σ_{rc} (MPa)	σ_c (MPa)	$\dot{\delta}$ (mm/min)	$\dot{\delta}_r$ (mm/min)	A (MPa/decade)
C70.200	5.8	5.80	0.2	0.2	0.5145
	5.8	6.34	1	0.2	
	5.8	6.69	10	0.2	
C70.130	2.69	2.69	0.2	0.2	0.1556
	2.69	2.82	1	0.2	
	2.69	2.95	10	0.2	
C70.90	1.68	1.68	0.2	0.2	0.1672
	1.68	1.77	1	0.2	
	1.68	1.96	10	0.2	
C70.75	1.54	1.54	0.2	0.2	0.1291
	1.54	1.57	1	0.2	
	1.54	1.75	10	0.2	
C70.55	0.92	0.92	0.2	0.2	0.0638
	0.92	0.95	1	0.2	
	0.92	1.03	10	0.2	
C70.40	0.41	0.41	0.2	0.2	0.0281
	0.41	0.43	1	0.2	
	0.41	0.46	10	0.2	
R63.140	1.59	1.59	0.2	0.2	0.2841
	1.59	1.79	1	0.2	
	1.59	2.07	10	0.2	
R63.80	1.05	1.05	0.2	0.2	0.1703
	1.05	1.09	1	0.2	
	1.05	1.33	10	0.2	
R63.50	0.43	0.43	0.2	0.2	0.0519
	0.43	0.48	1	0.2	
	0.43	0.52	10	0.2	
R82.80	1.21	1.21	0.2	0.2	0.0775
	1.21	1.27	1	0.2	
	1.21	1.34	10	0.2	
R82.60	0.66	0.66	0.2	0.2	0.0406
	0.66	0.68	1	0.2	
	0.66	0.73	10	0.2	

Table 7.4: Summary of the rate sensitivity of the properties of the eleven foams calculated using Equation 7.3.

From the results in Table 7.4, it is clear that the C70.200 (PVC/PUR) foam offers the highest value of A suggesting that it is the most rate-sensitive. The lowest value of A was found in R82.60 (Linear PEI) foam indicating that it exhibits the lowest rate sensitivity.

7.1.8 Summary of the rate-dependent properties of the composites and sandwich structures

From the results of the first part of this research study to characterise the mechanical properties of the constituent materials and the contact parameters during indentation, it has been shown that the flexural modulus of the skin and core materials do not exhibit any pronounced rate-dependency over the range of loading rates considered in this study. It is therefore assumed that the dynamic properties of the skin and foam materials are the same as those measured at quasi-static rates. Similarly, the contact stiffness parameters in the Meyer indentation law, ' n ' and ' C ', are also not affected by loading rate, suggesting that the statically-determined values can be used in modelling the dynamic impact response of the sandwich structures. The accuracy of these assumptions will clearly be fully evaluated following the low velocity impact tests on the various sandwich structures.

7.2 Impact test results on GFR epoxy beams and plates.

The following section will present the impact test results obtained following tests on the GFR epoxy composites. In each test, the maximum impact force during the impact event was determined from the signal from the piezo-electric cell. Theoretical predictions of the maximum impact force were obtained using the energy-balance models discussed in Chapter 6. Comparisons between the experimental results and the predicted impact forces were then undertaken to assess the validity of the models.

7.2.1 Impact tests on the GFR epoxy beams

Impact tests on the GFR epoxy beams were conducted according to the procedures described in Section 5.1. The impact mass was held constant at 1.976 kg and the drop-height was varied between 10 mm and 100 mm in order to vary the incident impact energy. The span was also varied between 160 mm and 200 mm for the eight-layer laminates and between 120 mm and 160 mm for the sixteen layer laminates. The dimensions of the beams were varied in order to fully establish the validity of the impact model. The energy-balance model used to model the impact response of the glass fibre reinforced epoxy laminates is shown in Equation 7.4. This model is very simple, assuming that all of the incident impact energy of the falling weight is absorbed by the elastic flexural response of the target. The results of the impact tests on the eight ply laminates are presented in Figures 7.41 and 7.42. The error bars in these figures indicate the standard deviations for the three specimens tested.

$$P_{\max} = \sqrt{\frac{48 mv^2 EI}{L^3}} \quad (7.4)$$

Where:

P_{max} = Maximum impact force (N)

m = Impactor mass (kg)

EI = Flexural rigidity of the beam (Nm^2)

L = Span (m)

v = Impact velocity (ms^{-1})

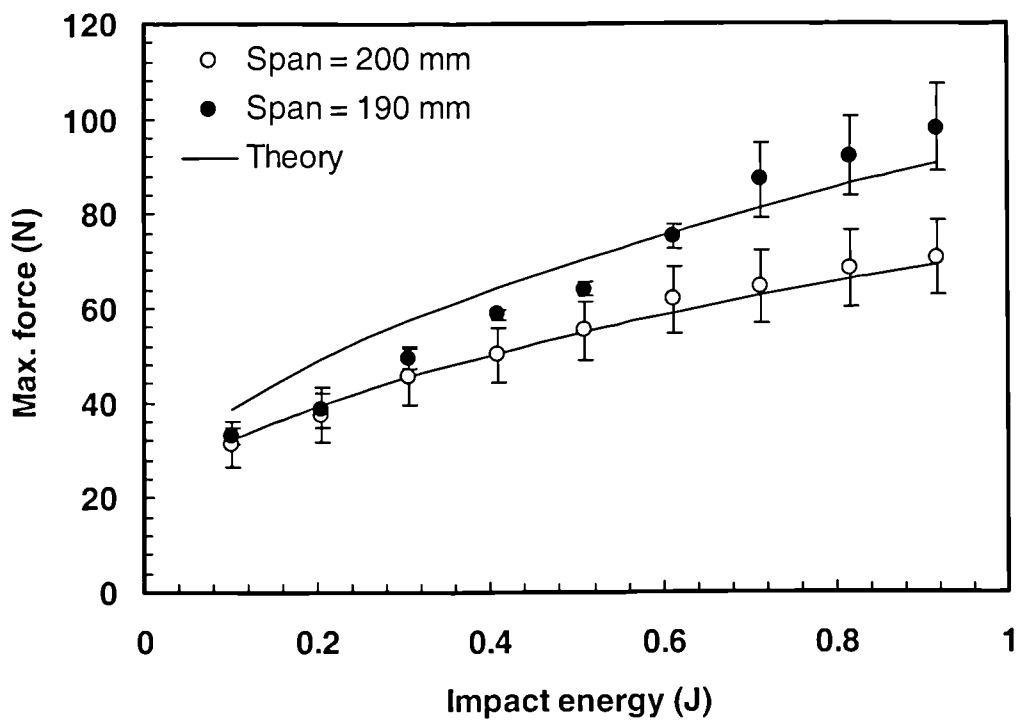


Figure 7.41: The variation of the maximum impact force with impact energy for the GFR epoxy laminate, nominal thickness = 2.0 mm (8 layer laminate).

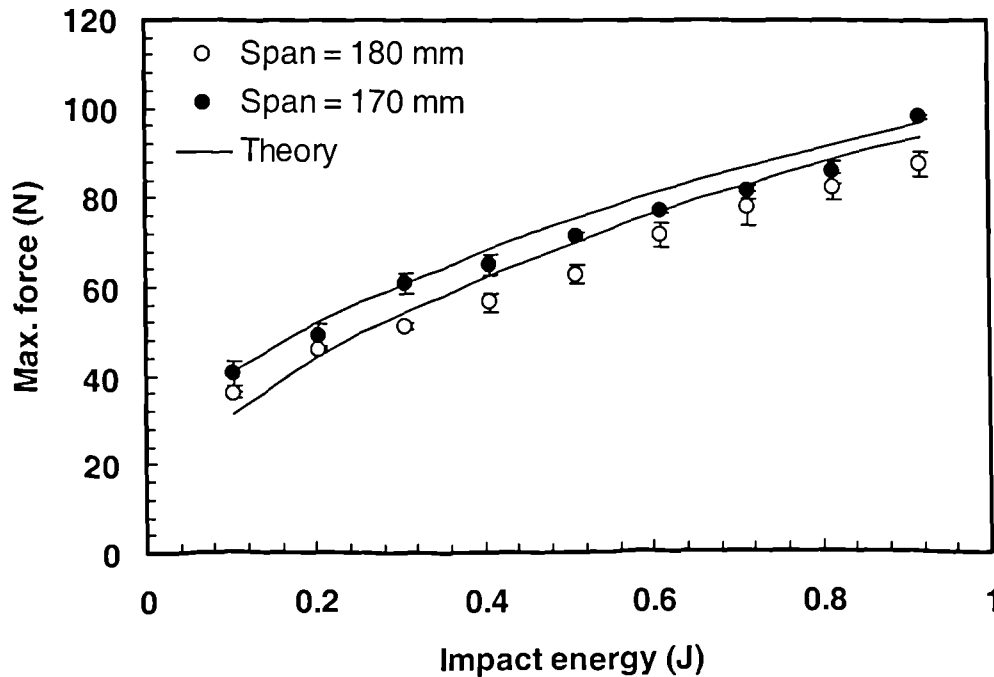


Figure 7.42: The variation of the impact force with impact energy for the GFR epoxy laminate, nominal thickness = 2.0 mm (8 layer laminate).

Generally, the energy-balance model used in this study proved to be successful in modelling the impact response of this structure. The theoretical values offered by the model agree well with the experimental data over the range of energies investigated. In Figure 7.41, the difference between the predicted values and the experimental values for beams with a 200 mm span is within five percent over a range of impact energies between 0.1 and 0.9 Joules. Clearly, this is very encouraging. As the span is reduced to 190 mm, the difference between the predicted and the experimental values is slightly higher over the same range of impact energies as shown in Figure 7.41. As the span was further reduced to 180 mm and 170 mm, agreement is still relatively good as shown in Figure 7.42. From Figures 7.41 and 7.42, it can be seen that changing the span over which the beam is supported has little effect on the accuracy of the energy-balance model. It is also clear that the maximum impact force recorded increases as the span decreases. This is to be expected since Equation 7.4 shows that $P_{max} \propto \sqrt{1/L^3}$. The

scatter in the experimental data is clearly much greater in the longer beams than the shorter specimens. The reason for this is not clear, although it may be due to variations in the quality of the laminates.

Further investigations to evaluate the ability of the energy-balance model to predict the impact response of laminated beams was made using thicker laminates based on sixteen plies. The results of the impact tests on these thicker laminates are presented in Figures 7.43 and 7.44. As before, the error bars in the figures indicate the standard deviations of the experimental data.

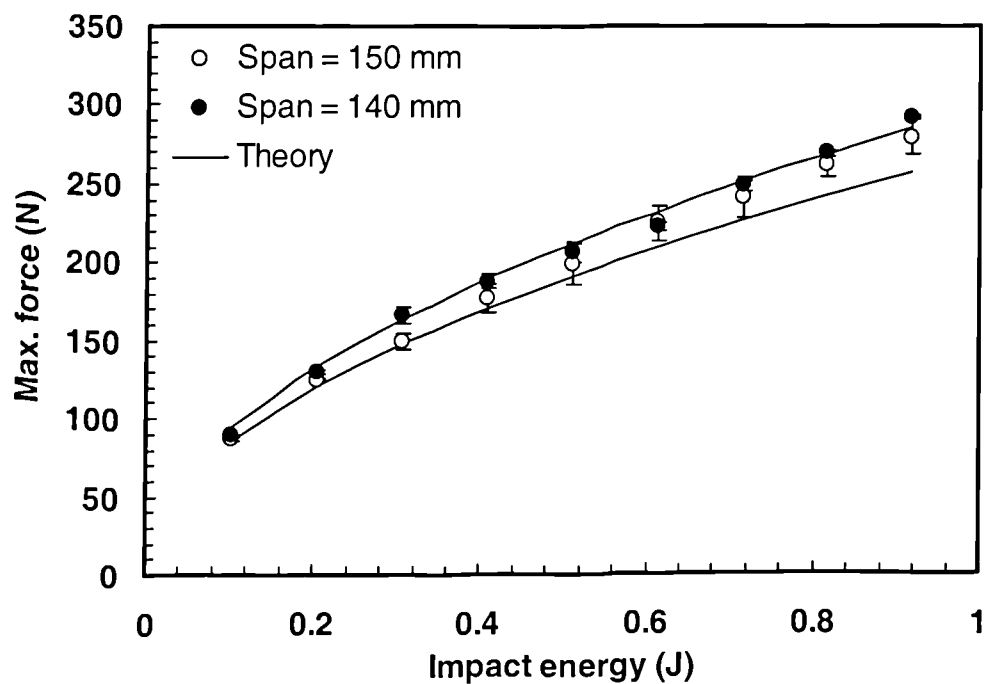


Figure 7.43: The variation of impact force with impact energy for the GFR epoxy laminate, nominal thickness = 4.0 mm (16 layer laminate).

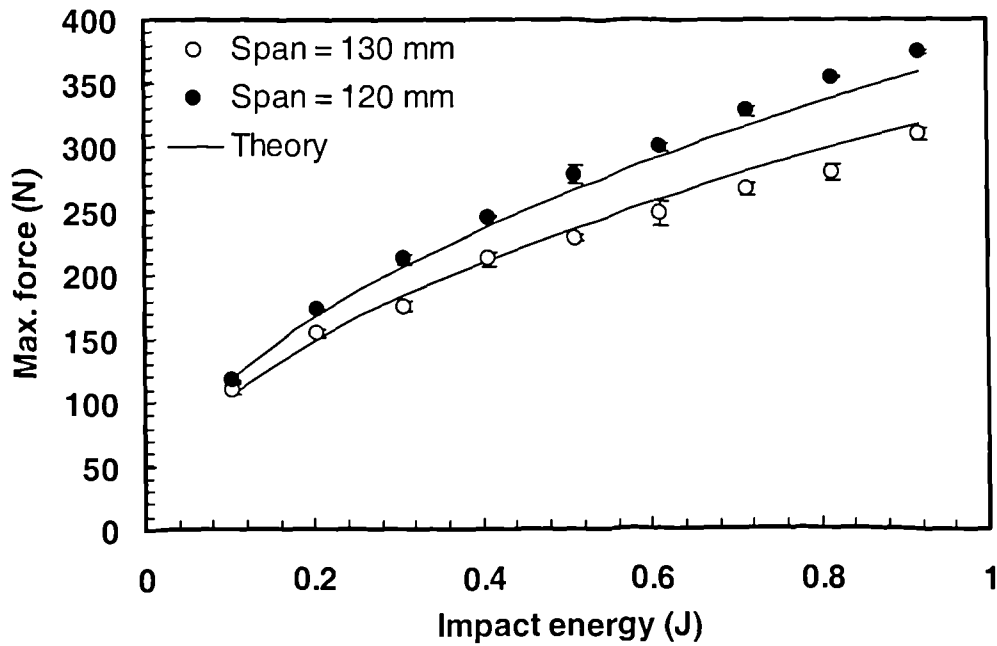


Figure 7.44: The variation of impact force with impact energy for the GFR epoxy laminate, nominal thickness = 4.0 mm (16 layer laminate).

As expected, the maximum impact force for a given energy in the sixteen-layer laminate is much higher than that measured on the thinner eight-layer laminate. This is clearly shown in Figure 7.45 where the maximum impact force data for eight-ply (2 mm thick) and sixteen-ply (4 mm thick) samples supported over a span of 160 mm are shown.

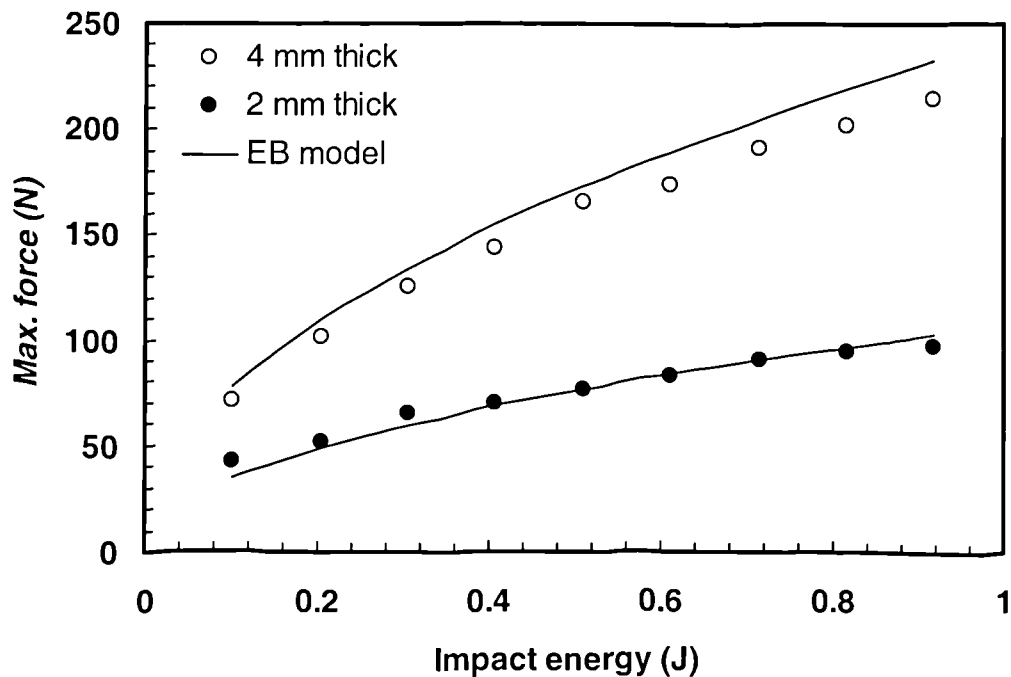


Figure 7.45: The variation of impact force with impact energy for the GFR epoxy laminate support span = 160 mm.

This can be explained by the fact that the thicker composites offer a higher flexural rigidity under flexural loading conditions. From Equation 7.4, one would expect that, for a given impact energy and span, the maximum force would vary according to $P_{max} \propto \sqrt{I}$ i.e. $P_{max} \propto \sqrt{h^3}$. The data in Figure 7.45 appear to support this conclusion. As far as the energy-balance model is concerned, the accuracy of the model for predicting the maximum impact force is very encouraging for both the eight and sixteen ply laminates. Even though the model is less complicated than the solution to the dynamic equation of motion used by the previous workers [1,2], the accuracy of the predictions is very encouraging. This approach offers an alternative technique for predicting the maximum impact force of laminated composite materials under impact loading. The energy-balance model was further examined by varying the support span for both the eight and the sixteen layer laminates for fixed values of incident impact energy. For

comparison, two different impact energies were used to illustrate the effect of varying the support span on the maximum impact force as shown in Figure 7.46.

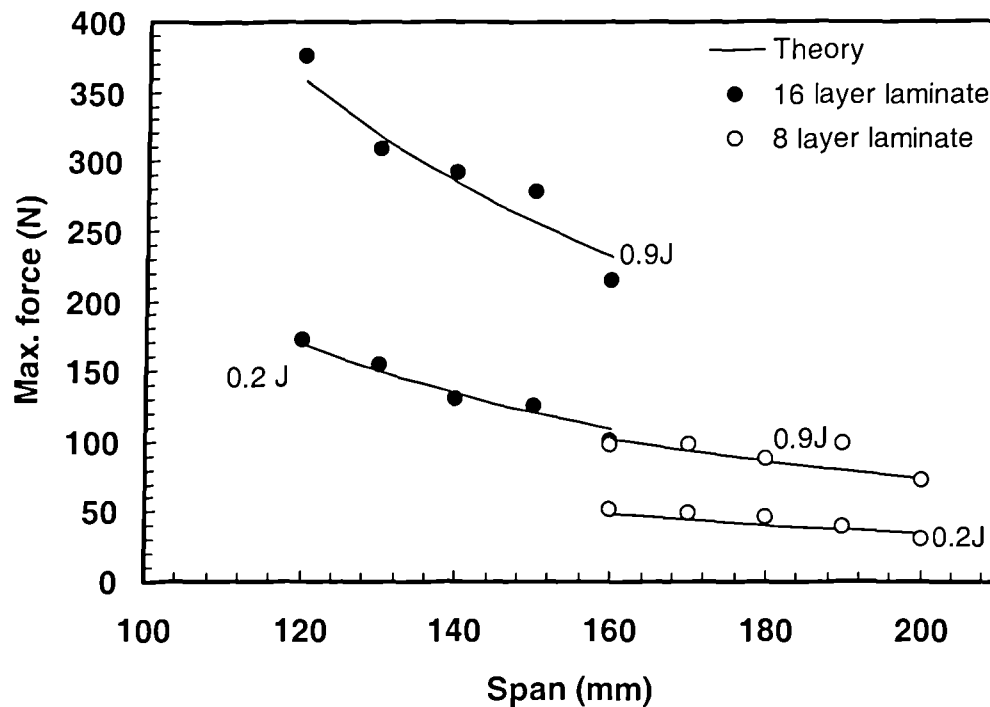


Figure 7.46: The variation of maximum impact force with span for the glass fibre reinforced epoxy resin composites following impact energies of 0.2 and 0.9 Joules.

From the figure, it is clear that, for both laminate systems, the impact force decreases as the span increases for a given impact energy. The reduction in impact force with increasing span is due to the fact that for a given specimen thickness, the specimen becomes more flexible as the span increases. This result is also expected as Equation 7.4 suggests that the maximum impact force should decrease with increasing span, L , as $P_{max} \propto \sqrt{1/L^3}$. The trends agree with the results reported by Cantwell *et al.* [1]. Clearly, agreement between theory and experiment is very good suggesting that the energy-balance model successfully models the response of these simple structures. These results also suggest that a quasi-static analysis is acceptable in order to model the impact response of glass fibre reinforced epoxy beam structures. Broutman and Rotem [16] have shown that glass fibre reinforced epoxies are rate-sensitive under impact loading

conditions. In contrast, this study has shown that no such rate sensitivity appears to exist in this material. However, the energy-balance model does not yield the complete force-time history for the impact event. The same energy-balance model was also used by Found and Howard [17] whilst investigating the impact response of CFRP. They showed that the maximum impact force is given as:

$$F_{\max} = \sqrt{2Uk} \quad (7.5)$$

where F_{\max} is the maximum impact force, U is the total impact energy and k is the flexural rigidity of the laminate. They observed similar trends where the theoretical values offered by the model tended to over-estimate the maximum impact force at impact energies above 1 Joule. Here an audible noise was heard indicating that matrix failure had occurred. A similar model to that described in [17] was used by Wisheart and Richardson [18] to investigate the low velocity impact response of a glass/polyester composite. They reported that good agreement was observed between the experimental and theoretical values of the peak force although some deviation of the model was observed at higher impact energies.

7.2.2 Impact tests on the circular laminated plates

The impact test procedure used to investigate impact response of the circular laminated plates was similar to that used to investigate the laminated beams. Here, the energy-balance model was modified to account for contact, shear and bending effects. Details of the development of the model are presented in Section 6.1.2 and a summary of the model is given in Equation 7.6.

$$\frac{1}{2}mv^2 = \frac{1}{2}K_b\delta_{\max}^2 + \frac{1}{4}K_m\delta_{\max}^4 + \frac{2}{5}\frac{(K_b\delta_{\max} + K_m\delta_{\max}^3)^{\frac{5}{3}}}{C^{\frac{2}{3}}} \quad (7.6)$$

Where K_b , K_s and K_m are the bending, shear and membrane stiffnesses respectively. The parameter 'C' is the contact parameter in the contact law and δ is the displacement of the target. Again, the drop-height was varied between 10 and 100 mm. The specimen was simply-supported on circular steel tubes with internal radii of 31 mm and 41 mm respectively. These results are shown in the Figure 7.47.

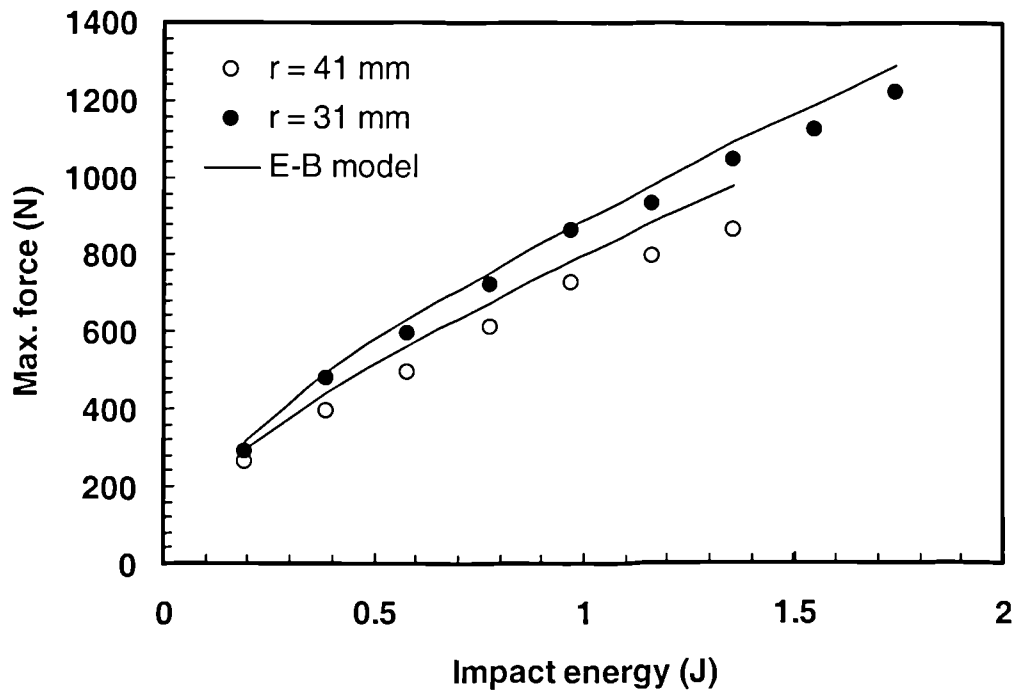


Figure 7.47: The variation of impact force with impact energy for the circular glass fibre reinforced epoxy laminates. Support radii of 31 mm and 41 mm were used.

From the impact test results shown in Figure 7.47, it is clear that the impact forces are significantly higher in the stiffer plate ($r = 31\text{mm}$) than in the more flexible plate ($r = 41\text{mm}$). Agreement between the experimental and predicted data is good over the range of impact energies considered. The energy-balance model tends to over-estimate the impact data. This may be due to the fact that the high impact forces are likely to generate damage in structure which will reduce the impact force. Differences between the model and the experimental data were relatively small for the tests on 41 mm diameter support. The reason is that an increase in the radius will reduce its structural rigidity. Similarly, it is apparent that the impact forces generated during impact on the circular plates are much greater than that measured on the less stiff beam structures.

The impact analysis was extended to determine the contribution of the bending/shear, contact and membrane terms in the energy absorption process by plotting the percentage of energy dissipated in each process against impact energy as shown in Figure 7.48. It is clear that the energy dissipated through shear and bending effects is most significant although it decreases as the impact energy increases. Energy dissipation in contact effects remains almost constant at approximately sixteen percent over the range of impact energies considered. On the other hand, the effect of membrane stiffening increases as the impact energy increases. This is to be expected since the out-of-plane deformations increase as the impact energy increases.

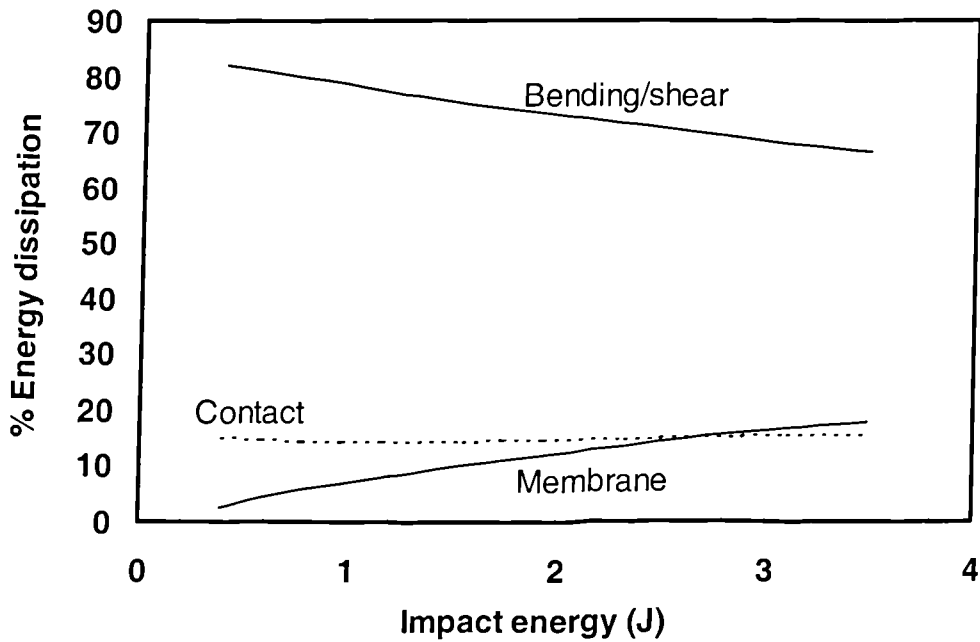


Figure 7.48: Energy dissipation analysis showing the percentage of the incident energy dissipated during impact on a circular laminated plate with a radius of 31 mm. Similar trends were observed in the 41 mm radius plates.

7. 3 Impact tests on sandwich beams with a foam-core

Impact tests on a series of eleven different sandwich foam-core materials were undertaken using the instrumented drop-weight impact tester used previously. The energy-balance model was developed to consider bending, shear and contact effects in the sandwich beam. The energy-balance model used to predict the impact response of sandwich beam structure was:

$$\frac{1}{2}mv^2 = \frac{P_{\max}^2}{2} \left(\frac{L^3}{48D} + \frac{L}{4AG} \right) + \frac{C \left(\frac{P_{\max}}{C} \right)^{\frac{n+1}{n}}}{n+1} \quad (7.7)$$

Where

P_{\max} = Maximum impact force (N)

L = Span (m)

$$D = E_f \frac{btd^2}{2} = \text{Flexural stiffness of the sandwich beam (Nm}^2\text{)}$$

$$A = \frac{bd^2}{c} \text{ (m}^2\text{)}$$

$$G = \text{Shear modulus of the core (Nm}^{-2}\text{)}$$

The impact energy was varied by increasing the drop-height of the impactor whilst the span was kept constant at 175 mm. The average thickness of the GFR epoxy skin which was bonded on the both faces was 0.5 mm. The results of the impact tests on the C70 (PVC/PUR) foams with densities between 40 kgm^{-3} and 75 kgm^{-3} are shown in Figure 7.49 and for the densities between 90 kgm^{-3} and 200 kgm^{-3} in Figure 7.50a and 7.50b.

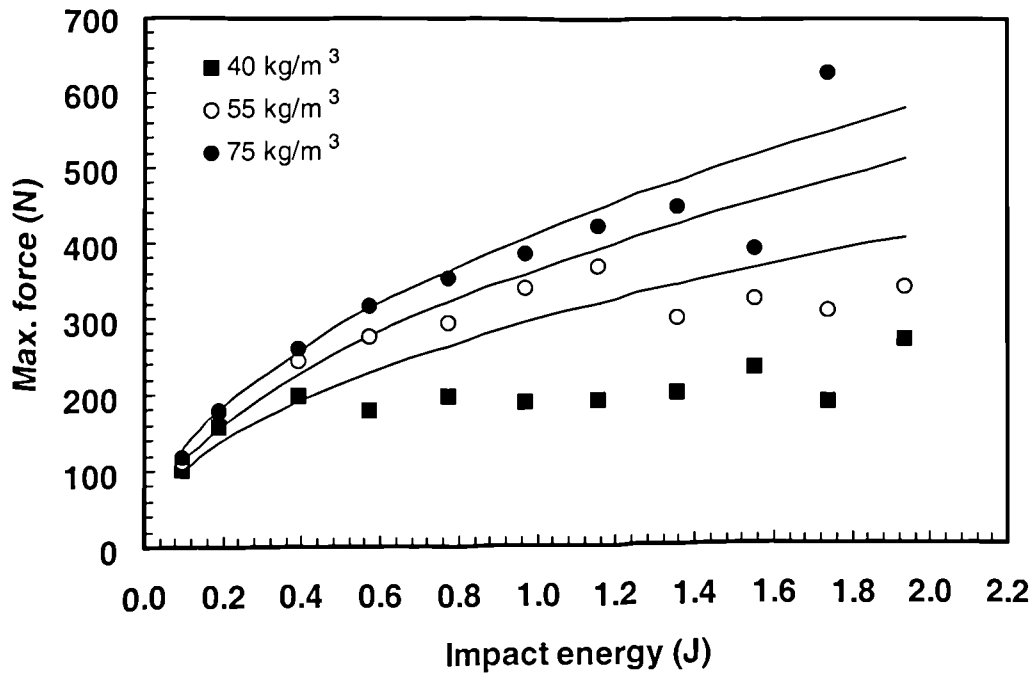


Figure 7.49: The variation of the maximum impact force with impact energy for the C70 (PUR/PVC) based sandwich structures. Span = 175 mm. The solid lines represent the values offered by the energy-balance model.

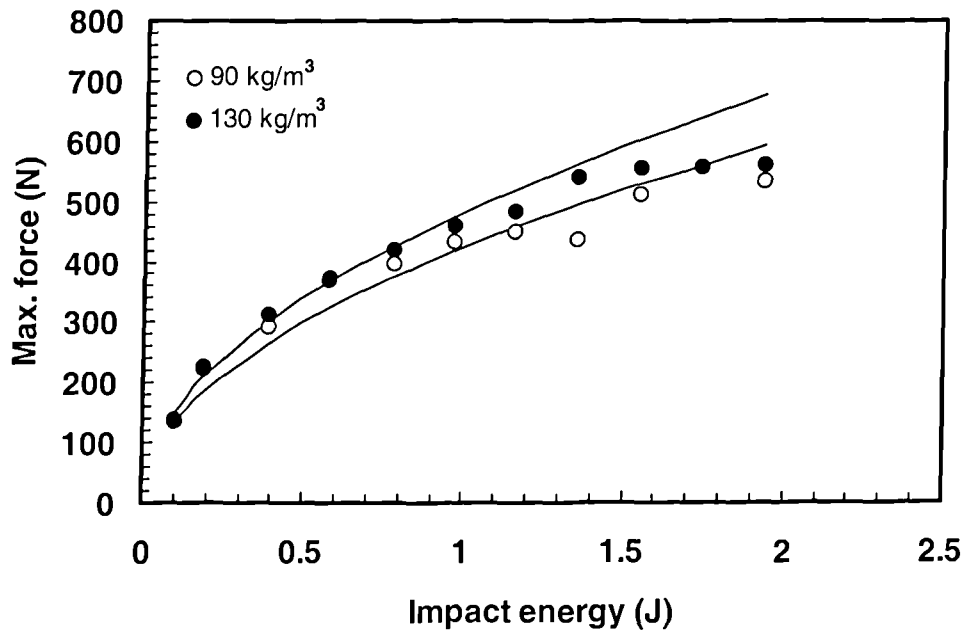


Figure 7.50a: The variation of the maximum impact force with impact energy for the C70 (PUR/PVC) based sandwich structures. Span = 175 mm. The solid lines represent the values offered by the energy-balance model.

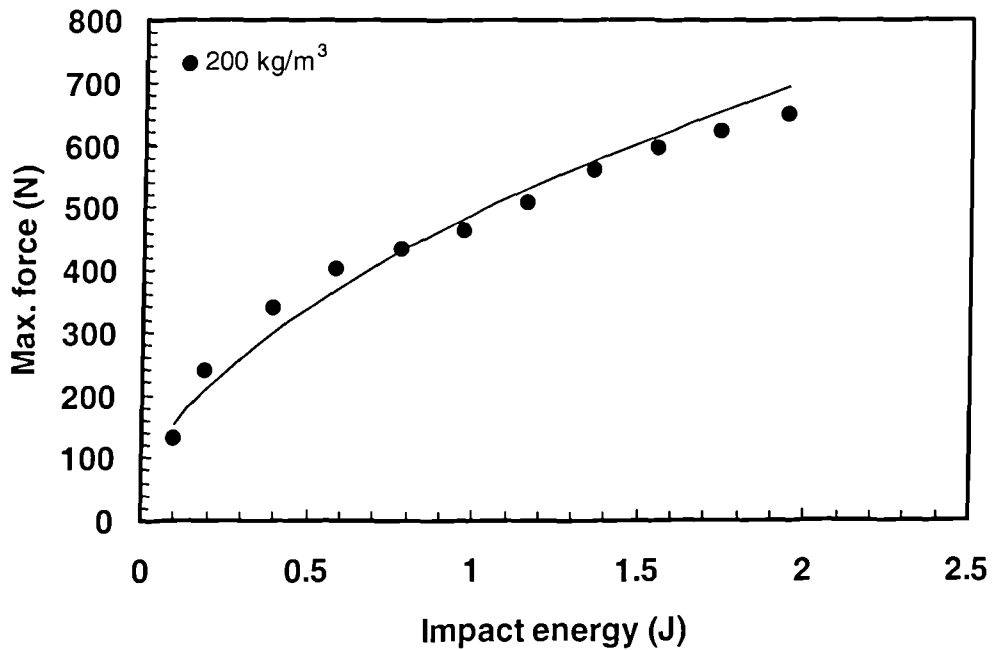


Figure 7.50b: The variation of the maximum impact force with impact energy for the C70 (PUR/PVC) based sandwich structures. Span = 175 mm. The solid lines represent the values offered by the energy-balance model.

From the experimental results shown in Figure 7.49, it is clear that the maximum impact force for a given incident energy increases as the density of the foam-core materials increases. This is to be expected since increasing the core density serves to increase the stiffness of the core and modify its indentation response. Agreement between the predicted values offered by the energy-balance model and the experimental data is reasonably good at low impact energies. Differences between the measured and predicted values can be attributed to the onset of damage in the foam-core sandwich beams as the impact energy increases. At this point, the stiffness of the beam is reduced significantly and no longer responds elastically as predicted by the energy-balance model. Above the damage threshold energy, the experimental values start to plateau and then drop as shown in Figure 7.49. However, for the stiffer foams, the damage threshold is higher and the plateau value may not be reached as shown in Figure 7.50. Similar observations are apparent in the R63 and the R82 group foams as shown in Figures 7.51 and 7.52.

It is also apparent in Figure 7.49 that the damage threshold energy increases as the density of the foam increases. Damage in the 40 kg/m^3 system initiated at approximately 0.6 Joules whereas damage in the stiffer 55 kg/m^3 sandwich structure occurred at 1.36 Joules. Observation of the specimens suggested that the drop was due to core cracking in low density foam systems and cracking in the skin in the stiffer foam systems. The damage observed was localised to the point of impact.

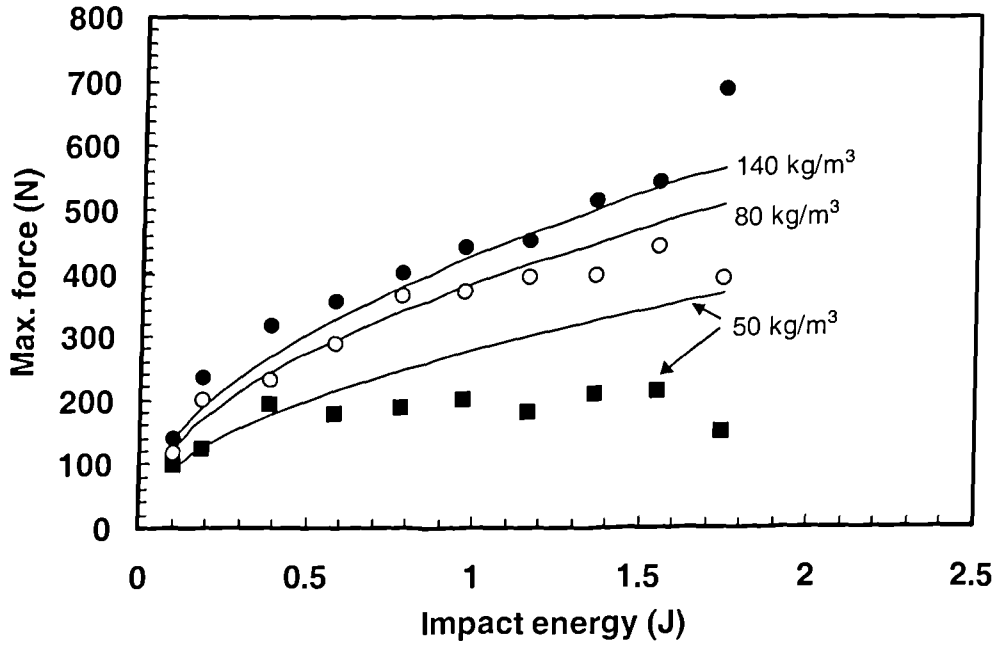


Figure 7.51: The variation of the maximum impact force with impact energy for the R63 (linear PVC) based sandwich structures. Span = 175 mm. The solid lines represent the predictions of the energy-balance model.

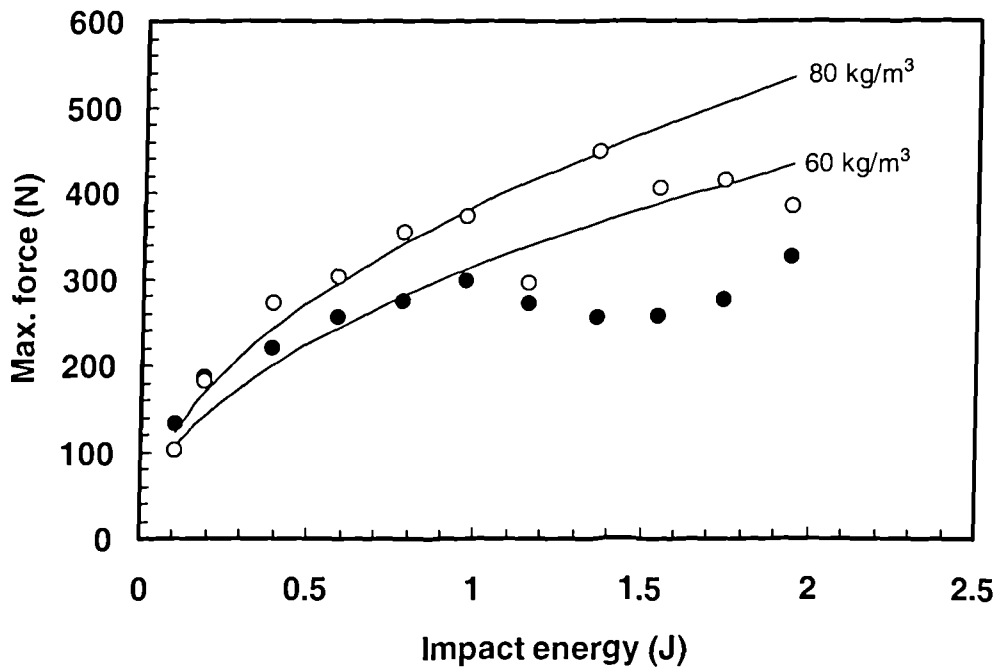


Figure 7.52: The variation of maximum impact force with impact energy for the R82 (Linear PEI) based sandwich structures. Span = 175 mm. The solid lines represent the predictions of the energy-balance model.

Further investigations were carried out to study the effect of skin thickness on the impact response of the foam core sandwich materials. The C70.40 foam-core beam was chosen to investigate this effect. The skin, which originally had a thickness of 0.5 mm, was increased to 1 mm and the plot of the maximum impact force versus impact energy is presented in Figure 7.53. Clearly, the maximum impact force recorded in the beams with the thicker skin is slightly higher than that in the thin-skinned system for a given impact energy. Clearly, the model breaks down at a low energy in the thin-skinned system (above 0.4 Joules) whereas it is still valid at energies close to 1 Joule in the thicker-skinned sandwich structures. This suggests that the thicker skin enhances the impact resistance of the beam. Therefore, the increase in the flexural stiffness of the beams has shifted the damage threshold to a higher impact energy. This finding is supported by the work of Anderson and Madenci [19] who reported that thicker-skinned sandwich beams offer a greater resistance to impact damage.

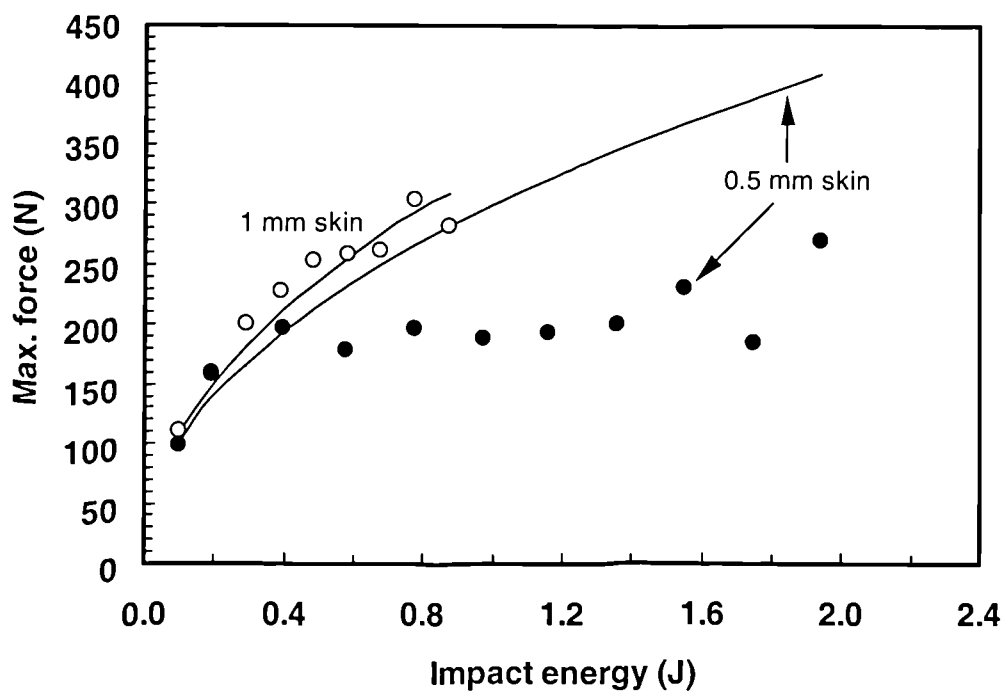


Figure 7.53: The variation of the maximum impact force with impact energy for two C70.40 (PVC/PUR) based sandwich structures with different skin thicknesses. The solid lines represent the predictions of the energy-balance model.

In order to further assess the energy-balance model, the variation of the maximum force predicted by the model with the shear modulus of the foam material at a given impact energy was monitored, Figure 7.54. Included in the figure are predictions offered for different values of the Meyer indentation constants 'C' and 'n'. It is interesting to note that the three curves loosely follow the impact data which tends towards a plateau value as the shear modulus is increased. The figure also highlights the sensitivity of the model to variations in the contact parameters.

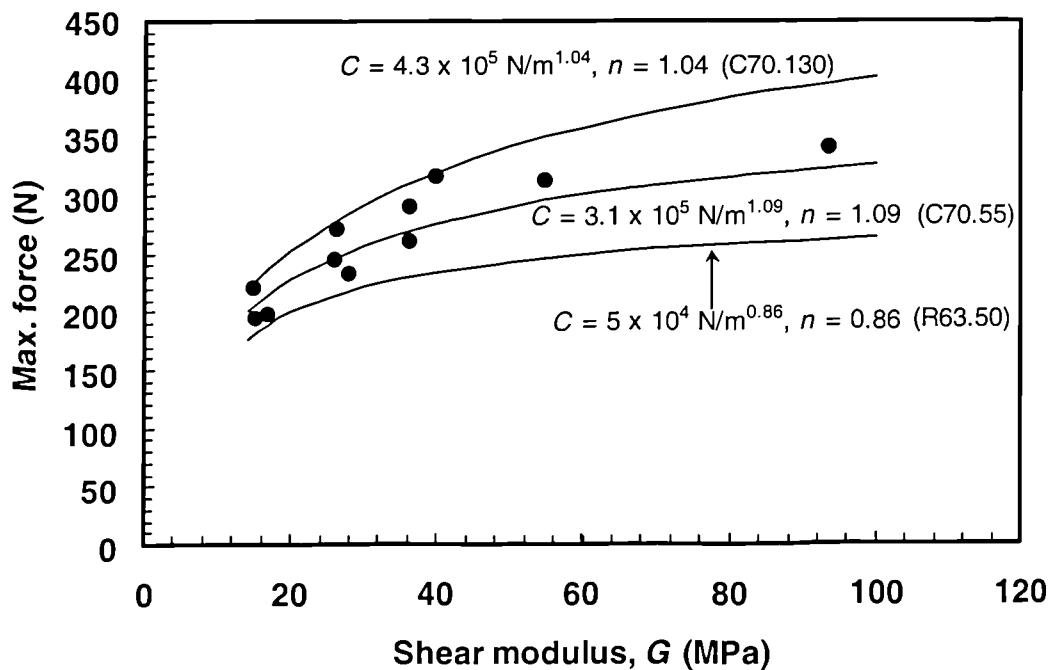


Figure 7.54: The variation of maximum impact force with shear modulus for various types of foam-core sandwich beams at an impact energy of 0.4 Joules. The solid lines represent the predictions offered by the energy-balance model for three different contact conditions.

In conclusion, it is clear that the impact response of the sandwich structure is strongly dependent on the properties of the foam-core material. Increasing the stiffness of the foam increases the impact force. It is also obvious that the damage threshold of the sandwich structures is strongly dependent on the properties of the foam core. It is also apparent that increasing skin thickness increases the impact force and resulting damage threshold energy.

7.4 Energy absorption analysis for the foam-based sandwich structures

This section will present an analysis that was conducted to further investigate the energy absorption behaviour of the sandwich structures under low velocity impact loading. Based on the energy-balance model described in Equation 7.7, the fraction of incident energy dissipated in bending, shear and contact can be calculated for each impact energy. These data provide useful information for highlighting the principal energy absorbing mechanisms during impact. The results of this analysis for four different foam systems are shown in Figures 7.55 to 7.58.

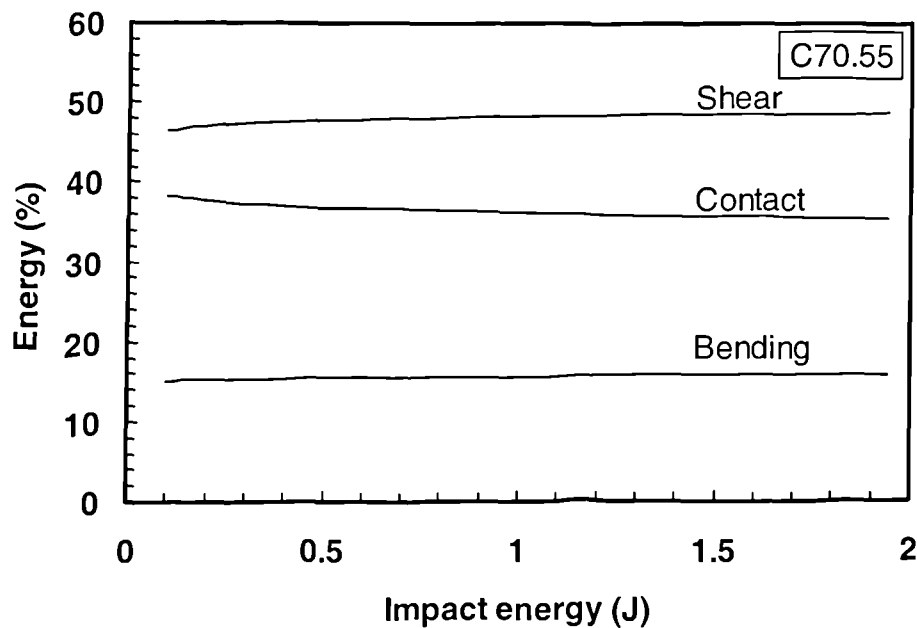


Figure 7.55: Energy breakdown during impact on a C70.55 (PVC/PUR) sandwich foam-core beam with a nominal density = 55 kg/m^3 .

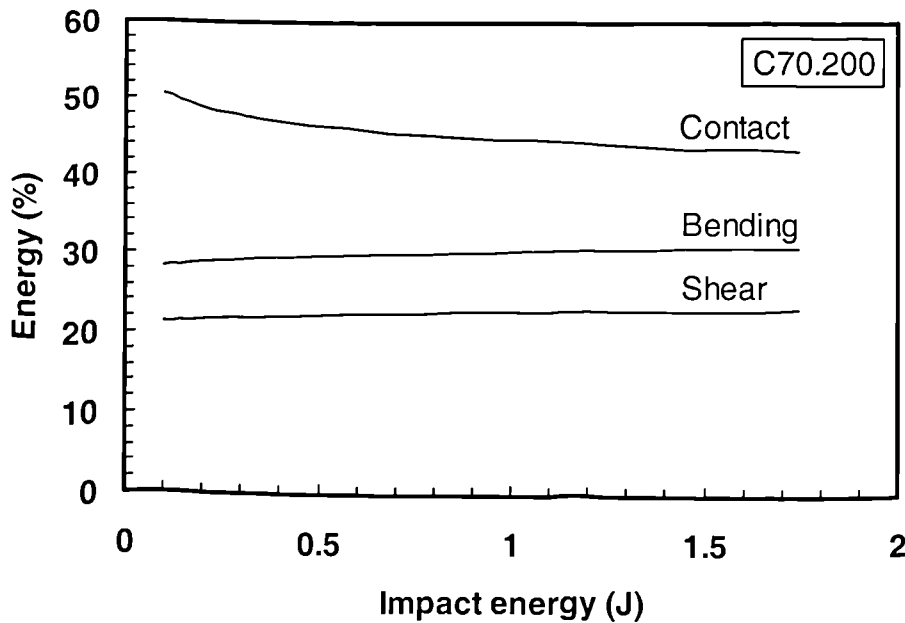


Figure 7.56: Energy breakdown during impact on a C70.200 (PVC/PUR) sandwich foam-core beam with a nominal density = 200 kg/m^3 .

For the C70 (PVC/PUR) foams shown in Figures 7.55 and 7.56, it is clear that in the low density foam i.e. the C70.55 system shown in Figure 7.55, shear deformations were the predominant energy absorbing mechanism followed by contact and bending. However, as the foam density increases, see for example the C70.200 foam with a density of 200 kg/m^3 , the dominant energy-absorbing mechanism was contact effects followed by bending. It is also apparent that as the density of the foam increases, energy absorption in bending increases. The results for the R63.80 and R82.80 foams are shown in Figures 7.57 and 7.58 respectively. Similar trends are apparent in both of these foams which have a nominal density of 80 kg/m^3 . Here, energy dissipation in shear dominates the breakdown of energy accounting for between 48 and 50 percent in the R63.80 sandwich structures and between 52 and 54 percent in the R82.80 system.

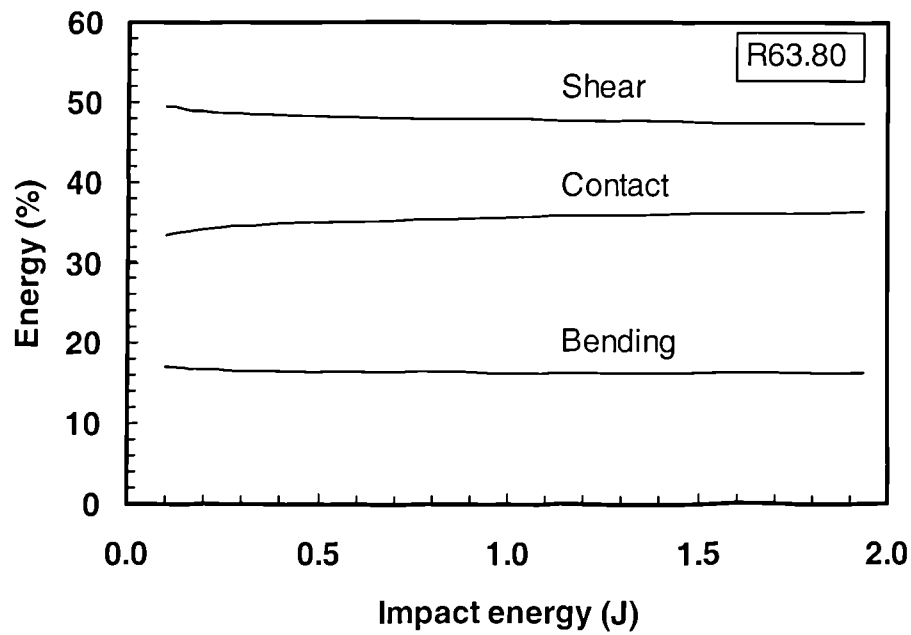


Figure 7.57: Energy breakdown during impact on a R63.80 (linear PVC) sandwich foam-core beam with a nominal density = 80 kg/m^3 .

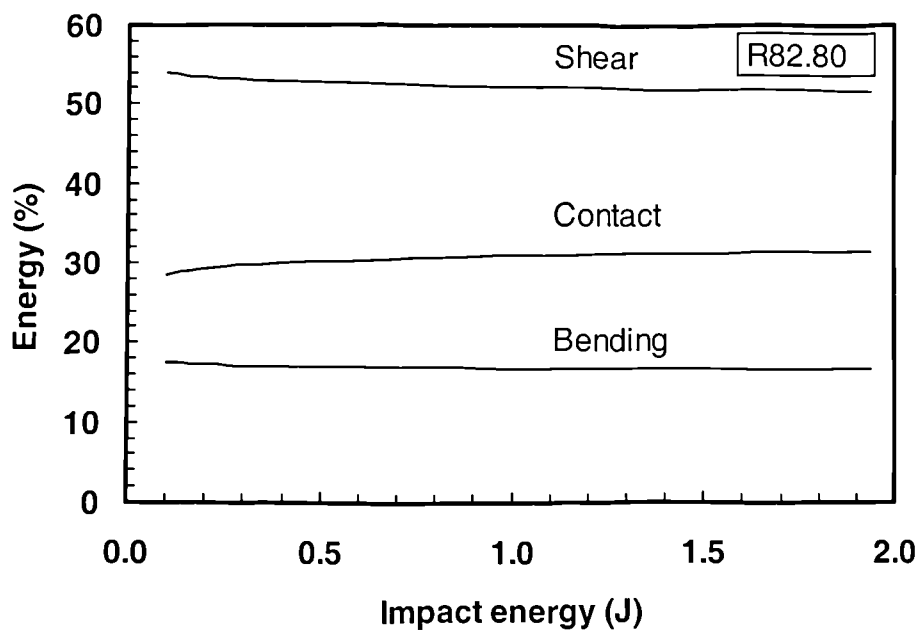


Figure 7.58: Energy breakdown during impact on a R82.80 (linear PEI) sandwich foam-core beam with a nominal density = 80 kg/m^3 .

From the previous results for the energy breakdown in the C70 foams, Figures 7.55 to 7.56, it is noticeable that, within the same family of foam materials, the energy dissipation during impact is determined by the foam density. In order to investigate this further, the energy dissipation profiles were determined as a function of foam density. The energy dissipation profiles for the C70 sandwich structures following a 0.4 Joule impact is shown in Figure 7.59. From the figure, it is clear that the energy absorbed in shear decreases with increasing foam density. In contrast, the energy absorbed in bending increases with increasing foam density.

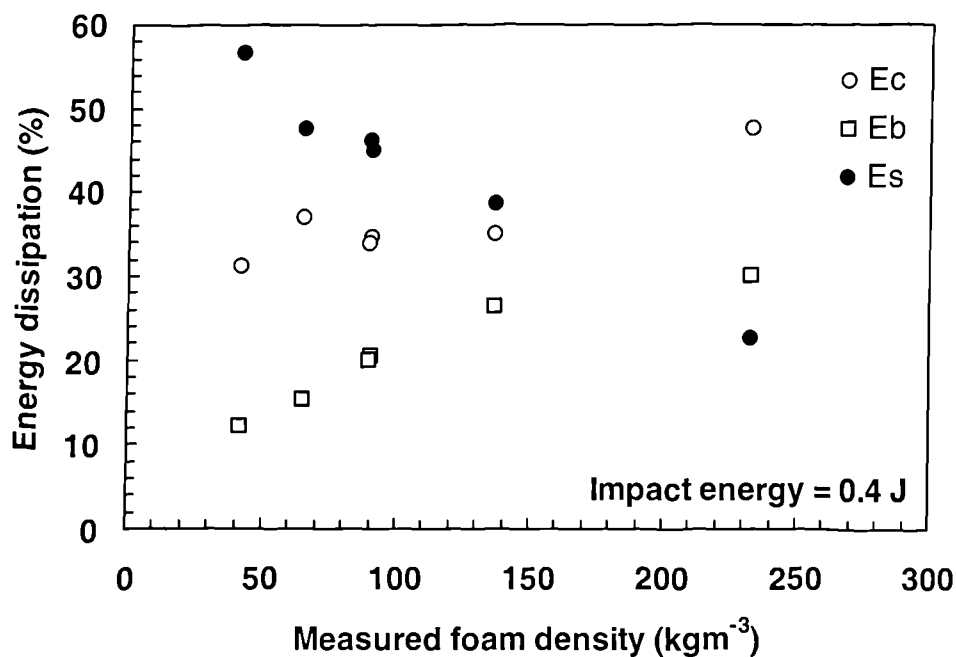


Figure 7.59: Plot showing the effect of foam density on the absorption of energy in the C70 group of foams. The subscripts c, b and s refer to contact, bending and shear respectively.

7.5 Impact test results on the aluminium honeycomb sandwich structures

The following section will present the impact test results obtained following tests on the aluminium honeycomb sandwich structures. In each test, the maximum impact force during the impact event was determined from the signal from the piezo-electric cell. Theoretical predictions of the maximum impact force were obtained using the energy-balance models discussed in Chapter 6. Comparisons between the experimental results and the predicted impact forces were then undertaken to assess the validity of the models.

7.5.1 Impact tests on aluminium honeycomb sandwich beams

Using the same drop-weight impact arrangement as before, impact tests were carried out on a series of aluminium honeycomb beams with different geometries in order to study the response of this material under impact loading. The span and thickness of the specimens was varied in order to investigate their effect on the impact behaviour of this sandwich structure. The aforementioned energy-balance model described in Equation 7.7 was used to determine the maximum impact force generated during the impact test. The results are presented in Figures 7.60 and 7.61. These beams have a thickness of 13 mm and the width was held consistent at 15 mm. As before, it is apparent that increasing the span has the effect of reducing the impact force, an effect that is due to the reduced stiffness of the longer beams. Equation 7.7 shows that the relationship between span, L and maximum impact force, P_{\max} is more complicated than in the simple composite beams due to the presence of shear effects in the core. Nevertheless, the equation does indicate that P_{\max} will decrease with increasing L . Clearly, agreement between the predicted values and the experimental data is good. These results suggest that the energy-balance model is capable of predicting the impact response over the range of impact energies considered here.

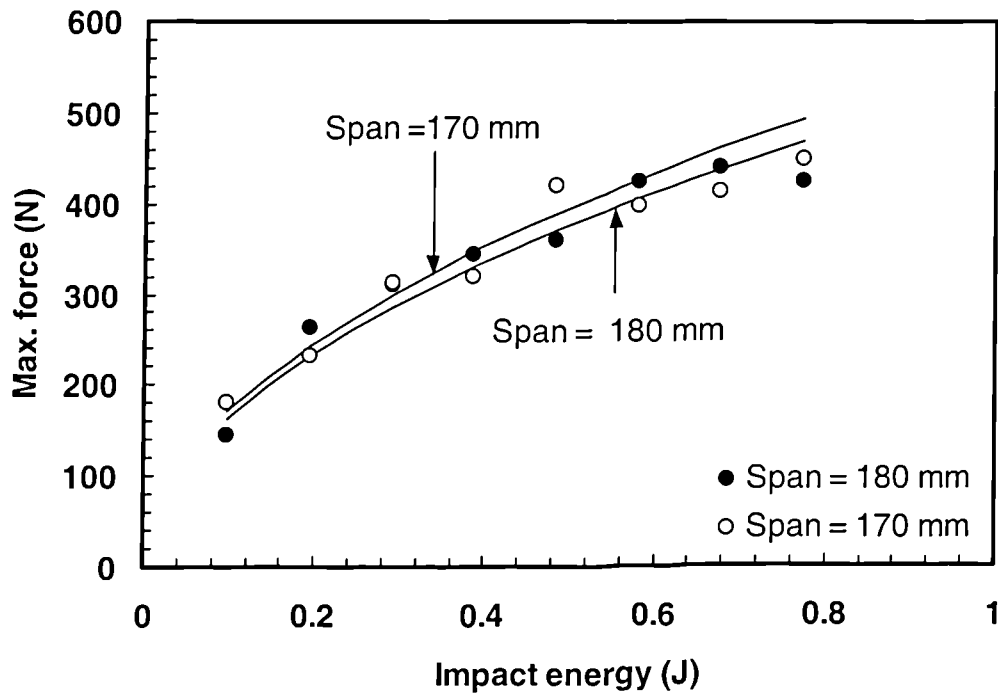


Figure 7.60: The variation of maximum impact force with impact energy for the aluminium honeycomb sandwich beam, thickness = 13 mm

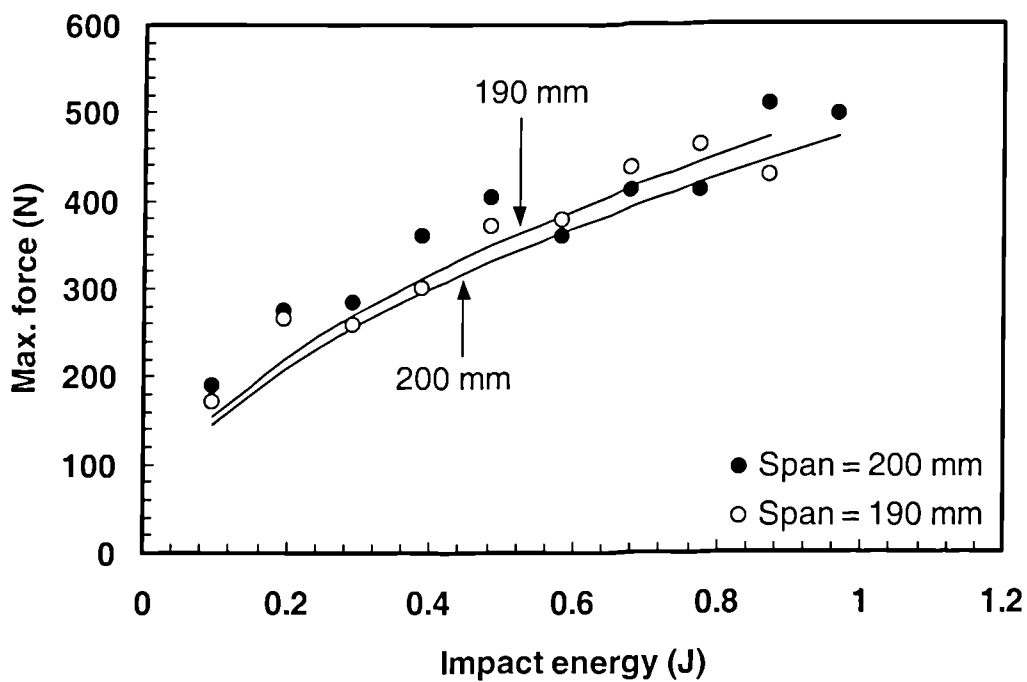


Figure 7.61: The variation of maximum impact force with impact energy for aluminium honeycomb sandwich beams, thickness = 13 mm

The effect of varying the span on the thicker sandwich structures can be clearly seen in Figure 7.62. From the figure, it is clear that as the span increases from 200 mm to 500 mm, the maximum impact force recorded at a given impact energy decreases. This is partly due to the fact that as the beam span increases, the flexibility of the structure increases, the structures are capable of absorbing greater energy elastically and the impact response remains within the elastic regime. It is also clear that as the span decreases the accuracy of the model reduces. This is due to the damage developing in the stiffer sandwich structures under the application of a larger impact force which does not account for in the energy-balance model. Therefore, the model tends to over-estimate the maximum impact force generated during the impact event.

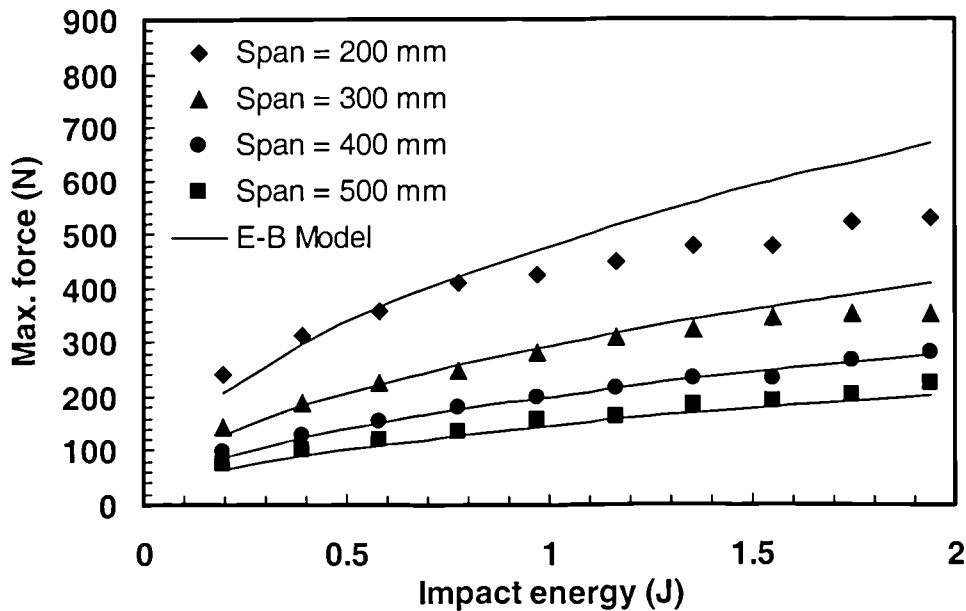


Figure 7.62: The variation of maximum impact force with impact energy for the aluminium honeycomb beams. Thickness = 25 mm and width = 20 mm.

The effect of beam thickness on the impact response of the aluminium honeycomb beam was further investigated by plotting the maximum impact force against the impact energy at a given span and impact energy for the two different core thicknesses. The plot is shown in Figure 7.63. It is apparent from the figure that the impact force is greater in the thicker beams than the thinner beams for a given impact energy and span. This is

expected since the maximum impact force, P_{\max} depends on the core thickness, c , as shown in Equation 7.8.

$$\frac{1}{2}mv^2 = \frac{P_{\max}^2}{2} \left[\frac{L^3}{6E_f bt (2t+2c)^2} + \frac{cL}{b(2t+2c)^2 G} \right] + \frac{C \left(\frac{P_{\max}}{C} \right)^{\frac{n+1}{n}}}{n+1} \quad (7.8)$$

Clearly, the thicker beam offers a higher stiffness than a thinner beam and hence a higher maximum force during impact. This is obvious where the flexural rigidity, D , in Equation 7.8 takes in the form $(E_f bt (2t+2c)^2)$, is a function of core thickness, c . From Figure 7.63, it is also clear that the energy-balance model offers reasonable predictions for the impact force within the elastic region.

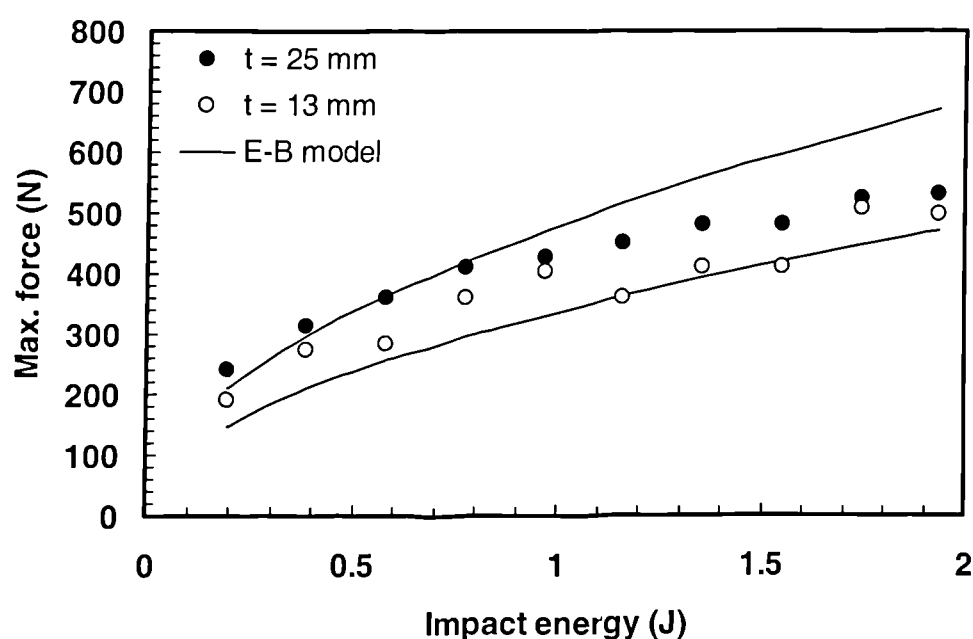


Figure 7.63: The variation of maximum impact force with impact energy for the aluminium honeycomb beams. The span = 200 mm, width = 20 mm and two different thickness have been used.

The analysis was further extended by evaluating the effect of varying span on the maximum impact force for 13 mm and 25 mm thick aluminium honeycomb systems and these results are presented in Figure 7.64. As expected, the maximum impact force generated decreases as the span increases due to the increased flexibility of the longer beams. At a given span, for example, 200 mm, the effect of changing the core thickness is obvious with the maximum impact force increasing from 364 Newtons to 449 Newtons as the core thickness increases from 13 mm to 25 mm. Again, this fact is due to the higher stiffness of the structure with a thicker core, since the bending stiffness, D , of the sandwich beam increase as the thickness increases. The effect of the beam thickness however is not that significant as shown in the figure.

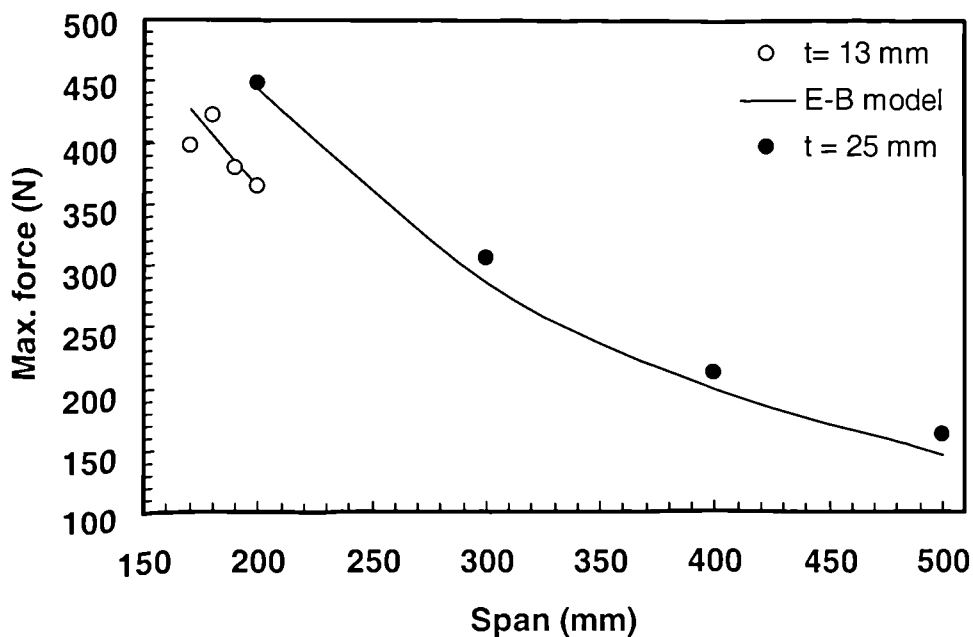


Figure 7.64: The variation of the maximum impact force with span for the sandwich aluminium honeycomb beams with a core thickness of 13 mm and 25 mm. Impact energy = 0.58 Joules.

An examination of the impact model indicates that the impact force depends only on the incident energy. This suggests that the mass and velocity can be varied, but if the energy remains constant, the impact force should remain unchanged. This is clearly a critical test for the energy-balance model. Therefore, the impact response of the aluminium honeycomb beams was further investigated by studying the effect of varying the impactor mass and impact velocity whilst maintaining the impact energy constant. An impact energy of 0.97 Joules was used as the reference energy in order to demonstrate the influence of impactor mass and velocity on the impact response. Details of the test variables are given in Table 7.4. In all cases, the impact energy is maintained at 0.97 Joules whilst the impact mass and the drop-height were varied accordingly. The plot of maximum impact force against impactor mass is presented in Figure 7.65.

Impactor mass (kg)	Drop height (m)	Maximum impact force (N)	Impact energy (J)
2.0	0.0495	413 (\pm 1.34)	0.97
2.3	0.0430	392 (\pm 1.13)	0.97
2.6	0.0380	400 (\pm 0.00)	0.97
3.3	0.0300	388 (\pm 0.21)	0.97
4.3	0.0230	412 (\pm 1.50)	0.97

Table 7.4: The parameters used to investigate the effect of impactor mass on the impact response of the aluminium sandwich honeycomb beam.

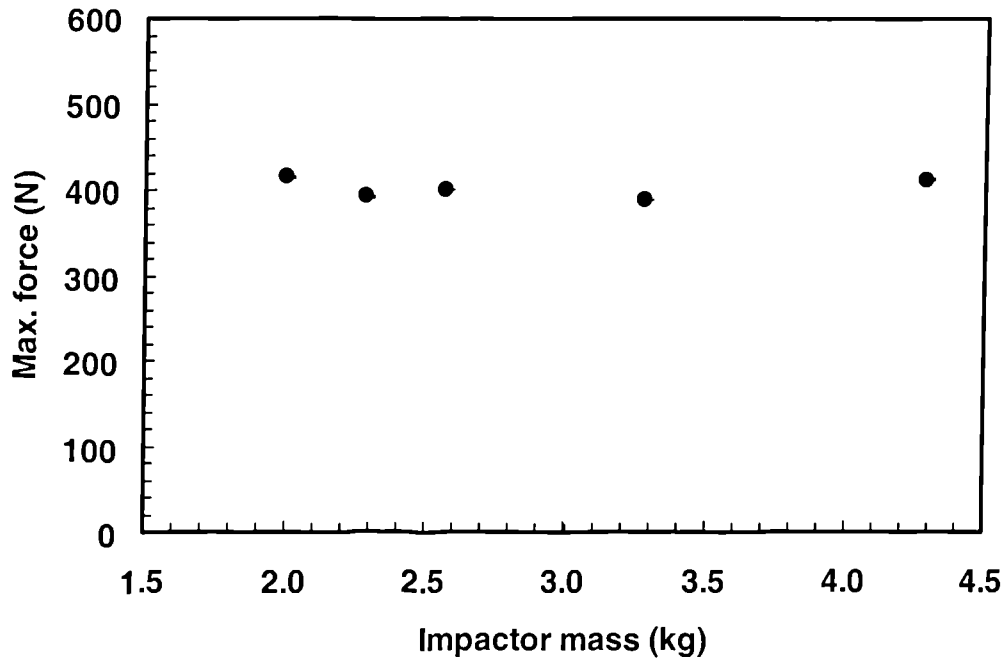


Figure 7.65: The variation of the maximum impact force with impactor mass at a constant impact energy of 0.97 Joules for an aluminium honeycomb beam. The span was 200 mm.

From the results, it is clear that varying both impactor mass and impact velocity for a constant energy does not affect the resulting maximum impact force, as the force remains constant over the range of impactor masses considered. After the tests, the impacted beams were sectioned to assess if the level of damage was the same in all beams. Cross-sections of the impacted specimens are shown in Figure 7.66. From the figure, it is clear that the damage mechanisms involved in these samples are very similar although the degree of the damage is slightly different from one to another, suggesting that the damage is dependent upon the location at which the impactor hit the honeycomb

cells. The micrographs (Figure 7.66) do show that damage is localised to the top of the sandwich structure, usually within the honeycomb core. It was noted that the band-saw introduced some damage into the cores. This may be due to the fact that the aluminium cell is relatively soft and susceptible to the cutting process. These results are similar to the work reported by Robinson and Davies [20] who suggested that the type and severity of impact damage is a function of the impact energy alone and not dependent on the impact velocity or impactor mass.

Dorey *et al.* [21] studied the effect of varying the impact velocity between 2.2 and 8.9 m/s at constant impact energies of 0.75 and 2.0 Joules and showed that the damage exhibited little variation over the range of impact velocities considered. It has been shown by Swanson [22] that the ratio of the impactor mass to the target may need to be at least 9:1 in order to yield in a quasi-static target response during impact. The average masses of the foam core and aluminium core sandwich beams were 20 and 18 grams respectively whereas for laminated composite and aluminium honeycomb sandwich plates, they were 135 and 180 grams. It is clear that all of the targets considered here satisfy this condition with a ratio greater than 9:1. Therefore, one would expect the beams to respond in a quasi-static mode.

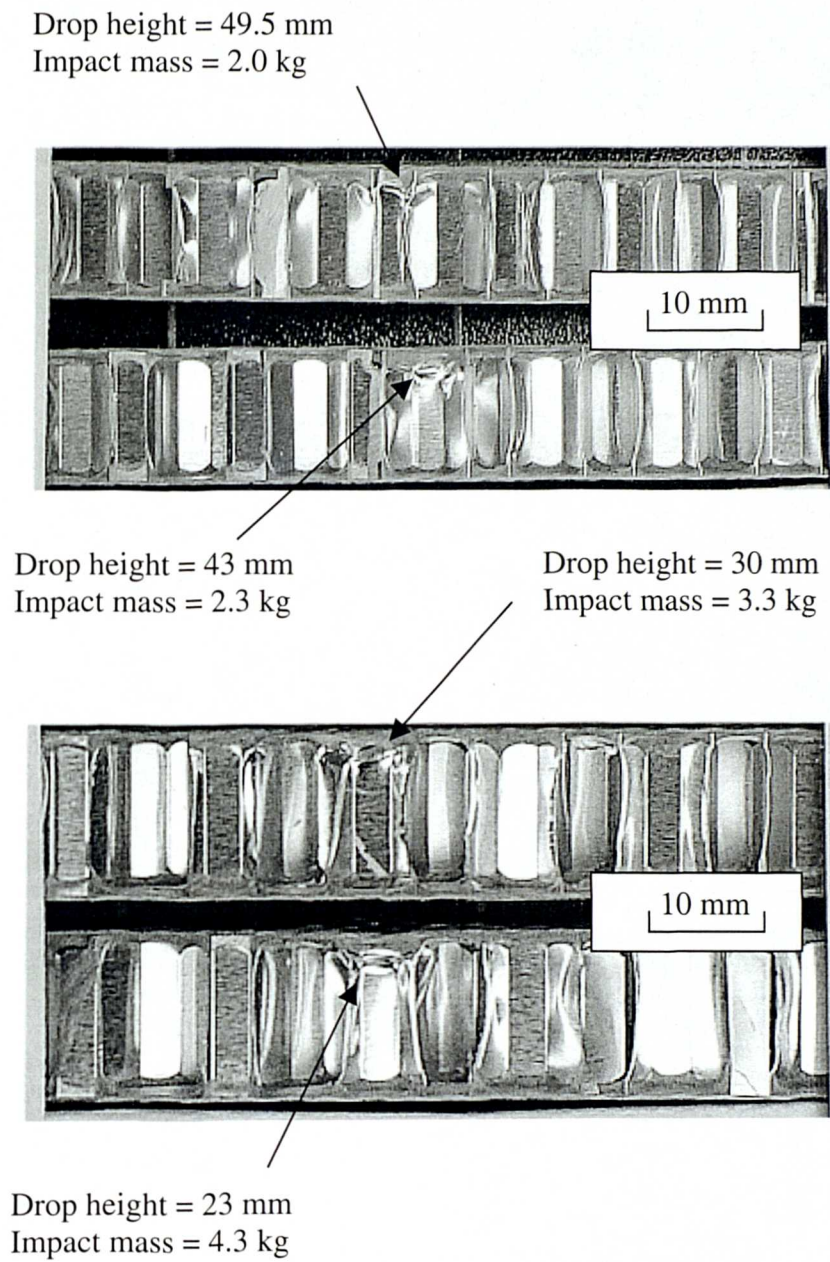


Figure 7.66: Cross-sections of the aluminium honeycomb sandwich panels after an impact energy of 0.97 Joules.

7.5.2 Impact tests on the aluminium honeycomb sandwich panels

The impact response of the aluminium honeycomb sandwich structure was further examined by conducting impact tests on sandwich plates, these being considered a more representative structure. Since no solution exists for the bending and shear behaviour of such types of centrally-loaded circular sandwich plates, the stiffness due to bending and shear was calculated experimentally. Here, the bending and shear stiffness K_{bs} was calculated by conducting tests in which the panel was loaded centrally and the displacement was measured using a displacement gauge positioned under the sample. A load-displacement relationship of the form of $P = K_{bs}\delta$ was used. The energy-balance model for the sandwich panel can now be written as:

$$\frac{1}{2}mv^2 = \frac{P_{\max}^2}{2} \left(\frac{1}{K_{bs}} \right) + \frac{C \left(\frac{P_{\max}}{C} \right)^{n+1}}{n+1} \quad (7.9)$$

Where

$$K_{bs} = \frac{K_b K_s}{K_b + K_s} = 8.5 \times 10^5 \text{ Nm}^{-1} \text{ (from } P = K_{bs}\delta \text{)}$$

δ = Displacement of the panel (m)

'C' and 'n' are the contact stiffness parameters in Meyer's law

The values of the contact parameters 'C' and 'n' used here were the same as those used in modelling the beam structure, i.e. $1.75 \times 10^6 \text{ N/m}^{1.16}$ and 1.16 respectively. In order to establish the value of the bending and shear stiffness, K_{bs} , a series of static flexural tests were carried out. The specimen was loaded up to a load of 250 Newtons and the displacement of the lower surface was measured using a displacement gauge. A plot of load versus displacement was made and a linear fit was applied to the points. A typical example of a plot used to determine the flexural response of a circular aluminium

honeycomb sandwich plates is shown in Figure 7.67. The data in the figure yields a value of K_{bs} of 8.5×10^5 N/m.

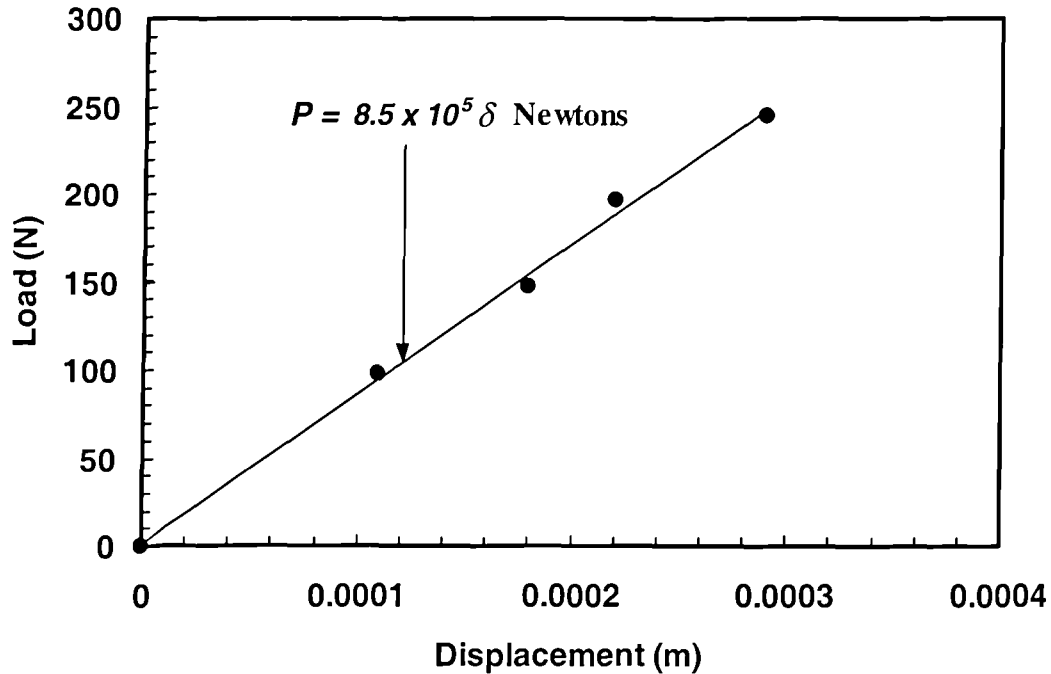


Figure 7.67: Typical example of the load-displacement trace for characterising the flexural response of the circular aluminium honeycomb sandwich plates.

The results of the impact tests on the circular aluminium honeycomb sandwich panels are shown in Figure 7.68. Included in the figure are the predictions offered by the energy-balance model. From the figure, it is clear that the maximum impact force is slightly over-estimated by the energy-balance model. This is perhaps expected since the method for determining the flexural stiffness of the plates is not very accurate. However, agreement is still good.

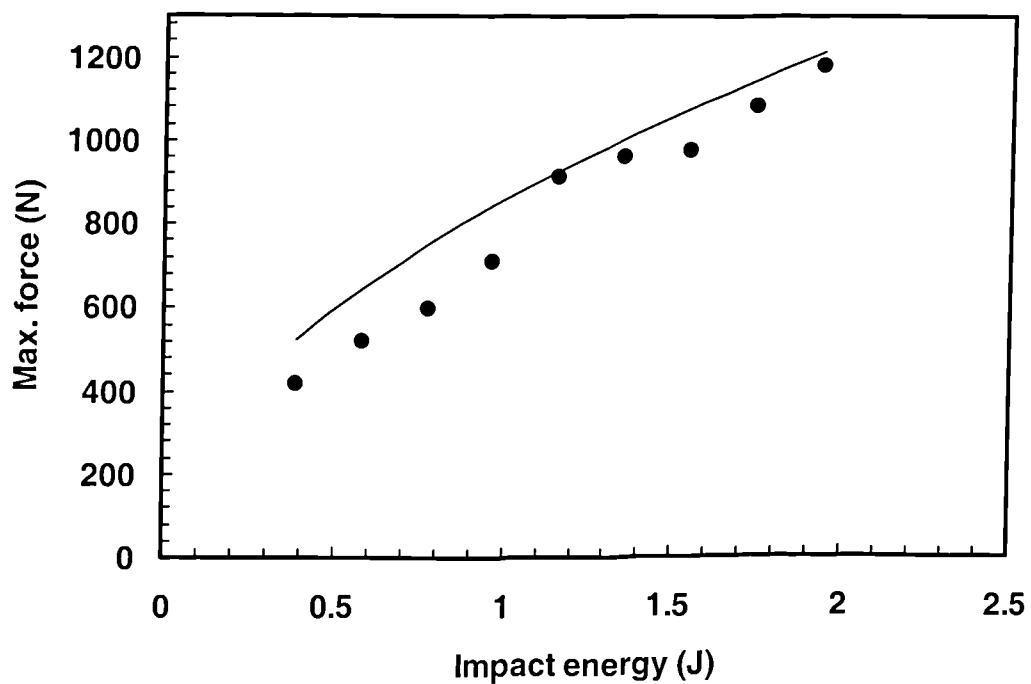


Figure 7.68: The variation of maximum impact force with impact energy for a simply-supported circular aluminium honeycomb sandwich panel with an internal diameter of 203 mm.

7.6 Energy absorption analysis for the aluminium honeycomb sandwich structures

A similar analysis was performed on the aluminium honeycomb sandwich beams and panels. The plot of a percentage of energy dissipation during impact as a function of impact energy for 13 mm thick aluminium honeycomb beam is shown in Figure 7.69. From the figure, it is interesting to note that the bending deformations are the predominant energy absorbing mechanism with a contribution between sixty-three and sixty-six percent over the range of impact energy considered. The second most dominant energy absorbing mechanism is contact deformation followed by shear deformation which absorbs between nineteen and twenty-one percent of the total impact energy.

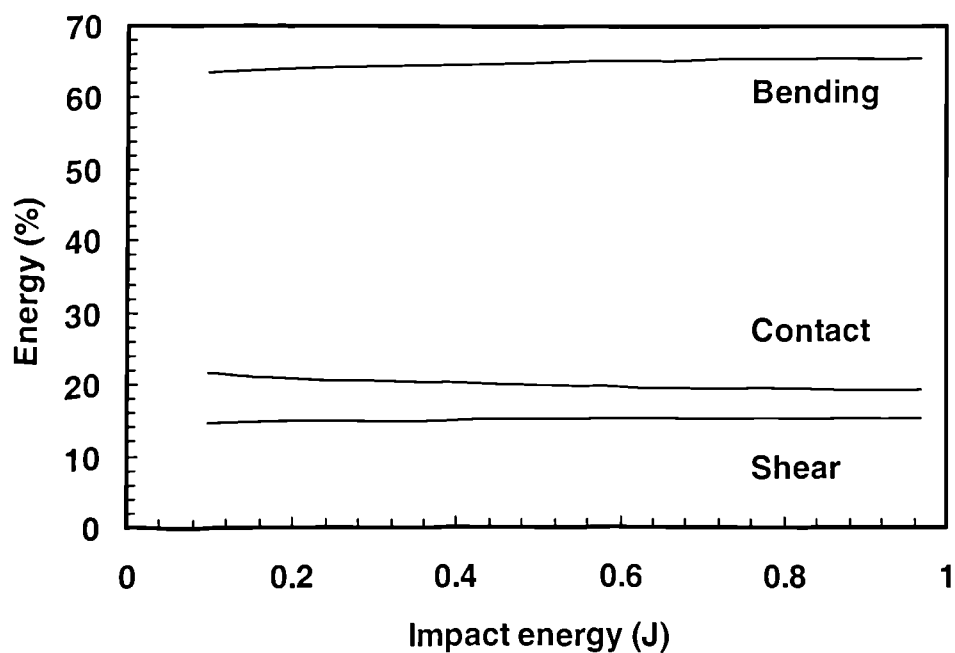


Figure 7.69: Energy breakdown during impact on an aluminium honeycomb sandwich beam. The span was 200 mm and core thickness is 13 mm.

The energy breakdown profiles in the aluminium honeycomb beams were further investigated by examining the effect of core thickness. A comparison between aluminium honeycomb beams based on 13 and 25 mm cores is shown in Figure 7.70.

From the figure, it is clear that the energy dissipation profile for the 25 mm thick beam is essentially the same as that for 13 mm beam with bending deformation being the key energy absorbing mechanism followed by contact and shear deformations. It is worth noting that the energy absorption due to bending and shear deformations decreases as the core thickness increases from 13 to 25 mm whereas the energy absorbed in contact deformation increases by between six and seven percent as the core thickness increases. These results tentatively agree with the foam data where increasing the stiffness of the beam resulted in an increase in energy absorbed in contact effects.

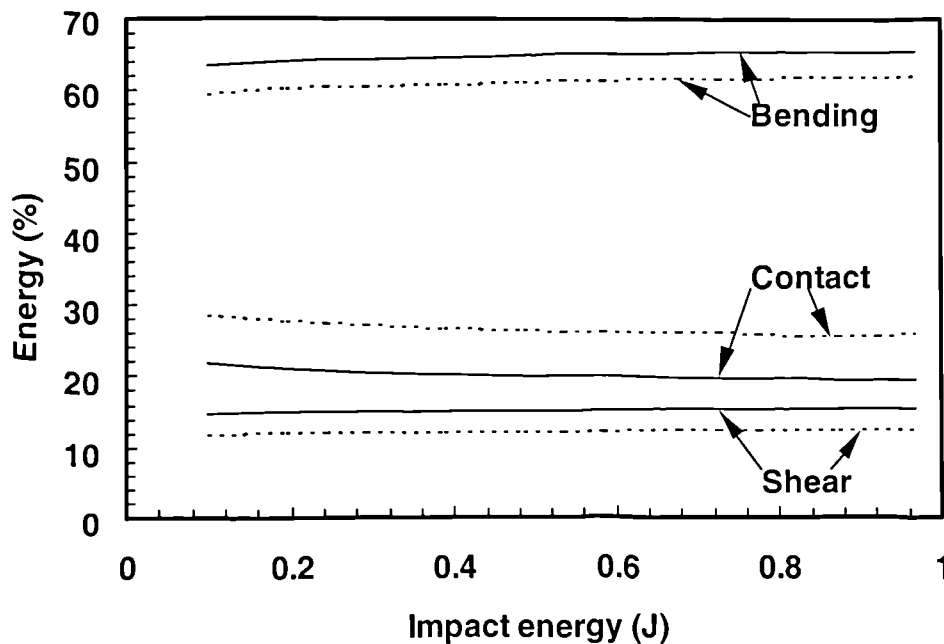


Figure 7.70: Energy breakdown during impact on an aluminium honeycomb sandwich beams. The span was 200 mm. The solid lines represent a core thickness of 13 mm and the dotted lines correspond to a core thickness of 25 mm.

In the case of a circular aluminium honeycomb sandwich plate with a radius of 101.5 mm, Figure 7.71, contact deformations are the predominantly energy absorption

mechanism with only forty to forty-five percent energy being absorbed in bending and shear deformations. Again, this suggests that contact effects are more significant in stiffer structures.

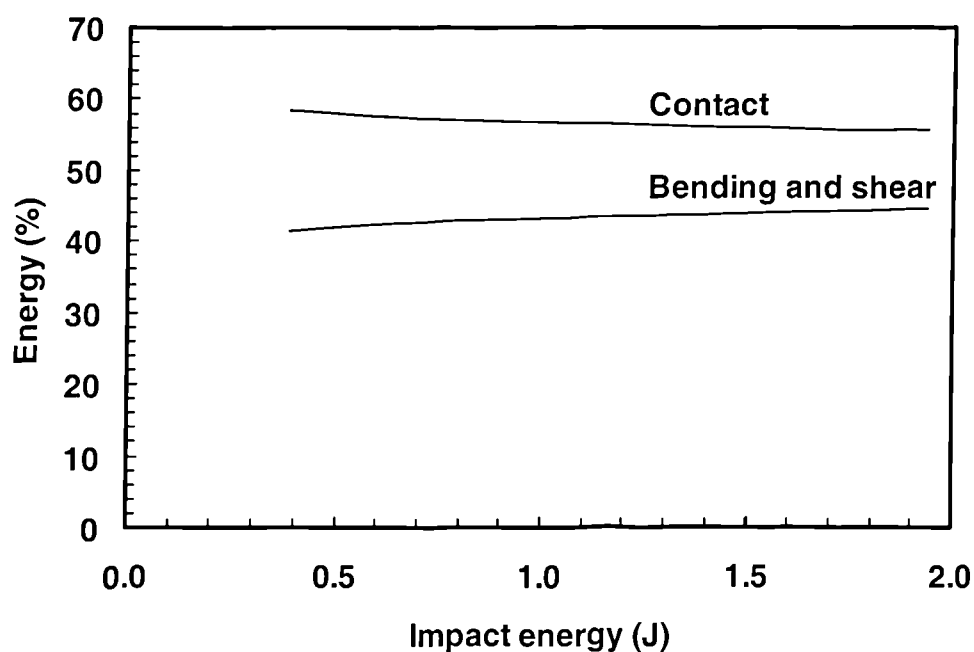


Figure 7.71: Energy breakdown during impact on an aluminium honeycomb sandwich plate with radius of 101.5 mm. The core thickness is 13 mm.

7.7 Damage development under low velocity impact loading

The following sections will discuss the damage and failure mechanisms observed following the impact tests on the composite beams and the sandwich structures. Images from a low magnification microscope and a digital camera have been used to identify and characterise the damage and modes of failure in the samples.

7.7.1 Impact damage in laminated composite beams

The nature of impact damage in a laminated composite structures is clearly very complex. Depending on the characteristics of the impacting bodies, the resulting damage may be local (contact), global (structural) or a combination of both. Local impact damage consists mainly of visible permanent indentation in the contact zone which normally involves matrix and fibre fracture and global impact damage is usually extensive with embedded delaminations. This type of impact damage is far more complex than the local contact damage described earlier. As far as this study is concerned, damage in the laminated composite beams consisted mainly of delamination and matrix cracking without a significant amount of fibre fracture. Delamination is known to reduce the residual compressive strength of a laminated structure [23]. Fibre cracks in the contact zone will cause a substantial reduction in the residual tensile strength of the structure, but have a little effect on the residual compressive strength [23]. The damage mechanisms under low velocity impact loading do not differ significantly from the failure mechanisms under static loading [23]. The failure process often starts at some point under the impacted area where the stress exceeds the failure stress. This can be seen as the small visible damage observed on the top surface of the beam. This may also be explained by the fact that the piezo-electric load cell is not sensitive enough to detect the changes in force due to the localised matrix micro-cracking. This evidence is supported by Sjoblom [24] who stated that the presence of matrix cracks does not dramatically affect the overall laminate stiffness, however, the tips of matrix cracks can act as initiation points for delaminations and fibre breaks to occur which can dramatically change the local and global stiffness of the composite

affect the load-time response. Optical micrographs showing damage in the eight-ply GFRP beams subjected to impact energies of 0.7 and 0.9 Joules are shown in Figure 7.72. From the micrograph in Figure 7.72a, it is clear that a large number of cracks and delaminations are present at an impact energy as low as 0.7 Joules. The cracks extended in size and number as the impact energy increases to 0.9 Joules, Figure 7.72b. It is worth noting that despite the presence of these cracks and delaminations, the prediction offered by the energy-balance model still agreed well with the experimental as shown earlier in Figure 7.41.

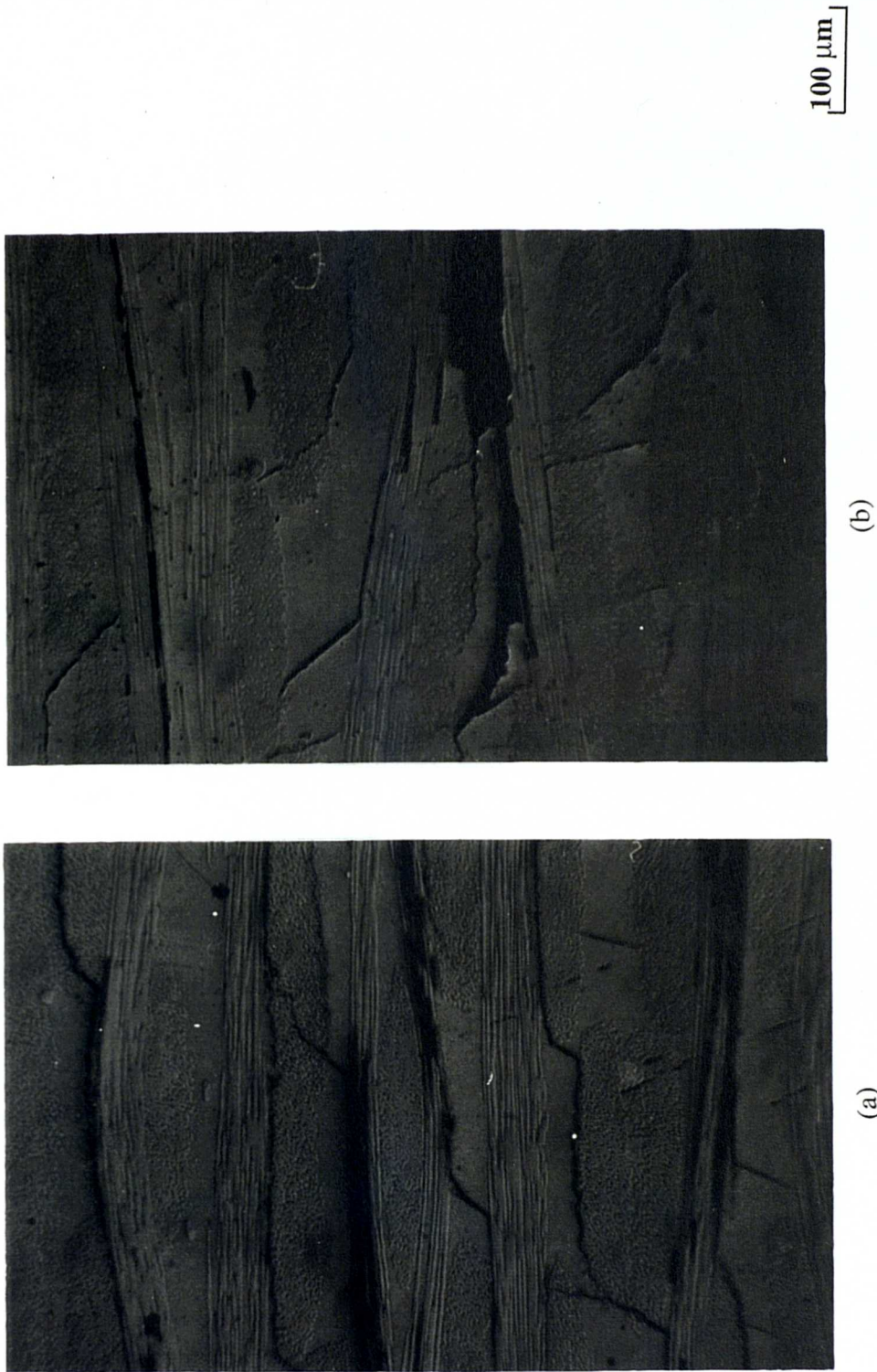


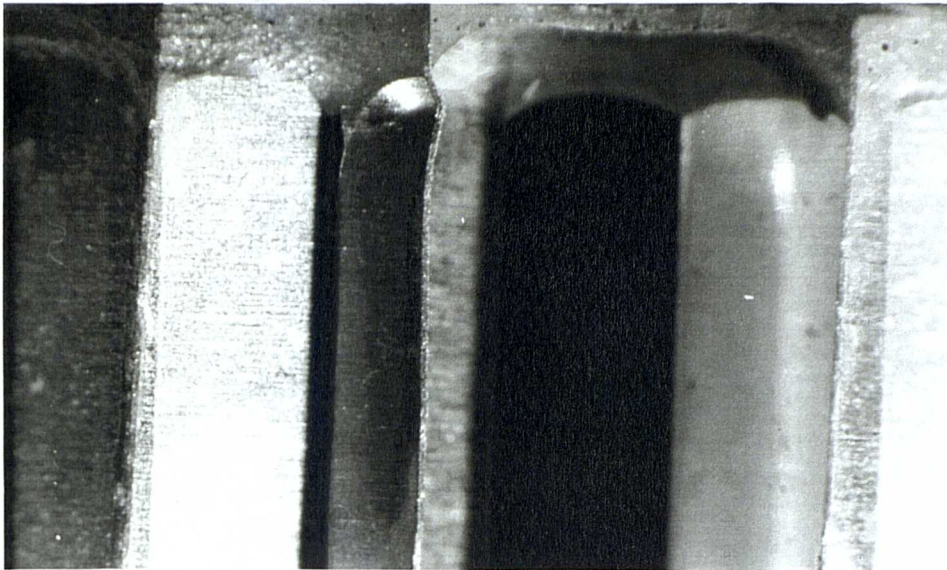
Figure 7.72: Optical micrographs showing damage in 8-ply GFRP beams subjected to impact energies of (a) 0.7 Joules and (b) 0.9 Joules.

7.7.2 Impact damage in the aluminium honeycomb beams and panels

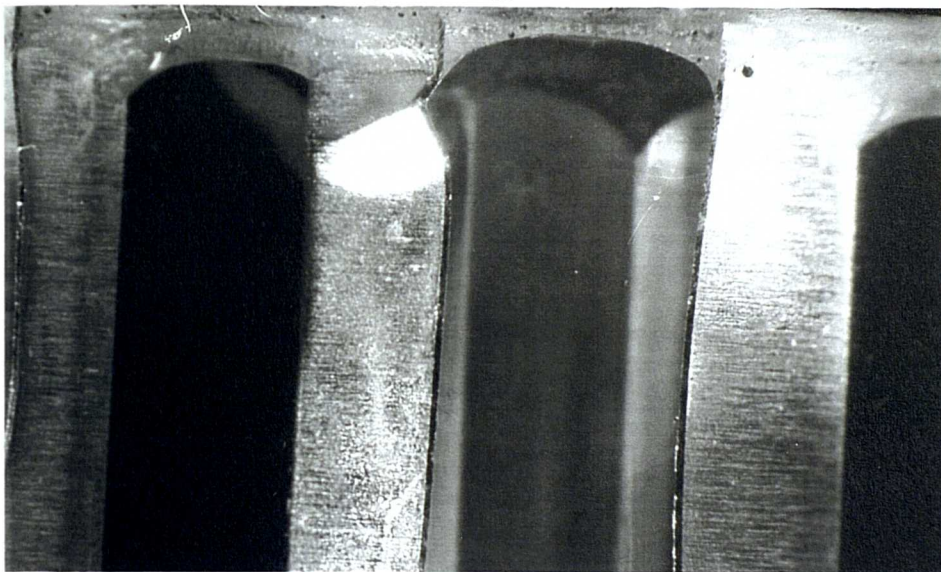
Damage initiation and propagation in the sandwich aluminium honeycomb beam was obviously different from that in the laminated beams due to their thin skins and lightweight core. Therefore, the aluminium honeycomb sandwich structures are more prone to damage. A series of photographs showing damage in aluminium honeycomb beams are presented in Figure 7.73.

Damage was observed in the honeycomb core cells at impact energies as low as 0.19 Joules. At this stage, it is worth noting that no visible damage was apparent on the top skin of the beam. As the impact energy was increased to 0.38 Joules, damage in the core cell becomes clearer taking the form of a buckled cell directly under the point of impact. As the energy increase to 0.58 Joules, more severely buckled-cells can be seen. At an impact energy of 0.78 Joules, buckling becomes more serious, spreading to the adjacent aluminium core cell and slight damage in the form of fibre cracking was observed to the top skin. However, it is interesting to note that at this level of damage in the aluminium core, the energy balance model still provide a very good prediction for the experimentally-determined values. This suggests that such impact damage in the aluminium honeycomb core does not directly affect the impact response of these structures. Anderson and Madenci [19] also reported similar observations following impact tests on an aluminium honeycomb sandwich structure. They stated that, even though the skin exhibited very little visible damage, the honeycomb core beneath the point of impact had suffered a significant cell buckling.

Impact energy = 0.19 J



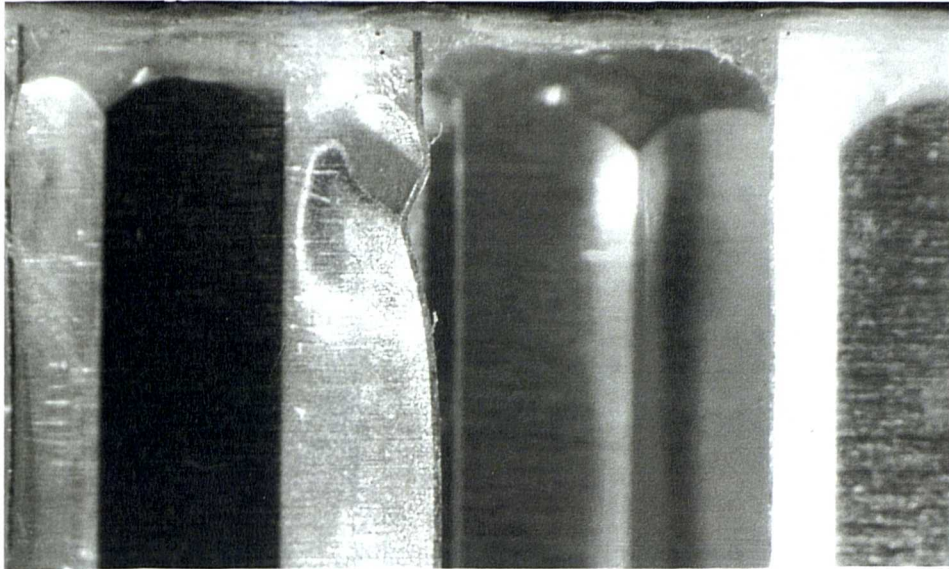
Impact energy = 0.38 J



3 mm

Figure 7.73a: Low power micrographs showing damage initiation and propagation in the aluminium honeycomb beams. The span = 190 mm and the thickness = 13 mm.

Impact energy = 0.58 J



Impact energy = 0.78 J

3 mm

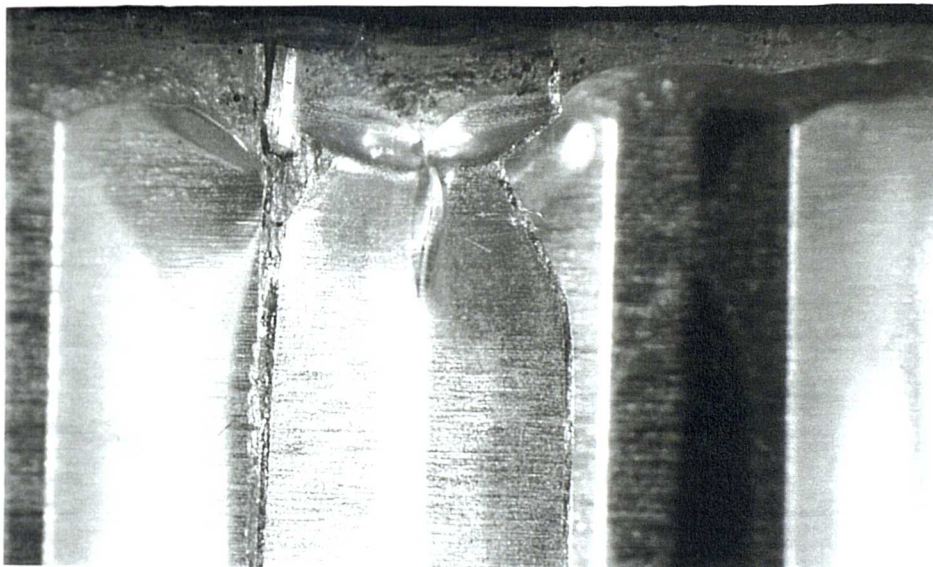


Figure 7.73b: Low power micrographs showing damage initiation and propagation in the aluminium honeycomb beams. The span = 190 mm and the thickness = 13 mm.

The study of damage in the aluminium honeycomb sandwich structures under the low velocity impact was further extended by comparing the damage in the circular panels to the damage observed in the aluminium honeycomb sandwich beams. Cross-sections of sandwich plates taken at various impact energies are presented in Figure 7.74. As can be seen, the level of damage is much great in the circular plates than in the beams. This is due to the fact that the impact forces are significantly higher in the stiffer plates.

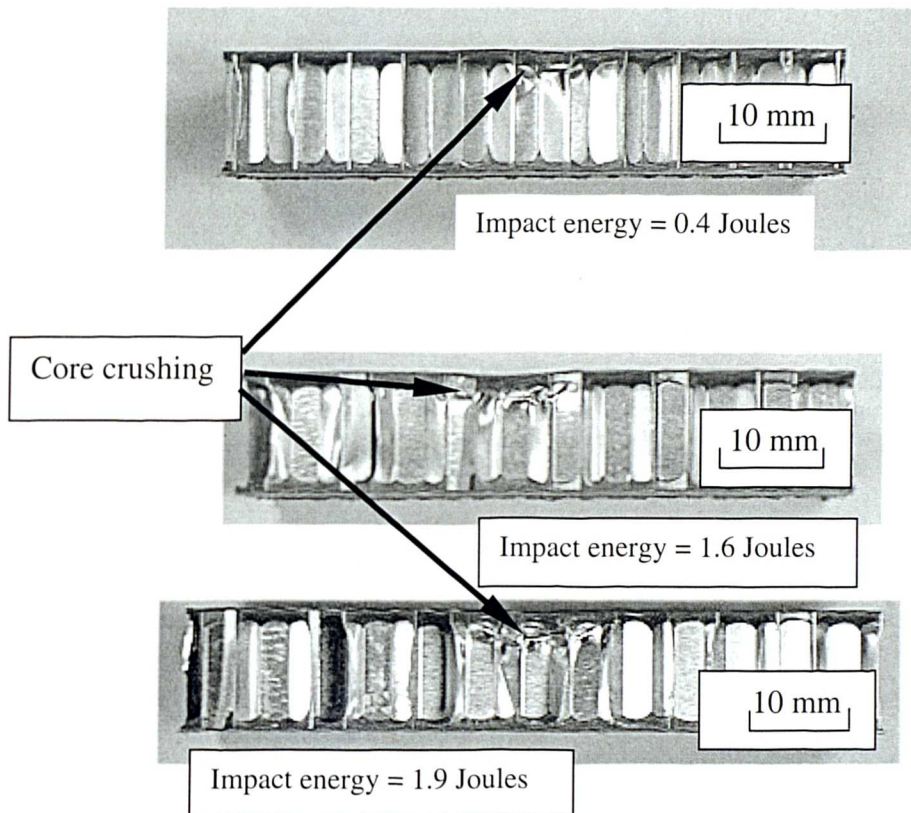


Figure 7.74: Images showing damage in the circular aluminium honeycomb plates. Plate diameter = 203 mm.

Figure 7.75 shows a series of images taken using a high-speed camera during impact tests on the aluminium honeycomb sandwich beam during a 0.97 Joule impact. It is clear that some bending of the beam occurs during impact with little evidence of much indentation occur during impact. From the figure, it is clear that the response of the aluminium can be considered within the quasi-static response.

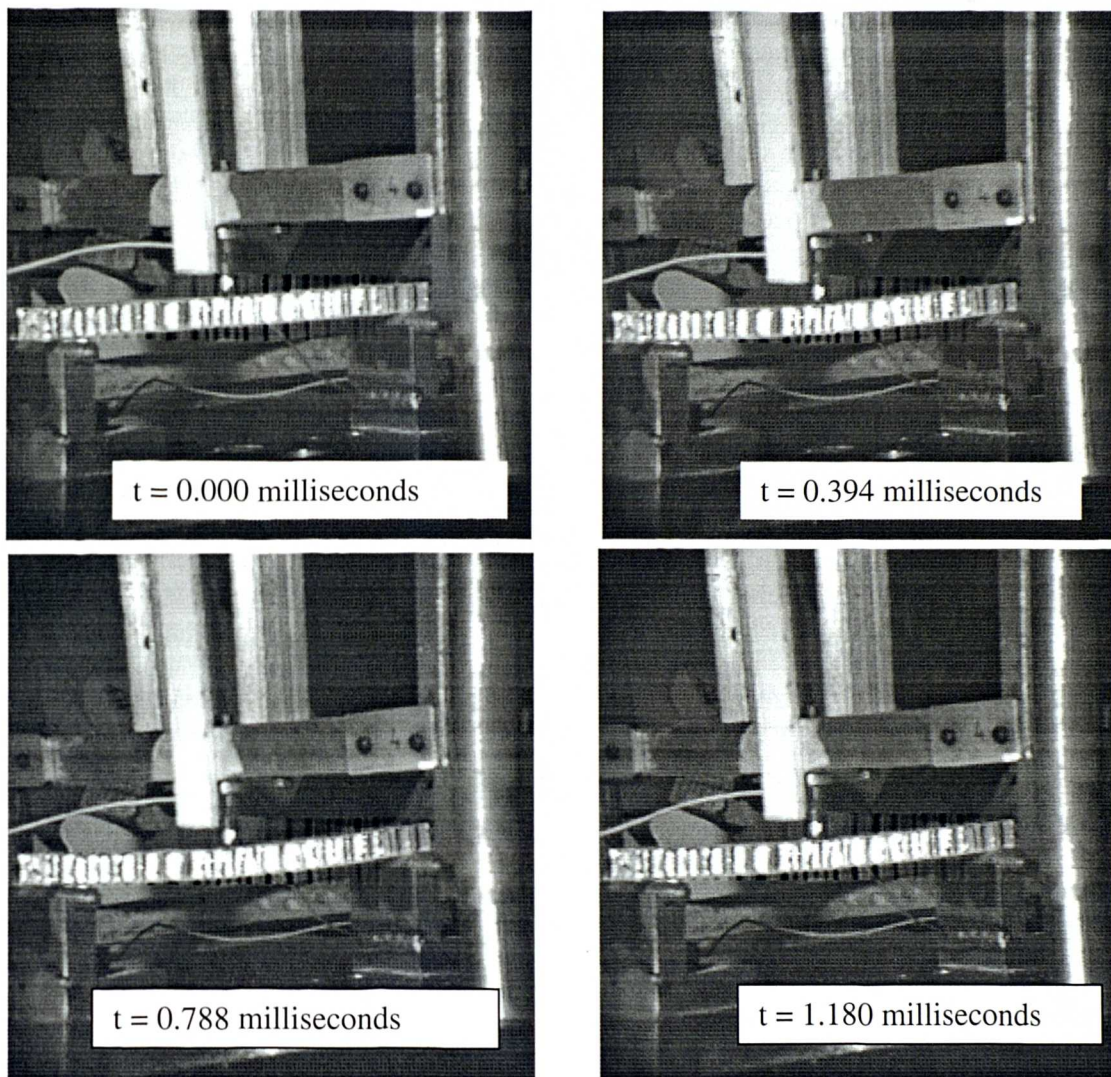


Figure 7.75: A series of images taken using a high-speed camera during impact test on the sandwich aluminium honeycomb beam. Impact energy = 0.97 Joule. 't' indicates the time at which the frame was taken.

7.7.3 Impact damage in the foam core sandwich beams

Damage initiation and propagation in the foam core sandwich beams was also investigated. As expected, the modes of failure in the foam core sandwich beams are very different from those observed in the aluminium honeycomb sandwich beams. This is due to the fact that the foams exhibit a range of properties from brittle to ductile depending on the density and properties of the polymeric foam materials itself. Micrographs of damaged beam samples subjected to low velocity impact are presented in Figure 7.76.

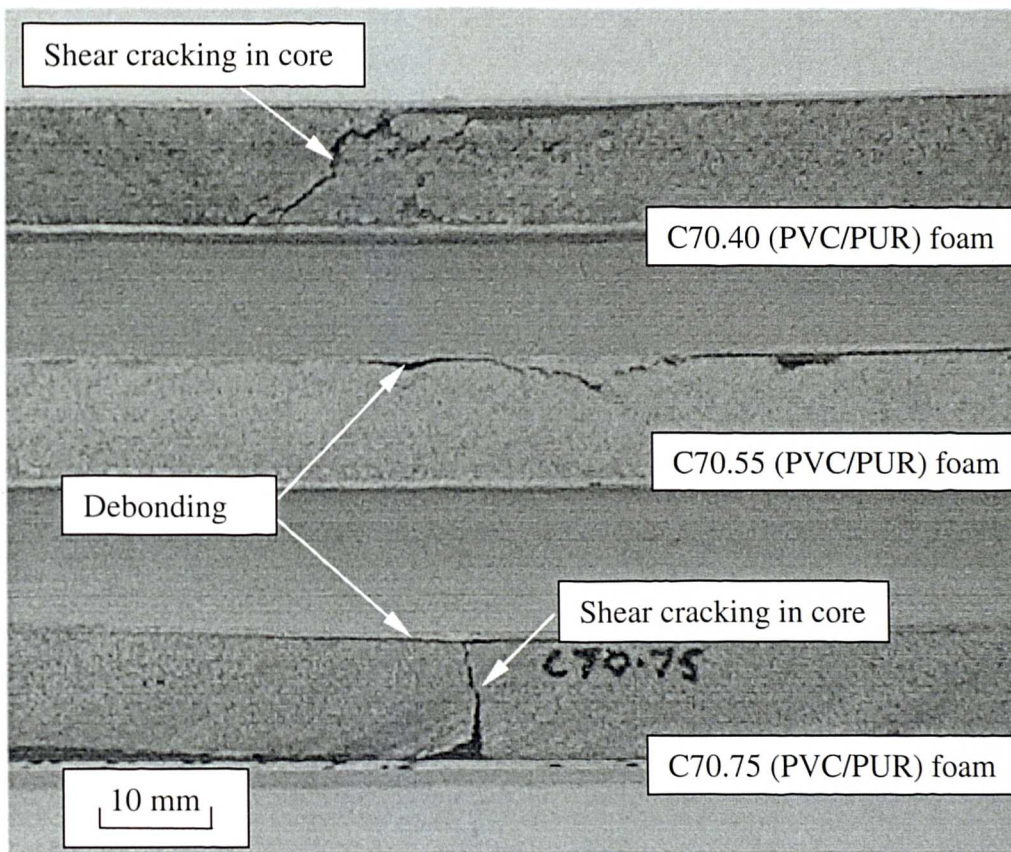


Figure 7.76a: Images showing damage in sandwich structures based on C70 foams. Impact energy = 1.36 Joules.

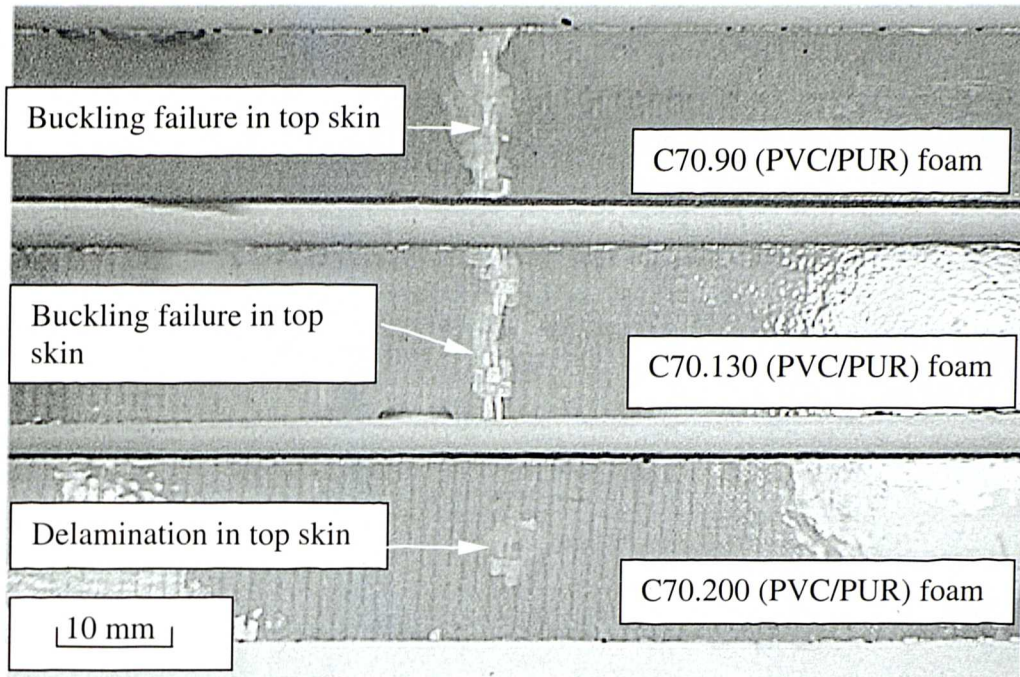


Figure 7.76b: Images showing damage in sandwich structures based on C70 foams. Impact energy = 1.74 Joules

As far as C70 foams are concerned, the systems with densities of 40 kg/m^3 , 55 kg/m^3 and 75 kg/m^3 are the most brittle as shown in Figure 7.76a. In brittle foam core sandwich structures, the common mode of failure was shear cracking through the depth of the core material. This is not surprising since these three foam cores offered the lowest values of work of fracture (55 , 130 and 210 J/m^2 for the 40 , 55 and 75 kg/m^3 core materials respectively). Failure in the higher density C70 (PVC/PUR) system i.e. the C70.90 and C70.130 system, occurred as a result of buckling in the top skin. Failure in the highest density C70.200 system was due to delamination in the top skin immediate to the point of impact, Figure 7.76b. From these figures, it is apparent that the failure in these sandwich structures is governed by the fracture properties of the core materials. Table 7.5 summarises the predominant failure modes in sandwich structures tested in this study. The R63 (Linear PVC) foams are considered the toughest group of foam cores in this study. Micrographs showing the failure modes in the R63-based foam-core structures are shown in Figure 7.76c. From the figure, it is clear that the failure takes in the form of a buckling fracture in the uppermost skin of the sandwich structure. A

similar mode of failure was also observed in the R82 (Linear PEI) foam-core sandwich structures, Figure 7.76d. From the trends shown previously, it is also worth noting that the failure modes in the sandwich structures is not only governed by the properties of the core material but also influenced by the degree of the support that is provided by the core material in resisting the impact forces generated during impact. If the core is very brittle, initial failure is likely to take the form of shear cracking through the thickness of the foam-core material. In contrast, if the foam is tough enough to prevent shear cracking from occurring, initial failure occurs as a result of buckling of the top skin. In this case, the elastic modulus of the foam is relatively low and the skin receives little support against buckling. For the higher density foams, such as C70.200 (200 kg/m^3), R63.140 (140 kg/m^3) and C70.130 (130 kg/m^3) with elastic moduli of 178, 90 and 109 MPa respectively, buckling is less likely to occur and failure, in the form of delamination within the top surface skin, occurs under the impactor as a result of the higher impact forces.

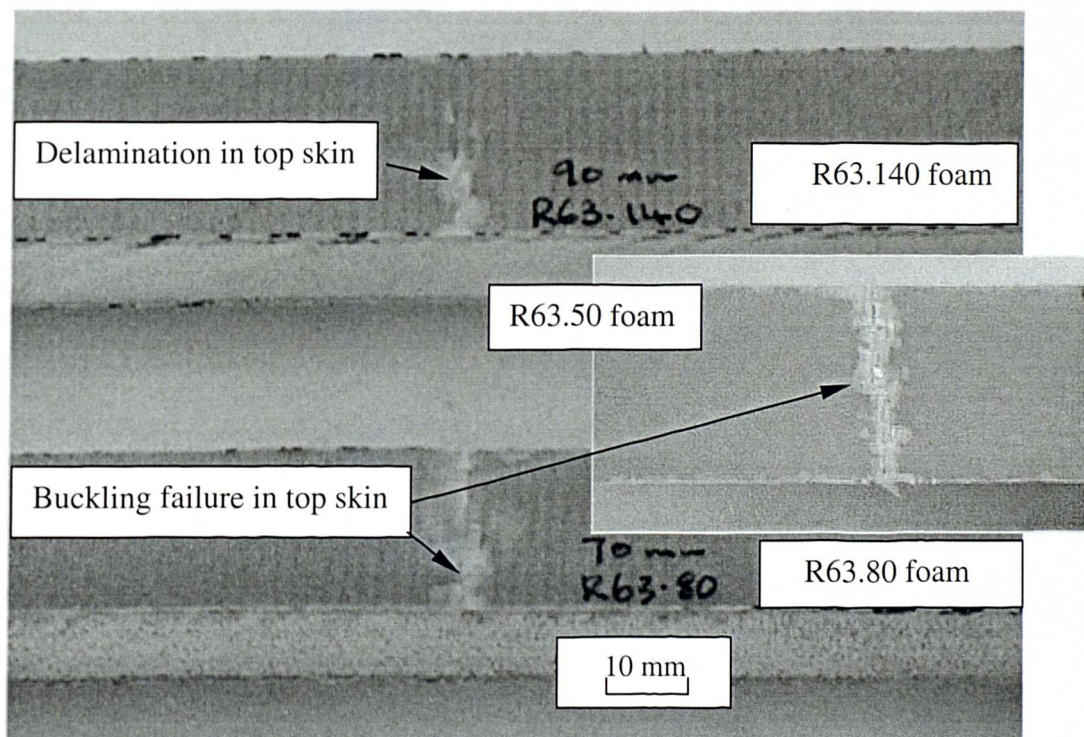


Figure 7.76c: Micrographs showing damage in the sandwich structures based on R63 foams. Impact energy = 1.4 Joules.

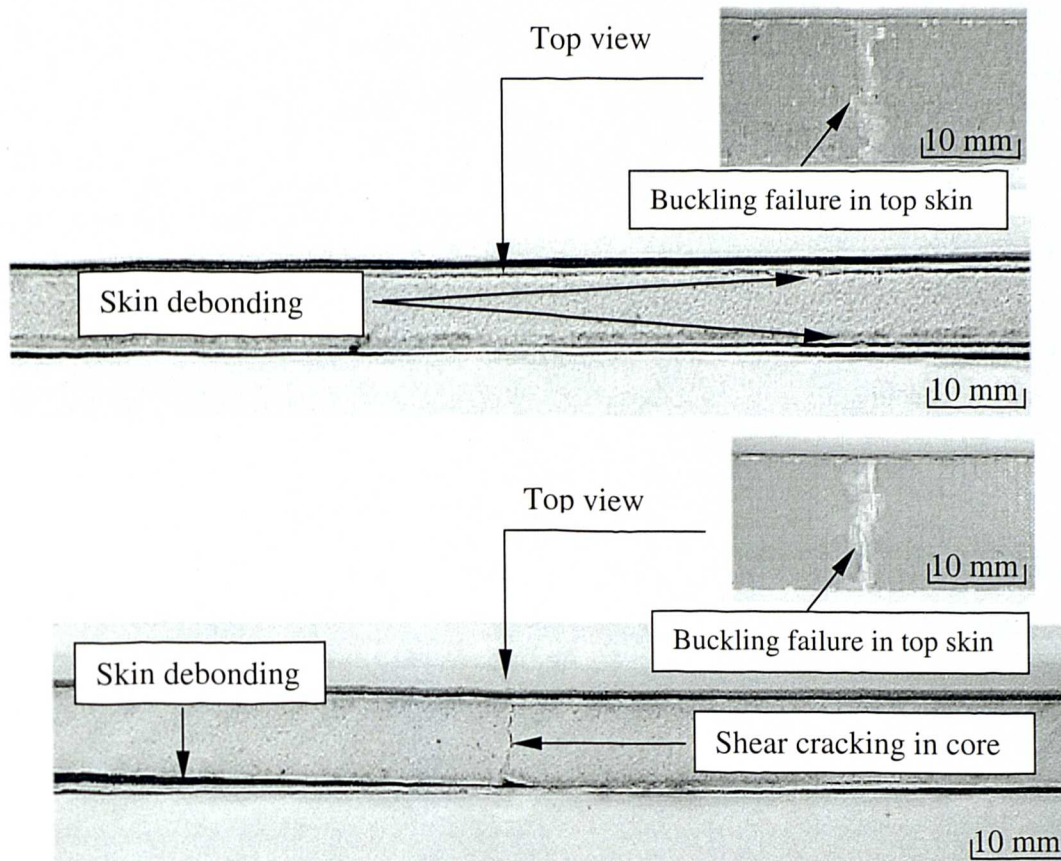


Figure 7.76d: Micrographs showing the modes of failure in the sandwich structures based on R82 foams. Impact energy = 1.4 Joules.

Figure 7.77 shows a series of images taken using a high-speed camera during impact on an R63.50 sandwich beam during a 0.97 Joule impact. Clearly, a significant degree of deformation with global and local (indentation) has taken place during the impact event. This is much greater than in the case of aluminium honeycomb beam when subjected to a similar impact energy. Clearly, the aluminium honeycomb beam is stiffer than foam-core sandwich beam. The fact that the beam responds in quasi-static mode supports the conclusion that an energy-balance can be applied to model the impact response of these sandwich structures.

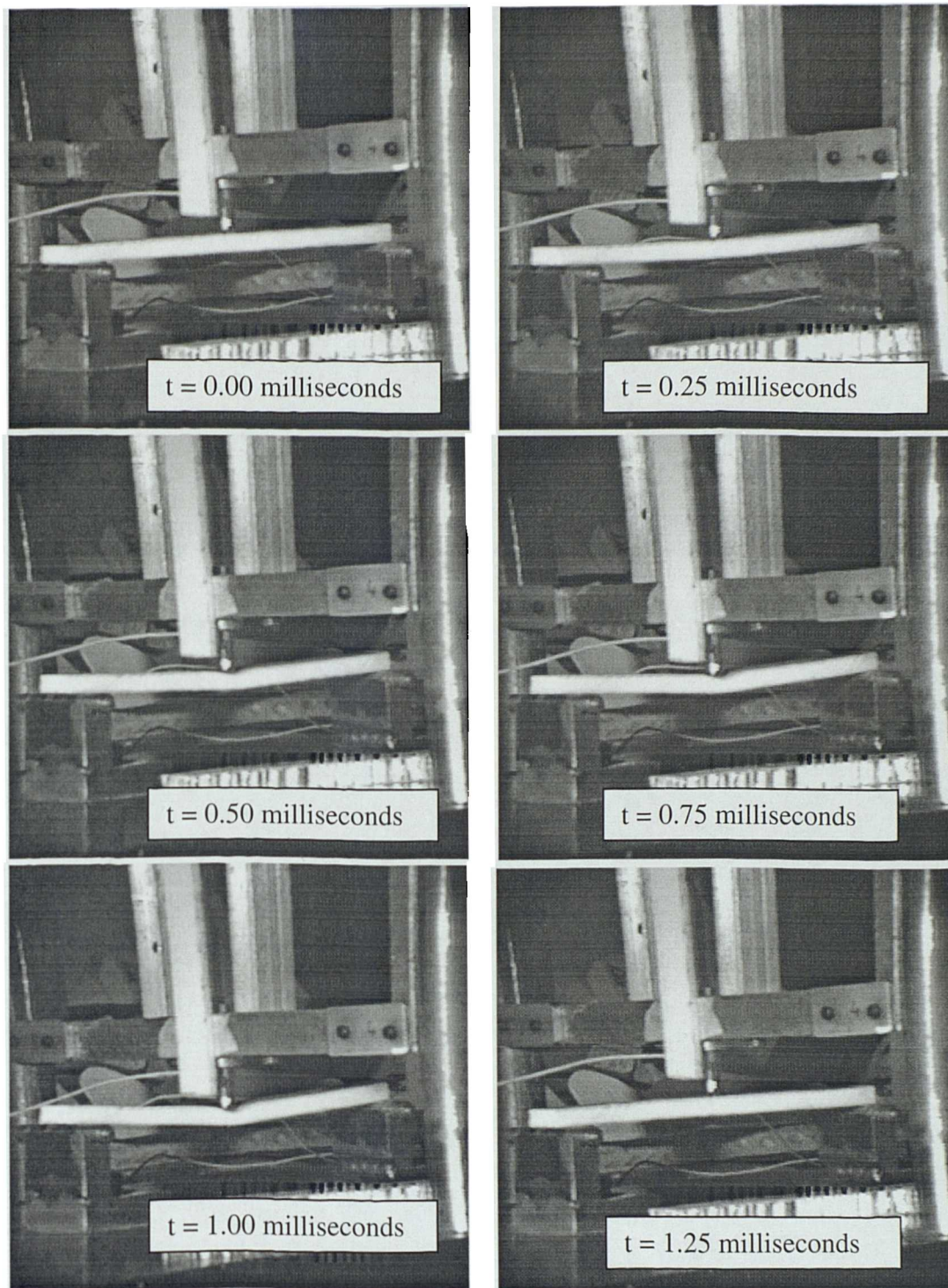


Figure 7.77: A series of images taken using a high-speed camera during impact tests on the R63.50 foam-core sandwich beam. Impact energy = 0.97 Joule and the span = 200 mm. 't' indicates the time at which the frame was taken in seconds.

Foam code	Foam description	Skin-core work of fracture (J/m^2)	Failure energy under impact (J)	Initial failure mode(s) under impact
C70.40	PVC/PUR	30.9	0.58	Shear cracking in core
C70.55		47.5	1.36	Shear cracking in core
C70.75		42.1	0.97	Shear cracking in core
C70.90		52.6	1.36	Buckling failure in top skin
C70.130		56.6	1.36	Buckling failure in top skin
C70.200		761.0	1.36	Delamination in top skin
R63.50	Linear PVC	354.6	0.58	Buckling failure in top skin
R63.80		120.9	0.97	Buckling failure in top skin
R63.140		-	1.36	Delamination in top skin
R82.60	Linear PEI	70.3	1.16	Buckling failure in top skin
R82.80		50.1	1.36	Buckling failure in top skin

Table 7.5: Summary of the skin-core interface fracture properties, the failure energies and failure modes in the eleven foams considered in this study.

7.8 References

1. W.J. Cantwell, M. Büsser and H.H. Kausch, "An analysis of the impact response of a composite beam", *Composites Engineering*, 1, pp 293-307, 1991.
2. A. Rotem, "Residual flexural strength of FRP composite specimens subjected to transverse impact loading", *SAMPE Journal*, pp 19-25, 1988.
3. J. Harding and L.M. Welsh, "A tensile testing technique for fibre-reinforced composites at impact rates of strain", *J. Materials Science*, 18, pp 1810-1826, 1983.
4. Q.M. Li, R.A.W. Mines and R.S. Birch, "The crush behaviour of Rohacell-51WF structural foam", *Int. J. of Solids and structures*, 37, pp 6321-6341, 2000.
5. L.J. Gibson and M.F. Ashby, "Cellular Solids: Structure and Properties", Second edition, Cambridge University Press, U.K., 1997.
6. D.W. Reitz, M.A. Schnetz and L.R. Glicksman, *J. Cellular Plastics*, 20, pp 104-105, 1984.
7. W.J. Cantwell, "The fracture properties of polymer foams", Confidential report for Airex Ltd, 2000.
8. A. McIntyre and G.E. Anderton, "Fracture properties of a rigid polyurethane foam over a range of densities", *Polymer*, 20, pp 247-253, 1979.
9. P. Davies, D. Choqueuse, L. Riou and A. Wahab, "Response of composite sandwich panels to impact loading", *Revue de l' Institute, Francais du Petrole*, 50, pp 75-82, 1995.
10. S. Abrate, "Impact on Composite Structures", Cambridge University Press, 1998.
11. R. Olsson, "Impact response of composite plates-a guide to closed form solutions", FFA TN 1992-33, The Aeronautical Research Institute of Sweden, 1992.
12. R.A.W. Mines, C.M. Worrall and A.G. Gibson, "Low velocity perforation behaviour of polymer composite sandwich panels", *Int. J. Impact Engng*, 21, pp 855-879, 1998.
13. R.A.W. Mines, C.M. Worrall and A.G. Gibson, "The static and impact behaviour of polymer composite sandwich beams", *Composites*, 25, pp 95-110, 1994.

14. A. Gilchrist and N.J. Mills, "Impact deformation of rigid polymeric foams: experiment and FEA modelling", *Int. J. Impact Engng.*, 25, pp 767-786, 2001.
15. J. Miltz and O. Ramon, "Energy absorption characteristics of polymeric foams used as cushioning materials", *Polymer Engineering and Science*, 30, pp 129-133, 1990.
16. L.J. Broutman and A. Rotem, "Impact strength and toughness of fibre composite materials", *ASTM STP 568*, pp 114-133, 1975.
17. M.S. Found and I.C. Howard, "Single and multiple impact behaviour of a CFRP laminate", *Composite structures*, 32, pp 159-163, 1995.
18. M. Wisheart and M.O.W. Richardson, "Low velocity response of simple geometry pultruded glass/polyester composite", *J. Materials Science*, 34, pp 395-406, 1999.
19. T. Anderson and E. Madenci, "Experimental investigation of low-velocity impact characteristics of sandwich composites", *Composite Structures*, 50, pp 239-247, 2000.
20. P. Robinson and G.A.O. Davies, "Impactor mass and specimen geometry effects in low velocity impact of laminated composites", *Int. J. Impact Engng*, Vol. 12, pp 189-207, 1992.
21. G. Dorey, P. Sigerty, K. Stellbrink and W.G.J. T'Hart, "Impact damage tolerance of carbon fibre and hybrid laminates", *Garteur TP-003*, Royal Aircraft Establishment Technical Report 87057, 1987.
22. S.R. Swanson, "Dynamic and scaling effects in impact of composite structures", 9th International Conference on Composite Materials (ICCM/9), 5, Woodhead Publishing Limited, pp 291-298, 1993.
23. T.C. Triantafillou and L.J. Gibson, "Failure mode maps for foam core sandwich beam", *Materials Science and engineering*, 95, pp 37-53, 1987.
24. P. Sjoblom, "Simple design approach against low velocity impact damage", 32nd Int. SAMPE Symposium, pp 529-539, 1987.

CHAPTER 8: CONCLUSIONS AND FURTHER WORK

Following this research study, a number of conclusions can be drawn and these are outlined as follows:

8.1 Mechanical tests

- From the flexural tests on the skin and core materials, it has been shown that the Young's modulus of these systems does not vary with crosshead displacement rate. This suggests that the materials are rate-insensitive.
- Following a series of indentation tests, it has also been shown that the indentation response of the sandwich structures does not vary with crosshead displacement rate, again suggesting a rate-insensitive behaviour.
- In contrast, the compression properties of the foam materials have shown a slight rate dependency. This is more pronounced in the higher density foams. For example, it has been shown that for high density C70.200 (PVC/PUR) foam, the increase can be up to fifteen percent.
- Tests to characterise the fracture toughness of the foam-core materials using the single edge notch bend (SENB) geometry revealed that the toughness of a foam is strongly dependent on its density. A higher foam density offers a greater resistance to fracture. The linear PVC foams were the toughest of three groups with PVC/PUR foams being the most brittle.
- Centre notch flexure (CNF) tests on all of the sandwich structures highlighted the low level of skin-core adhesion, particularly in the low-density foams.

8.2 Energy-balance model

- From the results obtained here, it is clear that the energy-balance model is capable of modelling the low velocity impact response of a range of simple laminates and sandwich structures. The accuracy of the predictions offered by the energy-balance model is very good particularly in the elastic regime. Differences between the

predictions and the experimental results are very small and generally less than five percent.

- The energy-balance model can also be used to establish the percentage of energy absorbed in shear, bending and contact deformations. From the energy partition analysis based on the energy-balance model, energy absorption in the low-density systems occurred predominantly in shear whereas contact effects were significant in the high-density systems. For example, at impact energy of 1.5 J, it has been shown that the energy dissipated in bending, shear and contact account for 14, 49 and 37 % in an intermediate density PVC/PUR foam whereas these figures are 32, 23 and 45 % for a high density PVC/PUR foam.
- The energy-balance model can also be used to identify the effect of varying core and skin properties as well as the geometry of the sandwich structure on the impact response.
- However, the energy-balance model breaks down when damage initiates in the sandwich structures. Further attempts to improve the model must include energy absorption in failure modes such as core crushing, skin-core debonding and fracture of the core.
- For a given impact energy, varying the impactor mass and impact velocity do not affect the impact response of the sandwich structure (i.e. maximum impact force). This suggests that the beam is responding in a quasi-static mode.

8.3 Impact response and damage

Different types of impact damage have been observed in this study depending on the properties of the materials and the test structure. In laminated composite beams and plates, matrix cracking and delamination under the point of impact is most common especially at intermediate and higher impact energies. In sandwich structures, core crushing, delamination in the skin, cracking in the skin, core cracking, skin-core debonding and cell buckling are the dominant modes of failure. The following conclusions were drawn upon examining the damaged specimens:

- In the lower density foam core, failure was dominated by core-associated failures such as core cracking.
- In higher density foam cores, skin-associated failure modes such as cracking and delamination are common.
- The skin thickness has a significant effect on the damage threshold energy. The damage threshold energy increases with increasing skin thickness. For example, the damage threshold increases from 0.4 J to 0.8 J by increasing the skin thickness from 0.5 mm to 1.0 mm.
- The fracture toughness of the core material also influences the damage threshold energy with a higher damage energy threshold being observed in tougher foams.
- The damage in the honeycomb sandwich structure takes the form of cell buckling in the aluminium honeycomb core.
- The damage threshold in the aluminium honeycomb beams increases as the span increases due to the increases in flexibility of the beam. For example, it has been shown that the damage threshold energy increases from 0.6 J to 1.6 J when the span increases from 200 to 300 mm.
- The core thickness plays an important role in determining the impact response of the aluminium honeycomb beams and panels. Thicker cores yield higher impact forces than thinner cores as a result of the increased flexural rigidity of the system.

8.4 Suggestion for further work

- It would be desirable to be able to accurately predict the damage threshold energy of the sandwich structures. In order to achieve this, appropriate failure criteria need to be selected for each of the failure modes.
- To extend the energy-balance model to consider energy absorption in fracture and failure modes.
- It would be interesting to consider larger components where $M_p / M_t \ll 10$ i.e. targets which no longer respond quasi-statically.

- To study the impact response of sandwich structures under high velocity impact loading.